THE STUDY OF TWO-PARTICLE RESPONSE FUNCTIONS IN STRONGLY CORRELATED ELECTRON SYSTEMS WITHIN THE DYNAMICAL MEAN FIELD THEORY

BY HYOWON PARK

A dissertation submitted to the

Graduate School—New Brunswick

Rutgers, The State University of New Jersey

in partial fulfillment of the requirements

for the degree of

Doctor of Philosophy

Graduate Program in Physics and Astronomy

Written under the direction of

Prof. Kristjan Haule

and approved by

_____

_____

_____

_____

_____

New Brunswick, New Jersey

October, 2011

ABSTRACT OF THE DISSERTATION

The study of two-particle response functions in strongly correlated electron systems within the dynamical mean field theory

by Hyowon Park

Dissertation Director: Prof. Kristjan Haule

In this thesis, we tackle various problems in strongly correlated electron systems, which can be addressed properly via the non-perturbative dynamical mean field theory (DMFT) approach using the continuous time quantum Monte Carlo method as an impurity solver. First, we revisit the old Nagaoka ferromagnetism problem in the $U = \infty$ Hubbard model and study the stability of the ferromagnetic state as a function of the temperature, the doping level, and the next-nearest-neighbor hopping t'. We then address the nature of the Mott transition in the two-dimensional Hubbard model at half-filling using cluster DMFT. Cluster DMFT can incorporate the short-range correlations beyond DMFT by extending the spatial range in which correlations are treated exactly to a finite cluster size. The non-local correlations reduce substantially the critical interaction U and modify the shape of the transition lines in the phase diagram.

We then concentrate on the calculation of two-particle response functions from the *ab initio* perspective by means of computing the one-particle excitation spectrum using the combination of the density functional theory (DFT) and DMFT and extracting the two-particle irreducible

vertex function from a local two-particle Green's function computed within DMFT. In particular, we derive the equations for calculating the magnetic/charge susceptibility and the pairing susceptibility in superconductivity. This approach is applied to the Hubbard model and the periodic Anderson model and we determine the phase diagram of magnetism and superconductivity in these models. We show that the superconducting phase is indeed stable near the magnetic phase where the pairing interaction mediated by spin fluctuations is dominantly enhanced. The non-local correlation effect to superconductivity is also discussed using the dual fermion approach and the dynamical vertex approximation. We finally apply the vertex function approach within DFT+DMFT to a Fe-based superconductor, $BaFe_2As_2$, and compute the dynamical magnetic susceptibility in this material. Our calculation results show a good agreement with the magnetic excitation spectra observed in a neutron scattering experiment. The response function calculation method derived in this thesis can capture both a localized and an itinerant nature of collective excitations in strongly correlated electron systems.

Acknowledgements

Most of all, I would like to thank my advisor Prof. Kristjan Haule for giving me an opportunity to work on cutting-edge projects in my research field, guiding me to be trained as a good theoretical physicist with his sincere care and helping me to overcome difficult moments during my Ph.D period with his generous understanding. I also appreciate him supporting me with the graduate assistantship during most of my Ph.D time so that I can focus on my research without worrying about the financial difficulty. I am also very grateful to Prof. Gabi Kotliar as my co-advisor for encouraging me to face various complicated problems in my research field and teaching me the way how to find a solution to the problems with his great insight in physics.

I also thank our former/current group members and visitors that I collaborated or discussed with. I would like to thank Chris Marianetti for helping me with the attentive guidance in the initial stage of my research. I also appreciate him offering me a post-doctoral position in his current group so that I can continue my research at Columbia university. I am also indebted to Ji-Hoon Shim, Kyoo Kim, Andreas Dolfen, Hongchul Choi, Junhee Lee, and Kyuho Lee for sharing great ideas related to my research and giving me helpful tips for my Ph.D life. I thank Maria Pezzoli, Jan Tomczak, Anna Toth, Cedric Weber, Camille Aron, Matthew Foster, Kostya Kechedzhi, Maxim Kharitonov, Andrei Kutepov, Tzen Ong, Youhei Yamaji, Quan Yin, Zhiping Yin, Kasturi Basu, Chuck-Hou Yee, and Wenhu Xu for having fruitful discussions and spending time joyfully for having a lunch with me.

I own gratitude to Prof. Leonard Feldman and Prof. Eric Gawiser for acting as my Ph.D committee members. I also thank Fran DeLucia and Shirley Hinds for giving me hands to finish numerous administration works, and I am grateful to Viktor Oudovenko for his generous help in the computer-related works. I appreciate Ron Ransome and Ted Williams helping me as a

graduate director. I also give many thanks to my friends outside the department of physics, Eunkyung Lee, Jaeyoung So, and so on, for sharing various recreational activities with me such as playing the basketball in the every Saturday morning.

Last but not least, I give my endless love to my parents for their great support and encouragement which enabled me to finish my Ph.D program. In particular, I am very grateful to them for their generosity of letting me choose to study physics from my undergraduate years and supporting my decision in all aspects.

Dedication

For My Parents

Table of Contents

List of Tables

List of Figures

Introduction

The discovery of superconductivity in heavy fermion materials in 1979 and cuprates (chemical compounds containing copper anions) in 1986 resulted in the emergence of a new field of research in condensed matter physics. These superconductors have attracted considerable interest owing to the unusually high critical temperature (T_c) of the cuprates (as high as 138K). These unexpectedly high T_c superconductors can provide many practical applications to the real life such as the electric power transmission without any resistance, magnetic resonance imaging (MRI) machines, magnetic levitation (Maglev), and so on. Moreover, the origin of superconductivity in these materials cannot be explained by the conventional Bardeen-Cooper-Schriffer (BCS) theory. The pairing interaction of Cooper pairs is not phonon-mediated, and many physicists believe that it is mediated by spin fluctuations; however this supposition has not been verified yet.

The discovery of Fe-based superconductors in 2008 generated widespread research, resulting in the publication of numerous papers on this subject within two years. The pairing mechanism of these materials is believed to be non-phonon-mediated, similar to that of other unconventional superconductors; therefore, physicists hope that these materials can provide an insight into the microscopic origin of unconventional superconductivity. The crystal structure of Fe-based superconductors consists of a layered structure of Fe atoms surrounded by tetrahedrally coordinated pnictogen and chalcogen atoms. Similar to the Cu plane in cuprate superconductors, the Fe plane plays an important role in superconductivity of these materials. These unconventional superconductors fall into the category of strongly correlated electron systems owing to the strong electron-electron interaction, as observed in the Mott insulating state of the parent compound in cuprates.

The theoretical study of strongly correlated electron systems has been a major challenge in condensed matter physics owing to the non-perturbative nature of the problem. Strong correlations are realized when the electron-electron interaction energy scale is comparable to the kinetic energy scale. The competition between the two energy scales yields exotic and complex phases such as the Mott insulating state and unconventional superconductivity in strongly correlated materials. The dynamical mean field theory (DMFT) is an effective method for capturing both localized and itinerant aspects of the strongly correlated electrons by describing the incoherent Hubbard bands and the coherent quasi-particle bands, respectively. The combination of DMFT and the density functional theory (DFT) has been successfully applied to the realistic electronic structure calculation of materials containing open shells of localized d or f orbitals as well as itinerant s or p orbitals.

Most response functions measured in condensed matter experiments are two-particle quantities such as magnetic susceptibility. The calculation of two-particle quantities for realistic materials is a challenging problem because it requires the computation of not only the one-particle Green's function obtained by the DFT+DMFT calculation but also the two-particle vertex function. The two-particle quantity involves the collective excitation spectra of magnetic or superconducting phases, which form the essence of strongly correlated electron systems. From a theoretical point of view, the calculation of these quantities based on the multi-orbital DFT+DMFT method can quantify the departure from both purely localized and itinerant pictures, and it can be directly compared with various experimental spectroscopic data.

In this thesis, we derive the equations for computing two-particle quantities with the realistic band structure calculation method, DFT+DMFT. For two-particle interaction, the irreducible vertex function is extracted from an auxiliary impurity problem in DMFT. In particular, we compute the magnetic susceptibility and pairing susceptibility for superconductivity. The calculation of the pairing susceptibility enables us to obtain T_c and the superconducting gap symmetry of strongly correlated model Hamiltonians, i.e., the Hubbard model and the periodic Anderson model. We apply this vertex function approach to the computation of magnetic

excitation spectra in the parent compound of the Fe based superconductor, $BaFe_2As_2$. Understanding the nature of the magnetic excitation spectra in Fe based superconductors is crucial to unraveling the origin of superconductivity in these materials. The magnetic excitation spectra measured via neutron scattering are in good agreement with our dynamical magnetic susceptibility calculation within DFT+DMFT, and we show that the nature of magnetic excitation in these materials contains both the localized and itinerant point of view.

This thesis is organized as follows. In Chapter 1, we introduce the basic electronic structure calculation methods that are widely adopted for strongly correlated electron systems: DFT, DMFT, and DFT+DMFT. For the auxiliary quantum impurity problem tackled in DMFT, we adopt a recently developed quantum impurity solver, i.e., the continuous time quantum Monte Carlo (CTQMC), which will be used throughout the following chapters. Chapter 2 addresses the old Nagaoka ferromagnetism problem in the $U = \infty$ Hubbard model via the DMFT approach. In Chapter 3, the nature of the Mott transition in the two-dimensional Hubbard model at half filling is studied using the cluster DMFT, a cluster extension of DMFT. The short-range correlations beyond DMFT are included within the cluster DMFT framework, and we show that the topology of the phase diagram studied using cluster DMFT is different from that obtained by single-site DMFT because of the difference in the nature of the insulating states.

In Chapters 4 to 7, we concentrate on the calculation of two-particle response functions for magnetism and superconductivity in strongly correlated electron systems. Chapter 4 introduces the two-particle vertex function calculation based on a realistic band structure calculation, implemented using DFT+DMFT. The equations for computing the magnetic susceptibility and the superconducting pairing susceptibility are derived. Chapter 5 is devoted to the derivation of two non-local approaches based on the vertex function calculation, i.e., the dual fermion (DF) approach and the dynamical vertex approximation (DΓA). These approaches can treat non-local correlations beyond DMFT. The equations for computing the pairing susceptibility within DF and DΓA are also derived. In Chapter 6, the vertex function approaches derived in Chapter 4 and 5 are applied to the one-band Hubbard model and the two-band periodic

Anderson model, which are the minimal models for describing the cuprate superconductor and the heavy fermion superconductor, respectively. T_c, the gap symmetry, and other relevant quantities for superconductivity are computed on the basis of DMFT as well as DF and DΓA. In Chapter 7, we describe the application of this vertex function approach to the dynamical magnetic susceptibility calculation in an Fe-based superconductor, $BaFe_2As_2$. By comparing our theoretical results with the neutron experimental data, we show that the magnetic excitation in $BaFe_2As_2$ has both a localized and an itinerant nature, and that the calculation in either purely localized or purely itinerant terms is not adequate to describe the experimental data.

Chapter 1

A Combination of the Density Functional Theory (DFT) and the Dynamical Mean Field Theory (DMFT)

In this chapter, we introduce the basic electronic structure calculation methods which are frequently used in strongly correlated systems, i.e., the density function theory (DFT), the dynamical mean field theory (DMFT), and the combination of them (DFT+DMFT). The basic concept of a state-of-the-art impurity solver, continuous time quantum Monte Carlo, is explained and the procedure of sampling the one-particle Green's function is also discussed.

1.1 DMFT

The dynamical mean field theory (DMFT) is a non-perturbative method which can capture both localized and itinerant nature of strongly correlated electron systems [7]. The essential idea of DMFT is to replace a lattice model by a single-site quantum impurity problem embedded in an effective medium determined self-consistently. The impurity model provides an intuitive picture of the local dynamics of a quantum many-body system. The quantum impurity problem is treated by various impurity solvers implemented in numerical or analytic techniques. The self-consistency condition captures the translation invariance and coherence effects of the lattice.

DMFT is a natural generalization of the classical Weiss mean-field theory to quantum many-body problems. However, the DMFT approach does not assume that all fluctuations are frozen. Rather, it freezes spatial fluctuations but takes full account of local quantum fluctuations. A key difference with the classical case is that the on-site quantum problem remains a many-body problem. As in classical statistical mechanics, this dynamical mean-field theory becomes exact

in the limit of infinite spatial dimensions $d \to \infty$.

The idea of DMFT is illustrated here on the example of the Hubbard model:

$$H = -\sum_{\langle i,j\rangle,\sigma} t_{ij} c^{\dagger}_{i\sigma} c_{j\sigma} + U \sum_{i} c^{\dagger}_{i\uparrow} c_{i\uparrow} c^{\dagger}_{i\downarrow} c_{i\downarrow} \tag{1.1}$$

where t_{ij} is the hopping energy from a site i to a site j and U is the on-site Coulomb energy. Here, the paramagnetic phase is assumed without any symmetry breaking. The mean-field description associates this Hamiltonian with single-site effective dynamics, which is conveniently described in terms of an imaginary-time action for the fermionic degrees of freedom at that site:

$$\begin{aligned} S_{eff} &= -\int_0^{\beta} d\tau \int_0^{\beta} d\tau' \sum_{\sigma} c^{\dagger}_{o\sigma}(\tau) \mathcal{G}_0^{-1}(\tau - \tau') c_{o\sigma}(\tau') \\ &\quad + U \int_0^{\beta} d\tau c^{\dagger}_{i\uparrow}(\tau) c_{i\uparrow}(\tau) c^{\dagger}_{i\downarrow}(\tau) c_{i\downarrow}(\tau) \end{aligned} \tag{1.2}$$

Here, $\mathcal{G}_0(\tau - \tau')$ plays the role of the Weiss effective field in the mean-field description. Its physical content is that of an effective amplitude for a fermion to be created on the isolated site o at time τ and destroyed at time τ'. The main difference with the classical case is that this Weiss function $\mathcal{G}_0$ is a function of time instead of a number. As a result, $\mathcal{G}_0$ takes into account local quantum fluctuations while the spatial fluctuation is ignored due to the mean-field approximation. $\mathcal{G}_0$ plays the role of a bare Green's function for the local effective action S_{eff}, however, it is different from the non-interacting local Green's function of the original lattice model.

The on-site (impurity) interacting Green's function G can be calculated from S_{eff} given in Eq. 1.2:

$$G(\tau - \tau') \equiv -\langle T_{\tau} c(\tau) c^{\dagger}(\tau') \rangle_{S_{eff}}. \tag{1.3}$$

On the imaginary axis, it is given by

$$G(i\omega_n) = \int_0^{\beta} d(\tau - \tau') G(\tau - \tau') e^{i\omega_n (\tau - \tau')} \tag{1.4}$$

where ω_n is the Matsubara frequency given by $\frac{(2n+1)\pi}{\beta}$. Solving a quantum impurity problem under the action S_{eff} is a difficult part of DMFT due to the non-perturbative nature of

the problem. This part is treated by powerful impurity solvers including the continuous time quantum Monte Carlo which will be introduced in a later section.

Within DMFT, the **k** dependent original lattice Green's function is constructed by

$$G(\mathbf{k}, i\omega_n) = \frac{1}{i\omega_n + \mu - \epsilon_{\mathbf{k}} - \Sigma(i\omega_n)} \tag{1.5}$$

where the self energy $\Sigma(i\omega_n)$ is computed from the impurity action as:

$$\Sigma(i\omega_n) = \mathcal{G}_0^{-1}(i\omega_n) - G^{-1}(i\omega_n) \tag{1.6}$$

Here, the self energy in the original lattice Green's function is approximated as purely local in space [8], and it is obtained by summing all local Feynman diagrams using an impurity solver. The local nature of the lattice self energy in the limit of infinite d can be seen from the diagrammatic technique within the perturbation expansion of the interaction U. The diagram for the self energy is constructed using a four-leg vertex at site i and a line of a full propagator connecting the vertices between two sites. The crucial observation in $d \to \infty$ is that whenever two internal vertices (i, j) can be connected by at least two paths, they must correspond to identical sites $i = j$. This can be shown by simple power counting. Since the hopping is scaled by $1/\sqrt{d}$, each path made of fermion propagators connecting i to j will involve at least a factor $(1/\sqrt{d})^{|i-j|}$. On the other hand, i being held fixed, the eventual summation to be performed on the internal vertex j will bring in a factor of order d^R where $R \equiv |i-j|$. Hence, one obtains an overall factor of $d^R(1/\sqrt{d})^{R \cdot P_{ij}}$ where P_{ij} is the number of paths joining i to j in the diagram. Thus if $P_{ij} > 2$, only those contributions with $i = j$ $(R = 0)$ will survive in the $d \to \infty$ limit.

The DMFT self-consistency is achieved by supplementing Eq. 1.2 with the expression relating $\mathcal{G}_0$ to local quantities computable from the effective action S_{eff}. In the limit of infinite d, one can show that the Weiss field $\mathcal{G}_0$ is related to the full Green's function as [7]:

$$\mathcal{G}_0^{-1}(i\omega_n) = i\omega_n + \mu - \sum_{ij} t_{oi} t_{oj} [G_{ij} - \frac{G_{io} G_{oj}}{G_{oo}}](i\omega_n) \tag{1.7}$$

where G_{oo} is the local component of the full Green's function. Here, the term $\frac{G_{io}G_{oj}}{G_{oo}}$ is subtracted owing to the cavity construction. In the momentum space,

$$\mathcal{G}_0^{-1}(i\omega_n) = i\omega_n + \mu - \frac{1}{N_k}\sum_{\mathbf{k}} t_{\mathbf{k}}^2 G_{\mathbf{k}}(i\omega_n) - \frac{(\frac{1}{N_k}\sum_{\mathbf{k}} t_{\mathbf{k}} G_{\mathbf{k}}(i\omega_n))^2}{G_{oo}(i\omega_n)}. \tag{1.8}$$

If the self energy is local,

$$\frac{1}{N_k}\sum_{\mathbf{k}} t_{\mathbf{k}} G_{\mathbf{k}} = -1 + (i\omega_n + \mu - \Sigma)G_{oo} \tag{1.9}$$

and

$$\frac{1}{N_k}\sum_{\mathbf{k}} t_{\mathbf{k}}^2 G_{\mathbf{k}} = -(i\omega_n + \mu - \Sigma) + (i\omega_n + \mu - \Sigma)^2 G_{oo} \tag{1.10}$$

where $G_{oo} = \frac{1}{N_k}\sum_{\mathbf{k}} G_{\mathbf{k}}$. Using above relations, the Weiss field $\mathcal{G}_0^{-1}$ is determined by:

$$\mathcal{G}_0^{-1}(i\omega_n) = \Sigma(i\omega_n) + G_{oo}^{-1}(i\omega_n). \tag{1.11}$$

Therefore, the DMFT self-consistency is closed by imposing the condition for $\mathcal{G}_0^{-1}(i\omega_n)$ such that the local (on-site) component of the lattice Green's function coincides with the impurity Green's function calculated from the effective action given in Eq. 1.3:

$$\sum_{\mathbf{k}} \frac{1}{i\omega_n + \mu - \epsilon_{\mathbf{k}} - \Sigma(i\omega_n)} = \frac{1}{i\omega_n + \mu - \Delta(i\omega_n) - \Sigma(i\omega_n)} \tag{1.12}$$

where the hybridization function Δ is given by $\Delta(i\omega) = i\omega + \mu - \mathcal{G}_0^{-1}(i\omega)$.

1.2 DFT

In this section, we discuss the basic idea of Density Functional Theory (DFT). DFT has been an efficient and powerful theory for computing the electronic properties in a many-body system since this method treats various physical quantities in terms of the electronic density. In the electronic structure calculation, we treat the Hamiltonian of interacting electrons in a solid which is given by

$$\hat{H} = -\frac{\hbar^2}{2m}\sum_i \nabla_i^2 + \sum_i V_{ext}(\mathbf{r}_i) + \frac{1}{2}\sum_{i\neq j}\frac{e^2}{|\mathbf{r}_i - \mathbf{r}_j|} \tag{1.13}$$

Here, m is the electron mass, e is the charge, and $\mathbf{r}_i$ is the spatial coordinate of electrons. The first term of the righthand side represents the kinetic energy of electrons, the second term is the

external potential due to the nuclei, and the third term shows the electron-electron interaction. Now, we set $m = \hbar = e = 1$.

The main idea of DFT is that any physical property of a solid state system can be represented as a functional of the ground state density $n(\mathbf{r})$. This idea is formulated in a famous paper by P. Hohenberg and W. Kohn in 1964 [9]. The Hohenberg-Kohn theorem states that "For any interacting solid-state system in an external potential $V_{ext}(\mathbf{r})$, the potential $V_{ext}(\mathbf{r})$ is uniquely determined by the ground state density $n(\mathbf{r})$". This theorem can be proved by contradiction. Let us assume that the two different external potentials, $V_{ext}^{(1)}(\mathbf{r})$ and $V_{ext}^{(2)}(\mathbf{r})$ exist. The different external potentials lead to distinct Hamiltonians $\hat{H}^{(1)}$ and $\hat{H}^{(2)}$ since the kinetic energy and the electron-electron interaction terms are universal regardless of the solid-state system. The two distinct Hamiltonians solved by the Schrodinger equation result in two different ground state wave functions $\psi^{(1)}$ and $\psi^{(2)}$. The ground state energy $E^{(1)}$ for $\hat{H}^{(1)}$ is given by

$$E^{(1)} = \left\langle \psi^{(1)} | \hat{H}^{(1)} | \psi^{(1)} \right\rangle < \left\langle \psi^{(2)} | \hat{H}^{(1)} | \psi^{(2)} \right\rangle \tag{1.14}$$

The inequality follows from the fact that $\psi^{(2)}$ is not the ground state wave function of $\hat{H}^{(1)}$ and this condition is strictly obeyed if the ground state is non-degenerate. The last term in Eq. 1.14 can be rewritten as

$$\begin{aligned} \left\langle \psi^{(2)} | \hat{H}^{(1)} | \psi^{(2)} \right\rangle &= \left\langle \psi^{(2)} | \hat{H}^{(2)} | \psi^{(2)} \right\rangle + \left\langle \psi^{(2)} | \hat{H}^{(1)} - \hat{H}^{(2)} | \psi^{(2)} \right\rangle \\ &= E^{(2)} + \int d\mathbf{r} [V_{ext}^{(1)}(\mathbf{r}) - V_{ext}^{(2)}(\mathbf{r})] n^{(2)}(\mathbf{r}) \end{aligned} \tag{1.15}$$

therefore,

$$E^{(1)} < E^{(2)} + \int d\mathbf{r} [V_{ext}^{(1)}(\mathbf{r}) - V_{ext}^{(2)}(\mathbf{r})] n^{(2)}(\mathbf{r}) \tag{1.16}$$

In the same way, the above inequality can be constructed for $E^{(2)}$ by interchanging the superscripts (1) and (2) as

$$E^{(2)} < E^{(1)} + \int d\mathbf{r} [V_{ext}^{(2)}(\mathbf{r}) - V_{ext}^{(1)}(\mathbf{r})] n^{(1)}(\mathbf{r}) \tag{1.17}$$

If we add Eq. 1.16 and Eq. 1.17, the above inequality leads to contradiction, i.e., $E^{(1)} + E^{(2)} < E^{(2)} + E^{(1)}$ if the ground state density $n^{(1)}$ and $n^{(2)}$ are assumed to be equal. Therefore, any

given ground state density $n(\mathbf{r})$ always uniquely determines the external potential $V_{ext}(\mathbf{r})$, hence the Hamiltonian $\hat{H}$. This theorem leads to the further conclusion that the wave function and other physical properties of the system can be uniquely determined as the functional of the ground state density $n(\mathbf{r})$ since $\hat{H}$ is unique, as the name of Density Functional Theory implies.

Within DFT, the basic variable needed for computing the electronic structure of the interacting solid-state system is the ground state density $n(\mathbf{r})$. However, the calculation of $n(\mathbf{r})$ requires us to solve the Hamiltonian in Eq. 1.13, and this problem has the many-body nature due to the electron-electron interaction term. In 1965, Kohn and Sham suggested an approach to replace the original many-body problem by an auxiliary independent-particle problem [10]. Within the Kohn-Sham (KS) ansatz, it is assumed that the exact ground state density $n(\mathbf{r})$ can be obtained from the density of independent particles by summing the squares of the auxiliary particle wavefunctions over spins and orbitals:

$$n(\mathbf{r}) \quad = \quad \sum_{i,\sigma} |\psi_i^\sigma(\mathbf{r})|^2 \tag{1.18}$$

Following the Hohenberg-Kohn theorem, the ground state energy can be expressed as a functional of the density n

$$E_{KS}[n] \quad = \quad T_s[n] + \int d\mathbf{r} V_{ext}(\mathbf{r}) n(\mathbf{r}) + E_H[n] + E_{xc}[n] \tag{1.19}$$

Here, $T_s[n]$ is the kinetic energy functional, $E_H[n]$ is the Hartree energy functional, and $E_{xc}[n]$ is the exchange-correlation functional. The Hartree energy is defined in analogy to the classical Coulomb interaction energy of the electron density $n(\mathbf{r})$ interacting with itself:

$$E_H[n] \quad = \quad \frac{1}{2} \int d^3r \int d^3r' \frac{n(\mathbf{r}) n(\mathbf{r}')}{|\mathbf{r} - \mathbf{r}'|} \tag{1.20}$$

And the exact functional form of $E_{xc}[n]$ is unknown. The kinetic energy part can be expressed as the sum of the kinetic energies of independent particles due to the KS ansatz.

$$T_s \quad = \quad -\frac{1}{2} \sum_{i,\sigma} \langle \psi_i^\sigma | \nabla^2 | \psi_i^\sigma \rangle \tag{1.21}$$

The auxiliary KS equation is obtained by minimizing the energy functional in Eq. 1.19 with respect to $\psi_i^{\sigma *}(\mathbf{r})$ with the constraint on the normalization condition $\epsilon_i (\int d^3r \psi_i^{\sigma *}(\mathbf{r}) \psi_i^\sigma(\mathbf{r}) - 1)$

where ϵ_i is the Lagrange multiplier.

$$\frac{\delta E_{KS}[n]}{\delta \psi_i^{\sigma *}(\mathbf{r})} = -\frac{1}{2}\nabla^2 \psi_i^{\sigma}(\mathbf{r}) + \left[V_{ext}^{\sigma}(\mathbf{r}) + \frac{\delta E_H[n]}{\delta n(\mathbf{r},\sigma)} + \frac{\delta E_{xc}[n]}{\delta n(\mathbf{r},\sigma)} \right] \psi_i^{\sigma}(\mathbf{r}) = \epsilon_i \psi_i^{\sigma}(\mathbf{r}) \quad (1.22)$$

This resulting equation is equivalent to the Schrodinger equation for independent auxiliary particles subject to the KS potential $V_{KS}^{\sigma}(\mathbf{r})$ given by $V_{ext}^{\sigma}(\mathbf{r}) + \frac{\delta E_H[n]}{\delta n(\mathbf{r},\sigma)} + \frac{\delta E_{xc}[n]}{\delta n(\mathbf{r},\sigma)}$ and this equation is exactly solvable if $E_{xc}[n]$ is known. Therefore, the self-consistent loop of the KS equation is organized in a following way.

1. First, the initial guess for the ground state density $n(\mathbf{r},\sigma)$ is given.
2. The KS potential $V_{KS}^{\sigma}(\mathbf{r})$ is constructed from the given density $n(\mathbf{r},\sigma)$.
3. The KS equation in Eq. 1.22 is solved resulting in eigenvalues ϵ_i and eigenfunctions $\psi_i^{\sigma}(\mathbf{r})$.
4. A new density $n(\mathbf{r},\sigma)$ is constructed using Eq. 1.18.
5. The calculation is repeated by going back to step 2 until the density $n(\mathbf{r},\sigma)$ converges.

In principle, from the Hohenberg-Kohn theorem, the exact ground state energy can be given by a functional of an electron density $n(\mathbf{r})$ obtained from the solution of the KS equation. However, since we do not know how to treat the exchange-correlation potential $V_{xc}(= \frac{\delta E_{xc}[n]}{\delta n(\mathbf{r},\sigma)})$ exactly, here we resort to an local density approximation (LDA). Within LDA, the exchange-correlation energy is simply given by an integral over all space with the exchange-correlation energy density $\varepsilon_{xc}(n(\mathbf{r},\sigma))$ which depends only upon the electron density $n(\mathbf{r})$ at the same point $\mathbf{r}$.

$$E_{xc}^{\sigma}[n] = \int d^3 r n(\mathbf{r}) \varepsilon_{xc}(n(\mathbf{r},\sigma)) \quad (1.23)$$

$\varepsilon_{xc}(n(\mathbf{r},\sigma))$ is assumed to be the same as in a homogeneous (uniform) electron gas with the same density $n(\mathbf{r},\sigma)$, therefore it can be computed using reliable techniques such as quantum Monte Carlo [11]. A detailed implementation of LDA is given in Ref. [12].

1.3 DFT+DMFT

In the previous section, the DFT approach for treating many-body interactions is explained and the LDA approximation is introduced for the practical electronic structure calculation. The

LDA approximation is reliable when the electron density does not have a large spatial variation. A weakly correlated system such as a good metal has an almost uniform wavefunction in space, and LDA is a good approximation for these s or p wide-band systems such as semiconductors.

For a strongly correlated system, electrons have both itinerant and localized aspects and the LDA approximation becomes very poor in these systems due to the large fluctuation of the ground state density. Materials with the strong correlation include the narrow d or f band systems such as transition metals, rare earth compounds, organic conductors, and so on. These strongly correlated materials require a higher accuracy for treating correlations of electrons beyond LDA. These correlations can be taken into account by employing DMFT since dynamical correlations are exactly treated within DMFT by including local higher order Feynman diagrams. However, it is impossible to apply DMFT to all electrons in a material due to the limited computational power. Recently, a new approach for the electronic structure calculation was implemented by combining LDA and DMFT referred as "LDA+DMFT" or "DFT+DMFT" [13, 14]. In this section, we derive the main formula of the DFT+DMFT method and discuss about the projection scheme to correlated orbitals.

Within DFT+DMFT, the grand potential Γ is expressed as a functional of the correlated Green's function $\mathcal{G}$ and the density ρ and it takes the form:

$$\Gamma[\mathcal{G},\rho] = -\mathrm{Tr}(G^{-1}) - \mathrm{Tr}[\Sigma^{tot}\cdot G] + \Phi[\mathcal{G},\rho] \tag{1.24}$$

where G is the total Green's function, Σ^{tot} is the total self energy, and Φ is the Luttinger-Ward functional which gives the relation $\Sigma = \frac{\partial\Phi}{\partial G}$. Here, Tr is trace which runs over all space (orbitals and momenta) and time (frequency). The quantities in the above functional are given by

$$G^{-1}_{\omega}(\mathbf{r},\mathbf{r}') = [i\omega + \mu + \nabla^2 - V_{ext}(\mathbf{r})]\delta(\mathbf{r}-\mathbf{r}') - \Sigma^{tot}_{\omega}(\mathbf{r},\mathbf{r}') \tag{1.25}$$

$$\Sigma^{tot}_{\omega}(\mathbf{r},\mathbf{r}') = [V_H(\mathbf{r}) + V_{xc}(\mathbf{r})]\delta(\mathbf{r}-\mathbf{r}') + [\Sigma_{\omega}(\mathbf{r},\mathbf{r}') - E_{DC}\delta(\mathbf{r}-\mathbf{r}')]\Theta(r<S) \tag{1.26}$$

$$\Phi[G,\rho] = \Phi_H[\rho] + \Phi_{xc}[\rho] + \Phi_{DMFT}[\mathcal{G}] - \Phi_{DC}[\mathcal{G}] \tag{1.27}$$

$$\rho = \widetilde{\mathrm{Tr}}(G) \tag{1.28}$$

where $\widetilde{\mathrm{Tr}}$ runs over only frequencies, V_{ext} is the external potential due to ions, and $V_{H(xc)}$ is

the Hartree (exchange-correlation) potential treated in the LDA method. Σ_ω is the self energy treated within DMFT and Φ_{DMFT} is the sum of all local two-particle irreducible skeleton diagrams constructed from $\mathcal{G}$ and the Coulomb interaction U. E_{DC} is the double counting energy and Φ_{DC} is the corresponding functional.

The functional in Eq. 1.24 can be extremized by taking the derivative with respect to both $\mathcal{G}$ and ρ as independent variables. One can note that G is a functional of both $\mathcal{G}$, i.e, $G[\Sigma[\mathcal{G}]]$ and ρ, i.e, $G[V_H[\rho] + V_{xc}[\rho]]$. Using the following relation:

$$\mathrm{Tr}[\Sigma^{tot} G] = \mathrm{Tr}[(V_H + V_{xc})\rho] + \mathrm{Tr}[(\Sigma - E_{DC})\mathcal{G}], \tag{1.29}$$

the minimization with respect to $\mathcal{G}$ leads to

$$\Sigma - E_{DC} = \frac{\delta \Phi_{DMFT}[\mathcal{G}]}{\delta \mathcal{G}} - \frac{\delta \Phi_{DC}[\mathcal{G}]}{\delta \mathcal{G}}, \tag{1.30}$$

and the minimization withe respect to ρ gives

$$V_H + V_{xc} = \frac{\delta \Phi_H[\rho]}{\delta \rho} + \frac{\delta \Phi_{xc}[\rho]}{\delta \rho}. \tag{1.31}$$

The functional minimization result shows that the Hartree and the exchange-correlation potential $V_{H(xc)}$ can be computed within LDA as discussed in Section 1.2. and the correlated self energy Σ is obtained within DMFT by summing all local Feynman diagrams using an auxiliary quantum impurity problem as discussed in Section 1.1. However, one should note that the density ρ computed within LDA+DMFT is different from the LDA ρ since ρ is computed in the presence of the DMFT self energy. Since the functional minimization is satisfied with the exact $\mathcal{G}$ and the exact ρ, one should perform a full charge (density) self-consistent calculation to obtain $\mathcal{G}$ and ρ.

The DMFT self-consistency condition is the same as given in Section 1.1 Namely, the local Green's function is the same as the impurity one, i.e., $\mathcal{G} = G_{imp}$ and the self energy is approximated to the impurity one, i.e., $\Sigma = \Sigma_{imp}$. This DMFT self-consistency condition can be given

as a explicit form:

$$\int_{(r,r')<S_\tau} d\mathbf{r}d\mathbf{r}' P(\mathbf{r}\mathbf{r}', \tau LL') \left\{ \left[i\omega + \mu + \nabla^2 - V_{KS}(\mathbf{r}) \right] \delta(\mathbf{r} - \mathbf{r}') - \sum_{L_1 L_2 \in H} P(\mathbf{r}'\mathbf{r}, \tau L_1 L_2) \overline{\Sigma}^\tau_{L_2 L_1} \right\}^{-1} = \left[\left(i\omega - E^\tau_{imp} - \Sigma^\tau - \Delta^\tau \right)^{-1} \right]_{LL'} \quad (1.32)$$

where P is the projection operator to the localized orbital basis, $V_{KS} = V_{ext} + V_H + V_{xc}$ as defined in the previous section, S is the muffin-tin radius, Δ^τ is the hybridization function, and E^τ_{imp} is the impurity level.

The above self-consistency condition also can be expressed in the Kohn-Sham (KS) basis for more efficient evaluation. At each LDA+DMFT iteraction, we solve the KS eigenvalue equation.

$$\left[-\nabla^2 + V_{KS}(\mathbf{r}) \right] \psi_{\mathbf{k}i}(\mathbf{r}) = \epsilon_{\mathbf{k}i} \psi_{\mathbf{k}i}. \quad (1.33)$$

Then the projection operator $\hat{P}$ is expressed in the KS basis, $\hat{P}_k(ij, \tau LL')$ where i, j runs over all bands and τ is the atom index inside the unit cell. The self energy given in the $(\mathbf{r}, \mathbf{r}')$ basis also can be transformed to the KS basis using the above projector:

$$\overline{\Sigma}_{\mathbf{k},ij}(\omega) = \sum_{\tau, L_1 L_2} P_{\mathbf{k}\tau}(ji, \tau L_2 L_1) \, \overline{\Sigma}^\tau_{L_1 L_2}(\omega) \quad (1.34)$$

In KS basis, the correlated Green's function on the left-hand side of Eq. 1.32 is expressed in a practical form replacing the integral over the space $(\mathbf{r}, \mathbf{r}')$ by the summation of the band indices (i, j)

$$\mathcal{G}^\tau_{LL'} = \sum_{\mathbf{k}ij} P_{\mathbf{k}\tau}(ij, LL') \left[\left(i\omega + \mu - \epsilon_{\mathbf{k}} - \overline{\Sigma}_{\mathbf{k}}(\omega) \right)^{-1} \right]_{ji} \quad (1.35)$$

Finally, the DMFT self-consistency condition is given in a practical form by

$$\sum_{\mathbf{k}ij} \left[\frac{P_{\mathbf{k}\tau}(ij, LL')}{i\omega + \mu - \epsilon_{\mathbf{k}} - \overline{\Sigma}_{\mathbf{k}}(\omega)} \right]_{ji} = \left[\frac{1}{i\omega - E^\tau_{imp} - \Sigma^\tau(\omega) - \Delta^\tau(\omega)} \right]_{LL'} \quad (1.36)$$

As a result, for a given self energy $\Sigma(\omega)$, the hybridization function Δ^τ and the impurity level E^τ_{imp} are obtained in a self-consistent way.

After this DMFT self-consistency condition is achieved, the electron density ρ also needs to be updated for a full charge self-consistent calculation using Eq. 1.28 from the converged G.

The projection operator (projector) $\hat{P}$ introduced in Eq. 1.32 performs the operation of extracting the correlated local Green's function $\mathcal{G}(\mathbf{r},\mathbf{r}')$ from the full Green's function $G(\mathbf{r},\mathbf{r}')$. We specify the projection scheme by the projection operator $P(\mathbf{r}\mathbf{r}',\tau LL')$, which defines the mapping between real-space objects and their orbital counterparts $(\mathbf{r},\mathbf{r}') \rightarrow (L,L')$. The operator $\hat{P}$ acts on the full Green's function $G(\mathbf{r},\mathbf{r}')$ and gives the correlated Green's function $\mathcal{G}^{\tau}_{LL'}$:

$$\mathcal{G}^{\tau}_{LL'} = \int d\mathbf{r}d\mathbf{r}' P(\mathbf{r}\mathbf{r}',\tau LL')G(\mathbf{r}\mathbf{r}'). \tag{1.37}$$

The integrals over $\mathbf{r}$ and $\mathbf{r}'$ are performed inside the sphere of size S around the correlated atom at position τ. The subscript L can index spherical harmonics lm, cubic harmonics, or relativistic harmonics jm_j, depending on the system symmetry.

The inverse process of embedding $\hat{E}$, i.e. the mapping between the correlated orbitals and real-space $(L,L') \rightarrow (\mathbf{r},\mathbf{r}')$, is defined by the same four-index tensor. However, instead of integrals over real-space, its application is through a discrete sum over the local degrees of freedom,

$$\Sigma(\mathbf{r},\mathbf{r}') = \sum_{\tau LL' \in H} P(\mathbf{r}'\mathbf{r},\tau L'L)\Sigma^{\tau}_{LL'} \tag{1.38}$$

Here, $LL' \in H$ means to only sum over correlated orbitals. Note that within the correlated Hilbert subspace, the embedding and projection should give unity $\hat{P}\hat{E} = I$, i.e.,

$$\int d\mathbf{r}d\mathbf{r}' P(\mathbf{r}\mathbf{r}',\tau L_1L_2)P(\mathbf{r}'\mathbf{r},\tau' L_3L_4) = \delta_{L_1L_4}\delta_{L_2L_3}\delta_{\tau\tau'}. \tag{1.39}$$

For the projection to the correlated Green's functon, the localized orbital basis needs to be properly chosen. One simple possibility is the projection onto the orbital angular momentum functions Y_L and $P(\mathbf{r}'\mathbf{r},\tau L'L)$ can be explicitly written as

$$P^0(\mathbf{r}\mathbf{r}',\tau LL') \quad = \quad Y_L(\hat{r}_\tau)\delta(r-r')Y^*_{L'}(\hat{r}'_\tau) \tag{1.40}$$

and also the projection onto the solution of the Schrödinger equation can be given by

$$P^1(\mathbf{r}\mathbf{r}',\tau LL') \quad = \quad Y_L(\hat{r}_\tau)u^0_l(r_\tau)u^0_{l'}(r'_\tau)Y^*_{L'}(\hat{r}'_\tau) \tag{1.41}$$

where $\mathbf{r}_\tau = \mathbf{r} - R_\tau$ is the vector defined with the origin placed at the atomic position R_τ, and $u_l^0(r)$ is the solution of the radial Schrödinger equation for angular momentum l at a fixed energy E_ν.

The projectors (1.40) and (1.41) also can be expressed in the Kohn-Sham basis:

$$P_{\mathbf{k}}(ij, \tau LL') = \int d\mathbf{r}d\mathbf{r}' \psi^*_{i\mathbf{k}}(\mathbf{r}) P(\mathbf{r}\mathbf{r}', \tau LL') \psi_{j\mathbf{k}}(\mathbf{r}'). \tag{1.42}$$

where $\psi_{i\mathbf{k}}(\mathbf{r})$ is the KS wave function. In the full-potential linearized augmented plane wave (LAPW) method [15], the basis function χ inside the Muffin-Tin (MT) sphere can be written as:

$$\chi_{\mathbf{k}+\mathbf{K}}(\mathbf{r}) = \sum_{L\tau\kappa} A^{\tau\kappa}_{\mathbf{k}+\mathbf{K},L} u_l^{\tau\kappa}(r_\tau) Y_L(\hat{r}_\tau) \tag{1.43}$$

where $\kappa = 0$ corresponds to the solution of the Schrödinger equation $u_l(E_\nu, r_\tau)$ at a fixed energy E_ν, $\kappa = 1$ to the energy derivative of the same solution $\dot{u}_l(E_\nu, r_\tau)$, and $\kappa = 2, 3, \ldots$ to a localized orbitals at additional linearization energies $E'_\nu, E''_\nu, \ldots$. Here τ runs over the atoms in the unit cell. The Kohn-Sham wavefunction $\psi_{i\mathbf{k}}(\mathbf{r})$ are superpositions of the basis functions

$$\psi_{i\mathbf{k}}(\mathbf{r}) = \sum_{\mathbf{K}} C^{\mathbf{k}}_{i\mathbf{K}}\ \chi_{\mathbf{k}+\mathbf{K}}(\mathbf{r}) \tag{1.44}$$

and take the following form inside the MT spheres:

$$\psi_{i\mathbf{k}}(\mathbf{r}) = \sum_{\tau L\kappa} \mathcal{A}^{\tau\kappa}_{iL}(\mathbf{k}) u_l^{\tau\kappa}(r_\tau) Y_L(\hat{r}_\tau) \tag{1.45}$$

where $\mathcal{A}^{\tau\kappa}_{iL}(\mathbf{k}) = \sum_{\mathbf{K}} A^{\tau\kappa}_{\mathbf{k}+\mathbf{K},L} C^{\mathbf{k}}_{i\mathbf{K}}$. Therefore, the projector P^0 and P^1 takes the following form in the KS basis:

$$\begin{aligned} P^0_{\mathbf{k}}(ij, \tau LL') &= \int d\mathbf{r}d\mathbf{r}' \psi^*_{i\mathbf{k}}(\mathbf{r}) Y_L(\hat{r}_\tau) \delta(r - r') Y^*_{L'}(\hat{r}'_\tau) \psi_{j\mathbf{k}}(\mathbf{r}') \\ &= \sum_{\kappa\kappa'} \mathcal{A}^{\tau\kappa *}_{iL}(\mathbf{k}) \mathcal{A}^{\tau\kappa'}_{jL'}(\mathbf{k}) \langle u_l^{\tau\kappa} | u_{l'}^{\tau\kappa'} \rangle \qquad (1.46) \\ P^1_{\mathbf{k}}(ij, \tau LL') &= \sum_{\kappa\kappa'} \mathcal{A}^{\tau\kappa}_{iL}(\mathbf{k}) A^{\tau\kappa' *}_{jL'}(\mathbf{k}) \langle u_l^{\tau\kappa} | u_l^0 \rangle \langle u_{l'}^0 | u_{l'}^{\tau\kappa'} \rangle. \qquad (1.47) \end{aligned}$$

As Ref. [14] explained in details, the projector P^0 leads to non-causal DMFT equations which result in an unphysical auxiliary impurity problem and P^1 does not take into account the

contributions due to the energy derivative of the radial wave function $\dot{u}_l(E_\nu, r)Y_L(\hat{r})$ and the localized orbitals at other energies $u_l(E'_\nu, r)Y_L(\hat{r})$, and hence misses some electronic spectral weight of the correlated orbital. Ref. [14] implemetented a new projector P^2 which simultaneously captures all spectral weight of the correlated system and obeys the causality condition. In order to obey causality, the projector P^2 in the KS basis is given by the separable form

$$P^2_{\mathbf{k}}(ij, \tau LL') = U^{\mathbf{k}\tau}_{iL} U^{\mathbf{k}\tau *}_{jL'}. \tag{1.48}$$

where

$$U^{\mathbf{k}\tau}_{iL} = \sum_{\kappa} \mathcal{A}^{\tau\kappa}_{iL}(\mathbf{k}) \langle u^{\tau\kappa}_l | u^{\tau 0}_l \rangle \sqrt{\frac{\sum_{\kappa_1\kappa_2} \mathcal{A}^{\tau\kappa_1}_{iL} \mathcal{A}^{\tau\kappa_2 *}_{iL} \langle u^{\tau\kappa_1}_l | u^{\tau\kappa_2}_l \rangle}{\sum_{\kappa_1\kappa_2} \mathcal{A}^{\tau\kappa_1}_{iL} \mathcal{A}^{\tau\kappa_2 *}_{iL} \langle u^{\tau\kappa_1}_l | u^{\tau 0}_l \rangle \langle u^{\tau 0}_l | u^{\tau\kappa_2}_l \rangle}} \tag{1.49}$$

The diagonal part of the projector P^2, $P^2_{\mathbf{k}}(ii, LL)$, is the same as $P^0_{\mathbf{k}}(ii, LL)$, therefore, this projection correctly captures the correlated partial spectral weight.

1.4 Continuous Time Quantum Monte Carlo (CTQMC)

A quantum impurity model in condensed matter physics was originally introduced to describe the behavior of correlated electrons in a magnetic transition metal embedded in a non-magnetic host metal. This quantum impurity problem plays an important role in the DMFT approximation as an auxiliary problem to capture the dynamical correlation of the system. Therefore, the powerful and effective implementation of a quantum impurity solver is at the heart of the DMFT method. In this section, we introduce the basic idea of the continuous time quantum Monte Carlo (CTQMC) method which will be used throughout this thesis as the impurity solver for a DMFT solution.

In the strong coupling version of CTQMC [16, 17, 18] the impurity partition function is expanded in Taylor series in powers of the hybridization function Δ. The resulting Feynman diagrams are sampled by the Monte Carlo importance sampling. At each perturbation order k,

the diagrams can be regrouped into a determinant of a matrix of size $k \times k$, denoted by $\bar{\Delta}_k$.

$$\begin{aligned} Z &= \int D[\psi^\dagger \psi] e^{-S_c} \cdot \sum_k \frac{1}{k!} \int_0^\beta d\tau_1 \int_0^\beta d\tau_1' \cdots \int_0^\beta d\tau_k \int_0^\beta d\tau_k' \\ &\sum_{\alpha_1 \alpha_1', \cdots, \alpha_k, \alpha_k'} \psi_{\alpha_1'}(\tau_1') \psi^\dagger_{\alpha_1}(\tau_1) \cdots \psi_{\alpha_k'}(\tau_k') \psi^\dagger_{\alpha_k}(\tau_k) \times \frac{1}{k!} Det(\bar{\Delta}_k) \end{aligned} \tag{1.50}$$

$$\bar{\Delta}_k \equiv \begin{pmatrix} \Delta_{\alpha_1 \alpha_1'}(\tau_1, \tau_1') & \Delta_{\alpha_1 \alpha_2'}(\tau_1, \tau_2') & \cdots & \Delta_{\alpha_1 \alpha_k'}(\tau_1, \tau_k') \\ \cdots & \cdots & \cdots & \cdots \\ \cdots & \cdots & \cdots & \cdots \\ \Delta_{\alpha_k \alpha_1'}(\tau_k, \tau_1') & \cdots & \cdots & \Delta_{\alpha_k \alpha_k'}(\tau_k, \tau_k') \end{pmatrix} \tag{1.51}$$

Here, S_c is the cluster part of the action including the local interaction matrix, ψ is the fermion operator, and α_{1-k} represents the bath degrees of freedom including spin and orbital indices or cluster momentum. $\bar{\Delta}_k$ is the hybridization matrix regrouped from the Δ elements at each perturbation order k.

Two Monte Carlo steps which need to be implemented are (i) insertion of two kinks at random times τ_{new} and τ'_{new} (chosen uniformly $[0, \beta)$), corresponding to a random baths α and α', and (ii) removal of two kinks by removing one creation operator and one annhilation operator. The detailed balance condition requires that the probability to insert two kinks at random times τ, τ', being chosen uniformly in the interval $[0, \beta)$, is

$$P_{add} = min \left[\left(\frac{\beta N_b}{k+1} \right)^2 \frac{\mathcal{Z}_{new}}{\mathcal{Z}_{old}} \frac{\mathcal{D}_{new}}{\mathcal{D}_{old}}, 1 \right] \tag{1.52}$$

where N_b is the number of baths, k is the current perturbation order (number of kinks/2), $\mathcal{Z}_{new}$ is the cluster matrix element

$$\mathcal{Z}_{new} = \langle T_\tau \psi_{\alpha'_{new}}(\tau'_{new}) \psi^\dagger_{\alpha_{new}}(\tau_{new}) \psi_{\alpha_1'}(\tau_1') \psi^\dagger_{\alpha_1}(\tau_1) \psi_{\alpha_k'}(\tau_k') \psi^\dagger_{\alpha_k}(\tau_k) \rangle_c \tag{1.53}$$

and $\mathcal{D}_{new}/\mathcal{D}_{old}$ is the ratio between the new and the old determinant of baths Δ. The factors of (βN_b) enter because of the increase of the phase space when adding a kink (increase of entropy) while the factor $1/(k+1)$ comes from factorials in Eq. 1.50. Similarly, the probability to remove two kinks, chosen randomly between $[1 \cdots k]$ is

$$P_{remove} = min \left[\left(\frac{k}{\beta N_b} \right)^2 \frac{\mathcal{Z}_{new}}{\mathcal{Z}_{old}} \frac{\mathcal{D}_{new}}{\mathcal{D}_{old}}, 1 \right]. \tag{1.54}$$

The expectation value of an observable ($\hat{O}$), expressible in terms of local fermionic operators ψ, can be calculated by sampling over the atomic (cluster) states by the Monte Carlo method:

$$\begin{aligned}\langle\hat{O}\rangle &= \frac{1}{Z}\int D[\psi^\dagger\psi]e^{-S_c}\cdot\sum_k\frac{1}{k!}\int_0^\beta d\tau_1\int_0^\beta d\tau_1'\cdots\int_0^\beta d\tau_k\int_0^\beta d\tau_k' \\ &\sum_{\alpha_1\alpha_1',\cdots,\alpha_k,\alpha_k'}\psi_{\alpha_1'}(\tau_1')\psi^\dagger_{\alpha_1}(\tau_1)\cdots\psi_{\alpha_k'}(\tau_k')\psi^\dagger_{\alpha_k}(\tau_k)\cdot\hat{O}\times\frac{1}{k!}Det(\bar{\Delta}) \qquad (1.55)\end{aligned}$$

In particular, the imaginary time local Green's function can be expressed as:

$$\begin{aligned}G_{\alpha\alpha'}(\tau-\tau') &= -\langle T_\tau\psi_\alpha(\tau)\psi^\dagger_{\alpha'}(\tau')\rangle \\ &= -\frac{1}{Z}\int D[\psi^\dagger\psi]e^{-S_c}\cdot\sum_k\frac{1}{k!}\int_0^\beta d\tau_1\int_0^\beta d\tau_1'\cdots\int_0^\beta d\tau_k\int_0^\beta d\tau_k' \\ &\sum_{\alpha_1\alpha_1',\cdots,\alpha_k,\alpha_k'}\psi_{\alpha_1'}(\tau_1')\psi^\dagger_{\alpha_1}(\tau_1)\cdots\psi_{\alpha_k'}(\tau_k')\psi^\dagger_{\alpha_k}(\tau_k)\psi_\alpha(\tau)\psi^\dagger_{\alpha'}(\tau') \\ &\times\frac{1}{k!}Det(\bar{\Delta}_k) \qquad (1.56)\end{aligned}$$

There are several ways of sampling the local Green's function:

- One can directly sample Eq. 1.56.
- Alternatively, one can compute the Green's function of conduction bath electrons. As the conduction electron operators are added in the partition function, the size of $\bar{\Delta}_k$ is increased from $k\times k$ to $(k+1)\times(k+1)$ by adding one row and one column. The impurity Green's function is obtained from the relation between the impurity Green's function and the conduction electron Green's function. The local Green's function can be obtained by sampling the determinant of hybridization matrix $\bar{\Delta}_k$ from which one row and one column are removed This procedure is explained in Ref. [17] in details.

Here, we give an alternative derivation for the formula to sample the local Green's function used in Ref. [17]. Since the Green's function is the time ordered average of two fermionic operators at different time, it can be computed by taking a derivative of $\ln Z$ with respect to

the element of the hybridization matrix, $\Delta_{\alpha_p\alpha'_q}(\tau_p,\tau'_q)$ as follows:

$$\begin{aligned} G_{\alpha'_q\alpha_p}(\tau'_q-\tau_p) &= -\langle T_\tau \psi_{\alpha'_q}(\tau'_q)\psi^\dagger_{\alpha_p}(\tau_p)\rangle \\ &= -\frac{1}{Z}\int D[\psi^\dagger\psi] e^{-S_c-\sum_{i,j=1,k}\int_0^\beta d\tau_i \int_0^\beta d\tau'_j \psi^\dagger_{\alpha_i}(\tau_i)\Delta_{\alpha_i\alpha'_j}(\tau_i,\tau'_j)\psi_{\alpha'_j}(\tau'_j)} \psi_{\alpha'_q}(\tau'_q)\psi^\dagger_{\alpha_p}(\tau_p) \\ &= \frac{\partial \ln Z}{\partial \Delta_{\alpha_p\alpha'_q}(\tau_p,\tau'_q)} \end{aligned} \tag{1.57}$$

This derivative with respect to $\Delta_{\alpha_p\alpha'_q}(\tau_p,\tau'_q)$ can also be applied to the Taylor expansion form of the partition function Z in Eq.1.50. As a result, the hybridization Δ_k at each perturbation order k is reduced to $(k-1)\times(k-1)$ matrix with the row and the column containing $\Delta_{\alpha_p\alpha'_q}(\tau_p,\tau'_q)$ removed

$$\begin{aligned} G_{\alpha'_q\alpha_p}(\tau'_q-\tau_p) &= \frac{\partial \ln Z}{\partial \Delta_{\alpha_p\alpha'_q}(\tau_p,\tau'_q)} \\ &= \frac{1}{Z}\int D[\psi^\dagger\psi] e^{-S_c}\cdot \sum_k \frac{1}{k!}\int_0^\beta d\tau_1 \int_0^\beta d\tau'_1 \cdots \int_0^\beta d\tau_k \int_0^\beta d\tau'_k \\ &\quad \sum_{\alpha_1\alpha'_1,\cdots,\alpha_k,\alpha'_k} \psi_{\alpha'_1}(\tau'_1)\psi^\dagger_{\alpha_1}(\tau_1)\cdots\psi_{\alpha'_k}(\tau'_k)\psi^\dagger_{\alpha_k}(\tau_k)\times\frac{1}{k!}\frac{\partial Det(\bar{\Delta}_k)}{\partial\Delta_{\alpha_p\alpha'_q}(\tau_p,\tau'_q)} \end{aligned} \tag{1.58}$$

where

$$\frac{\partial Det(\bar{\Delta}_k)}{\partial\Delta_{\alpha_p\alpha'_q}(\tau_p,\tau'_q)} = (-1)^{p+q}\cdot Det\left((\bar{\Delta}_k)'_{pq}\right) \tag{1.59}$$

and

$$(\bar{\Delta}_k)'_{pq} \equiv \begin{pmatrix} \Delta_{\alpha_1\alpha'_1} & \cdots & \Delta_{\alpha_1\alpha'_{q-1}} & \Delta_{\alpha_1\alpha'_{q+1}} & \cdots & \Delta_{\alpha_1\alpha'_k} \\ \cdots & \cdots & \cdots & \cdots & \cdots & \cdots \\ \Delta_{\alpha_{p-1}\alpha'_1} & \cdots & \Delta_{\alpha_{p-1}\alpha'_{q-1}} & \Delta_{\alpha_{p-1}\alpha'_{q+1}} & \cdots & \Delta_{\alpha_{p-1}\alpha'_k} \\ \Delta_{\alpha_{p+1}\alpha'_1} & \cdots & \Delta_{\alpha_{p+1}\alpha'_{q-1}} & \Delta_{\alpha_{p+1}\alpha'_{q+1}} & \cdots & \Delta_{\alpha_{p+1}\alpha'_k} \\ \cdots & \cdots & \cdots & \cdots & \cdots & \cdots \\ \Delta_{\alpha_k\alpha'_1} & \cdots & \Delta_{\alpha_k\alpha'_{q-1}} & \Delta_{\alpha_k\alpha'_{q+1}} & \cdots & \Delta_{\alpha_k\alpha'_k} \end{pmatrix}. \tag{1.60}$$

Here, $(\bar{\Delta}_k)'_{pq}$ is the matrix with the p-th row and the q-th column removed from $\bar{\Delta}_k$. In the matrix expression, τ and τ' indices are omitted for convenience.

The Monte Carlo weight P_k is given by

$$\begin{aligned} P_k &= \frac{1}{Z}\int D[\psi^\dagger\psi]e^{-S_c}\cdot\frac{1}{k!}\int_0^\beta d\tau_1\int_0^\beta d\tau_1'\cdots\int_0^\beta d\tau_k\int_0^\beta d\tau_k' \\ &\quad \sum_{\alpha_1\alpha_1',\cdots,\alpha_k,\alpha_k'}\psi_{\alpha_1'}(\tau_1')\psi^\dagger_{\alpha_1}(\tau_1)\cdots\psi_{\alpha_k'}(\tau_k')\psi^\dagger_{\alpha_k}(\tau_k)\times\frac{1}{k!}Det(\bar{\Delta}_k) \end{aligned} \tag{1.61}$$

such that $\sum_k P_k = 1$. Therefore, the Monte Carlo sampling of the Green's function is equivalent to the Monte Carlo average of the ratio between $Det\left((\bar{\Delta}_k)'_{pq}\right)$ and $Det(\bar{\Delta}_k)$ with extra sign $(-1)^{p+q}$ to be sampled in the Markov chain.

$$G_{\alpha_q'\alpha_p}(\tau_q'-\tau_p) = \sum_k P_k\cdot(-1)^{p+q}\cdot\frac{Det\left((\bar{\Delta}_k)'_{pq}\right)}{Det(\bar{\Delta}_k)} = \left\langle(-1)^{p+q}\cdot\frac{Det\left((\bar{\Delta}_k)'_{pq}\right)}{Det(\bar{\Delta}_k)}\right\rangle_{MC} \tag{1.62}$$

Hence, the element sampled for the Green's function during Monte Carlo is the inverse of $\bar{\Delta}_k$ as shown in the below equation:

$$G_{\alpha_q'\alpha_p}(\tau_q'-\tau_p) = \langle M_{pq}\rangle_{MC} \tag{1.63}$$

where $M_{pq}\equiv(\bar{\Delta}_k^{-1})_{pq}$.

In linear algebra, the $(-1)^{p+q}Det\left((\bar{\Delta}_k)'_{pq}\right)$ term is known as the cofactor of the matrix $\bar{\Delta}_k$ and it is known that the ratio of the cofactor to $Det(\bar{\Delta}_k)$ is the (p,q) element of $\bar{\Delta}_k^{-1}$. A simple proof is given below.

First, we introduce a new matrix where the j-th row and the i-th column of the $k\times k$ Δ_k matrix are shifted to the k-th row and the k-th column. The determinant of a matrix obtains a minus sign when one row or one column is exchanged with the adjacent ones, as a result, the

determinant of the new matrix gets an extra sign $(-1)^{i+j}$ compared to the determinant of Δ_k

$$Det(\bar{\Delta}_k) = (-1)^{i+j} \cdot Det \left(\begin{array}{cccccc|c} \Delta_{\alpha_1\alpha'_1} & \cdots & \Delta_{\alpha_1\alpha'_{i-1}} & \Delta_{\alpha_1\alpha'_{i+1}} & \cdots & \Delta_{\alpha_1\alpha'_k} & \Delta_{\alpha_1\alpha'_i} \\ \cdots & \cdots & \cdots & \cdots & \cdots & \cdots & \cdots \\ \Delta_{\alpha_{j-1}\alpha'_1} & \cdots & \Delta_{\alpha_{j-1}\alpha'_{i-1}} & \Delta_{\alpha_{j-1}\alpha'_{i+1}} & \cdots & \Delta_{\alpha_{j-1}\alpha'_k} & \Delta_{\alpha_{j-1}\alpha'_i} \\ \Delta_{\alpha_{j+1}\alpha'_1} & \cdots & \Delta_{\alpha_{j+1}\alpha'_{i-1}} & \Delta_{\alpha_{j+1}\alpha'_{i+1}} & \cdots & \Delta_{\alpha_{j+1}\alpha'_k} & \Delta_{\alpha_{j+1}\alpha'_i} \\ \cdots & \cdots & \cdots & \cdots & \cdots & \cdots & \cdots \\ \Delta_{\alpha_k\alpha'_1} & \cdots & \Delta_{\alpha_k\alpha'_{i-1}} & \Delta_{\alpha_k\alpha'_{i+1}} & \cdots & \Delta_{\alpha_k\alpha'_k} & \Delta_{\alpha_k\alpha'_i} \\ \hline \Delta_{\alpha_j\alpha'_1} & \cdots & \Delta_{\alpha_j\alpha'_{i-1}} & \Delta_{\alpha_j\alpha'_{i+1}} & \cdots & \Delta_{\alpha_j\alpha'_k} & \Delta_{\alpha_j\alpha'_i} \end{array} \right)$$

$$\equiv \quad (-1)^{i+j} \cdot Det \left(\begin{array}{c|c} \bar{A} & B \\ \hline C & d \end{array} \right) \tag{1.64}$$

Here, $\bar{A}$ is a $(k-1)\times(k-1)$ matrix, representing $(\bar{\Delta}_k)'_{ji}$ defined in Eq. 1.60. B is a $(k-1)\times 1$ matrix, C is a $1\times(k-1)$ matrix, and d is the (j,i) matrix element of Δ. The determinant of the block matrix can be computed using the LU decomposition

$$\left(\begin{array}{c|c} \bar{A} & B \\ \hline C & d \end{array} \right) = \left(\begin{array}{c|c} I & 0 \\ \hline C\cdot\bar{A}^{-1} & 1 \end{array} \right) \cdot \left(\begin{array}{c|c} \bar{A} & B \\ \hline 0 & d - C\cdot\bar{A}^{-1}\cdot B \end{array} \right). \tag{1.65}$$

therefore,

$$Det \left(\begin{array}{c|c} \bar{A} & B \\ \hline C & d \end{array} \right) = (d - C\cdot\bar{A}^{-1}\cdot B)\cdot Det\left(\bar{A}\right) \tag{1.66}$$

The ratio between $Det\left((\bar{\Delta}_k)'_{pq}\right)$ and $Det(\bar{\Delta}_k)$ with extra sign $(-1)^{p+q}$ is given by

$$(-1)^{i+j}\frac{Det\left((\bar{\Delta}_k)'_{ji}\right)}{Det(\bar{\Delta}_k)} = \frac{Det\left(\bar{A}\right)}{Det\left(\begin{array}{c|c} \bar{A} & B \\ \hline C & d \end{array} \right)} = (d - C\cdot\bar{A}^{-1}\cdot B)^{-1} \tag{1.67}$$

Moreover, the inverse of the block matrix is given by

$$\left(\begin{array}{c|c} \bar{A} & B \\ \hline C & d \end{array} \right)^{-1} = \left(\begin{array}{c|c} (\bar{A}^{-1} - d^{-1}B\cdot C)^{-1} & -(d - CA^{-1}B)^{-1}A^{-1}B \\ \hline -d^{-1}C(\bar{A}^{-1} - d^{-1}B\cdot C)^{-1} & (d - CA^{-1}B)^{-1} \end{array} \right) \tag{1.68}$$

The (i,j) element of $(\bar{\Delta}_k)^{-1}$ is the same as the (k,k) element of inverse of the block matrix.

$$(\bar{\Delta}_k)^{-1}_{ij} = \left(\begin{array}{c|c} \bar{A} & B \\ \hline C & d \end{array}\right)^{-1}_{kk} = (d - CA^{-1}B)^{-1} \tag{1.69}$$

Comparing Eq. 1.67 with Eq. 1.69, it is clear that the (i,j) element of the inverse matrix is the same as the ratio between $Det\left((\bar{\Delta}_k)'_{ji}\right)$ and $Det(\bar{\Delta}_k)$ with extra sign.

$$(\bar{\Delta}_k)^{-1}_{ij} = (-1)^{i+j}\frac{Det\left((\bar{\Delta}_k)'_{ji}\right)}{Det(\bar{\Delta}_k)} \tag{1.70}$$

As a result, the Green's function calculation within CTQMC is equivalent to the sampling of the inverse of $\bar{\Delta}_k$ as shown in Eq. 1.63. This sampling of the Green's function can be performed directly in the Matsubara frequency space by Fourier transforming from the imaginary time to the imaginary frequency. Due to the time translational invariance, the Green's function is a function of only one Matsubara frequency

$$G_{\alpha_i\alpha'_j}(i\nu_n) \quad = \quad \frac{1}{\beta}\sum_{\tau_i,\tau'_j} e^{i\nu_n(\tau_i-\tau'_j)}G_{\alpha_i\alpha'_j}(\tau_i-\tau'_j) = \langle M_{ij}(i\nu_n)\rangle_{MC} \tag{1.71}$$

These equations derived for sampling the one-particle Green's function can be generalized to sample the two-particle Green's function as will be shown in Section 4.2.

Chapter 2

A Dynamical Mean Field Theory (DMFT) Study of Nagaoka Ferromagnetism

In this chapter, we revisit Nagaoka ferromagnetism in the $U = \infty$ Hubbard model within the dynamical mean-field theory (DMFT) using the recently developed continuous time quantum Monte Carlo method as the impurity solver [19]. The stability of Nagaoka ferromagnetism is studied as a function of the temperature, the doping level, and the next-nearest-neighbor lattice hopping t'. We found that the nature of the phase transition as well as the stability of the ferromagnetic state is very sensitive to the t' hopping. Negative $t' = -0.1t$ stabilizes ferromagnetism up to higher doping levels. The paramagnetic state is reached through a first order phase transition. Alternatively, a second order phase transition is observed at $t' = 0$. Very near half-filling, the coherence temperature T_{coh} of the paramagnetic metal becomes very low and ferromagnetism evolves out of an incoherent metal rather than a conventional Fermi liquid. We use the DMFT results to benchmark the slave-boson method which might be useful in more complicated geometries.

2.1 Nagaoka ferromagnetism in the $U = \infty$ Hubbard model

The stability of the ferromagnetic phase in the $U = \infty$ Hubbard model is a long standing problem. Nagaoka [20] showed that for a single hole in a bipartite lattice the ground state is a fully polarized ferromagnet, and the term "Nagaoka ferromagnetism" is commonly used to describe this state. Whether a fully or a partially polarized phase persist to a finite hole density (δ) is controversial and has been the subject of numerous investigations [21].

The problem has been addressed with variational wave functions [22, 23, 24, 25, 26], slave particle methods [27, 28], quantum Monte Carlo (QMC) methods [29], and variational QMC methods [30]. In all these methods the ferromagnetism is stable up to a critical value of doping δ_c. It was also demonstrated by these approaches that the size of the ferromagnetic region depends strongly on the lattice through the electronic dispersion. The ferromagnetic state was found to be unstable even for the case of a single hole in the $U = \infty$ square lattice with a small positive next-nearest neighbor hopping t' [31]. At an intermediate or a large U, a flat band below the Fermi level [32] or a peak in the density of states below the Fermi level [33, 34, 35, 36], as realized in the fcc lattice [37, 38] or a Van Hove singularity [39], stabilize the ferromagnetic state.

Dynamical mean-field theory (DMFT) has also been used to address the Nagaoka problem, however the number of available impurity solvers in the $U = \infty$ case is very limited. Obermeier *et al.* [40] carried out the first DMFT study of this problem using the non-crossing approximation as the impurity solver. They found a partially polarized ferromagnetic state below a critical temperature T_c in the infinite dimensional hypercubic lattice. The existence of a ferromagnetic state in this model was later confirmed by a DMFT study which used numerical renormalization group as the impurity solver [41].

In this study, we revisit the problem of Nagaoka ferromagnetism in the $U = \infty$ Hubbard model within DMFT, using the recently developed continuous time quantum Monte Carlo (CTQMC) method as the impurity solver [17, 16]. This impurity solver allows the numerically exact solution of the DMFT equations at very low temperatures for all values of doping level δ even in the $U = \infty$ model. We find that at large doping, the ferromagnetism emerges from a conventional Fermi liquid, while at small doping the Curie temperature is very close to the coherence temperature, hence the ferromagnetism emerges from an incoherent state. We pay particular attention to the possibility of phase separation and its dependence on the sign of t'/t. Finally we benchmark simpler approaches to the problem such as the slave boson method. Within slave boson approach, several physical quantities such as the quasiparticle

renormalization amplitude or the susceptibility can not be determined reliably. Nevertheless we show that the total energy can be computed quite reliably within the simple slave boson approach due to error cancellation. This is important since the detailed modeling of optical lattices of cold atoms, which provide a clean realization of the Hubbard model, will require incorporating spatial inhomogeneities into the treatments of strong correlations. At present, this can only be done with simpler techniques such as slave bosons methods.

We study the Hamiltonian of the $U = \infty$ Hubbard model given by

$$\hat{H} = -\sum_{ij\sigma} t_{ij} \hat{P}_s \hat{c}^{\dagger}_{i\sigma} \hat{c}_{j\sigma} \hat{P}_s, \tag{2.1}$$

where $\hat{P}_s$ is a projection operator which removes states with double-occupied sites. We choose the lattice dispersion of the two dimensional square lattice with the nearest-neighbor (n.n) hopping t and the next-nearest-neighbor (n.n.n) hopping t'. The units are fixed by choosing $t = \frac{1}{2}$.

2.2 A DMFT+CTQMC approach

DMFT maps the partition function of the Hubbard model onto the partition function of an effective Anderson impurity model (AIM) resulting in the following effective action.

$$S_{eff} = S_{atom} + \int_0^{\beta} d\tau \int_0^{\beta} d\tau' \sum_{\sigma} c^{\dagger}_{\sigma}(\tau) \Delta_{\sigma}(\tau - \tau') c_{\sigma}(\tau') \tag{2.2}$$

where S_{atom} represents the action of the isolated impurity, and $\Delta_{\sigma}(\tau - \tau')$ is the hybridization function of the effective AIM. In this $U = \infty$ case, the double occupied state of the impurity should be excluded when evaluating S_{atom}. $\Delta_{\sigma}(\tau - \tau')$ is not initially known and it must be determined by the DMFT self-consistency condition given below. The impurity Green function and the impurity self-energy are given by the following equations

$$G_{\sigma}(\tau - \tau') = -\langle T c_{\sigma}(\tau) c^{\dagger}_{\sigma}(\tau') \rangle_{S_{eff}} \tag{2.3}$$

$$\Sigma_{\sigma}(i\omega_n) = i\omega_n + \mu - \Delta_{\sigma}(i\omega_n) - G^{-1}_{\sigma}(i\omega_n). \tag{2.4}$$

The DMFT self-consistency condition requires that the local Green's function of the lattice

coincides with the Green's function of the auxiliary AIM and identifies the equivalence between the lattice local self-energy and the self-energy of the corresponding AIM, i.e.,

$$\sum_{\mathbf{k}} \frac{1}{i\omega_n + \mu + h\sigma - \epsilon(\mathbf{k}) - \Sigma_\sigma(i\omega_n)} = \frac{1}{i\omega_n + \mu + h\sigma - \Delta_\sigma(i\omega_n) - \Sigma_\sigma(i\omega_n)}, \tag{2.5}$$

where the lattice dispersion of our choice is $\epsilon(\mathbf{k}) = -2t(\cos k_x + \cos k_y) - 4t' \cos k_x \cos k_y$ and h is the external magnetic field. For a given Weiss field $\Delta_\sigma(i\omega_n)$, the effective action S_{eff} is constructed and the AIM is solved for the new $G_\sigma(i\omega_n)$ and $\Sigma_\sigma(i\omega_n)$. Using the self-consistency condition Eq.5, the new Weiss field $\Delta_\sigma(i\omega_n)$ is computed. This iterative procedure is repeated until the Green's function is converged.

To solve the impurity problem of Eq. 2.2, the CTQMC impurity solver is used. In this method, the hybridization part of the effective action is treated as a perturbation around the atomic action and all diagrams are summed up by stochastic Metropolis sampling. [17] In this $U = \infty$ case, doubly occupied state of the atom is excluded from atomic eigenstates. CTQMC converges well in the low Matsubara frequency region, but it is poorly behaved in the high frequency region. Therefore, one needs the analytic expression for the self-energy in the high frequency limit and it has to be interpolated to the low frequency region. The high frequency expansion for the $U = \infty$ Hubbard model gives

$$Re[\Sigma_\sigma(\infty)] = m_{1\sigma}/m_{0\sigma}^2 + \mu \tag{2.6}$$

$$Im[\Sigma_\sigma(\infty)] = (1 - 1/m_{0\sigma})\omega \tag{2.7}$$

where $m_{0\sigma} = \langle\{c_\sigma, c_\sigma^\dagger\}\rangle = 1 - n_{-\sigma}$, $m_{1\sigma} = \langle\{[c_\sigma, H], c_\sigma^\dagger\}\rangle = -\mu(1 - n_{-\sigma}) - Tr[\Delta_{-\sigma} G_{-\sigma}]$. Note the appearance of the kinetic energy $Tr[\Delta_{-\sigma} G_{-\sigma}]$ in this expansion which is absent for finite U.

Within CTQMC, various spin dependent physical quantities can be calculated such as occupation numbers ($n_\uparrow$,$n_\downarrow$) and the local magnetic susceptibility (χ_{loc}). The $q = 0$ magnetic susceptibility of a lattice can be calculated from χ_{loc} by evaluating the two particle vertex functions, which is a numerically demanding task. To circumvent this difficulty, $\chi_{q=0}$ of a lattice

can be calculated from the ratio of magnetization to the external magnetic field ($\chi = \frac{dm}{dh}|_{h=0}$). The external field h alters the effective action (Eq. 2.2) by adding $h\sigma$ to atomic energies and the self-consistency condition (Eq. 2.5) is enforced to include the spin dependent $h\sigma$ term during DMFT iterations. The exclusion of the double occupancy ($U = \infty$) implies the Hubbard potential energy to vanish and the only relevant energy is the kinetic energy. The latter is given by $Tr[\Delta_\sigma G_\sigma]$, and it is related to the average of the perturbation order k as follows:

$$E_{kin,\sigma} = Tr[\Delta_\sigma G_\sigma] = -T\langle k_\sigma \rangle \tag{2.8}$$

where T is temperature. Therefore, it is possible to calculate the kinetic energy to high accuracy by evaluating $\langle k_\sigma \rangle$. The free energy, F, can also be derived from the kinetic energy as long as the system is in the Fermi liquid regime

$$F(T) \cong E_{kin} - \frac{\pi^2}{3} Z^{-1} \rho_0(\mu) T^2, \tag{2.9}$$

where Z is the renormalization residue and ρ_0 is the non-interacting density of states.

2.3 DMFT results

2.3.1 The reduced magnetization and the chemical potential vs the electron density

Fig. 2.1.(a) shows the reduced magnetization m_r=$(n_\uparrow - n_\downarrow)/(n_\uparrow + n_\downarrow)$ as a function of the electron density n at three distinct t'/t ratios. The result is notably different for different values of t'/t. The spontaneously broken ferromagnetic (FM) state ($m_r \neq 0$) is favored for $t'/t < 0$ while the FM state is unstable for $t'/t > 0$. The critical density (n_c) at which the transition occurs increases as t'/t increases, reducing the region of stability of the FM state. Moreover, at $t'/t = -0.1$ magnetization m_r changes abruptly at n_c=0.705 indicating a first order transition, while at $t'/t = 0$ magnetization m_r increases continuously indicating a second order phase transition at n_c=0.815.

Notice that close to half filling the Curie temperature is low and at fixed temperature

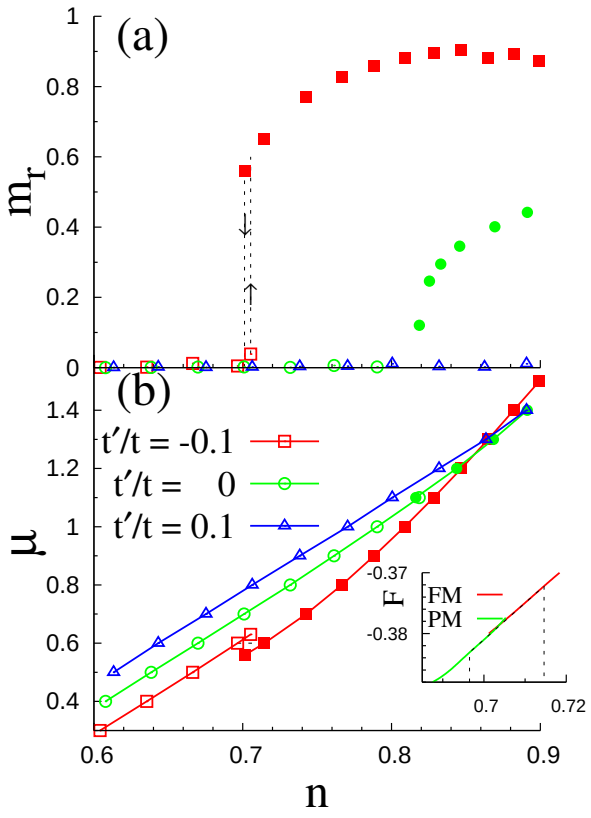

Figure 2.1: (a) The reduced magnetization m_r=$(n_\uparrow - n_\downarrow)/(n_\uparrow + n_\downarrow)$ vs the electron density n at t'/t=-0.1, 0, and 0.1 (b) the chemical potential μ vs n at t'/t=-0.1, 0, and 0.1. Filled points indicate a FM state. Inset : FM free energy and PM free energy vs n at t'/t=-0.1. The dotted line is constructed using the Maxwell construction. All calculations were performed at T=0.01.

($T = 0.01$) it becomes increasingly difficult to converge the DMFT equations near the transition temperature due to the standard critical slowing down.

Near half filling the quasiparticle bandwidth is small due to strong correlations hence the thermal fluctuations are comparable to the Curie temperature in this region. A stable FM state is possible only if T is sufficiently lower than T_{coh}. In the region above 0.95, an incoherent paramagnetic (PM) state becomes stable as T exceeds T_{coh}.

Inspecting the chemical potential as a function of density reveals that the nature of the transition changes with t'/t (see figure 2.1.(b)). For $t'/t = 0$ the transition is continuous while for $t'/t = -0.1$, there is a region of constant chemical potential which corresponds to a first-order transition. The flat chemical potential region ($n = 0.696 - 0.715$) indicates that two different DMFT solutions (FM, PM) can be converged depending on the initial conditions and it indicates phase separation (PS) of the FM and PM state. This region is determined by Maxwell construction which connects common tangents between two phases in the free energy vs n graph. (Fig. 2.1. inset)

2.3.2 The reduced magnetization vs the temperature

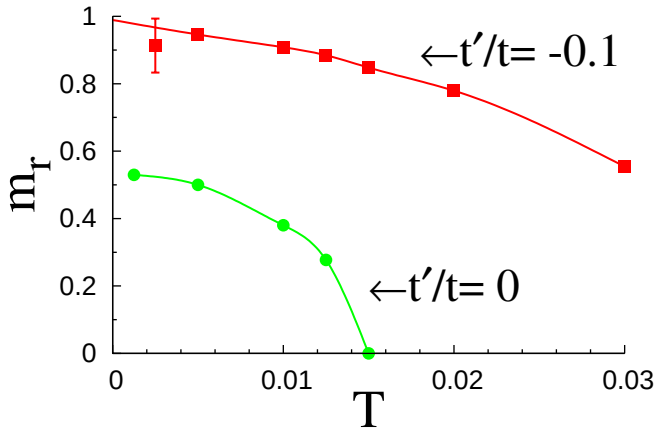

Figure 2.2: m_r vs T at fixed n =0.85 with t'/t=-0.1 and 0. The fully polarized FM state ($m_r = 1$) is expected only when t'/t=-0.1.

The original debate on the Nagaoka problem was focused on the existence of the fully

polarized FM state at finite δ in the $T \to 0$ limit. Therefore, it is necessary to investigate magnetization m_r at very low T. In Fig. 2.2 we show very low temperatures ($T = 0.001t$) results and it is clear that the magnetization saturates to a value smaller than unity for $t'/t = 0$ while it reaches unity at low temperatures for $t'/t = -0.1$. The fully polarized Nagaoka state is thus not stable for $t'/t = 0$ and moderately small doping ($\delta \sim 0.1$) while it is realized for $t'/t = -0.1$. As the spins become fully polarized ($t'/t = -0.1, T \to 0$), numerics requires high statistics and an error-bar is specified to take into account the numerical error.

2.3.3 The spectral function

The spectral functions are shown in Fig. 2.3. Since CTQMC delivers response functions on the imaginary frequency axis, one needs to perform the analytical continuation of the Green function to the real axis. Here we use the maximum entropy method [42]. The spectral functions show noticeable differences for small change in t'. At $t'/t = -0.1$, the majority spin spectral function shows a very small renormalization due to interactions ($Z \simeq 1$) and a large spectral peak in the occupied part of the spectra. The overall shape is similar to the non-interacting spectral function (Fig. 2.3. inset). The minority spin spectral function is much more correlated and shows a narrow quasiparticle band above the Fermi level and a tiny lower Hubbard band. In the magnetic state, the occupied part of the spectra is thus well described by a model of a weakly correlated FM metal.

At $t'/t = 0$ and $t'/t = 0.1$, the spectral functions consist of both the narrow quasiparticle band and the lower Hubbard band. In the $U = \infty$ Hubbard model, the upper Hubbard band disappears due to the exclusion of double occupancy.

The stability of the FM state at $t'/t = -0.1$ can be traced back to the large spectral peak in the occupied part of the spectra of the non-interacting DOS shown in the inset of Fig. 2.3. As explained above, the majority spin of the FM state shows only weak renormalization due to interactions. This is a consequence of the Pauli exclusion principle which constrains the motion of a hole in the polarized background and interactions, being less important in this case, do not

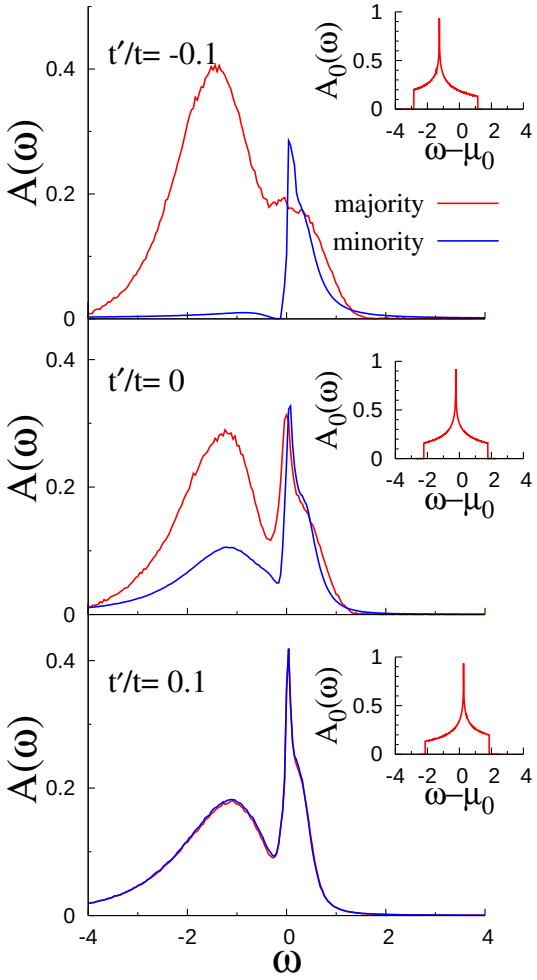

Figure 2.3: The spectral functions $A(\omega)$ at t'/t=-0.1 (top), 0 (middle), and 0.1 (bottom) for fixed n =0.85. Inset: Non-interacting spectral functions ($A_0(\omega)$) of the majority spin at the corresponding t'/t values. ($\mu_0 = \mu - Re\Sigma(0)$) All calculations were performed at T=0.01.

hamper the coherent motion of the hole through the polarized background. The kinetic energy of this state thus clearly depends on t'/t ratio and is reduced with decreasing t'/t. Contrary to the FM state, the correlations are very strong in the PM state regardless of the spectral peak in the non-interacting DOS and t'/t ratio. The coherent part of the spectra does not contribute much to the kinetic energy as the quasiparticle bandwidth shrinks due to the strong correlations. The incoherent part of the spectra in the form of the Hubbard bands arises from localized electrons and consequently it is almost independent of the specific lattice dispersion. Therefore, the kinetic energy of the PM state weakly depends on t'/t ratio. The peak in the occupied part of the spectra of the non-interacting DOS thus reduces the kinetic energy of the FM state compared to the PM state thus stabilizing ferromagnetism.

It is known from other studies [32] that a highly degenerate flat band in the occupied part of the spectra favors ferromagnetism at any finite U. However, this flat band ferromagnetism (an extreme limit of the Stoner ferromagnetism) argument is not applicable to the $t'/t = -0.1$ case of the Nagaoka ferromagnetism (the other extreme limit of the Stoner ferromagnetism). In a flat-band model, the ground state of the non-interacting system is highly degenerate due to the presence of the flat band. However, even a small Coulomb repulsion lowers the energy of the FM state (if the flat band is half-filled) and stabilizes the FM state. The role of the Coulomb interaction is simply to lift the huge degeneracy and "select" the states with the highest magnetization as unique ground states. In the infinite U model, the potential energy vanishes because of no doubly occupancy. However, the kinetic energy depends sensitively on the smoothness of the spin polarized background, and a disordered PM state can not gain the kinetic energy by the variation of t'/t while a FM state can.

2.3.4 The uniform susceptibility

The inverse of the uniform magnetic susceptibility ($\chi^{-1}_{q=0}$) of the PM state vs n at $t'/t = 0$ and 0.1 is shown in Fig. 2.4. The extrapolated line at $t' = 0$ indicates that χ diverges near $n = 0.815$, confirming the second order transition at the critical density ($n_c = 0.815$). At $t'/t = 0.1$, one

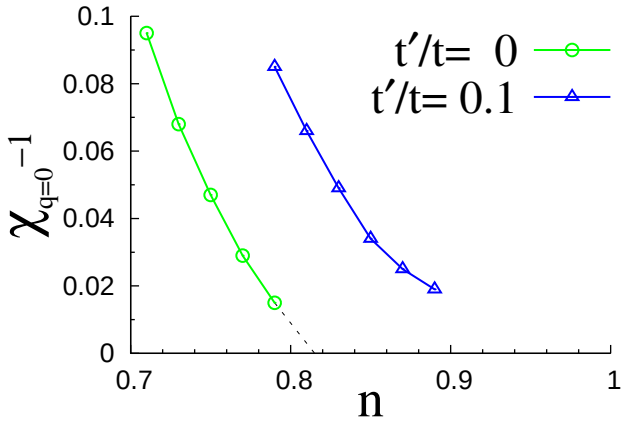

Figure 2.4: The uniform susceptibility ($\chi_{q=0}^{-1}$) vs n at $t'/t = 0$ and 0.1. The dotted line is for the extrapolation to $\chi_{q=0}^{-1} = 0$. (T=0.01)

might expect χ will diverge near $n = 1$. However, as T_{coh} becomes smaller than T near $n = 1$, the incoherent PM state is stabilized. In other words, at $t'/t = 0.1$, the crossover from the coherent PM state to the incoherent PM state occurs instead of the transition to the FM state.

2.3.5 The phase diagram

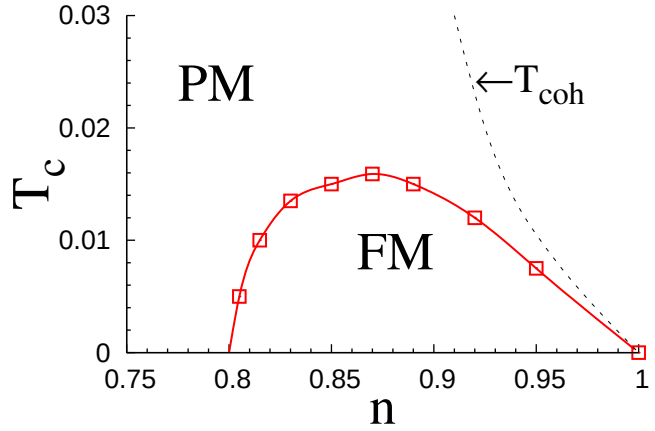

Figure 2.5: The critical temperature T_c vs n at $t' = 0$. n_c at $T = 0$ is obtained from the extrapolation. The dotted line represents the coherence temperature T_{coh} vs n.

Fig. 2.5 shows the critical temperature (T_c) vs n at $t'/t = 0$. In the region below T_c a partially polarized FM state is found, and it is determined by observing $n_\uparrow \neq n_\downarrow$ in a CTQMC result. This graph shows that the lower critical density (n_c) at $T = 0$ is around 0.8. At half

filling critical temperature should vanish due to the following reason: The kinetic energy at half filling is zero in both the PM and the FM state because of the blocking of charge density. The entropy of the paramagnet is much larger than the entropy of the ferromagnet due to the large spin degeneracy of the PM state. In other words, PM state is thermodynamically stable at any finite temperature at $n = 1$.

As the width of the quasiparticle band becomes smaller near $n = 1$, the coherence temperature T_{coh} is also reduced making it hard to sustain the quasiparticle coherent band. At $T > T_{coh}$, the PM state is clearly stabilized. The T_{coh} boundary can be determined from the imaginary part of self energy ($Im\Sigma(i\omega_n)$) on the imaginary frequency axis. In a coherent region ($T < T_{coh}$), the renormalization residue Z is well defined ($0 < Z < 1$) by evaluating the negative slope of $Im\Sigma(i\omega_n)$ at $\omega = 0$ ($Z = (1 - \frac{dIm\Sigma}{d\omega}|_{\omega=0})^{-1}$). However, in the incoherent regime ($T > T_{coh}$), the slope of $Im\Sigma(i\omega_n)$ at $\omega = 0$ becomes positive making the concept of Z ill defined (Fig. 2.7). Therefore, we determined T_{coh} as the temperature where the slope of the low energy self energy vanishes, and found that it is almost proportional to $\delta^{3/2}$, in surprising agreement with the findings of a previous study of doped Mott-insulator [43].

In a two-dimensional Hubbard model, a long-range magnetic order at a finite T is prohibited by the Mermin-Wagner theorem. A FM order is possible only at $T = 0$. At any finite T, Goldstone modes disorder the system [44], and it results in a correlation length which is finite but exponentially large in T^{-1}. DMFT does not capture this behavior. Therefore, T_c in the context of the two dimensional model should be interpreted as an estimate of the temperature where the correlation length gets very large. In higher dimensions, we expect a FM state at low T with the correct dependence on t'/t. The Nagaoka ferromagnetism study using the dispersion of realistic materials deserves further investigations since the energy balance between a FM state and a PM state or the character of the transition is very sensitive to the details of the lattice structure.

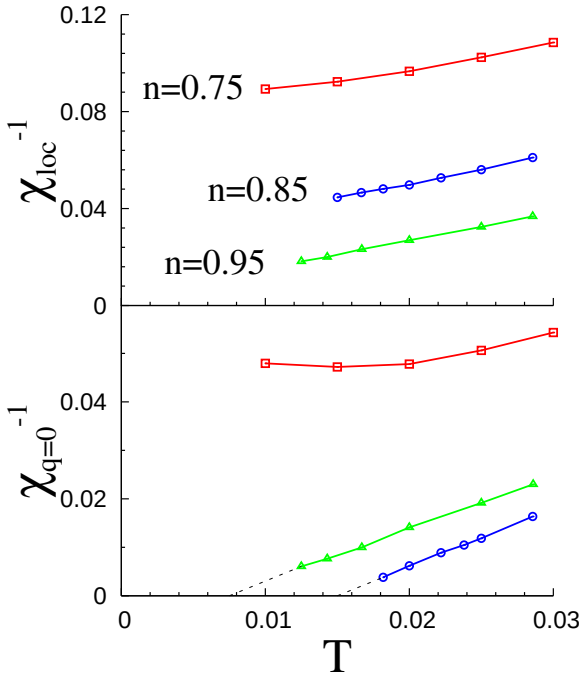

Figure 2.6: The local susceptibility (χ_{loc}^{-1}) vs T and the uniform susceptibility ($\chi_{q=0}^{-1}$) vs T ($t'/t = 0$)

2.3.6 The local susceptibility and the uniform susceptibility

In general, $n_\uparrow - n_\downarrow$ exhibits small fluctuations near the boundary of T_c due to the finite T. The fluctuations become especially severe through the transition from the FM state to the incoherent PM state near $n = 1$. Therefore, the boundary points can be determined more precisely by examining the temperature dependence of $\chi_{q=0}^{-1}$ (Fig. 2.6). $\chi_{q=0}^{-1}$ near a transition point obeys the Curie-Weiss form ($\chi_{q=0}^{-1} \sim T - T_c$). Both coherent ($n = 0.85$) and incoherent ($n = 0.95$) regions show linear dependence of $\chi_{q=0}^{-1}$ on T. The $\chi_{q=0}^{-1}$ for $n = 0.75$ barely depends on T, exhibiting Pauli paramagnetic behavior. χ_{loc}^{-1} is greater than $\chi_{q=0}^{-1}$ and it increases as n decreases. This is because in DMFT $\chi_{loc}^{-1} \sim T + T_{coh}$ and T_{coh} increases as n decreases [43].

2.3.7 The self energy

Fig. 2.7 shows the behavior of $Im\Sigma(i\omega_n)$ for the three different phases in the T_c phase diagram of Fig. 2.5. For $n = 0.85$ and $T = 0.01$, a coherent FM state is expected from the phase diagram. A coherent Fermi liquid is validated by investigating the negative slope of $Im\Sigma(i\omega_n)$ at $\omega = 0$.

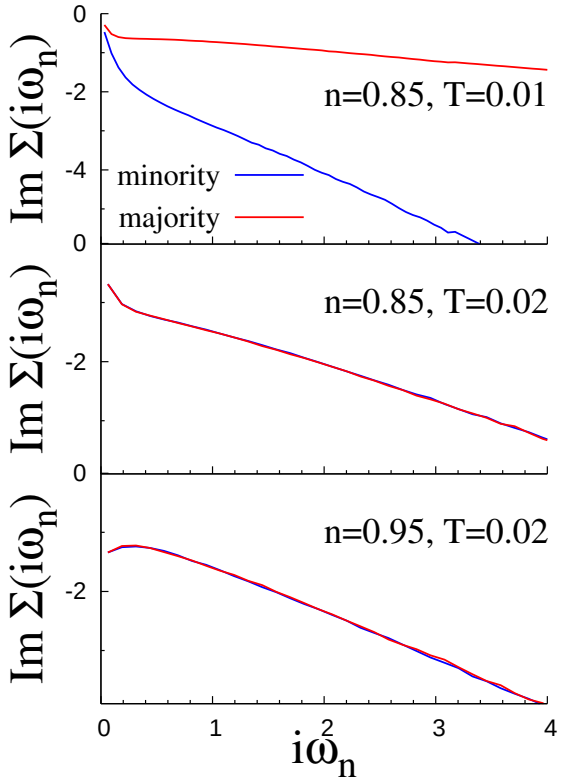

Figure 2.7: $Im\Sigma(i\omega_n)$ vs $i\omega_n$ at the coherent FM state (the top panel), the coherent PM state (the middle panel), and the incoherent PM state (the bottom panel). $(t'/t = 0)$

The slope for spin σ at the high frequency part is given by $-n_{-\sigma}/1-n_{-\sigma}$ (Eq. 7) and the inequality of the slope indicates $n_\uparrow \neq n_\downarrow$ confirming the FM state. The majority spin state has a smaller slope at high frequency because $n_{-\sigma}$ of the majority spin is smaller than that of the minority spin. Also, because the slope of the majority spin at $\omega = 0$ is smaller, Z of the majority spin is larger than that of the minority spin. This means the quasiparticle band of the minority spin is strongly renormalized by correlations while the majority spin state tends to be similar to the non-interacting energy dispersion. For $n = 0.85$ and $T = 0.02$, a coherent PM state is established by observing a negative slope at $\omega = 0$ and no spin symmetry breaking. For $n = 0.95$ and $T = 0.02$, an incoherent PM state is expected from the positive slope at $\omega = 0$ because the concept of Z is no longer valid and the application of Fermi liquid theory fails. Lastly, for fixed $T = 0.02$, as n increases from 0.85 to 0.95 the slope at high frequency also increases because $n_{-\sigma}$ increases.

2.4 Nagaoka Ferromagnetism from a 4-site plaquette

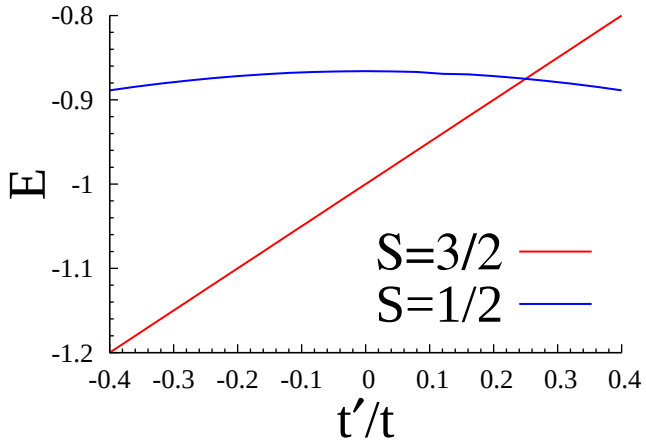

Figure 2.8: The lowest energies of a S=1/2 state and a S=3/2 state in a $U = \infty$ 4-site toy model varying t'/t. E is the energy in units of $t = 1/2$.

In order to provide a simple interpretation of why decreasing t' stabilizes the Nagaoka state, we examine the simplest possible model which retains the physics of the Nagaoka problem. We consider a 4-site plaquette with three electrons (one hole). The ground state of this model may

be characterized by the quantum number corresponding to the total spin angular momentum (ie. $S = \frac{3}{2}, \frac{1}{2}$) and the z-direction of the spin angular momentum ($S_z = \pm\frac{3}{2}, S_z = \pm\frac{1}{2}$). The whole Hamiltonian matrix is a 32×32 matrix excluding double-occupied sites and it is block-diagonalized to 6 distinct spin sectors by performing the unitary transform to the proper S, S_z basis. The ground state energy at each spin sector is determined by the exact diagonalization of Hamiltonian matrix.

The lowest energy in a $S = \frac{3}{2}$ sector is given by $-2t + t'$ and in the $S = \frac{1}{2}$ sector is given by $-\sqrt{3t^2 + t'^2}$. The energy dependence of a $S = \frac{3}{2}$ state is noticeably different from that of a $S = \frac{1}{2}$. In a $S = \frac{3}{2}$ case, doubly occupied states are excluded by the Pauli principle regardless of U. Therefore, the $U = \infty$ Hamiltonian is equivalent to the $U = 0$ Hamiltonian where the addition of the positive n.n.n hopping t' contributes linearly to the increase of the kinetic energy. However, doubly occupied states in a $S = \frac{1}{2}$ sector are excluded only for $U \to \infty$. Therefore, unlike the $S = \frac{3}{2}$ case, the energy dependence on t' is greatly reduced as the Hilbert space shrinks due to the infinite U.

A $S = \frac{3}{2}$ ground state is indicative of the Nagaoka ferromagnetic state while a $S = \frac{1}{2}$ ground state is indicative of a paramagnetic state. The $S = \frac{3}{2}$ state is the ground state for $t'/t < 0.24$ and the energy difference increases approximately linearly thereafter indicating that the Nagaoka state is stabilized as t'/t is decreased. This is in qualitative agreement with the DMFT results presented in the previous section. The energy of the $S = \frac{1}{2}$ state weakly depends on t' while the $S = \frac{3}{2}$ energy decreases as t'/t decreases. This also explains that the stability of Nagaoka ferromagnetism originates from the minimization of the kinetic energy.

2.5 A mean-field slave boson approach

In this section, Nagaoka ferromagnetism in a $U = \infty$ Hubbard model is studied using a mean-field slave boson approach. In a slave boson method, a fermion operator is accompanied by bosonic operators (ie. slave bosons) which keep track of the local occupation number. The three slave boson operators are $\hat{e}, \hat{p_\uparrow}, \hat{p_\downarrow}$ and they act on unoccupied sites, spin-up sites, and

spin-down sites, respectively. In this $U = \infty$ case, the doubly occupied sites are excluded. Constraints regarding the conservation of the occupation number are imposed with Lagrange multipliers $(\lambda, \lambda_\uparrow, \lambda_\downarrow)$. The slave boson Hamiltonian is given by

$$\hat{H} = -\sum_{ij\sigma} t_{ij}\hat{c}^\dagger_{i\sigma}\hat{z}_{i\sigma}\hat{z}^\dagger_{j\sigma}\hat{c}_{j\sigma} - \sum_{i\sigma} \lambda_{i\sigma}(\hat{p}^\dagger_{i\sigma}\hat{p}_{i\sigma} - \hat{c}^\dagger_{i\sigma}\hat{c}_{i\sigma}) + \sum_{i\sigma} \lambda_i(\hat{p}^\dagger_{i\sigma}\hat{p}_{i\sigma} + \hat{e}^\dagger_i\hat{e}_i - 1) \tag{2.10}$$

where $\hat{z}_{i\sigma} = \frac{1}{\sqrt{1-\hat{p}^\dagger_{i\sigma}\hat{p}_{i\sigma}}}\hat{e}^\dagger_i\hat{p}_{i\sigma}\frac{1}{\sqrt{1-\hat{e}^\dagger_i\hat{e}_i-\hat{p}^\dagger_{i-\sigma}\hat{p}_{i-\sigma}}}$. t_{ij}=t if i,j are n.n, and t_{ij}=t' if i,j are n.n.n. The non-interacting $\epsilon(\mathbf{k})$ is taken to be $-2t(\cos k_x + \cos k_y) - 4t' \cos k_x \cos k_y$ as in the previous section. The original Fock space has been enlarged including the slave boson fields. The partition function can be calculated from the Feynman functional path integral over the original fermi fields, slave boson fields, and Lagrange multipliers. The integral over the fermi fields is straightforward because the Hamiltonian is quadratic in the fermi fields. The integral over the slave boson fields and Lagrange multipliers should be performed using the saddle-point approximation, where the integral over the slave boson fields and Lagrange multipliers is approximated by putting their space and time independent mean-field values which minimize the Hamiltonian. The physical meaning of slave boson mean-field value is clear. The expectation value $\langle\hat{e}^\dagger\hat{e}\rangle$ corresponds to the fraction of unoccupied sites, i.e. the hole density $\delta(1-n)$. Similarly, $\langle\hat{p}^\dagger_\uparrow\hat{p}_\uparrow\rangle$ equals to the spin up occupation number $(n_\uparrow)$, and $\langle\hat{p}^\dagger_\downarrow\hat{p}_\downarrow\rangle$ corresponds to the spin down occupation number $(n_\downarrow)$.

The free energy can be derived from the partition function $(F = -k_B T \ln Z)$ and it is necessary to compare the free energies between ferromagnetic state and paramagnetic state to investigate the transition. The free energy is a function of magnetization $m = n_\uparrow - n_\downarrow$, δ, and T. At $T = 0$, the free energy becomes the ground state energy. The energies of the fully polarized ferromagnetic (FPFM) state $(m = n_\uparrow)$ and the paramagnetic (PM) state $(m = 0)$ are given by.

$$E_{FPFM}(\delta) = \frac{1}{N_s}\sum_{\mathbf{k}} \epsilon(\mathbf{k})\Theta(\mu - \epsilon(\mathbf{k})) \tag{2.11}$$

$$E_{PM}(\delta) = \frac{1}{N_s}\sum_{\mathbf{k},\sigma} Z\epsilon(\mathbf{k})\Theta(\mu^* - Z\epsilon(\mathbf{k})) \tag{2.12}$$

where N_s is the number of total sites, Z is the renormalization residue given by $2\delta/(1+\delta)$, μ is the

chemical potential in a fully polarized ferromagnetic state satisfying $(1/N_s)\sum_{\mathbf{k}}\Theta(\mu-\epsilon(\mathbf{k}))=n_\uparrow=1-\delta$, and $\mu^*=(\mu-\lambda_\sigma)$ is the effective chemical potential in a paramagnetic state satisfying $(1/N_s)\sum_{\mathbf{k}}\Theta(\mu^*-Z\epsilon(\mathbf{k}))=n_\uparrow=n_\downarrow=(1-\delta)/2$. The DOS of the FPFM state is the same as the non-interacting DOS ($\rho_0(\epsilon)$) while the DOS of the PM state is renormalized by a factor Z to $1/Z\cdot\rho_0(\epsilon/Z)$. Unlike the DMFT method, the slave boson approach considers only the renormalized quasiparticle DOS ignoring the incoherent contribution. E_{PM} is given by $Z\cdot E_0$ where E_0 is the non-interacting energy. In other words, as δ reduces to 0, the energy for a paramagnetic state is strongly renormalized by a factor $2\delta/(1+\delta)$ to avoid the doubly occupied states. That makes the FPFM state more stable at small δ.

In Fig. 2.9.(a), FPFM energy and PM energy vs n are shown for $t'/t=0.1$, 0 and -0.1. For all values of t'/t, the FPFM energy is stable at large n while the PM energy is stable at small n. The intermediate phase separated region is constructed by the Maxwell construction and is indicative of a fist order transition. At large n, as in the plaquette case, the energy curve for the paramagnet state depends weakly on t' while the FPFM energy is reduced with decreasing t'/t. This results is in qualitative agreement with the previous DMFT results. As t'/t decreases, the FPFM state becomes more stable and the critical density, n_c decreases. Just as in the DMFT, the large spectral weight of the non-interacting DOS at a low energy makes FPFM state energetically favorable at $t'/t=-0.1$. When t' is 0, the energy difference between FPFM and PM vanishes at n_c=2/3, in agreement with the previous slave boson calculations [27, 28].

We also calculate the inverse of uniform magnetic susceptibility (χ^{-1}) to study the instability of the PM state. The analytic expression is

$$\chi^{-1}|_{m=0}=\frac{1}{2\rho(\mu^*)}+\frac{2\mu^*}{1+\delta}+\frac{1}{N_s}\sum_{\mathbf{k}}\frac{4}{(1+\delta)^2}Z\epsilon(\mathbf{k})\Theta(\mu^*-Z\epsilon(\mathbf{k})) \tag{2.13}$$

where $\rho(\mu^*)$ is the renormalized DOS given by $1/Z\cdot\rho_0(\mu^*/Z)$.

The trends in χ^{-1} are consistent with the results shown in Fig. 2.9.(a). As t'/t decreases, spin susceptibility diverges at smaller density (see Fig. 2.9 (b)). However, the divergence of the spin susceptibility does not coincide with the thermodynamic phase transition identified by the total energy differences. The phase transition is thus always first order within the slave boson

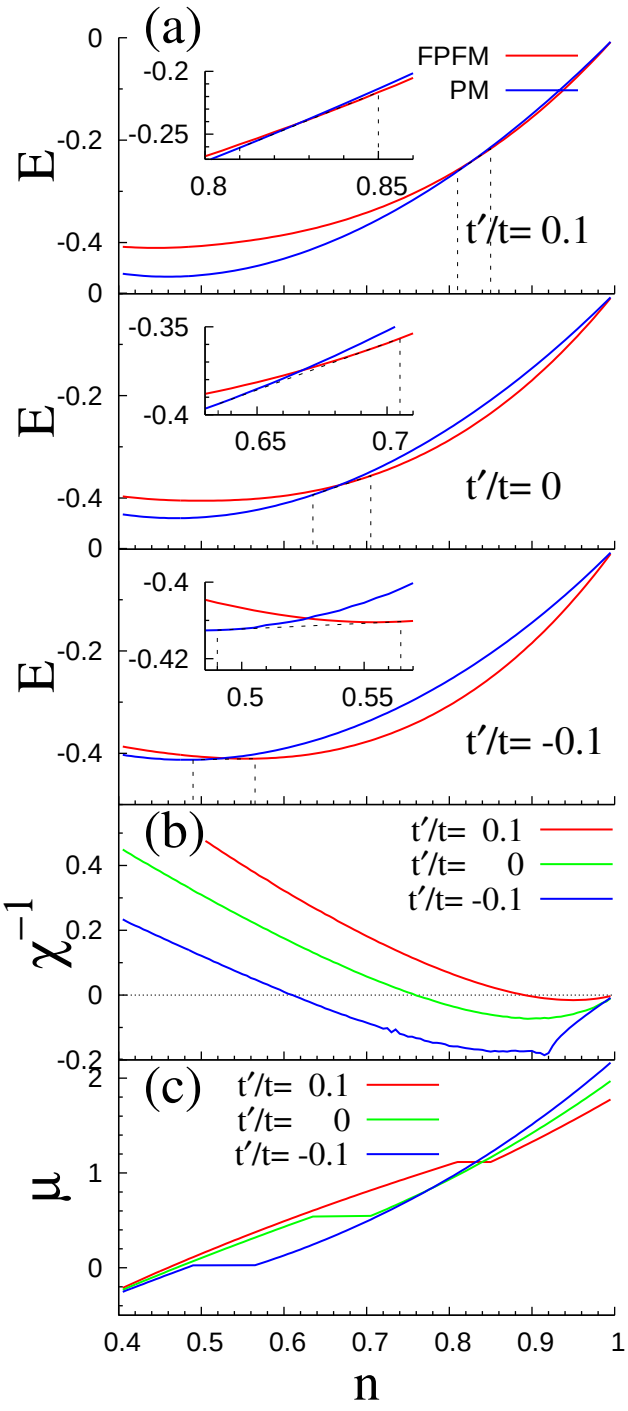

Figure 2.9: (a) Fully polarized ferromagnetic (FPFM) energy and paramagnetic (PM) energy vs n varying t'/t (0.1 (top), 0 (middle), and -0.1 (bottom)) Inset : Maxwell construction to determine the PS region. (b) The inverse of the uniform magnetic susceptibility (χ^{-1}) at m=0 vs n varying t'/t (0.1, 0, and -0.1). (c) The chemical potential (μ) vs n at t'/t = 0.1, 0, and -0.1.

		t'/t=-0.1	t'/t=0	t'/t=0.1
DMFT	n_c	0.705	0.815	N/A
($T = 0.01$)	order	First	Second	N/A
Slave boson	n_c	0.53	0.67	0.83
($T = 0$)	order	First	First	First

Table 2.1: n_c and the order of the ferromagnetism transition in a $U = \infty$ Hubbard model from both the DMFT+CTQMC approach and the slave boson approach with t'/t= -0.1, 0, and 0.1. N/A means no transition to FM state occurs.

approach.

Fig. 2.9 (c) shows that a flat chemical potential region exists at any t'/ts in a μ vs n graph. This is a generic feature of a first order transition and this region represents the coexistence of the FPFM and PM phase. This coexistence region is larger for negative t'/t favoring transition to the FPFM phase.

2.6 Comparison of the slave boson result and the DMFT+CTQMC result

The slave boson method overestimates the region of the stable FM state as compared to DMFT and it favors a first order transition (see Table 1). This is because the slave boson approach overestimates the paramagnetic kinetic energy as compared to the DMFT approach (Fig. 2.10). The quasiparticle residue Z of the DMFT approach is evaluated by $(1 - \frac{dIm\Sigma}{d\omega}|_{\omega=0})^{-1}$ on the imaginary frequency axis while Z of the slave boson approach is given by $2\delta/(1 + \delta)$. Fig. 2.11 shows that Z of the slave boson study is overestimated as compared to the DMFT+CTQMC case. The slave boson technique used in this chapter is based on the mean-field saddle-point approximation and it does not treat the strong correlation effect properly. Even though DMFT ignores the spatial correlation effect, the temporal correlations are treated exactly by CTQMC. Moreover, the mean-field slave boson approach evaluates the total energy as the sum of coherent quasiparticle energies (Eq. 2.12) while the total energy of DMFT+CTQMC includes contributions from both the incoherent and coherent effects. The over-estimated Z in the slave boson case underestimates the kinetic energy while the ignorance of contribution from the incoherent

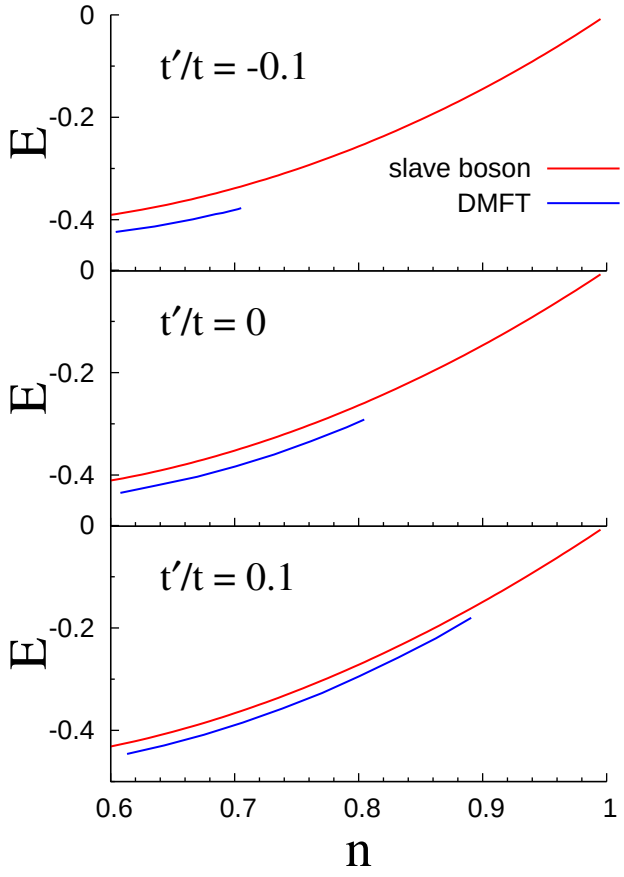

Figure 2.10: Paramagnetic energy from both the DMFT+CTQMC ($T = 0.01$) and the slave boson ($T = 0$) approach vs n at t'/t=-0.1 (the top panel), 0 (the middle panel), and 0.1 (the bottom panel).

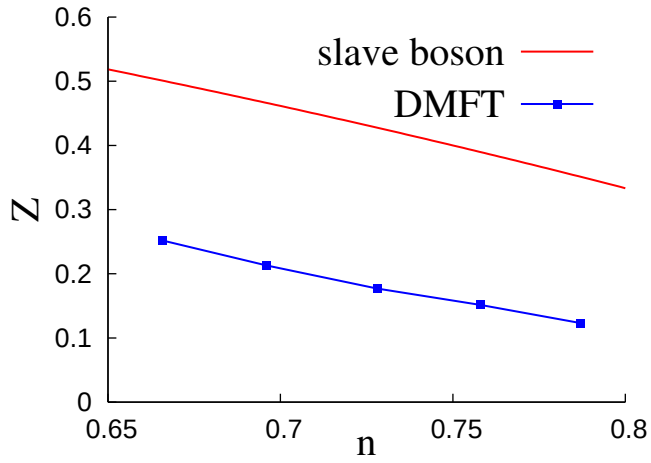

Figure 2.11: The renormalization residue (Z) of the slave boson method and the DMFT+CTQMC method ($t' = 0$).

part overestimates the energy. As a result, the two errors of the slave boson approach cancel each other giving a slightly overestimated energy as compared to the DMFT+CTQMC result.

Additionally, the χ^{-1} graph in the slave boson method almost coincides with the DMFT+CTQMC result comparing Fig. 2.4 and Fig. 2.9 (b). It is not certain how the renormalization residue Z affects χ^{-1} in the DMFT+CTQMC case, and the contribution from the incoherent part is also unclear. Therefore, further study will be required to fully understand the positive agreement of χ in the two methods.

2.7 Conclusion

To summarize, we investigated Nagaoka ferromagnetism in the $U = \infty$ Hubbard model including n.n hopping t and n.n.n hopping t'. This model was solved using DMFT with CTQMC, and the mean-field slave boson approach. Even a small value of t'/t yields a significant impact on the stability of Nagaoka ferromagnetism. The DMFT results show that the FM state is more stable for negative t'/t. This is supported by the slave boson method (see Table 1), and it can also be understood from diagonalization of the 4-site plaquette. The energy of the minimum spin state ($S = 1/2$) depends weakly on t'/t, while the energy of the maximum spin state ($S = 3/2$) depends linearly on t'/t. Therefore, the maximum spin state becomes more stable for negative t'/t.

In both the slave boson and DMFT methods, the paramagnetic energy does not vary much with t'/t due to the strong renormalization of the quasiparticle band (see Fig. 2.10). However, the fully polarized ferromagnetic energy depends on t'/t in a similar fashion as the non-interacting kinetic energy since the correlations are weaker in the broken symmetry state. The negative t'/t gives a high spectral peak in the occupied part of the spectra of the non-interacting system. As a result, the energy of the FM state is lower, and the ferromagnetism is stabilized in this case.

Within DMFT, the nature of the transition also varies with t'/t. A first order transition accompanied by the PS of the FM and PM state occurs at $t'/t = -0.1$ while a second order

transition occurs at $t'/t = 0$. In the slave boson approach, the transition is always first order regardless of t'/t. This is because the slave boson method overestimates the PM energy. The DMFT result shows that when $n \to 1$, the FM state becomes unstable as T exceeds T_{coh}. In other words, the ferromagnetic state is only stable within the coherent Fermi liquid regime.

The $U = \infty$ one band Hubbard model is a toy model and does not describe any specific material. However it is physically realizable in an optical lattice, due to the recent developments in controlling cold atoms in optical traps [45, 46]. These systems are highly tunable, and the hopping parameter t and the on-site interaction U can be adjusted by varying the ratio of the potential depth of the optical lattice to the recoil energy (V_0/E_R) or the ratio of interatomic scattering length to the lattice spacing (a_s/d). In order to realize the one-band Hubbard model with a large U ($U/t \geq 100$), $V_0/E_R \approx 30$ and $a_s/d \leq 0.01$ should be the range of parameters in the optical lattice (See Fig. 4 of Ref. 29). The tuning of the next-nearest neighbor hopping t' can be achieved by engineering optical lattices with a non-separable laser potential over each coordinate axis.

It will be very interesting to test these DMFT results experimentally. Usually, the atomic trap potential is applied to confine atoms in the optical lattice, and the potential varies smoothly having the minimum at the center of the trap. The phase separation between the FM and the PM phase at $t'/t = -0.1$ (taking place between the densities $n = 0.696 - 0.715$) can be observed in the optical lattice as three spatially separated distinct regions. The atom-rich FM region will tend to move to the center of the optical lattice to be energetically stabilized while the hole-rich PM region will reside on the edge of the optical lattice. Since the total spin is a conserved quantity, the FM region will be located at the center of the trap and will consist of two domains containing the up or down species. Raising the temperature will destroy the ferromagnetic magnetic state and, consequently, the spatial patterns within the trap.

Chapter 3

Cluster Dynamical Mean Field Theory of the Mott Transition

In this chapter, we address the nature of the Mott transition in the Hubbard model at half-filling using cluster Dynamical Mean Field Theory (DMFT) [47]. We compare cluster DMFT results with those of single site DMFT. We show that inclusion of the short range correlations on top of the on-site correlations, already treated exactly in single site DMFT, does not change the order of the transition between the paramagnetic metal and the paramagnetic Mott insulator, which remains first order. However, the short range correlations reduce substantially the critical U and modify the shape of the transition lines. Moreover, they lead to very different physical properties of the metallic and insulating phases near the transition, in particular in the region of the phase diagram where the two solutions coexist. Approaching the transition from the metallic side, we find an anomalous metallic state with very low coherence scale but relatively large quasiparticle renormalization amplitude at temperatures as low as $T = 0.01t$. The insulating state is characterized by the relatively narrow Mott gap with pronounced peaks at the gap edge. The transition from the insulating side is characterized by the continuous closure of the Mott Hubbard gap.

3.1 What is the Mott transition?

The correlation driven metal insulator transition is one of the most fundamental problems in condensed matter physics, and continues to receive intensive attention. It is realized in numerous transition metal oxides and some organic salts, by application of the pressure or isovalent chemical substitutions [48]. The metallic state far from the transition is well described

by the Fermi liquid theory, illustrating the wave-like properties of electrons in solids. In the insulating side, the electron behaves as a localized particle. Near the transition, the effective Coulomb repulsion between the carriers is of the same order as the kinetic energy term in the Hamiltonian. This regime probes the dual character of electron, namely the particle- and wave-like character, and requires a non-perturbative method for its description.

The nature of the metal to insulator transition depends strongly on the degree of magnetic frustration. In the limit of very large magnetic frustration, the insulating state is a simple paramagnetic state with local moments carrying log(2) entropy. The metallic state is a Fermi liquid with a very heavy mass. The mass increases as the transition is approached to match the large entropy of the frustrated paramagnetic insulator. This is the essence of the Brinkman-Rice theory of the metal insulator transition, which has been substantially extended by the single site DMFT of the Hubbard model in the paramagnetic phase [7]. The key predictions of this approach, such as the existence of a first order line ending in a second order Ising point, and numerous high temperature crossovers, have been verified experimentally [49]. The first order phase transition in a strongly frustrated situation has been confirmed by cluster DMFT studies [50, 51] and by other techniques [52].

The completely unfrustrated case is also well understood along the lines first drawn by Slater, and realized in the half filled one band Hubbard model with only nearest neighbor hoppings. Here, the metal insulator transition is driven by the long range magnetic ordering. The system is insulating and magnetic for arbitrarily small values of U, as a reflection of the perfect nesting of the band structure. The insulating gap results from the formation of a spin density wave that Bragg scatters the electronic quasiparticles.

The character of the metal insulator transition with an intermediate degree of frustration (when the long range magnetic order is fully suppressed, but with strong short range magnetic correlations) remains an open problem. Qualitative modifications of the character of the transition are expected, since at low temperatures the paramagnetic insulating state has very low entropy. This problem can be addressed by a sharp mathematical formulation studying the

paramagnetic solution of the cluster DMFT equations of the Hubbard model, keeping the short range correlations only. The early cluster DMFT studies received conflicting answers depending on different cluster schemes and different impurity solvers [53, 54]. However, by going to very low temperatures using new algorithmic developments, we completely settle this question.

3.2 The cluster DMFT Method

In order to study this problem of the Mott transtion, we apply cellular dynamical mean field theory (CDMFT) [55, 56] to the two-dimensional Hubbard model. The Hubbard model is an effective model which can treat the competition between the kinetic energy and the potential energy of electrons in the lattice. The kinetic energy term originates from the hopping (t) of fermions to adjacent sites and the potential energy term is the on-site Coulomb energy (U) of doubly occupied electrons. The metal to insulator transition is controlled by the ratio U/t. Here, we choose the two dimensional square lattice with only the nearest neighbor hopping t.

$$\hat{H} = -t \sum_{i,j,\sigma} f^{\dagger}_{i,\sigma} f_{j,\sigma} + U \cdot \sum_{i} f^{\dagger}_{i,\uparrow} f^{\dagger}_{i,\downarrow} f_{i,\downarrow} f_{i,\uparrow} \tag{3.1}$$

Cluster DMFT is an extended version of DMFT as it maps the lattice problem to an auxiliary cluster quantum impurity problem embedded in a self-consistent electronic bath. The short-range correlations ignored within DMFT can be captured within cluster DMFT inside the cluster size. CDMFT, one scheme of cluster DMFT, uses plaquette as a reference frame and the lattice problem is divided into 2×2 plaquettes for the problem treated here. Equivalently, the original unit cell of a single site increases to a 2×2 supercell. As a result, the original Brillouin zone is reduced by half and the quantities within the supercell depends on the cluster degrees of freedom.

The matrix of tight-binding hoppings $t_c(\tilde{k})$ is a 4×4 matrix defined on the cluster degrees of freedom. $\tilde{k}$ runs over the reduced Brillouin zone of the problem. $t_c(\tilde{k})$ can be given on the real space basis within the cluster. In the 2×2 cluster, the real space vector $\mathbf{R}$=(0,0), (1,0),

(0,1), and (1,1). $t_c(\tilde{k})$ for the square lattice in Eq. 3.1 is given as follows.

$$t_c(\tilde{k})_{\mathbf{R}_1,\mathbf{R}_2} = \begin{pmatrix} 0 & -t(1+e^{i\tilde{k}_x}) & -t(1+e^{i\tilde{k}_y}) & 0 \\ -t(1+e^{-i\tilde{k}_x}) & 0 & 0 & -t(1+e^{i\tilde{k}_y}) \\ -t(1+e^{-i\tilde{k}_y}) & 0 & 0 & -t(1+e^{i\tilde{k}_x}) \\ 0 & -t(1+e^{-i\tilde{k}_y}) & -t(1+e^{-i\tilde{k}_x}) & 0 \end{pmatrix} \quad (3.2)$$

This hopping matrix can be Fourier transformed to a cluster momenta (**K**) basis. The cluster momenta **K** are (0,0),(π,0),(0,π), and (π,π) within the 2×2 cluster. Within CDMFT, the translation symmetry is broken inside the cluster, hence the off-diagonal terms appears in the hopping matrix.

$$t_c(\tilde{k})_{\mathbf{K}_1,\mathbf{K}_2} = \frac{1}{N_c} \sum_{\mathbf{R}_1,\mathbf{R}_2} e^{i(\mathbf{K}_1\cdot\mathbf{R}_1 - \mathbf{K}_2\cdot\mathbf{R}_2)} \cdot t_c(\tilde{k})_{\mathbf{R}_1,\mathbf{R}_2} \quad (3.3)$$

$$t_c(\tilde{k})_{\mathbf{K}_1,\mathbf{K}_2} = \begin{pmatrix} \epsilon^0(\tilde{k}) & i\cdot\epsilon^2(\tilde{k}) & i\cdot\epsilon^3(\tilde{k}) & 0 \\ -i\cdot\epsilon^2(\tilde{k}) & \epsilon^1(\tilde{k}) & 0 & i\cdot\epsilon^3(\tilde{k}) \\ -i\cdot\epsilon^3(\tilde{k}) & 0 & -\epsilon^1(\tilde{k}) & i\cdot\epsilon^2(\tilde{k}) \\ 0 & -i\cdot\epsilon^3(\tilde{k}) & -i\cdot\epsilon^2(\tilde{k}) & -\epsilon^0(\tilde{k}) \end{pmatrix} \quad (3.4)$$

where $\epsilon^0(\tilde{k}) = -t(2+\cos(\tilde{k}_x)+\cos(\tilde{k}_y))$, $\epsilon^1(\tilde{k}) = t(\cos(\tilde{k}_x)-\cos(\tilde{k}_y))$, $\epsilon^2(\tilde{k}) = t\sin(\tilde{k}_x)$, and $\epsilon^3(\tilde{k}) = t\sin(\tilde{k}_y)$.

The cluster self energy Σ_c treats electron correlations within the cluster size exactly but inter-correlations between clusters are ignored within CDMFT. The 2×2 cluster is special since Σ_c is diagnoal on the cluster momenta basis as the inter-cluster self energies are ignored.

$$\Sigma_c = \begin{pmatrix} \Sigma_{00} & & & \\ & \Sigma_{\pi 0} & & \\ & & \Sigma_{0\pi} & \\ & & & \Sigma_{\pi\pi} \end{pmatrix} \quad (3.5)$$

The cluster Green's function G_c is also diagonal on the cluster momenta basis since the off-diagonal terms originating from the hopping matrix in Eq. 3.4 vanishes as G_c is averaged over

the $\tilde{k}$ points in the reduced Brillouin zone. Therefore, cluster momenta are the good quantum number in 2×2 CDMFT and the other cluster quantities can be also given on the cluster momenta basis.

Similar as DMFT, a self-consistent hybridization Δ_c is determined from the condition the cluster Green's function G_c is same as the impurity Green's function computed from an impurity solver with the impurity hybridization Δ_c. The cluster quantities, Δ_c, G_c, and Σ_c are represented by an 8×8 diagonal matrix in the cluster momenta space including the spin degrees of freedom. The hopping matrix $t_c(\tilde{k})$ is given in Eq. 3.4. Finally, the self-consistent condition for Δ_c is determined as the following equation.

$$\begin{aligned} \Delta_c(i\omega) &= i\omega + \mu - \Sigma_c(i\omega) - G_c^{-1} \\ &= i\omega + \mu - \Sigma_c(i\omega) - \left[\frac{1}{N_{\tilde{k}}} \sum_{\tilde{k}} \frac{1}{(i\omega + \mu) \cdot \mathbf{1} - t_c(\tilde{k}) - \Sigma_c(i\omega)} \right]^{-1} \end{aligned} \tag{3.6}$$

where $\mathbf{1}$ is an identity matrix and $\tilde{k}$ runs over the reduced Brillouin zone.

The cellular DMFT approach has already given numerous insights into frustrated models of kappa organics [57, 50] as well as the doping driven Mott transition in the Hubbard model, when treated with a variety of impurity solvers [58]. Here, we summarize briefly other recent studies of the metal insulator transition in the Hubbard model using cluster DMFT. In Ref. [53] a different type of cluster scheme, dynamical cluster approximation, was employed and the Hirsch-Fye quantum Monte Carlo method was used as the impurity solver. The lowest temperature reached was too high to see the metal insulator transition in small clusters. In this study, only the largest cluster of size 64 was able to identify a gap at the value of U comparable to our critical U. In Ref. [50], the first order metal-insulator transition was found for Kagome lattice at large frustration t'=0.8t. The shape of the phase diagram is consistent with our phase diagram in Fig. 3.1 but the temperature scale, at which the transition was identified, is factor of three larger than found in our study. This is likely due to different type of band dispersion employed in their work. This work also used the Hirsch-Fye quantum Monte Carlo method.

In our study, the auxiliary cluster problem is solved with the numerically exact continuous

time quantum Monte Carlo (CTQMC) method [17, 16]. CTQMC allows us to reach very low temperature compared to the previous studies and the character of the Mott transition within cluster DMFT is clearly revealed. The cluster DMFT results are explained in the following section.

3.3 Cluster DMFT results

3.3.1 The phase diagram

Fig.3.1a shows the phase diagram of the Hubbard model within cluster DMFT at half-filling in the absence of long range order. For interaction strength $U < U_{c2}(T)$, we find a metallic solution while for $U > U_{c1}(T)$, a Mott insulating solution exists. The two transition lines $U_{c1}(T)$ and $U_{c2}(T)$ cross at a second order endpoint, at temperature $T_{MIT} \sim 0.09t$ and interaction strength $U_{MIT} \sim 6.05t$. It is clear that one of the most salient features of the single site DMFT phase diagram (shown in Fig. 3.1b), namely the existence of a first order phase transition, survives in plaquette-DMFT.

Still there are substantial modifications to the single site DMFT results when U/t is close to its critical value. Namely,

1. Strong short ranged antiferromagnetic correlations significantly reduce the value of critical U at which the second order endpoint occurs. Note that the plaquette-DMFT critical $U(\sim 6.05t)$ is in very favorable agreement with the Monte-Carlo crossover U at which the pseudogap develops at intermediate temperatures accessible by determinantal Monte Carlo (figure 5 in Ref. [59]). This critical U will increase if the system is more frustrated at short distance. For example, the inclusion of the next nearest hopping t' has this effect and was studied in Ref. [60].

2. The shape of the coexistence region, where both metallic and insulating solutions exist, is significantly different. The high temperature crossover lines (dashed line above $T \sim 0.1t$ in Fig.3.1) are similar since at high temperature the entropy of the paramagnetic insulator

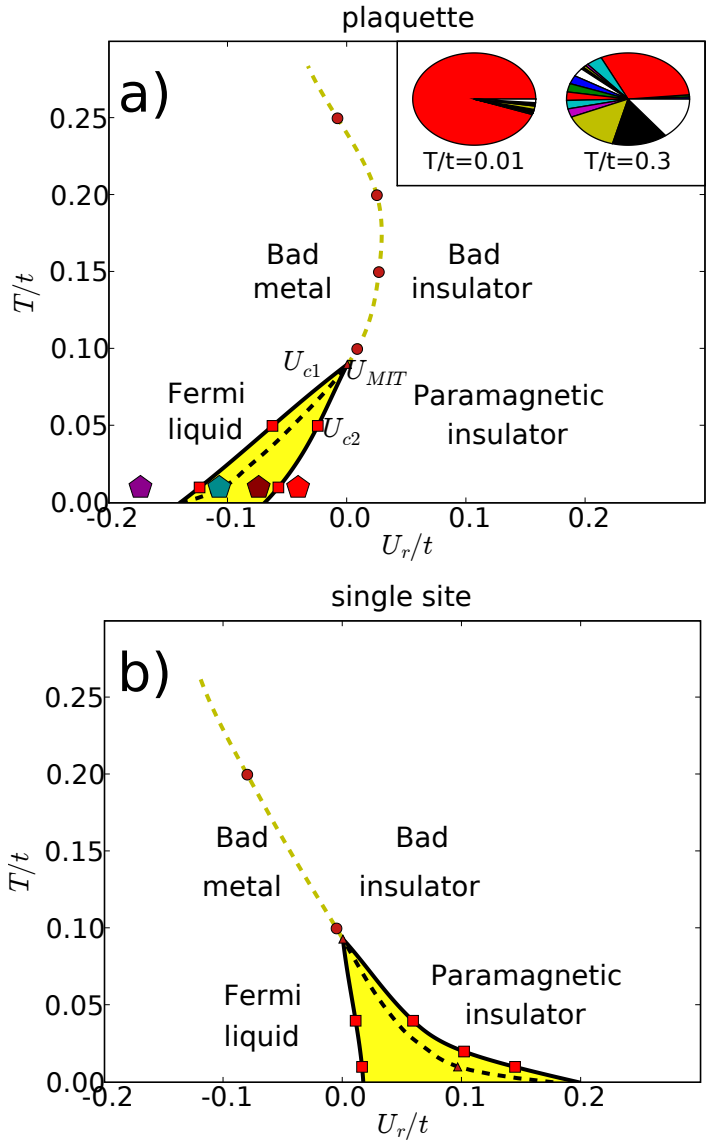

Figure 3.1: a) The phase diagram of the paramagnetic half-filled Hubbard model within plaquette-CDMFT. Inset: The histogram of the two insulating states. It shows the probability for a given cluster eigenstate among the 16 eigenstates of the half-filled plaquette. The singlet plaquette ground state has the highest probability. b) For comparison, the corresponding phase diagram of the single site DMFT (using the same 2D density of states) is shown. The coexistence region is shown as the shaded region. The dashed line marks the crossover above the critical point. The crossover line was determined by the condition that the imaginary part of the self-energy at few lowest Matsubara frequencies is flat at the crossover value of U. For easier comparison, the x-axis is rescaled and the reduced value of $U_r = \frac{U-U_{MIT}}{U_{MIT}}$ is used. The critical value of U is $U_{MIT} = 6.05t$ in cluster case and $U_{MIT} = 9.35t$ in single site case. Pentagons in panel a) mark the points in phase diagram for which we present the local spectral functions in Fig.3.2.

is of the order of log(2) in both cluster and single site approach. As the temperature is increased, the large entropy insulating state wins over the lower entropy metallic state. At low temperature, the situation is very different. In single site DMFT, the metal wins at low temperature in the transition region because the emergence of the itinerant quasiparticle inside the Mott gap lowers the free energy of the strongly disordered Mott state. In the cluster case, the Mott insulator at very low temperature is very different and has small entropy due to short range singlet formation. The small entropy of this state can be confirmed by the "valence histogram" shown in the inset of Fig.1a. The high temperature insulating state, which has entropy of the order of log(2), populates many states of the plaquette with significant probability. In contrast, there is only one significant eigenvalue of the density matrix in low temperature, corresponding to the singlet state. The insulating phase at low temperature has thus very small entropy, and the bad metal has larger entropy, hence decreasing temperature favors insulator over metal. The actual first order line (dashed line in Fig. 3.1a inside the coexistence region, where the free energy of the two phases equals) therefore bends back and critical U decreases with decreasing temperature. It is apparent that the zero temperature transition in cluster-DMFT happens at U_{c1} and not at U_{c2} as in DMFT.

While the shape of the DMFT phase diagram strongly resembles the phase diagram of the Cr-doped V_2O_3, the reentrant shape of the cluster-DMFT transition resembles more the $\kappa-$organic diagram [61] as pointed out in Ref. [50]. The well known reentrant behavior of these systems might be qualitatively understood within this approach. If the temperature is varied at fixed pressure (here fixed U/t) the system is Mott insulating at very low temperature, becomes metallic at intermediate temperature and insulating again at high temperature. In our model, the short range spin-fluctuations stabilize the Mott state at low T, while metallic phase intervenes at intermediate temperature where the local singlet formation is less efficient than quenching of local moment by Kondo effect. Finally at high temperature the large entropy local moment state wins and the system is again insulating.

3.3.2 The spectral function

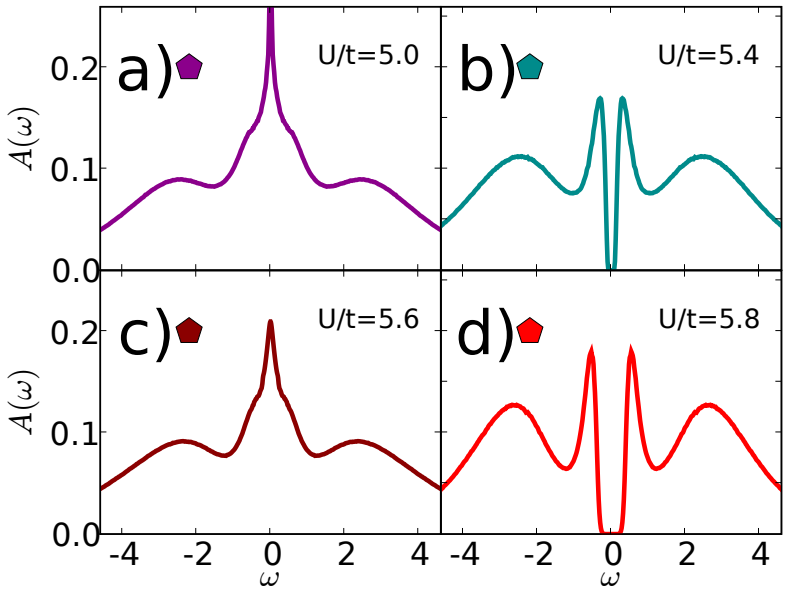

Figure 3.2: The local spectral function for four representative values of U/ts and temperature $T = 0.01t$ marked by pentagons in Fig.1. a) For U below U_{c1} the system is in Fermi liquid regime with rather large coherence temperature. b) In the coexistence region, the insulating solution has a small but finite gap ($\sim 0.2t$). c) The metallic solution in the same region is strongly incoherent and the value at zero frequency decreases due to the finite scattering rate (see self-energy in Fig. 3.3a). d) For U above U_{c2}, the Mott gap steadily increases with U. In addition to the Hubbard bands, quite pronounced peaks at the gap edge can be identified. Similar peaks can be seen also in single site DMFT, but they are substantially more pronounced here due to the small size of the gap within CDMFT.

To understand the effects brought about by the short range magnetic correlations near the transition, we focus on the local spectral functions displayed in Fig. 3.2. As in single site DMFT, below U_{c1} (Fig. 3.2a) the system is a normal Fermi liquid with a reduced width of the quasiparticle peak ($Z \sim 0.4$) and well developed Hubbard bands around $-2.5t$ and $2.5t$.

The insulator in the coexistence region (Fig. 3.2b) is however very different than Mott insulator in single site DMFT. The Mott gap is small and it vanishes at U_{c1} where the insulating solution ceases to exist. At low temperature very pronounced peaks at the gap edge appear. These peaks are a clear hallmark of the coherence peaks characteristic of a Slater spin density wave. This has been noticed earlier in numerous studies of the Hubbard model [62, 63, 54], as well as in the single site DMFT solution in the ordered phase of the unfrustrated lattice, which

captures the physics of perfect nesting.

With increasing U above U_{c2} (Fig. 3.2d) the Mott gap increases but the peaks at the gap edge remain very pronounced. Only at very large U comparable to the critical U of the single site DMFT they lose some of their strength and dissolve into a featureless Hubbard band.

The metallic state, which competes with the insulator in the coexistence region, (Fig. 3.2c) has similar width of the quasiparticle peak as the Fermi liquid state at $U < U_{c1}$. Hence the quasiparticle renormalization amplitude, as extracted at finite but low temperature $T = 0.01t$ is rather large. On the other hand, this metallic solution has somewhat reduced height of the quasiparticle peak which is mostly due to incoherent nature of the solution.

At the heart of the cluster DMFT physics is the competition between the formation of an itinerant band and short range spin fluctuations. The latter are absent in single site DMFT since only the local moment formation is accounted for by DMFT. The competition between spin fluctuations and Kondo screening leads to two important effects: i) the metallic state is a strongly incoherent metal, ii) the quasiparticle renormalization amplitude Z as will be shown in Fig. 3.4 is finite at the metal insulator transition and the Brinkman-Rice scenario of diverging effective mass is absent in this model.

3.3.3 The cluster self energy

The incoherence can also be identified from the raw data on the imaginary axis. In Fig. 3.3 we show the imaginary self-energy for the different cluster momenta K, which can be thought as the orbitals of the multi-orbital model associated with the cluster. In plaquette geometry, the self-energy is diagonal in cluster momentum base and the on-site, nearest-neighbor, and next-nearest-neighbor self-energies can be constructed as the linear combination of these orbital self-energies[58].

Below U_{c1}, the self-energies of all four orbitals are very similar and results are close to the single-site DMFT. The metallic phase in the coexistence region Fig. 3.3c has a large scattering rate in the $(\pi, 0)$ orbital, in the orbital which contributes most of the spectral weight at the

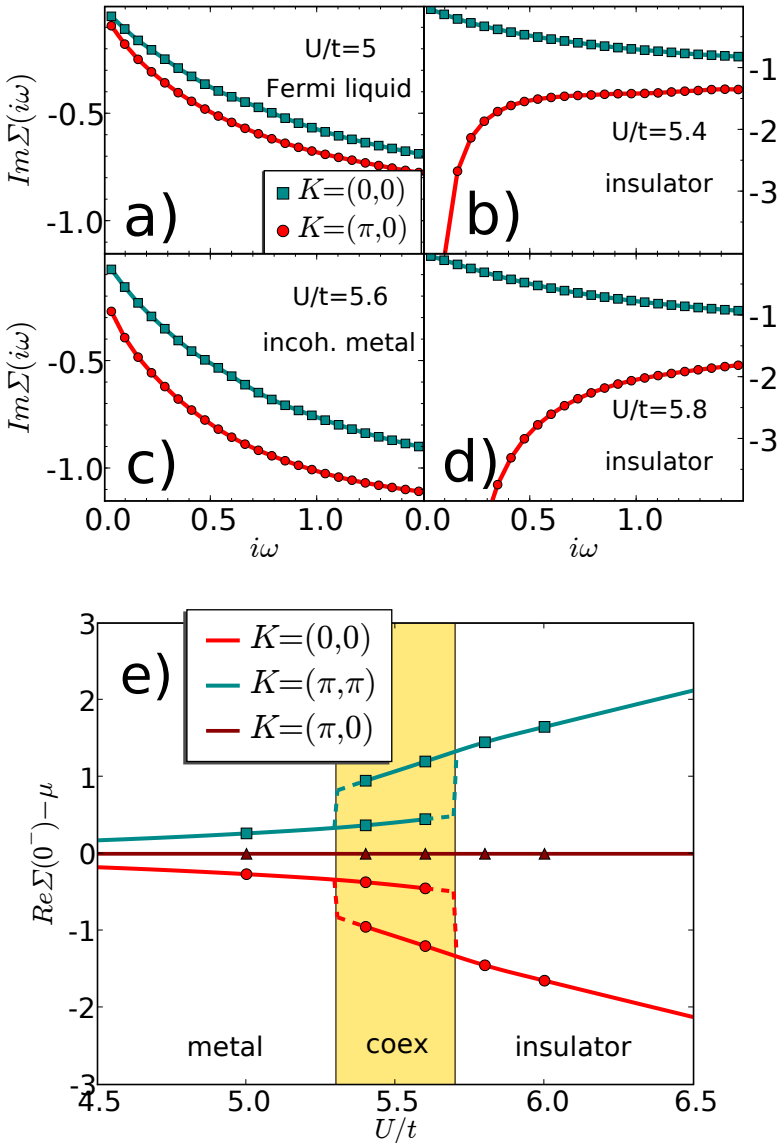

Figure 3.3: top: The imaginary part of the cluster self energies for the same parameters as in Fig.2. Due to particle-hole symmetry, the (π,π) and $(0,0)$ cluster self-energies have the same imaginary part and we show only one of them. Below the metal-insulator transition shown here in a), the momentum dependence of the self-energy is rather weak and the cluster solution is very similar to the single site DMFT solution. In the coexistence region, the metallic solution shown here in c) is strongly incoherent especially in the $(\pi,0)$ orbital. For the insulating solutions in b) and d), the $(\pi,0)$ scattering rate diverges which opens the gap in the spectra. bottom: e) $Re\Sigma_K(0^-)-\mu$ as a function of U. Due to particle-hole symmetry, $Re\Sigma_{K=(\pi,0)}-\mu$ vanishes.

fermi level. The coherence scale in this strongly incoherent metal is thus severely reduced. The scattering rate as a function of temperature is not quadratic even at $T = 0.01t$ and remains large $\sim 0.2t$ at that temperature.

In Fig. 3.3b,d the Mott insulating state can be identified by the diverging imaginary part of the $\Sigma_{(\pi,0)}(i\omega)$. Due to particle hole symmetry, the real part of the same quantity vanishes. Therefore, the only way to open a gap in the single particle spectrum is to develop a pole at zero frequency $\Sigma_{(\pi,0)} \simeq C/(i\omega)$. We checked that the insulating state in the coexistence region has the characteristic $1/(i\omega)$ behavior at very low temperature and the coefficient C in the coexistence region decreases as U decreases. The closure of the gap at the U_{c1} transition point is confirmed by the vanishing of C at that point.

The other two orbitals expel their Fermi surfaces by a different mechanism identified in Ref. [64], namely the real parts of the self-energy are such that the effective chemical potential $\mu_{eff} = \mu - \Sigma(0^-)$ moves out of the band. The separation of the two orbitals gradually increases as U increases, and it jumps at the critical U showing the hysteresis behavior displayed in Fig. 3.3e.

3.3.4 The quasi-particle resudue Z

The important issue in the metal insulator transition (MIT) is whether the short range magnetic exchange in the Hubbard type of models allow the Brinkman-Rice scenario of diverging effective mass. In Fig. 3.4 we plot the quasiparticle renormalization amplitude Z of the four different orbitals of the plaquette. As shown in Fig. 3.4, the growth of the effective mass in cluster DMFT is cut-off by the exchange interaction and the spatial coherence is lost way before the quasiparticles acquire a large effective mass. The lattice $Z_{\mathbf{k}}$ is a linear combination of the two values plotted in Fig. 3.4. The quasiparticles at $(\pi, 0)$ and $(0, \pi)$ are renormalized more strongly than those away from the two points. More importantly, close to U_{c1}, where the system is still coherent at $T = t/100$, the quasiparticle renormalization amplitude is rather large for the plaquette without frustration ($Z \sim 0.36$). Very near and inside the coexistence region, the

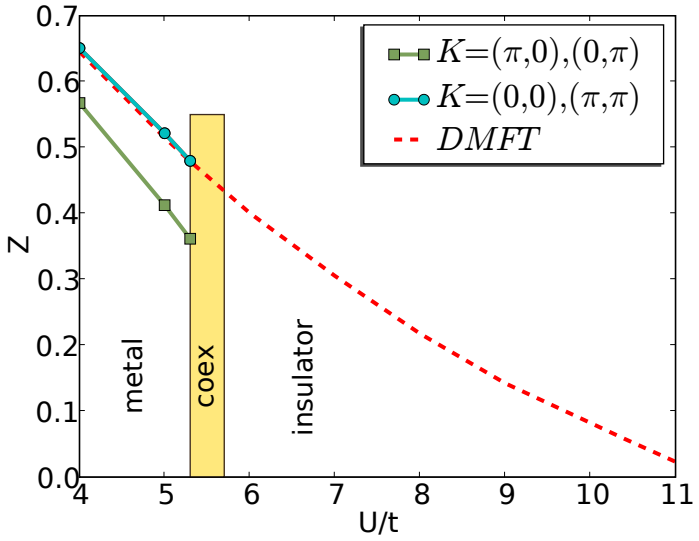

Figure 3.4: The quasi-particle residue Z vs U/t for different orbitals in CDMFT. Below the transition point, the $(0,0)$ and (π,π) orbitals have essentially the same Z as single site DMFT (dotted line) while the quasiparticles are more renormalized in $(\pi,0)$ orbital. At the transition, both Z's are rather large (0.36 and 0.48).

metallic state remains very incoherent at our lowest temperature $T = t/100$. We therefore can not determine the low energy Z which might vanish at U_{c2} at zero temperature.

3.4 Conclusion

In conclusion, we used essentially exact numerical method, CTQMC and clarified the nature of the Mott transition in cluster DMFT. The short range correlations, which are accounted for in this study but are absent in single site DMFT, do not change the order of the Mott transition, which remains first order with coexistence of metallic and insulating solutions.

Our cluster DMFT study predicts the existence of an anomalous metallic state within the coexistence region with very low coherence temperature. This regime could be relevant to the interpretation of experiments in VO_2 [65] and $PrNiO_3$ under the applied pressure [66] where an anomalous metallic state was reported. Recent optical measurements of VO_2 [65] show that in the narrow temperature range close to the transition, where the system percolates, the metallic puddles show an unconventional optical response. The resistivity measurement of $PrNiO_3$ under

the applied pressure [66] report the non-Fermi liquid metallic state near the Mott transition boundary.

On the theoretical side, the plaquette DMFT brings new light on the nature of the interaction driven MIT. The cluster DMFT of this problem retains aspects of Mott physics, as described in single site DMFT, and Slater physics. It does that by having two orbitals ($(\pi, 0)$ and $(0, \pi)$) exhibit a Mott transition while the remaining orbitals ($(0, 0)$ and (π, π)) undergo a band transition. This Slater-Mott transition requires momentum space differentiation and has no analog in single site DMFT.

Chapter 4

The Calculation of Two-particle Quantities within DFT+DMFT

In this chapter, we derive the equations for computing the magnetic/charge susceptibility and the superconducting pairing susceptibility using the two-particle vertex functions based on DMFT. First, we discuss the advantages of the vertex function approach for computing the two-particle response functions compared to the alternative cluster DMFT method. And the Monte Carlo sampling procedure of the two-particle Green's function χ by continuous time quantum Monte Carlo (CTQMC) is explained in the next section. Since χ sampled by CTQMC is reliable only at low frequency, we propose an extrapolation method based on singular value decomposition for the high frequency values of χ. Using this sampled χ, the magnetic/charge susceptibility can be computed using the Bethe-Salpeter equation in the particle-hole channel. Finally, we derive the equations for computing the pairing vertex based on DMFT vertex functions. The pairing vertex represents the pairing interaction between the electrons in a Copper pair. The critical temperature (T_c) and the gap symmetry of superconductivity can be determined by computing the leading eigenvalue and the corresponding eigenfunction of the pairing matrix in the particle-particle channel.

4.1 Motivation for the vertex function approach

Dynamical Mean Field Theory (DMFT) is a powerful theory for computing the electronic structure of strongly correlated solid state systems [7, 67]. It maps the problem of a solid to an auxiliary impurity problem where the local correlations are treated exactly while the non-local correlations are ignored. In this way, both the coherent quasi-particle bands and the incoherent

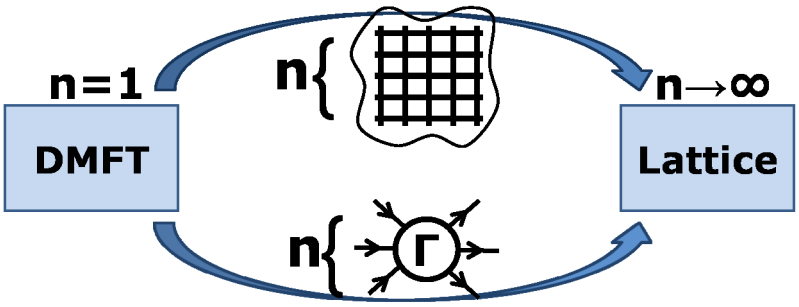

Figure 4.1: Two routes for treating the non-local correlations beyond DMFT.

atomic like excitations are captured by this method. In combination with Density Functional Theory (DFT), DMFT has been successful in describing the correlated electronic structure of many realistic materials including the multiple valences in plutonium [68], the coherence scale of $CeIrIn_5$ [69], the correlated band structure of the Fe based high T_c superconductors [70] and many others.

In some cases, non-local correlations are vital to describe the exotic phenomena qualitatively different from the local physics described within DMFT. To name just a few examples: i) the Mott transition accompanied by the antiferromagnetic correlations which result in a different topology of the phase diagram [47], ii) the d-wave superconductivity in models of cuprates arising from the spin fluctuations [71, 58], iii) the Mott transition at the optimal doping of the Hubbard model [72] accompanied by the signs of quantum criticality [73, 74]. This non-local correlations, not captured by DMFT, can be described by two types of the extensions of DMFT (see Fig. 4.1).

One popular route is to extend the spatial range in which the correlations are treated exactly. These cluster DMFT methods [55, 56] result in an auxiliary impurity problem spanning a cluster of sites. The bottleneck of this approach is that the solution of the resulting quantum impurity problem becomes computationally very expensive with increasing cluster sites. The number of atomic states grows exponentially as $4^{N_b * N_s}$ where N_b is the number of bands and N_s is the number of cluster sites. Therefore, the cluster DMFT approach is difficult to extend to

multi-orbital systems in realistic materials.

The second route of including non-local correlations is to use diagrammatic approaches employing the n-particle vertex functions. In the limit of the infinite dimension z, the self energy contains only local diagrams [7]. The next leading non-local diagram of the self energy scales as $1/\sqrt{z}$ and this type of diagram can be constructed through the use of the momentum dependent propagators while the irreducible two-particle vertex function is assumed to be purely local [75, 76]. Generally, the irreducible n-particle vertex function needs to be assumed to be local for the higher order non-local contribution to the self energy.

DMFT can be thought as the lowest order version of the vertex function approach, since the self energy, i.e., the one-particle irreducible vertex function is assumed to be local. As n increases, more diagrams are treated with the non-local propagators and the exact solution is recovered when n goes to infinity. In this approach, the vertex functions of lower order than n include the non-local correlations along with long-range correlations. In contrast, within cluster DMFT the long range correlations beyond the cluster size are ignored. Moreover, the vertex function calculation is rather inexpensive compared to the cluster DMFT method since it requires a solution of only the single-site quantum impurity problem, but it does require the computation of higher order correlation functions of the quantum impurity problem. This approach is a promising route to treat the non-local correlation in realistic strongly correlated materials. It has been recently used to compute the magnetic susceptibility of the Fe based superconductor within the DFT+DMFT approach [77].

In this chapter, we derive formulas for the vertex function approach to compute the two-particle response functions such as the magnetic susceptibility and the superconducting pairing susceptibility. This approach is derived here for the multi-orbital case and was implemented within the DFT+DMFT method as a part of this thesis.

4.2 Sampling of the two-particle Green's function

In Section 1.4, we showed that the one-particle Green's function is constructed by removing one row and one column in the hybridization matrix Δ_k. In similar way, the two-particle Green's function can be sampled by removing two rows and two columns in the hybridization matrix Δ_k. The average of the four time-ordered fermionic operators can be obtained by taking the derivative of $\ln Z$ with respect to the elements of Δ twice, similar as in Eq. 1.57, i.e.,

$$\begin{aligned} \overline{\chi}^{\,sq}_{\,pr}(\tau_p,\tau_q,\tau'_r,\tau'_s) &= \langle T_\tau \psi^\dagger_{\alpha_p}(\tau_p)\psi^\dagger_{\alpha_q}(\tau_q)\psi_{\alpha'_r}(\tau'_r)\psi_{\alpha'_s}(\tau'_s)\rangle \\ &= \frac{\partial^2 \ln Z}{\partial\Delta_{\alpha_p\alpha'_s}(\tau_p,\tau'_s)\partial\Delta_{\alpha_q\alpha'_r}(\tau_q,\tau'_r)} \end{aligned} \tag{4.1}$$

If we take the same derivative of the Taylor expansion form in Eq. 1.50, we get

$$\begin{aligned} \overline{\chi}^{\,sq}_{\,pr}(\tau_p,\tau_q,\tau'_r,\tau'_s) &= \frac{\partial}{\partial\Delta_{\alpha_p\alpha'_s}(\tau_p,\tau'_s)}\left(\frac{\partial \ln Z}{\partial\Delta_{\alpha_q\alpha'_r}(\tau_q,\tau'_r)}\right) \\ &= \frac{1}{Z}\int D[\psi^\dagger\psi]e^{-S_c}\cdot\sum_k \frac{1}{k!}\int_0^\beta d\tau_1\int_0^\beta d\tau'_1\cdots\int_0^\beta d\tau_k\int_0^\beta d\tau'_k \\ &\quad \sum_{\alpha_1\alpha'_1,\cdots,\alpha_k,\alpha'_k} \psi_{\alpha'_1}(\tau'_1)\psi^\dagger_{\alpha_1}(\tau_1)\cdots\psi_{\alpha'_k}(\tau'_k)\psi^\dagger_{\alpha_k}(\tau_k) \\ &\quad \times\frac{1}{k!}\frac{\partial}{\partial\Delta_{\alpha_p\alpha'_s}(\tau_p,\tau'_s)}\left(\frac{\partial Det(\bar{\Delta}_k)}{\partial\Delta_{\alpha_q\alpha'_r}(\tau_q,\tau'_r)}\right) \end{aligned} \tag{4.2}$$

The derivative of the determinant of the matrix $\bar{\Delta}_k$ with respect to two independent matrix elements is equivalent to removing two rows and two columns containing the two elements. We denote the resulting $(k-2)\times(k-2)$ matrix by $(\bar{\Delta}_k)''_{pqrs}$,

$$\frac{\partial}{\partial\Delta_{\alpha_p\alpha'_s}(\tau_p,\tau'_s)}\left(\frac{\partial Det(\bar{\Delta}_k)}{\partial\Delta_{\alpha_q\alpha'_r}(\tau_q,\tau'_r)}\right) = (-1)^{p+q+r+s}\cdot Det((\bar{\Delta}_k)''_{pqrs}) \tag{4.3}$$

and it takes the form

$$(\bar{\Delta}_k)''_{pqrs} \equiv \begin{pmatrix} \Delta_{\alpha_1\alpha'_1} & \cdots & \Delta_{\alpha_1\alpha'_{s-1}} & \cdots & \Delta_{\alpha_1\alpha'_{r-1}} & \cdots & \Delta_{\alpha_1\alpha'_k} \\ \cdots & \cdots & \cdots & \cdots & \cdots & \cdots & \cdots \\ \Delta_{\alpha_{p-1}\alpha'_1} & \cdots & \Delta_{\alpha_{p-1}\alpha'_{s-1}} & \cdots & \Delta_{\alpha_{p-1}\alpha'_{r-1}} & \cdots & \Delta_{\alpha_{p-1}\alpha'_k} \\ \cdots & \cdots & \cdots & \cdots & \cdots & \cdots & \cdots \\ \Delta_{\alpha_{q-1}\alpha'_1} & \cdots & \Delta_{\alpha_{q-1}\alpha'_{s-1}} & \cdots & \Delta_{\alpha_{q-1}\alpha'_{r-1}} & \cdots & \Delta_{\alpha_{q-1}\alpha'_k} \\ \cdots & \cdots & \cdots & \cdots & \cdots & \cdots & \cdots \\ \Delta_{\alpha_k\alpha'_1} & \cdots & \Delta_{\alpha_k\alpha'_{s-1}} & \cdots & \Delta_{\alpha_k\alpha'_{r-1}} & \cdots & \Delta_{\alpha_k\alpha'_k} \end{pmatrix} \tag{4.4}$$

Therefore, the Monte Carlo sampling of $\overline{\chi}^{\,sq}_{\,pr}$ is equivalent to the Monte Carlo average of the ratio between $Det((\bar{\Delta}_k)''_{pqrs})$ and $Det(\bar{\Delta}_k)$ with extra sign.

$$\overline{\chi}^{\,sq}_{\,pr}(\tau_p, \tau_q, \tau'_r, \tau'_s) = \left\langle (-1)^{p+q+r+s} \frac{Det((\bar{\Delta}_k)''_{pqrs})}{Det(\bar{\Delta}_k)} \right\rangle_{MC} \tag{4.5}$$

The ratio between $Det((\bar{\Delta}_k)''_{pqrs})$ and $Det(\bar{\Delta}_k)$ can be computed using the LU decomposition of the block matrix similar to Eq. 1.66. For the calculation of LU decomposition, we shifts the p-th and q-th rows and the s-th and r-th columns of matrix $\bar{\Delta}_k$ to the bottom rows and the rightmost columns. We denote the resulting matrix by $\widetilde{\Delta}_k$, i.e.,

$$Det(\bar{\Delta}_k) \quad = (-1)^{p+q+r+s} \quad \cdot Det(\widetilde{\Delta}_k) \tag{4.6}$$

The matrix $\widetilde{\Delta}_k$ takes the explicit form

$$\widetilde{\Delta} \equiv \left(\begin{array}{ccccccc|c|c} \Delta_{\alpha_1\alpha'_1} & \cdots & \Delta_{\alpha_1\alpha'_{s-1}} & \cdots & \Delta_{\alpha_1\alpha'_{r-1}} & \cdots & \Delta_{\alpha_1\alpha'_k} & \Delta_{\alpha_1\alpha'_s} & \Delta_{\alpha_1\alpha'_r} \\ \cdots & \cdots & \cdots & \cdots & \cdots & \cdots & \cdots & \cdots & \cdots \\ \Delta_{\alpha_{p-1}\alpha'_1} & \cdots & \Delta_{\alpha_{p-1}\alpha'_{s-1}} & \cdots & \Delta_{\alpha_{p-1}\alpha'_{r-1}} & \cdots & \Delta_{\alpha_{p-1}\alpha'_k} & \Delta_{\alpha_{p-1}\alpha'_s} & \Delta_{\alpha_{p-1}\alpha'_r} \\ \cdots & \cdots & \cdots & \cdots & \cdots & \cdots & \cdots & \cdots & \cdots \\ \Delta_{\alpha_{q-1}\alpha'_1} & \cdots & \Delta_{\alpha_{q-1}\alpha'_{s-1}} & \cdots & \Delta_{\alpha_{q-1}\alpha'_{r-1}} & \cdots & \Delta_{\alpha_{q-1}\alpha'_k} & \Delta_{\alpha_{q-1}\alpha'_s} & \Delta_{\alpha_{q-1}\alpha'_r} \\ \cdots & \cdots & \cdots & \cdots & \cdots & \cdots & \cdots & \cdots & \cdots \\ \Delta_{\alpha_k\alpha'_1} & \cdots & \Delta_{\alpha_k\alpha'_{s-1}} & \cdots & \Delta_{\alpha_k\alpha'_{r-1}} & \cdots & \Delta_{\alpha_k\alpha'_k} & \Delta_{\alpha_k\alpha'_s} & \Delta_{\alpha_k\alpha'_r} \\ \hline \Delta_{\alpha_p\alpha'_1} & \cdots & \Delta_{\alpha_p\alpha'_{s-1}} & \cdots & \Delta_{\alpha_p\alpha'_{r-1}} & \cdots & \Delta_{\alpha_p\alpha'_k} & \Delta_{\alpha_p\alpha'_s} & \Delta_{\alpha_p\alpha'_r} \\ \hline \Delta_{\alpha_q\alpha'_1} & \cdots & \Delta_{\alpha_q\alpha'_{s-1}} & \cdots & \Delta_{\alpha_q\alpha'_{r-1}} & \cdots & \Delta_{\alpha_q\alpha'_k} & \Delta_{\alpha_q\alpha'_s} & \Delta_{\alpha_q\alpha'_r} \end{array}\right)$$

$$= \left(\begin{array}{c|c|c} \bar{A} & B & C \\ \hline D & f & g \\ \hline E & h & l \end{array}\right) \tag{4.7}$$

Here $\bar{A}$ is a $(k-2)\times(k-2)$ matrix, previously denoted by $(\bar{\Delta}_k)''_{pqrs}$. B and C are $(k-2)\times 1$ matrices, D and E are $1\times(k-2)$ matrices, and f, g, h, l are the matrix elements of Δ. The determinant of this block matrix is computed by the LU decomposition in similar way as in Eq. 1.65

$$\left(\begin{array}{c|c|c} \bar{A} & B & C \\ \hline D & f & g \\ \hline E & h & l \end{array}\right) = \left(\begin{array}{c|c|c} I & 0 & 0 \\ \hline D & 1 & 0 \\ \hline E & (\frac{h-E\bar{A}^{-1}B}{f-D\bar{A}^{-1}B}) & 1 \end{array}\right) \cdot$$

$$\left(\begin{array}{c|c|c} \bar{A} & B & C \\ \hline 0 & f-D\bar{A}^{-1}B & g-D\bar{A}^{-1}C \\ \hline 0 & 0 & l-E\bar{A}^{-1}C-(\frac{h-E\bar{A}^{-1}B}{f-D\bar{A}^{-1}B})\cdot(g-D\bar{A}^{-1}C) \end{array}\right) \tag{4.8}$$

$$
\begin{aligned}
Det\left(\begin{array}{c|c|c} \bar{A} & B & C \\ \hline D & f & g \\ \hline E & h & l \end{array}\right) &= Det(\bar{A})\cdot[(f-D\bar{A}^{-1}B)\cdot(l-E\bar{A}^{-1}C)-(h-E\bar{A}^{-1}B)\cdot(g-D\bar{A}^{-1}C)] \\
&= \frac{1}{Det(\bar{A})}\cdot\Big[Det\left(\begin{array}{c|c} \bar{A} & B \\ \hline D & f \end{array}\right)\cdot Det\left(\begin{array}{c|c} \bar{A} & C \\ \hline E & l \end{array}\right) \\
&\quad -Det\left(\begin{array}{c|c} \bar{A} & B \\ \hline E & h \end{array}\right)\cdot Det\left(\begin{array}{c|c} \bar{A} & C \\ \hline D & g \end{array}\right)\Big] \qquad (4.9)
\end{aligned}
$$

As a result, the ratio between $Det((\bar{\Delta}_k)''_{pqrs})$ and $Det(\bar{\Delta}_k)$ can be expressed by the elements of the matrix $(\bar{\Delta}_k)^{-1}$

$$
\begin{aligned}
(-1)^{p+q+r+s}\frac{Det((\bar{\Delta}_k)''_{pqrs})}{Det(\bar{\Delta}_k)} &= \frac{Det(\bar{A})}{Det(\widetilde{\Delta}_k)} \\
= \frac{Det\left(\begin{array}{c|c} \bar{A} & B \\ \hline D & f \end{array}\right)}{Det(\widetilde{\Delta}_k)}\cdot\frac{Det\left(\begin{array}{c|c} \bar{A} & C \\ \hline E & l \end{array}\right)}{Det(\widetilde{\Delta}_k)} &- \frac{Det\left(\begin{array}{c|c} \bar{A} & B \\ \hline E & h \end{array}\right)}{Det(\widetilde{\Delta}_k)}\cdot\frac{Det\left(\begin{array}{c|c} \bar{A} & C \\ \hline D & g \end{array}\right)}{Det(\widetilde{\Delta}_k)} \\
&= (\widetilde{\Delta}_k)^{-1}_{k,k}\cdot(\widetilde{\Delta}_k)^{-1}_{k-1,k-1}-(\widetilde{\Delta}_k)^{-1}_{k,k-1}\cdot(\widetilde{\Delta}_k)^{-1}_{k-1,k} \\
&= (\bar{\Delta}_k)^{-1}_{qr}\cdot(\bar{\Delta}_k)^{-1}_{ps}-(\bar{\Delta}_k)^{-1}_{qs}\cdot(\bar{\Delta}_k)^{-1}_{pr} \qquad (4.10)
\end{aligned}
$$

Finally, the connected part of the two-particle Green's function is given by subtracting the disconnected diagrams from $\overline{\chi}$ in Eq. 4.1

$$
\begin{aligned}
\chi^{\,sq}_{\,pr}(\tau_p,\tau_q,\tau'_r,\tau'_s) &= \left\langle T_\tau\psi^\dagger_{\alpha_p}(\tau_p)\psi^\dagger_{\alpha_q}(\tau_q)\psi_{\alpha'_r}(\tau'_r)\psi_{\alpha'_s}(\tau'_s)\right\rangle \\
&\quad -\left\langle T_\tau\psi^\dagger_{\alpha_p}(\tau_p)\psi_{\alpha'_s}(\tau'_s)\right\rangle\cdot\left\langle T_\tau\psi^\dagger_{\alpha_q}(\tau_q)\psi_{\alpha'_r}(\tau'_r)\right\rangle \\
&\quad +\left\langle T_\tau\psi^\dagger_{\alpha_p}(\tau_p)\psi_{\alpha'_r}(\tau'_r)\right\rangle\cdot\left\langle T_\tau\psi^\dagger_{\alpha_q}(\tau_q)\psi_{\alpha'_s}(\tau'_s)\right\rangle \\
&= \left(\langle M_{ps}\cdot M_{qr}\rangle_{MC}-\langle M_{ps}\rangle_{MC}\cdot\langle M_{qr}\rangle_{MC}\right) \\
&\quad -\left(\langle M_{pr}\cdot M_{qs}\rangle_{MC}-\langle M_{pr}\rangle_{MC}\cdot\langle M_{qs}\rangle_{MC}\right) \qquad (4.11)
\end{aligned}
$$

Just as the one-particle Green's function, the two-particle Green's function can also be sampled directly in the Matsubara frequency space. First, we define the Fourier transform of

the matrix $M_{ij}(\tau_i, \tau_j)$

$$M_{ij}(i\nu_1, i\nu_2) = \frac{1}{\beta}\sum_{\tau_i,\tau_j'} e^{i(\nu_1\tau_i - \nu_2\tau_j')} M_{ij}(\tau_i, \tau_j') \tag{4.12}$$

Due to the time translation invariance, the two-particle Green's function depends on the three Matsubara frequencies ($i\nu$,$i\nu'$, and $i\omega$)

$$\begin{aligned}
\chi_{\substack{sq\\pr}}(i\nu, i\nu')_{i\omega} &= \frac{1}{\beta^2}\int_0^\beta d\tau_p \int_0^\beta d\tau_q \int_0^\beta d\tau_r' \int_0^\beta d\tau_s' e^{i(\nu\tau_p + (\nu'+\omega)\tau_q - \nu'\tau_r' - (\nu+\omega)\tau_s')} \chi_{\substack{sq\\pr}}(\tau_p, \tau_q, \tau_r', \tau_s') \\
&= [\langle M_{ps}(i\nu, i\nu+i\omega)\cdot M_{qr}(i\nu'+i\omega, i\nu')\rangle_{MC} \\
&\quad - \langle M_{ps}(i\nu, i\nu+i\omega)\rangle_{MC}\cdot\langle M_{qr}(i\nu'+i\omega, i\nu')\rangle_{MC}] \\
&\quad -[\langle M_{pr}(i\nu, i\nu')\cdot M_{qs}(i\nu'+i\omega, i\nu+i\omega)\rangle_{MC} \\
&\quad - \langle M_{pr}(i\nu, i\nu')\rangle_{MC}\cdot\langle M_{qs}(i\nu'+i\omega, i\nu+i\omega)\rangle_{MC}]
\end{aligned} \tag{4.13}$$

This is the full and connected two-particle Green's function of the impurity problem, which sampled by the Monte Carlo method. It is the central quantity of the vertex function approach, from which the local two-particle irreducible vertex is obtained. In later sections, we will discuss how to compute the magnetic/charge susceptibility and the superconducting pairing susceptibility using this sampled vertex function.

4.3 The high frequency asymptotics of the two-particle Green's function

The two-particle Green's function $\chi_{\substack{\alpha\delta\\\beta\gamma}}(i\nu, i\nu')_{i\omega}$ sampled by CTQMC is stored as a $N \times N$ complex matrix where N is $n_\nu \times n_b^2 \times n_s^2$ and n_ν is the number of Matsubara frequencies, n_b is the number of orbitals, and n_s is 2. Here, the range of $i\nu$ and $i\nu'$ is restricted to the low energy region since χ falls off with the frequency as $\frac{1}{\nu^2}$ and the sampled Monte Carlo data contain a lot of noise at high frequencies. The one-particle Green's function or the self energy also has noise at the high frequencies, but it is replaced by the analytic formula given as a function of lattice parameters such as the bare interaction U and the electron density n.

For the two-particle quantities, the approximate formula for the high frequency asymptotics

of the irreducible vertex function Γ^{irr} was derived in Ref. [78]. The Monte Carlo method can sample χ without severe noise only at the restricted low frequency region while this analytic expression for Γ^{irr} is valid only in the high frequency region. The Bethe-Salpeter equation (refer to Eq. 4.27) which relates Γ^{irr} and χ is a matrix equation in the frequency space, therefore, low frequency values and high frequency values are mixed and it is not sufficient to have one quantity only at high frequency and different quantity at low frequency. Ref. [78] uses the blocked Bethe-Salpeter equation to resolve this problem.

Here, we propose a high frequency extrapolation method for χ employing the singular value decomposition (SVD) for the $\chi_{\substack{\alpha\delta \\ \beta\gamma}}(i\nu, i\nu')_{i\omega}$ matrix. For each spin and orbital component $\alpha, \beta, \gamma, \delta$ and at fixed center of mass frequency $i\omega$, we decompose $\chi(i\nu, i\nu')$ matrix by SVD method

$$\chi(i\nu, i\nu') = \sum_k \phi_k^L(i\nu) \cdot \lambda_k \cdot \phi_k^R(i\nu') \tag{4.14}$$

where λ_k is the k-th singular value and $\phi_k^{L/R}$ is the corresponding left/right singular vector. The range of $i\nu$ and $i\nu'$ is limited to within the sampled range, i.e., $-\nu_c \leq \nu \leq \nu_c$ and $-\nu_c \leq \nu' \leq \nu_c$.

Generally, the high frequency asymptotics of χ is not analytically known function since the Bethe-Salpeter equation mixes up the low frequency part and the high frequency part. The advantage of the SVD form is that the mixture of the low frequency and the high frequency is effectively decoupled and it is sufficient to extrapolate the high frequency part of the singular vectors. One should note that at the high frequency region where only one frequency $i\nu$ goes to infinity, the low frequency values of $\phi_k(i\nu')$ also contribute to the asymptotics. Our simulation shows that the high frequency behavior of the singular vector $\phi_k^{L/R}$ in Eq. 4.14 can be extrapolated using the sampled values of $\phi_k^{L/R}$. In the limit of $i\nu \to \infty$ with the fixed $i\nu'$ and $i\omega$, the high frequency behavior of χ is proportional to the polarization function χ^0 since the full vertex $\Gamma(i\nu \to \infty, i\nu')_{i\omega}$ is asymptotically approaching a constant at high frequency.

The two-particle Green's function χ consists of the full vertex function and the four external

legs

$$\chi(i\nu, i\nu') \quad = \quad g(i\nu) \cdot g(i\nu + i\omega) \cdot \Gamma(i\nu, i\nu') \cdot g(i\nu' + i\omega) \cdot g(i\nu') \tag{4.15}$$

The local Green's function g is diagonal in the spin and the orbital space at high frequencies and Γ is the full vertex function. As a result, the asymptotic behavior of χ at $i\nu \to \infty$ and the finite $i\nu'$ is given by

$$\chi(i\nu \to \infty, i\nu') \quad \propto \quad g(i\nu) \cdot g(i\nu + i\omega) \tag{4.16}$$

Similar relation is also valid for $\chi(i\nu, i\nu' \to \infty)$. Using this asymptotic behavior, the singular vectors of Eq. 4.14 at high frequency region are given by

$$\phi_k^{L(R)}(i\nu \to \infty) \quad \cong \quad c_k^{L(R)} \cdot g(i\nu) \cdot g(i\nu + i\omega) \tag{4.17}$$

Singular vectors contain substantial amount of noise at high frequency, hence we need to carefully extract the coefficients $c_k^{L(R)}$ from the numerically sampled data. We use the following approximation

$$c_k^{L(R)} \quad = \quad \frac{1}{N_\nu} \sum_{i\nu = i\nu_s}^{i\nu_c} \left(\frac{\phi_k^{L(R)}(i\nu)}{g(i\nu) \cdot g(i\nu + i\omega)} \right) \tag{4.18}$$

where $i\nu$ runs over last few Matsubara points Here, $i\nu$ values range from $i\nu_s$ to $i\nu_c$ and N_ν is the number of Matsubara points for the average. The resulting singular vector, valid at both high and low frequency is thus obtained by

$$\tilde{\phi}_k^{L(R)}(i\nu) = \begin{cases} \phi_k^{L(R)}(i\nu) & \text{if} \quad |\nu| \leq |\nu_c| \\ c_k^{L(R)} \cdot g_{\alpha(\delta)}(i\nu) \cdot g_{\beta(\gamma)}(i\nu + i\omega) & \text{if} \quad |\nu| \geq |\nu_c| \end{cases} \tag{4.19}$$

Finally, the high frequency approximation for the two-particle Green's function $\tilde{\chi}$ is constructed by

$$\tilde{\chi}(i\nu, i\nu')_{i\omega} \quad = \quad \sum_{k<k_c} \tilde{\phi}_k^L(i\nu) \cdot \lambda_k \cdot \tilde{\phi}_k^R(i\nu') \tag{4.20}$$

where k runs over a few largest singular values. Singular vectors that correspond to small singular values contain increasingly severe noise. As we will show below, the irreducible vertex

is computed by inverting χ, therefore, the noise from small singular values can severely impact the quality of the irreducible vertex. Therefore, we keep only the large singular values ($k < k_c$) for constructing the high frequency tails of χ. For the low frequency values, the χ already sampled from CTQMC is still used.

$$\chi(i\nu, i\nu') = \begin{cases} \chi(i\nu, i\nu') & \text{if } |\nu| \wedge |\nu'| \leq \nu_c \\ \tilde{\chi}(i\nu, i\nu') & \text{if } |\nu| \vee |\nu'| \geq \nu_c \end{cases} \tag{4.21}$$

We believe that our method to determine the asymptotic behavior of χ is very efficient provided that the reliable data for χ at reasonable range of frequencies $i\nu$ and $i\nu'$ is available. More importantly, our method is also applicable to the general multi-orbital situation.

4.4 Calculation of the magnetic and the charge susceptibility

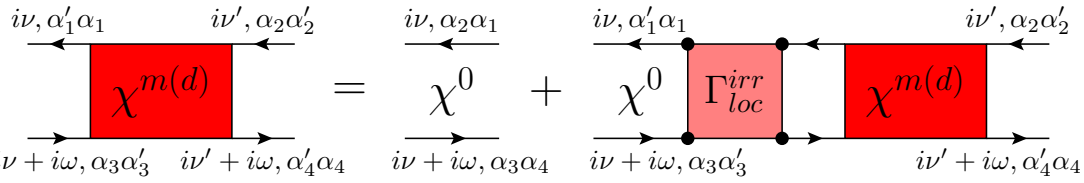

Figure 4.2: The Feynman diagram for the Bethe-Salpeter equation in the spin (charge) channel. The non-local susceptibility is obtained by replacing the local propagator by the non-local propagator.

In this section, we explain how to compute the magnetic and the charge susceptibility $\chi^{(m/d)}(\mathbf{q}, i\omega)$ from the *ab initio* perspective within the DFT+DMFT method. First, the local (impurity) Green's function is computed for the correlated orbitals as a result of the DFT+DMFT self-consistent loop. The local (impurity) polarization bubble $\chi^0(i\nu)_{i\omega}$ is computed from this fully interacting one-particle Green's function by

$$\chi^0_{loc,\substack{\alpha_1\sigma_1,\alpha_2\sigma_2\\ \alpha_3\sigma_3,\alpha_4\sigma_4}}(i\nu, i\nu')_{i\omega} = -T \cdot G_{\alpha_2\alpha_1,\sigma_1}(i\nu) \cdot G_{\alpha_3\alpha_4,\sigma_3}(i\nu + i\omega) \cdot \delta_{i\nu,i\nu'} \cdot \delta_{\sigma_1\sigma_2} \cdot \delta_{\sigma_3\sigma_4} \tag{4.22}$$

Here, σ_{1-4} are the spin indices and α_{1-4} are the orbital indices which run over correlated orbital states on the atom. And T is the temperature. The Green's function is diagonal in the spin

and the Matsubara frequency space due to the spin conservation and the time translational invariance. However, it is generally off-diagonal in the orbital space since the different orbital characters can mix at a generic momentum point For solids with high symmetry of the lattice, the local propagator is diagonal in orbital space when expressed in the crystral field harmonics.

The local two-particle Green's function χ_{loc}^{sample} is sampled by CTQMC using the converged DFT+DMFT solution. The procedure of sampling χ_{loc}^{sample} is explained in detail in section. 4.2. CTQMC samples only the connected diagrams of χ_{loc}, i.e., the rightmost diagram of Fig. 4.2. The full χ_{loc} is obtained by adding the local polarization bubble to the sampled diagram.

$$\chi_{loc,\,\alpha_3\sigma_3,\alpha_4\sigma_4}^{\alpha_1\sigma_1,\alpha_2\sigma_2}(i\nu,i\nu')_{i\omega} \quad = \quad [\chi_{loc}^{0}+\chi_{loc}^{sample}]_{\alpha_3\sigma_3,\alpha_4\sigma_4}^{\alpha_1\sigma_1,\alpha_2\sigma_2}(i\nu,i\nu')_{i\omega} \tag{4.23}$$

The matrix size of χ_{loc} at a fixed $i\omega$ is given as $N\times N$ where N is (the number of spins)$^2\times$(the number of orbitals)$^2\times$(the number of Matsubara frequencies $i\nu$). Due to the large matrix size, it is desirable to use spin symmetry to reduce the matrix size. Under the spin rotation, the two-particle response functions in the particle-hole channel can be decomposed into the magnetic (m) channel and the density (d) channel as follows:

$$\chi_{loc,\,\alpha_3,\alpha_4}^{m(d),\alpha_1,\alpha_2}(i\nu,i\nu')_{i\omega} \quad = \quad \chi_{loc,\,\alpha_3\uparrow,\alpha_4\uparrow}^{\alpha_1\uparrow,\alpha_2\uparrow}(i\nu,i\nu')_{i\omega}-(+)\chi_{loc,\,\alpha_3\uparrow,\alpha_4\downarrow}^{\alpha_1\uparrow,\alpha_2\downarrow}(i\nu,i\nu')_{i\omega} \tag{4.24}$$

The two-particle irreducible vertex function Γ_{loc}^{irr} is the vertex function which can not be separated into two parts by cutting two propagators. Γ_{loc}^{irr} is assumed to be local in the same basis in which the DMFT self-energy is local. In order to extract Γ_{loc}^{irr}, we employ the Bethe-Salpeter equation (see Fig. 4.2) which relates the local two-particle Green's function (χ_{loc}) sampled by CTQMC, with both the local polarization function (χ_{loc}^{0}) and Γ_{loc}^{irr}.

$$\Gamma_{loc\,\alpha_3,\alpha_4}^{irr,m(d),\alpha_1,\alpha_2}(i\nu,i\nu')_{i\omega}=[(\chi_{loc}^{0})_{i\omega}^{-1}-\chi_{loc}^{m(d)-1}]_{\alpha_3,\alpha_4}^{\alpha_1,\alpha_2}(i\nu,i\nu')_{i\omega}. \tag{4.25}$$

Γ_{loc}^{irr} also depends on three Matsubara frequencies ($i\nu$, $i\nu'$; $i\omega$) just as χ_{loc}.

Once the irreducible vertex Γ_{loc}^{irr} is obtained, the momentum dependent two-particle Green's function is constructed using again the Bethe-Salpeter equation (Fig. 4.2) by replacing the local polarization function χ_{loc}^{0} by the non-local one $\chi_{\mathbf{q},i\omega}^{0}$. Since Γ_{loc}^{irr} is local, we can sum over the

momentum $\mathbf{k}$ inside the non-local polarization bubble

$$\chi^0_{\substack{\alpha_1\sigma_1,\alpha_2\sigma_2\\ \alpha_3\sigma_3,\alpha_4\sigma_4}}(i\nu,i\nu')_{\mathbf{q},i\omega} = -\frac{T}{N_k}\sum_{\mathbf{k}} G_{\alpha_2\alpha_1,\sigma_1}(\mathbf{k},i\nu)\cdot G_{\alpha_3\alpha_4,\sigma_3}(\mathbf{k}+\mathbf{q},i\nu+i\omega)\cdot\delta_{i\nu,i\nu'}\cdot\delta_{\sigma_1\sigma_2}\cdot\delta_{\sigma_3\sigma_4} \tag{4.26}$$

to bring the Bethe-Salpeter equation into a simplified form

$$\chi^{m(d)}_{\substack{\alpha_1,\alpha_2\\ \alpha_3,\alpha_4}}(i\nu,i\nu')_{\mathbf{q},i\omega} = [(\chi^0)^{-1}_{\mathbf{q},i\omega} - \Gamma^{irr,m(d)}_{loc}]^{-1}_{\substack{\alpha_1,\alpha_2\\ \alpha_3,\alpha_4}}(i\nu,i\nu')_{\mathbf{q},i\omega}. \tag{4.27}$$

Finally, the spin and charge susceptibility $\chi^{m(d)}(\mathbf{q},i\omega)$ is obtained by closing the two particle Green's function with spin or charge bare vertex γ (γ is 1/2 for spin and γ is 1 for charge) and summing over frequencies ($i\nu$,$i\nu'$) and orbitals ($\alpha_{1,2}$) on the four external legs

$$\chi^{m(d)}(\mathbf{q},i\omega) = 2\gamma^2\sum_{i\nu,i\nu'}\sum_{\alpha_1\alpha_2}\chi^{m(d)}_{\substack{\alpha_1,\alpha_2\\ \alpha_1,\alpha_2}}(i\nu,i\nu')_{\mathbf{q},i\omega}. \tag{4.28}$$

The algorithm for computing the magnetic and the charge susceptibility is sketched in Fig.4.3

4.5 The calculation of the superconducting pairing susceptibility

4.5.1 The irreducible vertex function in the particle-particle channel $\Gamma^{irr,p-p}$

The two-particle vertex functions depend on four spin σ_{1-4} and four orbital α_{1-4} indices, and three Matsubara frequencies ($i\nu$,$i\nu'$, and $i\omega$) and momentums ($\mathbf{k}$,$\mathbf{k}'$, and $\mathbf{q}$) which are labeled on the external legs.

Depending on the nature of the quasi-particle scattering, the two-particle vertex function can be expressed in terms of two distinct types of diagrams, so called channels. They are the particle-hole and the particle-particle channels. A representative of the particle-particle and the particle-hole channel is depicted in Fig. 4.4(a).

As already discussed in the previous section, the spin degrees of freedom in the particle-hole channel can be decomposed into either magnetic (m) channel or charge (d) channel distinguished by the different spin eigenstates if the spin-orbit coupling is small. The magnetic

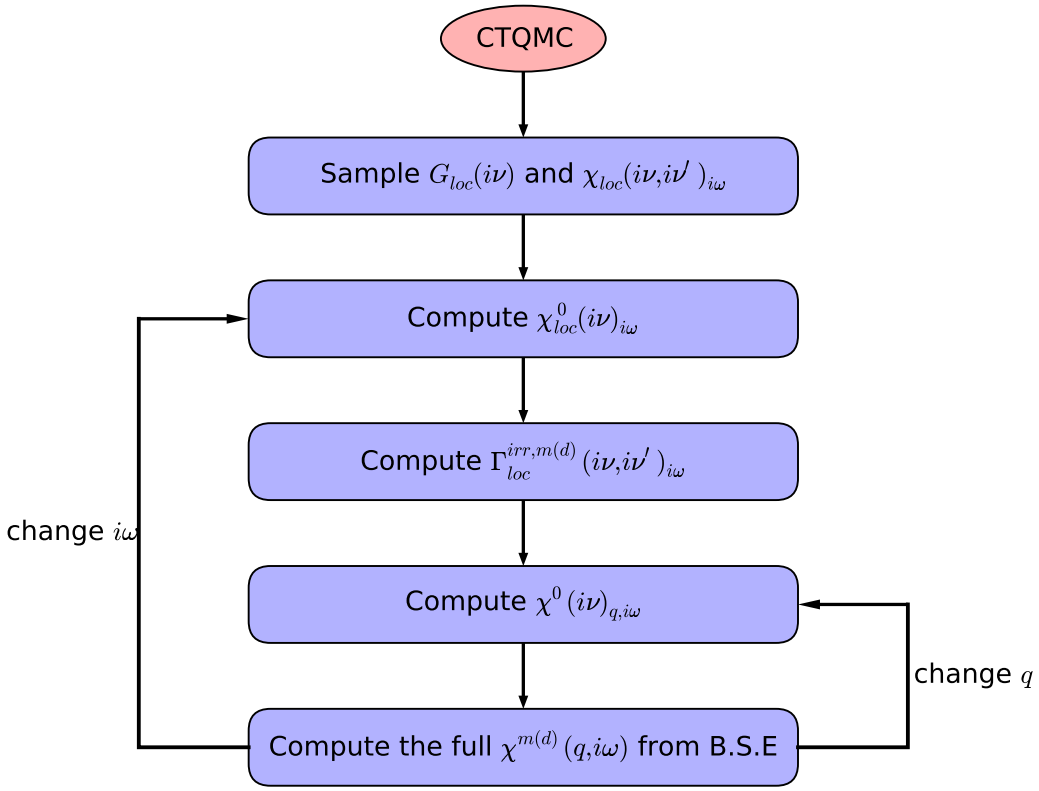

Figure 4.3: The flow chart for computing the magnetic and the charge susceptibility

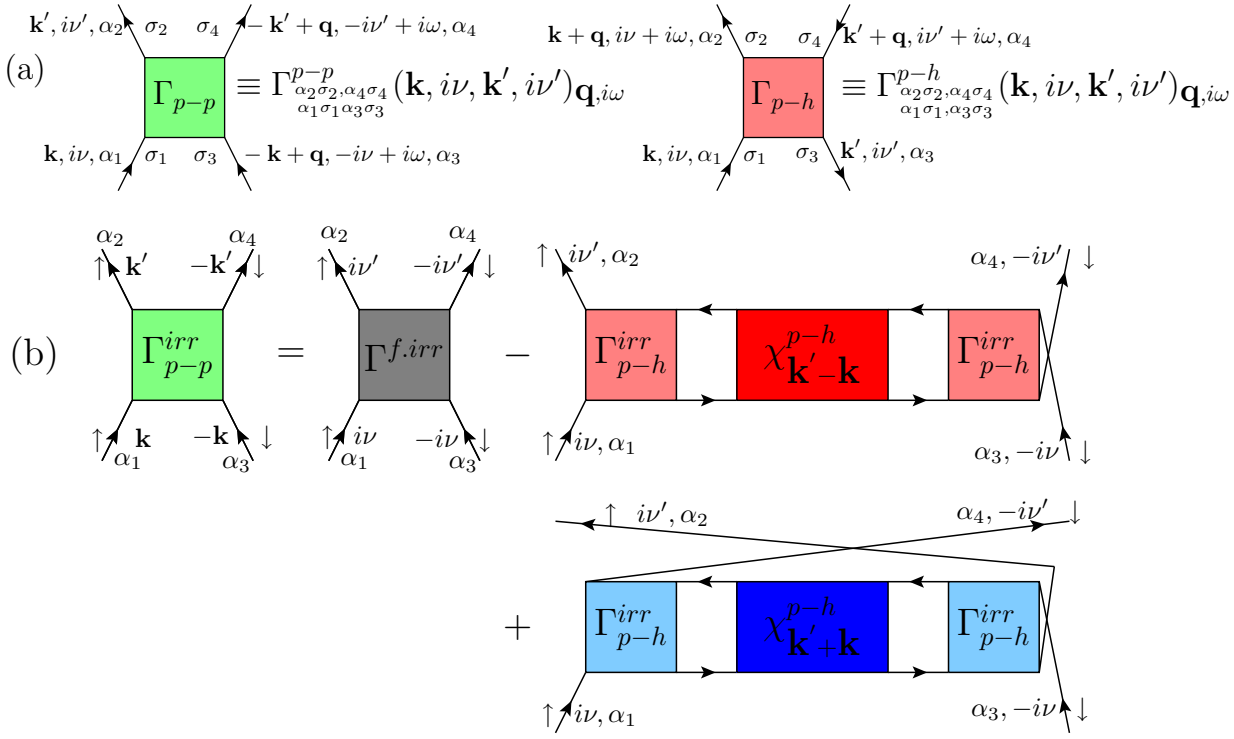

Figure 4.4: (a) The spin, orbital, momentum, and frequency labels of vertex functions in the particle-particle $(p-p)$ channel and the particle-hole $(p-h)$ channel. (b) The decomposition of the irreducible vertex function in the particle-particle channel $\Gamma^{irr,p-p}$.

channel contains either the longitudinal spin configuration (denoted as $p-h1$) or the transverse configuration (denoted as $p-h2$). In the magnetic susceptibility, the paramagnetic spin rotational symmetry ensures that $2\langle \hat{S}^z \cdot \hat{S}^z \rangle = \frac{1}{2}(\langle \hat{S}^+ \cdot \hat{S}^- \rangle + \langle \hat{S}^- \cdot \hat{S}^+ \rangle)$ where $\hat{S}$ is the spin operator. Here, $\langle \hat{S}^z \cdot \hat{S}^z \rangle$ represents the longitudinal susceptibility while $\langle \hat{S}^+ \cdot \hat{S}^- \rangle$ indicates the transverse term. As a result, one can express the vertex function in the magnetic channel with explicit spin indices ($\uparrow$, $\downarrow$) as a function of $p-h1$ and $p-h2$ channels.

$$\Gamma^{p-h,(m)} = \Gamma^{p-h1}_{\substack{\uparrow\uparrow \\ \uparrow\uparrow}} - \Gamma^{p-h1}_{\substack{\uparrow\downarrow \\ \uparrow\downarrow}} = \Gamma^{p-h2}_{\substack{\downarrow\downarrow \\ \uparrow\uparrow}} \tag{4.29}$$

In a similar way, the charge channel also can be represented in both $p-h1$ and $p-h2$ channels.

$$\Gamma^{p-h,(d)} = \Gamma^{p-h1}_{\substack{\uparrow\uparrow \\ \uparrow\uparrow}} + \Gamma^{p-h1}_{\substack{\uparrow\downarrow \\ \uparrow\downarrow}} = 2\Gamma^{p-h2}_{\substack{\uparrow\uparrow \\ \uparrow\uparrow}} - \Gamma^{p-h2}_{\substack{\downarrow\downarrow \\ \uparrow\uparrow}} \tag{4.30}$$

The last equality is derived using $\Gamma^{p-h1}_{\substack{\uparrow\uparrow \\ \uparrow\uparrow}} = \Gamma^{p-h2}_{\substack{\uparrow\uparrow \\ \uparrow\uparrow}}$.

The particle-particle channel describes the Cooper pairing for superconductivity. And this channel also can be decomposed according to spin configurations into the singlet (s) channel and the triplet (t) channel. The singlet channel has the odd symmetry under the exchange of two external spins while the triplet channel has the even symmetry.

$$\Gamma^{p-p,(s)} = \frac{1}{2}[\Gamma^{p-p}_{\substack{\uparrow\downarrow \\ \uparrow\downarrow}} - \Gamma^{p-p}_{\substack{\downarrow\uparrow \\ \uparrow\downarrow}}] \tag{4.31}$$

$$\Gamma^{p-p,(t)} = \frac{1}{2}[\Gamma^{p-p}_{\substack{\uparrow\downarrow \\ \uparrow\downarrow}} + \Gamma^{p-p}_{\substack{\downarrow\uparrow \\ \uparrow\downarrow}}] \tag{4.32}$$

From now on, we concentrate on superconductivity in the singlet channel. In this case, the Cooper pair has the odd symmetry under the spin exchange. One can note that the vertex function in the particle-particle channel Γ^{p-p} acquires a minus sign by crossing the two outgoing legs due to the exchange of two fermion operators. Since the vertex Γ^{p-p} is odd under the exchange of spin in the singlet channel, Γ^{p-p} has to be even under the exchange of momentum, orbital, and frequency.

Here, we introduce several kinds of vertex functions which we will use later. We first concentrate on the particle-hole channel. The connected two-particle Green's function $\overline{\chi}$ matrix defined as

$$\overline{\chi}^{2,4}_{1,3} = \langle \psi_1^\dagger \psi_4^\dagger \psi_3 \psi_2 \rangle - \langle \psi_1^\dagger \psi_2 \rangle \cdot \langle \psi_4^\dagger \psi_3 \rangle \ + \langle \psi_1^\dagger \psi_3 \rangle \cdot \langle \psi_4^\dagger \psi_2 \rangle \tag{4.33}$$

is related to the polarization bubble χ^0 and the irreducible vertex Γ^{irr} by the Bethe-Salpeter equation

$$\chi = \chi^0 + \overline{\chi} = [(\chi^0)^{-1} - \Gamma^{irr}]^{-1}. \tag{4.34}$$

$$\overline{\chi} = [(\chi^0)^{-1} - \Gamma^{irr}]^{-1} - \chi^0 = [(\chi^0 \cdot \Gamma^{irr} \cdot \chi^0)^{-1} - (\chi^0)^{-1}]^{-1}. \tag{4.35}$$

Here, χ^0 is given by $-T \cdot G \cdot G$. We omit spin, orbital, momentum, and frequency labels for convenience.

The two-particle full vertex function Γ^{full} is defined as all connected diagrams obtained by removing two external polarization bubbles from $\overline{\chi}$

$$\begin{aligned} \Gamma^{full} &= (\chi^0)^{-1} \cdot \overline{\chi} \cdot (\chi^0)^{-1} \\ &= [(\Gamma^{irr})^{-1} - \chi^0]^{-1} \\ &= \Gamma^{irr} + \Gamma^{irr} \cdot \chi^0 \cdot \Gamma^{irr} + \Gamma^{irr} \cdot \chi^0 \cdot \Gamma^{irr} \cdot \chi^0 \cdot \Gamma^{irr} + \cdots \end{aligned} \tag{4.36}$$

As a result, Γ^{full} is given by dressing Γ^{irr} with χ^0.

In contrast to Γ^{irr}, the reducible vertex function $\widetilde{\Gamma}$ is defined as the vertex function which can be separated into two parts by cutting two propagators. $\widetilde{\Gamma}$ is obtained by subtracting the irreducible part from Γ^{full}.

$$\begin{aligned} \widetilde{\Gamma} &= \Gamma^{full} - \Gamma^{irr} \\ &= \Gamma^{irr} \cdot \chi^0 \cdot \Gamma^{irr} + \Gamma^{irr} \cdot \chi^0 \cdot \Gamma^{irr} \cdot \chi^0 \cdot \Gamma^{irr} + \cdots \\ &= \Gamma^{irr} \cdot \chi \cdot \Gamma^{irr} \end{aligned} \tag{4.37}$$

Considering both particle-hole and particle-particle channels, we can define the vertex which is irreducible with respect to all channels. The fully irreducible vertex $\Gamma^{f.irr}$ consists of diagrams which can not be separated into two parts by cutting any two propagators, either particle-particle or particle-hole pair of propagators.

The irreducible vertex function in the particle-particle channel $\Gamma^{irr,p-p}$, which gives the pairing interaction for Cooper pairs, consists of the fully irreducible vertex function $\Gamma^{f.irr}$ and the reducible vertex functions in the other particle-hole channels $\widetilde{\Gamma}^{p-h} = \Gamma^{full,p-h} - \Gamma^{irr,p-h}$.

We keep track of the spin, orbital, and frequency labels as shown in Fig. 4.4. Note that we plot $\widetilde{\Gamma}$ in the expanded form $\Gamma^{irr} \cdot \chi \cdot \Gamma^{irr}$ in Fig. 4.4(b). Moreover, we concentrate on uniform and static superconductivity, i.e. $\mathbf{q} = 0, i\omega = 0$,

$$\Gamma^{irr,p-p}_{\substack{\alpha_2\uparrow,\alpha_4\downarrow \\ \alpha_1\uparrow,\alpha_3\downarrow}}(k,k')_{q=0} = \Gamma^{f-irr}_{\substack{\alpha_2\uparrow,\alpha_4\downarrow \\ \alpha_1\uparrow,\alpha_3\downarrow}}(k,k')_{q=0} - \widetilde{\Gamma}^{p-h1}_{\substack{\alpha_2\uparrow,\alpha_3\downarrow \\ \alpha_1\uparrow,\alpha_4\downarrow}}(k,-k')_{k'-k} + \widetilde{\Gamma}^{p-h2}_{\substack{\alpha_4\downarrow,\alpha_3\downarrow \\ \alpha_1\uparrow,\alpha_2\uparrow}}(k,k')_{-k'-k} \quad (4.38)$$

Here, the label $k = (\mathbf{k}, i\nu)$ represents both momentum and frequency.

$\Gamma^{irr,p-p}$ in the spin singlet state, which is denoted by $\Gamma^{irr,p-p,(s)}$, is obtained by antisymmetrizing the spin space as in Eq. 4.31. One spin configuration for Eq. 4.31 is given in Eq. 4.38 and depicted in Fig. 4.4(b). The other spin configuration can be obtained in a similar way as

$$\Gamma^{irr,p-p}_{\substack{\alpha_2\downarrow,\alpha_4\uparrow \\ \alpha_1\uparrow,\alpha_3\downarrow}}(k,k')_{q=0} = \Gamma^{f-irr}_{\substack{\alpha_2\downarrow,\alpha_4\uparrow \\ \alpha_1\uparrow,\alpha_3\downarrow}}(k,k')_{q=0} - \widetilde{\Gamma}^{p-h2}_{\substack{\alpha_2\downarrow,\alpha_3\downarrow \\ \alpha_1\uparrow,\alpha_4\uparrow}}(k,-k')_{k'-k} + \widetilde{\Gamma}^{p-h1}_{\substack{\alpha_4\uparrow,\alpha_3\downarrow \\ \alpha_1\uparrow,\alpha_2\downarrow}}(k,k')_{-k'-k} \quad (4.39)$$

Due to the exchange of the spin label, $p-h1$ and $p-h2$ channels are also exchanged. Using Eq. 4.29 and Eq. 4.30, $p-h1$ and $p-h2$ channels can be represented as the magnetic/charge channel

$$\Gamma^{p-h1}_{\substack{\uparrow\downarrow \\ \uparrow\downarrow}} = \frac{1}{2}[\Gamma^{p-h,(d)} - \Gamma^{p-h,(m)}] \quad (4.40)$$

$$\Gamma^{p-h2}_{\substack{\downarrow\downarrow \\ \uparrow\uparrow}} = \Gamma^{p-h,(m)} \quad (4.41)$$

$\Gamma^{irr,p-p}$ in Eq. 4.38 and Eq. 4.39 also can be represented as the magnetic/charge channel

$$\Gamma^{irr,p-p}_{\substack{\alpha_2\uparrow,\alpha_4\downarrow \\ \alpha_1\uparrow,\alpha_3\downarrow}}(k,k')_{q=0} = \Gamma^{f-irr}_{\substack{\alpha_2\uparrow,\alpha_4\downarrow \\ \alpha_1\uparrow,\alpha_3\downarrow}}(k,k')_{q=0} - \frac{1}{2}[\widetilde{\Gamma}^{p-h,(d)} - \widetilde{\Gamma}^{p-h,(m)}]^{\alpha_2,\alpha_3}_{\alpha_1,\alpha_4}(k,-k')_{k'-k} + \widetilde{\Gamma}^{p-h,(m)}_{\substack{\alpha_4,\alpha_3 \\ \alpha_1,\alpha_2}}(k,k')_{-k'-k} \quad (4.42)$$

$$\Gamma^{irr,p-p}_{\substack{\alpha_2\downarrow,\alpha_4\uparrow \\ \alpha_1\uparrow,\alpha_3\downarrow}}(k,k')_{q=0} = \Gamma^{f-irr}_{\substack{\alpha_2\downarrow,\alpha_4\uparrow \\ \alpha_1\uparrow,\alpha_3\downarrow}}(k,k')_{q=0} - \widetilde{\Gamma}^{p-h,(m)}_{\substack{\alpha_2,\alpha_3 \\ \alpha_1,\alpha_4}}(k,-k')_{k'-k} + \frac{1}{2}[\widetilde{\Gamma}^{p-h,(d)} - \widetilde{\Gamma}^{p-h,(m)}]^{\alpha_4,\alpha_3}_{\alpha_1,\alpha_2}(k,k')_{-k'-k} \quad (4.43)$$

Finally $\Gamma^{irr,p-p,(s)}$ is obtained using Eq. 4.31 as

$$\begin{aligned}\Gamma^{irr,p-p,(s)}_{\substack{\alpha_2,\alpha_4 \\ \alpha_1,\alpha_3}}(k,k')_{q=0} &= \Gamma^{f-irr,(s)}_{\substack{\alpha_2,\alpha_4 \\ \alpha_1,\alpha_3}}(k,k')_{q=0} + \frac{1}{2}[\frac{3}{2}\widetilde{\Gamma}^{p-h,(m)} - \frac{1}{2}\widetilde{\Gamma}^{p-h,(d)}]^{\alpha_2,\alpha_3}_{\alpha_1,\alpha_4}(k,-k')_{k'-k} \\ &\quad + \frac{1}{2}[\frac{3}{2}\widetilde{\Gamma}^{p-h,(m)} - \frac{1}{2}\widetilde{\Gamma}^{p-h,(d)}]^{\alpha_4,\alpha_3}_{\alpha_1,\alpha_2}(k,k')_{-k'-k} \quad (4.44)\end{aligned}$$

One can note that the reducible vertex $[\frac{3}{2}\widetilde{\Gamma}^{p-h,(m)} - \frac{1}{2}\widetilde{\Gamma}^{p-h,(d)}]$ is symmetrized under the exchange of orbitals ($\alpha_2 \leftrightarrow \alpha_4$), momentum, and frequency ($k' \leftrightarrow -k'$).

It is well known from BCS theory that the attractive pairing vertex in the s-wave symmetry channel can mediate the pairing interaction for Cooper pairs. The pairing vertex given in Eq. 4.44 is constructed from the Coulomb interaction vertex and the vertex has the repulsive nature in the average. Therefore, the pairing susceptibility calculated using this repulsive vertex can not develop a pole in the s-wave channel and s-wave superconductivity is excluded among the possible pairing channels.

Although the pairing vertex in Eq. 4.44 is repulsive in the s-wave channel, the momentum dependent pairing vertex can be effectively attractive in higher angular momentum channels such as d-wave or extended s-wave. Indeed, this non-local symmetry is realized in many high T_c superconductors where the pairing is believed to be mediated by spin fluctuations.

In order to evaluate the non-local pairing vertex $\Gamma^{irr,p-p,(s)}$, we resort here to the DMFT approximation. In this approximation, we assume that the fully irreducible vertex $\Gamma^{f.irr}$ is local and the irreducible vertices in the particle-hole channels ($\Gamma^{irr,(m)}$,$\Gamma^{irr,(d)}$) are local as well. These irreducible vertices can be computed from the corresponding impurity quantities. On the other hand, the irreducible vertex in the particle-particle channel is not local but will be computed from the particle-hole diagrams as depicted in Fig.4.4(b). Explicitly, the magnetic/charge susceptibility are obtained by the Bethe-Salpeter equation

$$\chi^{p-h,(m/d)}_{\substack{\alpha_2,\alpha_4\\ \alpha_1,\alpha_3}}(i\nu_1,i\nu_2)_{\mathbf{q},i\omega} = [(\chi_0^{p-h})^{-1}_{\mathbf{q},i\omega} - \Gamma^{irr,p-h,(m/d)}_{loc}]^{\alpha_2,\alpha_4}_{\alpha_1,\alpha_3}(i\nu_1,i\nu_2)_{\mathbf{q},i\omega} \qquad (4.45)$$

and the reducible magnetic/charge vertex is obtained from this non-local magnetic/charge susceptibility by

$$\begin{aligned}\widetilde{\Gamma}^{p-h,(m/d)}_{\substack{\alpha_2,\alpha_4\\ \alpha_1,\alpha_3}}(i\nu,i\nu')_{\mathbf{q},i\omega} = &\sum_{i\nu_1,i\nu_2}\sum_{\substack{\alpha'_2,\alpha'_4\\ \alpha'_1,\alpha'_3}}\Gamma^{irr,p-h,(m/d)}_{loc,\,\substack{\alpha_2,\alpha'_2\\ \alpha_1,\alpha'_1}}(i\nu,i\nu_1)_{i\omega}\cdot\chi^{p-h,(m/d)}_{\substack{\alpha'_2,\alpha'_4\\ \alpha'_1,\alpha'_3}}(i\nu_1,i\nu_2)_{\mathbf{q},i\omega}\\ &\cdot\Gamma^{irr,p-h,(m/d)}_{\substack{\alpha'_4,\alpha_4\\ \alpha'_3,\alpha_3}}(i\nu_2,i\nu')_{i\omega} \qquad (4.46)\end{aligned}$$

Here, the non-local polarization is $\chi^{0,p-h}(i\nu)_{\mathbf{q},i\omega} = -\frac{T}{N_k}\sum_{\mathbf{k}} G(\mathbf{k},i\nu)\cdot G(\mathbf{k}+\mathbf{q},i\nu+i\omega)$ and the non-local Green's function $G(\mathbf{k},i\nu)$ is dressed with the local DMFT self-energy. Note that Eq. 4.45 was used before in the previous section (Eq. 4.27) to compute the non-local magnetic/charge susceptibility.

Finally, the non-local pairing vertex is obtained from the particle-hole reducible vertices by

$$\begin{aligned}\Gamma^{irr,p-p,(s)}_{\substack{\alpha_2,\alpha_4\\ \alpha_1,\alpha_3}}(\mathbf{k},i\nu,\mathbf{k}',i\nu') &= \Gamma^{f-irr,(s)}_{\substack{\alpha_2,\alpha_4\\ \alpha_1,\alpha_3}}(i\nu,i\nu') + [\frac{3}{2}\widetilde{\Gamma}^{p-h,(m)} - \frac{1}{2}\widetilde{\Gamma}^{p-h,(d)}]^{\alpha_2,\alpha_3}_{\alpha_1,\alpha_4}(i\nu,-i\nu')_{\mathbf{k}'-\mathbf{k},i\nu'-i\nu} \\ &\quad + \frac{1}{2}[\frac{3}{2}\widetilde{\Gamma}^{p-h,(m)} - \frac{1}{2}\widetilde{\Gamma}^{p-h,(d)}]^{\alpha_4,\alpha_3}_{\alpha_1,\alpha_2}(i\nu,i\nu')_{-\mathbf{k}'-\mathbf{k},-i\nu'-i\nu} \qquad (4.47)\end{aligned}$$

In practice, one can compute the only one term of $[\frac{3}{2}\widetilde{\Gamma}^{p-h,(m)} - \frac{1}{2}\widetilde{\Gamma}^{p-h,(d)}]$ and symmetrize the result with respect to orbitals ($\alpha_2 \leftrightarrow \alpha_4$), momentum ($\mathbf{k}' \leftrightarrow -\mathbf{k}'$), and frequency ($i\nu' \leftrightarrow -i\nu'$).

Within our DMFT approximation, Γ^{f-irr} is assumed to be purely local. Indeed, Ref. [71] confirms the weak momentum dependence of Γ^{f-irr} vertex within cluster DMFT. Since Γ^{f-irr} is local, it could be in principle computed from the corresponding impurity vertex. In the following, we concentrate on the non-local pairing symmetry, such as d-wave, p-wave, or extended s-wave. In these cases, the local Γ^{f-irr} does not contribute to the non-local pairing gap symmetry.

4.5.2 The calculation of the superconducting critical temperature and the gap symmetry

In the previous subsection, the non-local irreducible vertex function in the particle-particle channel $\Gamma^{irr,p-p}$ is computed using DMFT vertex functions. The $\Gamma^{irr,p-p}$ vertex accounts for the pairing interaction of Cooper pairs and as a result the superconducting instability. Eq. 4.47 shows that this pairing vertex contains the spin fluctuation diagrams and the orbital (charge) fluctuation diagrams. In general, the spin fluctuation contribution is much larger near a magnetic phase transition.

The pairing susceptibility χ^{p-p} is computed by dressing the pairing polarization bubble $\chi^{0,p-p}(\mathbf{k},i\nu)$ with the pairing vertex $\Gamma^{irr,p-p,(s)}$ using the Bethe-Salpeter equation in the particle-particle channel.

$$\begin{aligned}\chi^{p-p} &= \chi^{0,p-p} - \chi^{0,p-p}\cdot\Gamma^{irr,p-p,(s)}\cdot\chi^{0,p-p} \\ &\quad + \chi^{0,p-p}\cdot\Gamma^{irr,p-p,(s)}\cdot\chi^{0,p-p}\cdot\Gamma^{irr,p-p,(s)}\cdot\chi^{0,p-p} - \dots \\ &= \chi^{0,p-p}\cdot[\mathbf{1} + \Gamma^{irr,p-p,(s)}\cdot\chi^{0,p-p}]^{-1} \qquad (4.48)\end{aligned}$$

The critical temperature T_c of the superconducting state is determined as the temperature where this pairing susceptibility diverges. The sufficient condition for the divergence is at least one eigenvalue of the pairing matrix $-\Gamma^{irr,p-p,(s)} \cdot \chi^{0,p-p}$ reaches one. Therefore, T_c can be computed by solving the following eigenvalue equation without the need to compute the full pairing susceptibility.

$$-\frac{T}{N_k}\sum_{\mathbf{k}',i\nu'}\sum_{\substack{\alpha_2,\alpha_4\\ \alpha_5,\alpha_6}} \Gamma^{irr,p-p,(s)}_{\substack{\alpha_2,\alpha_4\\ \alpha_1,\alpha_3}}(\mathbf{k},i\nu,\mathbf{k}',i\nu')\cdot\chi^{0,p-p}_{\substack{\alpha_5,\alpha_6\\ \alpha_2,\alpha_4}}(\mathbf{k}',i\nu')\cdot\phi^{\lambda}_{\alpha_5\alpha_6}(\mathbf{k}',i\nu') = \lambda\cdot\phi^{\lambda}_{\alpha_1\alpha_3}(\mathbf{k},i\nu) \quad (4.49)$$

Here, λ is the eigenvalue of the pairing kernel matrix and T_c is determined as the temperature at which the leading eigenvalue approaches unity. The corresponding eigenvector ϕ^{λ} gives the pairing symmetry in momentum and orbital space of the superconducting state which will be stable below T_c. Not just momentum but also the orbital contribution to the gap symmetry might play an important role in the Fe-based superconductors due to their multi-orbital nature.

The pairing bubble diagram $\chi^{0,p-p}$ is computed as a product of DMFT Green's functions. This Green's function is dressed with the local DMFT self energy.

$$\chi^{0,p-p}_{\substack{\alpha_2,\alpha_4\\ \alpha_1,\alpha_3}}(\mathbf{k},i\nu)_{\mathbf{q}=0,i\omega=0} \quad = \quad T\cdot G_{\alpha_1\alpha_2,\uparrow}(\mathbf{k},i\nu)\cdot G_{\alpha_3\alpha_4,\downarrow}(-\mathbf{k},-i\nu) \quad (4.50)$$

One can note that the polarization bubble in the particle-particle channel ($\chi^{0,p-p}$) has no minus sign while the particle-hole polarization bubble $\chi^{0,p-h}$ has it due to the closed loop of the diagram. As will be shown in the next chapter, this pairing bubble $\chi^{0,p-p}$ can incorporate the non-local fluctuation effect beyond DMFT replacing the DMFT Green's function by the Green's function computed with non-local methods.

The eigenvalue problem in Eq. 4.49 involves the diagonalization of a non-Hermitian matrix of size $N_\nu \times N_k \times N_{orb}^2$ where N_ν is the number of frequency, N_k is the number of k points, and N_{orb} is the number of orbitals. The spin degree of freedom is projected to the singlet state. For reliable results, we need at least 20 frequency points and 1000 k points in the Brillouin zone. For the multi-orbital case with five relevant d orbitals, the matrix size can be larger than 500,000. Therefore, it is desirable to transform this matrix into a Hermitian form for which there exists very efficient algorithms such as the Lanczos method to obtain the largest eigenvalue

and eigenfunction. The original χ^{p-p} given in Eq. 4.48 can be expressed in a symmetric way

$$\begin{aligned}\chi^{p-p} &= \chi^{0,p-p}\cdot[\mathbf{1}+\Gamma^{irr,p-p,(s)}\cdot\chi^{0,p-p}]^{-1}\\ &= \sqrt{\chi^{0,p-p}}\cdot\sqrt{\chi^{0,p-p}}\cdot[\mathbf{1}+\Gamma^{irr,p-p,(s)}\cdot\chi^{0,p-p}]^{-1}\cdot(\sqrt{\chi^{0,p-p}})^{-1}\cdot\sqrt{\chi^{0,p-p}}\\ &= \sqrt{\chi^{0,p-p}}\cdot[\mathbf{1}+\sqrt{\chi^{0,p-p}}\cdot\Gamma^{irr,p-p,(s)}\cdot\sqrt{\chi^{0,p-p}}]^{-1}\cdot\sqrt{\chi^{0,p-p}} \qquad (4.51)\end{aligned}$$

As a result, the gap function in Eq. 4.49 can be brought to a Hermitian form by

$$-\frac{T}{N_k}\sum_{\mathbf{k}',i\nu}\sum_{\substack{\alpha_2\alpha_4\alpha_5\\ \alpha_6\alpha_7\alpha_8}}\sqrt{\chi^{0,p-p}_{\substack{\alpha_2,\alpha_4\\ \alpha_1,\alpha_3}}(\mathbf{k},i\nu)}\cdot\Gamma^{irr,p-p,(s)}_{\substack{\alpha_5,\alpha_7\\ \alpha_2,\alpha_4}}(\mathbf{k},i\nu,\mathbf{k}',i\nu')\cdot\sqrt{\chi^{0,p-p}_{\substack{\alpha_6,\alpha_8\\ \alpha_5,\alpha_7}}(\mathbf{k}',i\nu')}\cdot\phi^{\lambda}_{\alpha_6\alpha_8}(\mathbf{k}',i\nu')=\lambda\cdot\phi^{\lambda}_{\alpha_1\alpha_3}(\mathbf{k},i\nu) \qquad (4.52)$$

One can note that $\sqrt{\chi^{0,p-p}}\cdot\Gamma^{irr,p-p,(s)}\cdot\sqrt{\chi^{0,p-p}}$ matrix is a Hermitian matrix (in single orbital case it is also real). Therefore, we use the Lanczos algorithm to compute the leading and the subleading eigenvalues and the corresponding eigenfunctions.

The eigenfunction computed using the non-Hermitian gap equation in Eq. 4.49 is related to the eigenfunction ϕ^{λ} in Eq. 4.52.

$$\sqrt{\chi^{0,p-p}}\cdot\Gamma^{irr,p-p,(s)}\cdot\sqrt{\chi^{0,p-p}}\cdot\phi^{\lambda} = \lambda\cdot\phi^{\lambda} \qquad (4.53)$$

$$\Gamma^{irr,p-p,(s)}\cdot\chi^{0,p-p}((\sqrt{\chi^{0,p-p}})^{-1}\cdot\phi^{\lambda}) = \lambda\cdot((\sqrt{\chi^{0,p-p}})^{-1}\cdot\phi^{\lambda}) \qquad (4.54)$$

This equation shows that eigenvalues of the non-Hermitian gap equation (Eq. 4.49) are the same as eigenvalues of the Hermitian gap equation (Eq. 4.52). And the right eigenvector of Eq. 4.49 is given as $(\sqrt{\chi^{0,p-p}})^{-1}\cdot\phi^{\lambda}$ where ϕ^{λ} is the eigenvector of Eq. 4.52. In a similar way, the left eigenvector is given as $\sqrt{\chi^{0,p-p}}\cdot\phi^{\lambda}$

The pairing susceptibility χ^{p-p} can be represented as a function of eigenvalues λ and eigenfunctions ϕ^{λ} of the Hermitian pairing matrix (Eq. 4.52) using the eigendecomposition of the matrix.

$$\begin{aligned}\chi^{p-p}(k,k') &= \sqrt{\chi^{0,p-p}(k)}\cdot[\mathbf{1}+\sqrt{\chi^{0,p-p}}\cdot\Gamma^{irr,p-p,(s)}\cdot\sqrt{\chi^{0,p-p}}]^{-1}\cdot\sqrt{\chi^{0,p-p}(k')}\\ &= \sqrt{\chi^{0,p-p}(k)}\cdot[U\cdot U^{\dagger}-U\cdot\Lambda\cdot U^{\dagger}]^{-1}\cdot\sqrt{\chi^{0,p-p}(k')}\\ &= \sqrt{\chi^{0,p-p}(k)}\cdot U\cdot[\mathbf{1}-\Lambda]^{-1}\cdot U^{\dagger}\cdot\sqrt{\chi^{0,p-p}(k')}\\ &= \sum_{\lambda}\frac{1}{1-\lambda}\cdot(\sqrt{\chi^{0,p-p}(k)}\cdot\phi^{\lambda}(k))\cdot(\sqrt{\chi^{0,p-p}(k')}\cdot\phi^{\lambda}(k')) \qquad (4.55)\end{aligned}$$

where Λ is the diagonal matrix whose i-th diagonal element is the i-th eigenvalue λ_i of the Hermitian pairing matrix and U is the unitary matrix whose columns are the corresponding eigenvectors. It is obvious that the pairing susceptibility diverges when the leading eigenvalue obtained from Eq. 4.52 approaches one. The corresponding eigenfunction represents the momentum structure of χ^{p-p}, i.e., the gap symmetry of the SC state.

The overall procedure for computing the pairing susceptibility is depicted in Fig. 4.5.

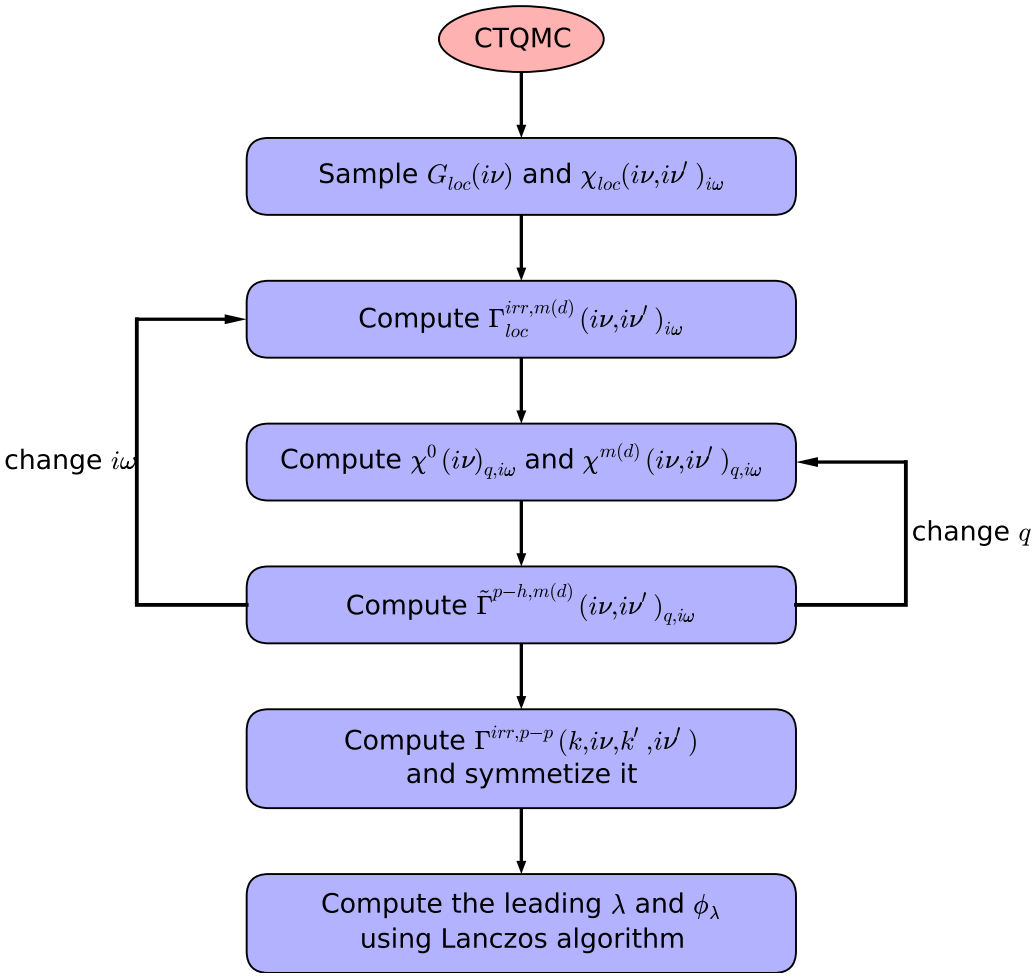

Figure 4.5: The flow chart for computing the pairing susceptibility

4.5.3 Relevant quantities for superconductivity

The projected pairing interaction

The pairing vertices $\Gamma^{irr,p-p,(s)}$ projected to different symmetry channels are denoted by $\overline{\Gamma}^{(\alpha),p-p}$ and can be computed by

$$\overline{\Gamma}^{(\alpha),p-p}_{\substack{\alpha_2,\alpha_4\\ \alpha_1,\alpha_3}} = \frac{\sum_{\mathbf{k},\mathbf{k}'} g^{(\alpha)}(\mathbf{k}) \cdot \Gamma^{irr,p-p,(s)}_{\substack{\alpha_2,\alpha_4\\ \alpha_1,\alpha_3}}(\mathbf{k},\pi T,\mathbf{k}',\pi T) \cdot g^{(\alpha)}(\mathbf{k}')}{\sum_{\mathbf{k}} \left(g^{(\alpha)}(\mathbf{k})\right)^2} \tag{4.56}$$

Here, $g^{(\alpha)}(\mathbf{k})$ represents different pairing channels, for example, $g^{(\alpha)}(\mathbf{k}) = (\cos(k_x) - \cos(k_y))$ for the d-wave and $g^{(\alpha)}(\mathbf{k}) = (\cos(k_x) + \cos(k_y))$ for the extended s-wave. Since $\Gamma^{irr,p-p,(s)}$ falls off rapidly with frequency, the pairing vertex value for the lowest Matsubara point is considered similar as in Ref. [79]. This pairing interaction is repulsive in the s-wave channel but it can be attractive in other symmetry channels.

The projected pairing bubble

The pairing bubble summed over the Matsubara frequencies $\overline{\chi}^{0,p-p}$ also can be projected to different symmetry channels in a similar way as in Eq. 4.56.

$$\overline{\chi}^{0,p-p}_{\substack{\alpha_2,\alpha_4\\ \alpha_1,\alpha_3}} = \frac{T\sum_{\mathbf{k},i\nu} g(\mathbf{k}) \cdot \chi^{0,p-p}_{\substack{\alpha_2,\alpha_4\\ \alpha_1,\alpha_3}}(\mathbf{k},i\nu) \cdot g(\mathbf{k})}{\sum_{\mathbf{k}} \left(g(\mathbf{k})\right)^2} \tag{4.57}$$

The effective $\overline{U}$

As discussed in subsection 4.5.1, the spin-fermion interaction vertex within DMFT is given by the local irreducible vertex in the particle-hole channel $\Gamma^{irr,p-h}$. In the case of weak interactions, this irreducible vertex function is usually approximated by the bare interaction or the effectively screened interaction U which is independent of frequency but still retains the spin and the orbital dependence. This is the so called random phase approximation (RPA). Within this

approximation, the reducible particle-hole vertex in Eq. 4.47 is simplified to

$$\begin{aligned}\Gamma^{irr,p-p}_{\substack{\alpha_2,\alpha_4\\ \alpha_1,\alpha_3}}(\mathbf{k},i\nu,\mathbf{k}',i\nu') &= \frac{3}{2}\sum_{\substack{\alpha_2',\alpha_4'\\ \alpha_1',\alpha_3'}} U^{(m)}_{\substack{\alpha_2,\alpha_2'\\ \alpha_1,\alpha_1'}} \cdot \chi^{p-h,(m)}_{\substack{\alpha_2',\alpha_4'\\ \alpha_1',\alpha_3'},\mathbf{k}'-\mathbf{k},i\nu'-i\nu} \cdot U^{(m)}_{\substack{\alpha_4',\alpha_4\\ \alpha_3',\alpha_3}} \\ &\quad -\frac{1}{2}\sum_{\substack{\alpha_2',\alpha_4'\\ \alpha_1',\alpha_3'}} U^{(d)}_{\substack{\alpha_2,\alpha_2'\\ \alpha_1,\alpha_1'}} \cdot \chi^{p-h,(d)}_{\substack{\alpha_2',\alpha_4'\\ \alpha_1',\alpha_3'},\mathbf{k}'-\mathbf{k},i\nu'-i\nu} \cdot U^{(d)}_{\substack{\alpha_4',\alpha_4\\ \alpha_3',\alpha_3}} \end{aligned} \tag{4.58}$$

Here, $U^{(m/d)}_{\substack{\alpha_2,\alpha_4\\ \alpha_1,\alpha_3}}$ are the bare interaction with the orbital dependence in the magnetic and the density channel and $\chi^{p-h,(m/d)}_{\substack{\alpha_2,\alpha_4\\ \alpha_1,\alpha_3}}$ is the RPA magnetic or charge susceptibility. This bare interaction matrix includes the intra-(inter-) orbital interaction term, the Hund's coupling term, and the pair-hopping term [80, 81].

In the vertex calculation, the spin-fermion interaction vertex depends on frequencies given as $\Gamma^{irr,p-h}$. The effective spin-fermion vertex $\overline{U}$ within DMFT can be determined by equating the $\Gamma^{irr,p-p}$ vertex at the lowest Matsubara point in Eq. 4.47 with the RPA form in Eq. 4.58

$$\widetilde{\Gamma}^{p-h,(m/d)}_{\substack{\alpha_2,\alpha_4\\ \alpha_1,\alpha_3}}(\pi T,\pi T)_{\mathbf{q},i\omega=0} = \sum_{\substack{\alpha_2',\alpha_4'\\ \alpha_1',\alpha_3'}} \overline{U}^{(m/d)}_{\substack{\alpha_2,\alpha_2'\\ \alpha_1,\alpha_1'},\mathbf{q}} \cdot \chi^{p-h,(m/d)}_{\substack{\alpha_2',\alpha_4'\\ \alpha_1',\alpha_3'},\mathbf{q},i\omega=0} \cdot \overline{U}^{(m/d)}_{\substack{\alpha_4',\alpha_4\\ \alpha_3',\alpha_3},\mathbf{q}} \tag{4.59}$$

Here, $\overline{U}$ is evaluated only at $i\omega$=0 assuming the $i\omega$ dependence of $\overline{U}$ is weak. The $\widetilde{\Gamma}^{p-h,(m/d)}$ vertex at higher $i\omega$ values can be computed more efficiently from the RPA form in Eq. 4.59 using the computed $\overline{U}$ at $i\omega$=0. In the single orbital case, $\overline{U}^{(m/d)}_{\mathbf{q}}$ is given as

$$\overline{U}^{(m/d)}_{\mathbf{q}} = \sqrt{\frac{[\Gamma^{irr,p-h,(m/d)} \cdot \chi^{p-h(m/d)} \cdot \Gamma^{irr,p-h,(m/d)}](\pi T,\pi T)_{\mathbf{q},i\omega=0}}{\sum_{i\nu,i\nu'} \chi^{p-h,(m/d)}(i\nu,i\nu')_{\mathbf{q},i\omega=0}}} \tag{4.60}$$

The effective $\overline{U}_{\mathbf{q}}$ is now slightly depends on the momentum transfer $\mathbf{q}$, and can be averaged over all $\mathbf{q}$ points in the Brillouin zone.

$$\overline{U}^{(m/d)}_{eff} = \frac{1}{N_{\mathbf{q}}}\sum_{\mathbf{q}} \overline{U}^{(m/d)}_{\mathbf{q}} \tag{4.61}$$

Chapter 5

Non-local Vertex Corrections beyond DMFT

In this chapter, we introduce two different methods for incorporating non-local correlations beyond DMFT using the two-particle vertex function approach. First, we derive the equations for the dual fermion (DF) method as first proposed in Ref. [82, 83]. Then we concentrate on the self-consistent calculation scheme for computing the non-local one- and two-particle correlation functions of physical electrons as derived in Ref. [82, 83]. Next we derive the DF equations using the cumulant approach proposed in Ref. [84] as an alternative derivation. Finally, we explain how to compute the superconducting critical temperature and the symmetry of the gap function within the DF method. We also derive the alternative method for the inclusion of non-local correlations first proposed in Ref. [76, 85]. In this method, also called dynamical vertex approximation (DΓA), the relation between the non-local self energy and the two-particle vertex function is more transparent and avoids the introduction of auxiliary degrees of freedom, but it is a non-self-consistent and non conserving approximation. We also discuss here for the first time how to compute the pairing susceptibility within DΓA.

5.1 The dual fermion (DF) method

5.1.1 Derivation of the method

The dual fermion (DF) method is an approach for incorporating long-range correlations on top of the local correlations included in DMFT. The non-local correlations beyond DMFT are treated by the perturbative diagram approach applied to auxiliary degrees of freedom, dual fermions. The derivation of DF equations shown in this section closely follows Ref. [82, 83].

First, we consider the action of interacting f electrons

$$S[f^\dagger, f] = \sum_{\mathbf{k},\omega,\sigma} (\epsilon(\mathbf{k}) - \mu - i\omega) f^\dagger_{\mathbf{k},\omega,\sigma} f_{\mathbf{k},\omega,\sigma} + U \sum_i \int_0^\beta n_{i,\uparrow}(\tau) n_{i,\downarrow}(\tau) d\tau \tag{5.1}$$

where $\epsilon(\mathbf{k})$ is the energy dispersion of fermions, μ is the chemical potential, and U is the on-site Coulomb interaction.

This action of f electrons can be divided into two parts, i.e., a local impurity part S_{imp} and a non-local part

$$S = S_{imp} + \sum_{\mathbf{k},\omega,\sigma} (\epsilon(\mathbf{k}) - \Delta_\omega) f^\dagger_{\mathbf{k},\omega,\sigma} f_{\mathbf{k},\omega,\sigma} \tag{5.2}$$

where $S_{imp} = \sum_{i,\omega,\sigma} (\Delta - \mu - i\omega) f^\dagger_{i,\omega,\sigma} f_{i,\omega,\sigma} + U \sum_i \int_0^\beta n_{i,\uparrow}(\tau) n_{i,\downarrow}(\tau) d\tau$. The impurity part describes the action of local electrons hybridized with a conduction bath and it can be solved exactly using an impurity solver. The non-local part can be treated perturbatively by introducing auxiliary fermionic degrees of freedom and this is the main idea of the DF approach.

In order to introduce the auxiliary fermions, we pay attention to the formula for the partition function given as the Feynman integral of the action, i.e, $Z = \int D[f^\dagger f] e^{-S[f^\dagger, f]}$

$$Z[f^\dagger, f] = \int D[f^\dagger f] e^{-\sum_{\mathbf{k},\omega} S_{imp}[f^\dagger, f] - \sum_{\mathbf{k},\omega} (\epsilon(\mathbf{k}) - \Delta_\omega) f^\dagger_{\mathbf{k},\omega} f_{\mathbf{k},\omega}} \tag{5.3}$$

From now on, the spin indices are omitted for convenience. By performing the Hubbard-Stratonovich transformation to the non-local part of the partition function, dual fermions are introduced in an exact way

$$\begin{aligned} e^{-\sum_{\mathbf{k},\omega} (\epsilon(\mathbf{k}) - \Delta_\omega) f^\dagger_{\mathbf{k},\omega} f_{\mathbf{k},\omega}} &\equiv - \left(\prod_{\mathbf{k},\omega} \frac{\epsilon(\mathbf{k}) - \Delta_\omega}{\alpha^2_\omega} \right) \cdot \int D[d^\dagger d] e^{-\sum_{\mathbf{k},\omega} \alpha_\omega (f^\dagger_{\mathbf{k},\omega} d_{\mathbf{k},\omega} + d^\dagger_{\mathbf{k},\omega} f_{\mathbf{k},\omega})} \\ &\quad \cdot e^{\sum_{\mathbf{k},\omega} \frac{\alpha^2_\omega}{\epsilon(\mathbf{k}) - \Delta_\omega} d^\dagger_{\mathbf{k},\omega} d_{\mathbf{k},\omega}} \\ &= - \left(\prod_{\mathbf{k},\omega} \frac{\epsilon(\mathbf{k}) - \Delta_\omega}{\alpha^2_\omega} \right) \cdot \int D[d^\dagger d] e^{-\sum_{i,\omega} \alpha_\omega (f^\dagger_{i,\omega} d_{i,\omega} + d^\dagger_{i,\omega} f_{i,\omega})} \\ &\quad \cdot e^{\sum_{\mathbf{k},\omega} \frac{\alpha^2_\omega}{\epsilon(\mathbf{k}) - \Delta_\omega} d^\dagger_{\mathbf{k},\omega} d_{\mathbf{k},\omega}} \end{aligned} \tag{5.4}$$

where d is the DF operator. Here, α is an arbitrary function and we assume it is a local quantity which depends only on frequency. Since α is local, the relation $\sum_{\mathbf{k},\omega} \alpha (f^\dagger_{\mathbf{k},\omega} d_{\mathbf{k},\omega} + d^\dagger_{\mathbf{k},\omega} f_{\mathbf{k},\omega}) =$

$\sum_{i,\omega}\alpha(f^{\dagger}_{i,\omega}d_{i,\omega}+d^{\dagger}_{i,\omega}f_{i,\omega})$ is satisfied and original fermions and dual fermions couple only locally, i.e., only a fermion f_i and a dual fermion d_i on the same lattice site. In this way, the non-locality is retained only in the quadratic dual fermion part of the action while original fermions have only local degrees of freedom.

Now the coupling term between original fermions and dual fermions in the partition function is expanded by the Taylor expansion and original fermions can be integrated out exactly at each site by the impurity action since they are given by local degrees of freedom.

$$\begin{aligned}
\langle e^{-\sum_{\omega}\alpha_{\omega}(f^{\dagger}_{\omega}d_{\omega}+d^{\dagger}_{\omega}f_{\omega})}\rangle &= 1+\sum_{\omega_1\omega_2}\alpha_{\omega_1}\alpha_{\omega_2}\langle f_{\omega_1}f^{\dagger}_{\omega_2}\rangle d^{\dagger}_{\omega_1}d_{\omega_2}\delta_{\omega_1-\omega_2,0}+ \\
&\quad \frac{1}{4}\sum_{\omega_1\omega_2\omega_3\omega_4}\alpha_{\omega_1}\alpha_{\omega_2}\alpha_{\omega_3}\alpha_{\omega_4}\langle f_{\omega_1}f_{\omega_2}f^{\dagger}_{\omega_3}f^{\dagger}_{\omega_4}\rangle d^{\dagger}_{\omega_1}d^{\dagger}_{\omega_2}d_{\omega_3}d_{\omega_4}\delta_{\omega_1+\omega_2-\omega_3-\omega_4,0} \\
&\quad +\cdots \\
&= \exp[\sum_{\omega}\alpha_{\omega}\alpha_{\omega}d^{\dagger}_{\omega}d_{\omega}\langle f_{\omega}f^{\dagger}_{\omega}\rangle+ \\
&\quad \frac{1}{4}\sum_{\nu,\nu',\omega}\alpha_{\nu}\alpha_{\nu'+\omega}\alpha_{\nu'}\alpha_{\nu+\omega}d^{\dagger}_{\nu}d^{\dagger}_{\nu'+\omega}d_{\nu'}d_{\nu+\omega}(\langle f_{\nu}f_{\nu'+\omega}f^{\dagger}_{\nu'}f^{\dagger}_{\nu+\omega}\rangle- \\
&\quad \delta_{\omega,0}\langle f_{\nu}f^{\dagger}_{\nu+\omega}\rangle\langle f_{\nu'+\omega}f^{\dagger}_{\nu'}\rangle+\delta_{\nu,\nu'}\langle f_{\nu}f^{\dagger}_{\nu'}\rangle\langle f_{\nu'+\omega}f^{\dagger}_{\nu+\omega}\rangle)+\cdots] \qquad (5.5)
\end{aligned}$$

Here, $\langle\rangle=\langle\rangle_{imp}$. As a result, the connected one- and two-particle Green's functions are coupled to DF operators $d^{\dagger}d$, $(d^{\dagger}d^{\dagger}dd)$, and so on. The linked cluster theorem assures that only connected diagrams of original fermions contribute to the exponential in Eq.5.5. The Kronecker delta δ in the above equation is derived from the time translational invariance of f operators.

After introducing the DF operators, the partition function given in Eq.5.3 depends on both f and d operators. However as shown above, these f electron degrees of freedom can be integrated out separately. Up to now, the derivation is valid for arbitrary α_{ω}. By choosing α_{ω} as the inverse of the impurity Greens function g^{-1}_{imp}, the partition function of DF becomes

$$\begin{aligned}
Z[d^{\dagger},d] &= -\left(\prod_{\mathbf{k},\omega}\frac{\epsilon(\mathbf{k})-\Delta_{\omega}}{g^{-2}_{imp,\omega}}\right)\cdot\left(\prod_{i}Z^{i}_{imp}\right)\cdot\int D[d^{\dagger}d]e^{-\sum_{\mathbf{k},\omega}[-\frac{g^{-2}_{imp}}{\epsilon(\mathbf{k})-\Delta_{\omega}}+g^{-1}_{imp}]d^{\dagger}_{\mathbf{k},\omega}d_{\mathbf{k},\omega}} \\
&\quad \cdot e^{\frac{1}{4}\sum_{i,\nu,\nu',\omega}\gamma^{(4)}\cdot d^{\dagger}_{i,\nu}d^{\dagger}_{i,\nu'+\omega}d_{i,\nu'}d_{i,\nu+\omega}+\cdots} \qquad (5.6)
\end{aligned}$$

where Z^{i}_{imp} is the impurity partition function ($\int D[f^{\dagger}f]e^{-S^{i}_{imp}[f^{\dagger}f]}$), g_{imp} is the impurity Greens function ($-\left\langle f_i f^{\dagger}_i\right\rangle_{imp}$), and $\gamma^{(4)}_{imp}$ is the connected two-particle vertex function of the impurity.

$\gamma^{(4)}_{imp}$ is obtained by removing the external propagators (g_{imp}) from the connected two-particle Green's function (χ) as

$$\gamma^{(4)}_{imp}(i\nu, i\nu')_{i\omega} = g^{-1}_{i\nu} \cdot g^{-1}_{i\nu+i\omega} \cdot \chi(i\nu, i\nu')_{i\omega} \cdot g^{-1}_{i\nu'} \cdot g^{-1}_{i\nu'+i\omega} \tag{5.7}$$

In a similar way, the n-particle interaction among dual fermions is given by the n-particle impurity vertex functions.

Since we derived the partition function for dual fermions, the DF quantities such as the Green's function and the self energy can be computed from this partition function. The bare Green's function of DF is computed as the inverse of the coefficient of Gaussian term in Eq. 5.6

$$G^{(0)}_{dual} = (\frac{g^{-2}_{imp}}{\epsilon(\mathbf{k}) - \Delta_\omega} - g^{-1}_{imp})^{-1} = g_{\mathbf{k}} - g_{imp} \tag{5.8}$$

where $g_{\mathbf{k}} = 1/(g^{-1}_{imp} - \epsilon(\mathbf{k}) + \Delta_\omega)$, i.e., the non-local Green's function with local DMFT self energy. This equation shows that the bare propagator of DF is the same as the purely non-local part of the DMFT Green's function.

One way to solve the DF problem is to use the conventional diagrammatic approach. We need to solve an interacting problem with a DF propagator G_{dual} and the retarded type of interaction $\gamma^{(4)}$, $\gamma^{(6)}$, and so on. Here, we consider only the $\gamma^{(4)}$ interaction. And the lowest order self-energy diagram

$$\Sigma^{(0)}_{dual}(i\nu) = T \cdot \sum_{i\nu'} \gamma^{(4)}_{imp}(i\nu, i\nu')_{i\omega=0} \cdot G^{loc}_{dual}(i\nu') \tag{5.9}$$

and the second lowest order diagram

$$\begin{aligned}\Sigma^{(1)}_{dual}(\mathbf{k}, i\nu) = & \frac{T^2}{2 \cdot N_k N_q} \cdot \sum_{\mathbf{k}',\mathbf{q}} \sum_{i\nu', i\omega} \gamma^{(4)}_{imp}(i\nu, i\nu')_{i\omega} \cdot \gamma^{(4)}_{imp}(i\nu', i\nu)_{i\omega} \cdot \\ & G_{dual}(\mathbf{k}', i\nu') \cdot G_{dual}(\mathbf{k}' + \mathbf{q}, i\nu' + i\omega) \cdot G_{dual}(\mathbf{k} + \mathbf{q}, i\nu + i\omega)\end{aligned} \tag{5.10}$$

are considered for the non-local correlation effect. As Ref. [82, 83] shows, these low order diagrams already capture a certain aspect of non-local physics in the Hubbard model. The smallness of the higher order diagram is justified in the weak coupling limit and the strong coupling limit. In the weak coupling limit, the leading contribution to the full vertex function

($\gamma^{(4)}$, $\gamma^{(6)}$, ...) is the bare interaction U since the perturbation around U works in this limit, i.e., $\gamma^{(4)} \propto U$, $\gamma^{(6)} \propto U^2$, and so on. In the strong coupling limit, $G_{dual} \propto g_{imp}^2 \cdot (\epsilon(\mathbf{k}) - \Delta_\omega)$, and $(\epsilon(\mathbf{k}) - \Delta_\omega)$ is extremely small in the atomic limit. Therefore, the lowest order DF diagram can capture non-local physics well in the region where the perturbation from the DMFT result is small. In the region where the non-local corrlation effect is strong, higher order diagrams such as the ladder type will need to be considered.

$\Sigma_{dual}^{(0)}$ is a local quantity since only the local part of G_{dual} contribute to the self energy in Eq. 5.9. As discussed in the literature [82, 83], the self-consistent condition for the DF method is such that $G_{dual}^{loc} = 0$ and as a result Σ_{dual} is always zero when only $\Sigma_{dual}^{(0)}$ term is considered as the DF self energy. In this case, the DMFT self-consistency is recovered by the following equation

$$\frac{1}{N_k} \sum_{\mathbf{k}} G_{dual}^{(0)}(\mathbf{k}, i\omega) = 0 \quad \Rightarrow \quad \frac{1}{N_k} \sum_{\mathbf{k}} g_{\mathbf{k}} = g_{imp} \tag{5.11}$$

The non-local correlations beyond DMFT are treated by the non-local self energy $\Sigma_{dual}^{(1)}(\mathbf{k}, i\nu)$ term given in Eq. 5.10. The overall self-consistent procedure of computing the DF Green's function and the DF self energy will be explained later.

5.1.2 The relation between original fermions and dual fermions

The original fermion Green's function is related to the DF Green's function in an exact way by the one-to-one correspondence between the original fermion and the dual fermion. This relation can be derived by taking the derivative of both the DF partition function in Eq. 5.6 and the original partition function in Eq. 5.3 with respect to $\epsilon_{\mathbf{k}}$

$$\frac{\partial}{\partial \epsilon_{\mathbf{k}}} \ln Z = -\left\langle f_{\mathbf{k},\omega} f_{\mathbf{k},\omega}^\dagger \right\rangle = -\frac{1}{\epsilon(\mathbf{k}) - \Delta_\omega} - \frac{g_{imp}^{-2}}{(\epsilon(\mathbf{k}) - \Delta_\omega)^2} \left\langle d_{\mathbf{k},\omega} d_{\mathbf{k},\omega}^\dagger \right\rangle \tag{5.12}$$

$$G_{\mathbf{k},i\omega} = -\frac{1}{\epsilon(\mathbf{k}) - \Delta_\omega} + \frac{g_{imp}^{-2}}{(\epsilon(\mathbf{k}) - \Delta_\omega)^2} G_{\mathbf{k},i\omega}^{dual} \tag{5.13}$$

The self-energy of the original fermion also can be related to the DF self-energy using the

relation in Eq. 5.13

$$\Sigma_{\mathbf{k},i\omega} = i\omega + \mu - \epsilon_{\mathbf{k}} - G^{-1}_{\mathbf{k},i\omega} = \Sigma_{imp} + \frac{\Sigma_{dual,\mathbf{k}}}{1 + g_{imp} \cdot \Sigma_{dual,\mathbf{k}}} \tag{5.14}$$

The non-local self-energy becomes separable into the local part which is the impurity self-energy, as in DMFT, and the non-local part which is a function of the DF self-energy and the impurity Green's function.

The connected two-particle Green's function χ of the original fermion can be obtained in a similar way as the one-particle Green's function. In this case, one needs to take the derivative of the partition function with respect to $\epsilon_{\mathbf{k}}$ twice

$$\chi_{\alpha\beta\gamma\delta} = \overline{\chi}_{\alpha\beta\gamma\delta} - G_{\alpha\delta}G_{\beta\gamma} + G_{\alpha\gamma}G_{\beta\delta} \tag{5.15}$$

$$\overline{\chi}_{\alpha\beta\gamma\delta} = \left\langle f^{\dagger}_{\alpha} f^{\dagger}_{\beta} f_{\gamma} f_{\delta} \right\rangle = \frac{1}{Z}\frac{\partial}{\partial \epsilon_{\alpha\delta}}\left(\frac{\partial}{\partial \epsilon_{\beta\gamma}} Z\right) = \frac{1}{Z}\frac{\partial}{\partial \epsilon_{\alpha\delta}}\left(-Z G_{\beta\gamma}\right) \tag{5.16}$$

where $\alpha - \delta$ represents the $\mathbf{k}$ and $i\omega$ indices. Using Eq. 5.13, χ of the original fermions can be related to the connected DF two-particle Green's function χ^{dual} by

$$\begin{aligned}\chi_{\alpha\beta\gamma\delta} = {} & \left(\overline{\chi}^{dual}_{\alpha\beta\gamma\delta} - G^{dual}_{\alpha\delta}G^{dual}_{\beta\gamma} + G^{dual}_{\alpha\gamma}G^{dual}_{\beta\delta}\right) \\ & \cdot\left(\frac{g^{-1}_{imp}}{\epsilon(\mathbf{k}) - \Delta_{\omega}}\right)_{\alpha} \cdot \left(\frac{g^{-1}_{imp}}{\epsilon(\mathbf{k}) - \Delta_{\omega}}\right)_{\beta} \cdot \left(\frac{g^{-1}_{imp}}{\epsilon(\mathbf{k}) - \Delta_{\omega}}\right)_{\gamma} \cdot \left(\frac{g^{-1}_{imp}}{\epsilon(\mathbf{k}) - \Delta_{\omega}}\right)_{\delta}\end{aligned} \tag{5.17}$$

One can note that χ of the original fermions is obtained by multiplying additional factors at each external leg. The details of the derivation is given in Ref. [86].

The two-particle vertex function is obtained by removing the four external propagators from χ.

$$\Gamma_{\alpha\beta\gamma\delta} = G^{-1}_{\alpha} \cdot G^{-1}_{\beta} \cdot \chi_{\alpha\beta\gamma\delta} \cdot G^{-1}_{\gamma} \cdot G^{-1}_{\delta} = F_{\alpha} \cdot F_{\beta} \cdot \Gamma^{dual}_{\alpha\beta\gamma\delta} \cdot F_{\gamma} \cdot F_{\delta} \tag{5.18}$$

where $F_{\alpha} = G^{-1}_{\alpha} \cdot \left(\frac{g^{-1}_{imp}}{\epsilon(\mathbf{k}) - \Delta_{\omega}}\right)_{\alpha} \cdot G^{dual}_{\alpha} = \left(\frac{1}{1 + g_{imp} \cdot \Sigma_{dual}}\right)_{\alpha}$. This non-local vertex function of original fermions will be used to compute the pairing susceptibility as will be shown later.

5.1.3 The self-consistent calculation scheme

The DF self energy can be constructed as a functional derivative of a Baym-Kadanoff functional, i.e., $\Sigma_{dual} = \frac{\delta \Phi_{dual}}{\delta G_{dual}}$ where Φ_{dual} is the Baym-Kadanoff functional. In this case, the DF method

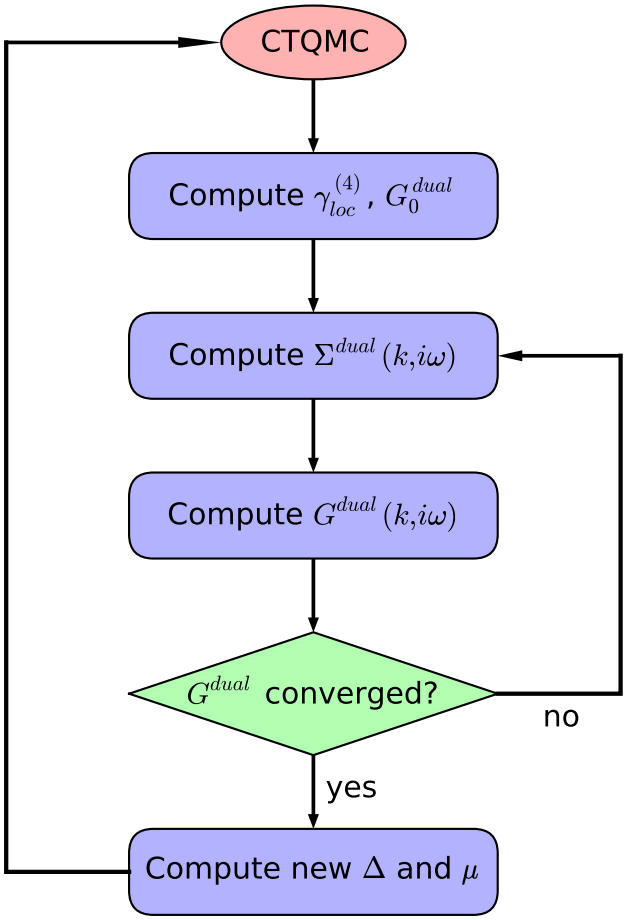

Figure 5.1: The calculation procedure of the DF method

is a conserving approximation. In other words, the DF self energy is constructed using impurity vertex functions and dressed DF Green's functions. And then the DF Green's function is dressed again by the resulting non-local self energy in a self-consistent way. The conserving approximation of the DF approach ensures the basic conservation laws and sum-rules for the corresponding original fermions.

The dressed DF Green's function depends on the hybridization Δ of the impurity. And this Δ is determined from another self-consistent condition such that the local part of dual fermion Greens function G^{loc}_{dual} vanishes ensuring that the lowest order diagram also vanishes. This self-consistent condition for Δ completes the double self-consistent loop as illustrated in Fig. 5.1. Now we explain in details how the self-consistent calculation is implemented.

1. The CTQMC impurity solver samples the impurity two-particle Green's function $\chi_{imp}(i\nu, i\nu')_{i\omega}$ and (one-particle) Green's function $G_{imp}(i\nu)$. The full impurity vertex function is computed by Eq. 5.7. The bare propagator for DF is also given by Eq. 5.8.

2. The self energy of DF is computed for the lowest order and the second order diagram using Eq. 5.9 and Eq. 5.10. This non-local DF self energy captures the non-local correlation beyond DMFT.

3. The bare DF Green's function is dressed by the computed DF self energy employing the Dyson equation.

$$G_{dual}(\mathbf{k}, i\omega) \quad = \quad [G^{(0)}_{dual}(\mathbf{k}, i\omega) - \Sigma_{dual}(\mathbf{k}, i\omega)]^{-1} \tag{5.19}$$

4. The computed DF Green's function is used again for computing the self energy going back to the step 2. This DF loop is continued until the DF Green's function and the DF self energy are converged.

5. Once the DF quantities are converged, the new hybridization Δ is computed to satisfy the condition that the local part of DF Green's function is zero.

$$\Delta_{new} \quad = \quad \Delta_{old} + g^{-2}_{imp} \cdot G_{dual,loc} \tag{5.20}$$

In the case of the fixed density n calculation, the chemical potential μ is updated such that the density of original fermion, which is computed from the resulting non-local Green's function, is the same as the desired n. The Green's function of original fermion is related to the DF Green's function with an exact relation as explained in the previous subsection.

$$\frac{T}{N_k}\sum_{\mathbf{k},i\omega} G(\mathbf{k},i\omega)e^{i\omega 0^-} \quad = \quad n \tag{5.21}$$

Using these new Δ and μ, the new impurity vertex function is computed by going to the step 1. This big self-consistent loop is continued until the convergence is reached.

5.1.4 The comparison of the DF approach and the irreducible cumulant approach

Various extensions of the single site DMFT to include long range correlations have been proposed in the literatures. For example, Ref. [84] discusses the possibility of including the non-local correlations using the expansion around the irreducible cumulants. In this subsection, we show for the first time that this cumulant approach is equivalent to the DF approach.

The main idea of the cumulant expansion is to express the interacting lattice problem in terms of the irreducible cumulant M and the dressed (renormalized) hopping ε instead of the self energy Σ and the Green's function G. This cumulant expansion is derived in a straightforward way in Ref. [84]. Here, we refer to the alternative derivation explained in the Appendix of Ref. [84]. This alternative derivation introduces the auxiliary fermionic fields ξ. In this way, M can be interpreted as the generalized self energy and ε can be the Green's function of the auxiliary fields.

First, the general lattice Hamiltonian is divided into the local part and the non-local part.

$$\hat{H} \quad = \quad \sum_{i,j} E_{ij}\cdot f_i^\dagger f_j + U\sum_i n_{i,\uparrow}n_{i,\downarrow} \tag{5.22}$$

where E_{ij} represents the non-local term. Using the Hubbard-Stratonovich transformation,

$$e^{-\sum_{i,j,\omega} E_{ij} f_{i,\omega}^\dagger f_{j,\omega}} \equiv -\prod_{i,j} E_{ij}\cdot \int D[\xi^\dagger\xi] e^{-\sum_{i,\omega}(f_{i,\omega}^\dagger \xi_{i,\omega}+\xi_{i,\omega}^\dagger f_{i,\omega})+\sum_{i,j,\omega} E_{ij}^{-1}\xi_{i,\omega}^\dagger \xi_{j,\omega}} \tag{5.23}$$

the partition function can be expressed in terms of auxiliary fields $\xi^\dagger$, ξ

$$\begin{aligned} Z &= \int D[f^\dagger f] e^{-S_{loc}[f^\dagger, f] - \sum_{i,j,\omega} E_{ij} f^\dagger_{i,\omega} f_{j,\omega}} \\ &= -\prod_{i,j} E_{ij} \cdot \prod_i Z_{loc} \cdot \int D[\xi^\dagger \xi] e^{\sum_{i,j,\omega} E^{-1}_{ij} \xi^\dagger_{i,\omega} \xi_{j,\omega} - \sum_{i,\omega} S_{int}[\xi^\dagger_{i,\omega}, \xi_{i,\omega}]} \end{aligned} \tag{5.24}$$

One can note that this Hubbard-Stratonovich transform is similar as the transform used in the DF approach except that α is set to one in this case.

The interaction term for auxiliary fields is given by

$$\begin{aligned} \sum_{i,\omega} S_{int}[\xi^\dagger_{i,\omega}, \xi_{i,\omega}] &= -\ln \left\langle e^{-\sum_{i,\omega} (f^\dagger_{i,\omega} \xi_{i\omega} + \xi^\dagger_{i,\omega} f_{i,\omega})} \right\rangle_{loc} \\ &= \sum_i \sum_{n=0}^{\infty} \frac{1}{(2n)!} \sum_{\omega_1 \cdots \omega_{2n}} C_i^{(2n)}(\omega_1, \cdots, \omega_{2n}) \xi^\dagger_{i,\omega_1} \cdots \xi^\dagger_{i,\omega_n} \xi_{i,\omega_{n+1}} \cdots \xi_{i,\omega_{2n}} \end{aligned} \tag{5.25}$$

where $C_i^{(2n)}(\omega_1, \cdots, \omega_{2n})$ is the n-particle bare cumulant representing the n-particle interaction for auxiliary fields, $\xi^\dagger$ and ξ. One can see that these bare cumulants are local and connected diagrams assured by the linked-cluster theorem. If the local part of the Hamiltonian is chosen to be the atomic Hamiltonian, the one-particle bare cumulant is just the atomic Green's function, two-particle cumulant is the atomic two-particle Green's function, and so on.

The bare propagator of $\xi^\dagger$ and ξ fields, or equivalently the bare hopping term $E_{\mathbf{k}}$ is obtained from the inverse of the coefficient in the Gaussian term of Eq. 5.24. The non-local fluctuation is treated by computing the one-particle irreducible cumulant $M_{\mathbf{k}}$. The conventional diagram calculation can be employed to construct it using $C_i^{(2n)}$ and ε since the auxiliary fields obey the standard Wick's theorem.

Here, we apply this cumulant approach to treat the non-local correlations specifically around the DMFT solution. In this case, the local part of the Hamiltonian becomes the impurity one, i.e., $\sum_i \Delta_i \cdot f_i^\dagger f_i + U \sum_i n_{i,\uparrow} n_{i,\downarrow}$ where Δ is the hybridization with the conduction bath. As a result, the bare hopping term is given by $E_{\mathbf{k}} - \Delta$ and the bare cumulants in Eq. 5.25 is given by the impurity n-particle Green's function, i.e.,

$$C_i^{(2)} = -\left\langle c_i c_i^\dagger \right\rangle_{imp} = \frac{1}{Z_{imp}} \int D[c_i^\dagger c_i] e^{-S_{imp}} c_i^\dagger c_i = g_{imp} \tag{5.26}$$

$$C_i^{(4)} = \left\langle c_{i,1}^\dagger c_{i,2}^\dagger c_{i,3} c_{i,4} \right\rangle_{imp} - \left\langle c_{i,1}^\dagger c_{i,4} \right\rangle_{imp} \left\langle c_{i,2}^\dagger c_{i,3} \right\rangle_{imp} + \left\langle c_{i,1}^\dagger c_{i,3} \right\rangle_{imp} \left\langle c_{i,2}^\dagger c_{i,4} \right\rangle_{imp} = \chi_{imp} \tag{5.27}$$

The renormalized hopping $\varepsilon_{\mathbf{k}}$ term is given by dressing the bare propagator with the cumulant $M_{\mathbf{k}}$. Within the expansion around DMFT,

$$\varepsilon_{\mathbf{k}} = [(E_{\mathbf{k}} - \Delta)^{-1} - M_{\mathbf{k}}]^{-1} \tag{5.28}$$

If only the lowest order cumulant $M_{\mathbf{k}}^{(0)} = g_{imp}$ is considered,

$$\begin{aligned} \varepsilon_{\mathbf{k}} &= \frac{1}{(E_{\mathbf{k}} - \Delta)^{-1} - M_{\mathbf{k}}^{(0)}} = -g_{imp}^{-1} - g_{imp}^{-2} \cdot (E_{\mathbf{k}} - \Delta)^{-1} - g_{imp}^{-3} \cdot (E_{\mathbf{k}} - \Delta)^{-2} - \cdots \\ &= -g_{imp}^{-2} \cdot [(E_{\mathbf{k}} - \Delta) - g_{imp}^{-1}]^{-1} - g_{imp}^{-1} = g_{imp}^{-2} [\frac{1}{i\nu + \mu - E_{\mathbf{k}} - \Sigma_{imp}} - g_{imp}] \end{aligned} \tag{5.29}$$

One should note that $\varepsilon_{\mathbf{k}}$ is related to the bare DF propagator defined in Eq. 5.8, i.e., $\varepsilon_{\mathbf{k}} = g_{imp}^{-2} \cdot G_{dual,\mathbf{k}}^{(0)}$. Namely, the renormalized hopping $\varepsilon_{\mathbf{k}}$ is obtained from the DF Green's function by multiplying g_{imp}^{-1} at the external legs. One can readily see that the DMFT self-consistent condition is achieved by the condition $\varepsilon_{\mathbf{k}} = 0$ when only $M_{\mathbf{k}}^{(0)}$ is considered.

In a similar way, the irreducible cumulant $M_{\mathbf{k}}$ can be related to the DF self energy by multiplying g_{imp} at each external leg. Let us consider the next order irreducible cumulant $M_{\mathbf{k}}^{(1)}$. This cumulant is constructed by using the bare cumulant $C^{(4)} = \chi_{imp}$ and the renormalized $\varepsilon_{\mathbf{k}}$.

$$\begin{aligned} M^{(1)}(\mathbf{k}, i\nu) &= \frac{T^2}{2 \cdot N_k N_q} \cdot \sum_{\mathbf{k}',\mathbf{q}} \sum_{i\nu',i\omega} \chi_{imp}(i\nu, i\nu')_{i\omega} \cdot \chi_{imp}(i\nu', i\nu)_{i\omega} \\ &\quad \cdot \varepsilon(\mathbf{k} + \mathbf{q}, i\nu + i\omega) \cdot \varepsilon(\mathbf{k}' + \mathbf{q}, i\nu' + i\omega) \cdot \varepsilon(\mathbf{k}', i\nu') \end{aligned} \tag{5.30}$$

Here, $\chi_{imp} = g_{imp} \cdot g_{imp} \cdot \gamma_{imp}^{(4)} \cdot g_{imp} \cdot g_{imp}$ where $\gamma_{imp}^{(4)}$ is the two-particle impurity vertex function, and $\varepsilon_{\mathbf{k}} = g_{imp}^{-2} \cdot G_{dual,\mathbf{k}}^{(0)}$. As a result, $M_{\mathbf{k}}^{(1)}$ is related to Σ_{dual} by

$$\begin{aligned} M^{(1)}(\mathbf{k}, i\nu) &= \frac{T^2}{2 \cdot N_k N_q} \cdot \sum_{\mathbf{k}',\mathbf{q}} \sum_{i\nu',i\omega} g_{imp}^2(i\nu) \cdot \gamma_{imp}^{(4)}(i\nu, i\nu')_{i\omega} \cdot \gamma_{imp}^{(4)}(i\nu', i\nu)_{i\omega} \\ &\quad \cdot G_{dual}^{(0)}(\mathbf{k} + \mathbf{q}, i\nu + i\omega) \cdot G_{dual}^{(0)}(\mathbf{k}' + \mathbf{q}, i\nu' + i\omega) \cdot G_{dual}^{(0)}(\mathbf{k}', i\nu') \\ &= g_{imp}^2(i\nu) \cdot \Sigma_{dual}^{(1)}(\mathbf{k}, i\nu) \end{aligned} \tag{5.31}$$

Now, the relation given in Eq. 5.29 can be generalized to the case at which the general $M_{\mathbf{k}}$ is considered.

$$\begin{aligned}\varepsilon_{\mathbf{k}} &= [E_{\mathbf{k}}^{-1} - M_{imp}^{(0)} - M_{\mathbf{k}}^{(1)}]^{-1} = [g_{imp}^2 \cdot (G_{dual,\mathbf{k}}^{(0)})^{-1} - g_{imp}^2 \cdot \Sigma_{dual,\mathbf{k}}^{(1)}]^{-1} \\ &= g_{imp}^{-2} \cdot [(G_{dual,\mathbf{k}}^{(0)})^{-1} - \Sigma_{dual,\mathbf{k}}^{(1)}]^{-1} = g_{imp}^{-2} \cdot G_{dual,\mathbf{k}} \end{aligned} \tag{5.32}$$

As a result, $\varepsilon_{\mathbf{k}}$ is always equivalent to $g_{imp}^{-2} \cdot G_{dual,\mathbf{k}}$.

The lattice Green's function $G_{\mathbf{k}}$ can be related to quantities within the cumulant approach. $G_{\mathbf{k}}$ can be interpreted as the irreducible cumulant ($M_{\mathbf{k}}$) dressed by the bare hopping ($E_{\mathbf{k}} - \Delta$)

$$G_{\mathbf{k}} = [M_{\mathbf{k}}^{-1} - (E_{\mathbf{k}} - \Delta)]^{-1} = -(E_{\mathbf{k}} - \Delta)^{-1} + (E_{\mathbf{k}} - \Delta)^{-1} \cdot \varepsilon_{\mathbf{k}} \cdot (E_{\mathbf{k}} - \Delta)^{-1} \tag{5.33}$$

This result can be also obtained by taking the derivative of the S_{int} term in Eq. 5.24 with respect to ξ and $\xi^\dagger$ as discussed in Ref. [84] Using Eq. 5.32, this expression becomes equivalent to formula given in the DF approach.

$$G_{\mathbf{k}} = \frac{1}{\Delta - E_{\mathbf{k}}} + \frac{g_{imp}^{-1}}{\Delta - E_{\mathbf{k}}} \cdot G_{dual} \cdot \frac{g_{imp}^{-1}}{\Delta - E_{\mathbf{k}}} \tag{5.34}$$

Within the cumulant approach, the non-local self-energy $\Sigma_{\mathbf{k}}$ is given by

$$\begin{aligned}\Sigma_{\mathbf{k}} &= \Sigma_{imp} + \Sigma_{nloc} = \Sigma_{imp} + (M_{imp}^{(0)})^{-1} - (M_{imp}^{(0)} + M_{\mathbf{k}}^{(1)})^{-1} \\ &= \Sigma_{imp} + g_{imp}^{-1} - [g_{imp} + g_{imp}^2 \cdot \Sigma_{dual,\mathbf{k}}^{(1)}]^{-1} \\ &= \Sigma_{imp} + \frac{\Sigma_{dual,\mathbf{k}}^{(1)}}{1 + g_{imp} \cdot \Sigma_{dual,\mathbf{k}}^{(1)}} \end{aligned} \tag{5.35}$$

This self energy is also equivalent to $\Sigma_{\mathbf{k}}$ computed within the DF method given in Eq. 5.14.

The cumulant quantities that we discussed and the corresponding DF quantities are summarized in Table. 5.1.

5.1.5 The pairing susceptibility within the DF method

In this subsection, we discuss how to compute the pairing susceptibility and as a result T_c and the SC gap symmetry within the DF method. As discussed in the previous chapter, the non-local pairing vertex function is computed from the reducible vertex function in the particle-hole

	Cumulant	Dual Fermion
The propagator	$\varepsilon_{\mathbf{k}}(= g_{imp}^{-2} \cdot G_{dual,\mathbf{k}})$	$G_{dual,\mathbf{k}}$
Two-particle interaction	$\chi_{imp}(= g_{imp}g_{imp}\gamma^{(4)}g_{imp}g_{imp})$	$\gamma^{(4)}$
Non-local self energy	$M_{\mathbf{k}}^{(1)}(= g_{imp}^2 \cdot \Sigma_{dual,\mathbf{k}}^{(1)})$	$\Sigma_{dual,\mathbf{k}}^{(1)}$
The lattice $G_{\mathbf{k}}$	$-\frac{1}{\Delta - E_{\mathbf{k}}} + \frac{1}{\Delta - E_{\mathbf{k}}} \cdot \varepsilon_{\mathbf{k}} \cdot \frac{1}{\Delta - E_{\mathbf{k}}}$	$-\frac{1}{\Delta - \epsilon_{\mathbf{k}}} + \frac{g_{imp}^{-1}}{\Delta - \epsilon_{\mathbf{k}}} \cdot G_{dual,\mathbf{k}} \cdot \frac{g_{imp}^{-1}}{\Delta - \epsilon_{\mathbf{k}}}$
The lattice $\Sigma_{\mathbf{k}}$	$\Sigma_{imp} + \frac{1}{M_{imp}^{(0)}} - \frac{1}{M_{imp}^{(0)} + M_{\mathbf{k}}^{(1)}}$	$\Sigma_{imp} + \frac{\Sigma_{dual,\mathbf{k}}^{(1)}}{1 + g_{imp} \cdot \Sigma_{dual,\mathbf{k}}^{(1)}}$

Table 5.1: The comparison of quantities within the cumulant approach and the corresponding DF quantities.

channel $\widetilde{\Gamma}_{\mathbf{q}}^{p-h}$. Within DMFT, this non-local $\widetilde{\Gamma}_{\mathbf{q}}^{p-h}$ is obtained by approximating the irreducible vertex $\Gamma^{irr,p-h}$ by a local quantity.

Within the DF method, the vertex function of the original fermion is obtained from the corresponding DF vertex function using the relation given by Eq. 5.18. As already shown in Ref. [86, 87], the non-local DF vertex function can be computed using the the Bethe-Salpeter equation by dressing the DF irreducible vertex $\Gamma_{dual}^{irr,p-h,(m/d)}$ by the DF polarization bubble $\chi_{dual,\mathbf{q},i\omega}^{0,p-h}$

$$\begin{aligned} \Gamma_{dual}^{p-h,(m/d)}(i\nu, i\nu')_{\mathbf{q}i\omega} &= [(\Gamma_{dual}^{irr,p-h,(m/d)})_{i\omega}^{-1} - \chi_{dual,\mathbf{q},i\omega}^{0,p-h}]^{-1} \\ &= [(\gamma^{(4),(m/d)})_{i\omega}^{-1} - \chi_{dual,\mathbf{q},i\omega}^{0,p-h}]^{-1} \end{aligned} \tag{5.36}$$

Here, $\Gamma_{dual}^{irr,p-h,(m/d)}$ considers only the bare two-particle vertex $\gamma^{(4),(m/d)}$ as discussed in Ref. [86, 87]. We concentrate on the particle-hole channel and we decompose the particle-hole channel into the magnetic (m) and the charge (d) channels. $\chi_{dual,\mathbf{q},i\omega}^{0,p-h}$ is computed from the DF Green's function G_{dual} by

$$\chi_{p-h}^{0,dual}(i\nu)_{\mathbf{q},i\omega} = -\frac{T}{N_k} \sum_{\mathbf{k}} G_{dual}(\mathbf{k}, i\nu) \cdot G_{dual}(\mathbf{k}+\mathbf{q}, i\nu + i\omega) \tag{5.37}$$

Finally, the non-local $\Gamma^{p-h,(m/d)}$ of the original fermion is obtained using Eq. 5.18

$$\Gamma^{p-h,(m/d)}(\mathbf{k}, i\nu, \mathbf{k}', i\nu')_{\mathbf{q},i\omega} = F_k \cdot F_{k+q} \cdot \Gamma_{dual}^{p-h,(m/d)}(i\nu, i\nu')_{\mathbf{q},i\omega} \cdot F_{k'} \cdot F_{k'+q} \tag{5.38}$$

where $F_k = (\frac{1}{1 + g_{imp}(i\nu) \cdot \Sigma_{dual}(\mathbf{k}, i\nu)})$ and $k = (\mathbf{k}, i\nu)$.

$\Gamma^{p-h,(m/d)}$ constructed within the DF method has several differences from $\Gamma^{p-h,(m/d)}$ computed within DMFT. First of all, $\Gamma^{p-h,(m/d)}$ within DF can incorporate the non-local effect

beyond DMFT since the DF vertex is constructed from the non-local DF propagator which is dressed by the non-local DF self energy. Moreover, DF $\Gamma^{p-h,(m/d)}$ depends on three momentum $\mathbf{k}$, $\mathbf{k}'$, and $\mathbf{q}$, i.e., $\Gamma^{p-h,(m/d)}(\mathbf{k}, i\nu, \mathbf{k}', i\nu')_{\mathbf{q},i\omega}$. Within DMFT, the non-local $\Gamma^{p-h,(m/d)}$ is computed by assuming $\Gamma^{irr,p-h}$ is local and as a result the non-local vertex depends only on the momentum transfer $\mathbf{q}$, i.e., $\Gamma^{p-h,(m/d)}(i\nu, i\nu')_{\mathbf{q},i\omega}$. Finally, $\Gamma^{p-h,(m/d)}$ calculated from Eq. 5.38 is the full vertex $\Gamma^{full,p-h}$ in the particle-hole channel, therefore, the irreducible vertex $\Gamma^{irr,p-h}$ needs to be subtracted to obtained the reducible vertex $\widetilde{\Gamma}^{p-h}$. In principle, $\Gamma^{irr,p-h}$ can be computed from the full vertex $\Gamma^{full,p-h}$ by inverting the Bethe-Salpeter equation. We checked that generally $\Gamma^{irr,p-h}$ is very weakly momentum dependent and one can assume that $\Gamma^{irr,p-h}$ is local as in DMFT.

The pairing vertex, the irreducible vertex in the particle-particle channel, is constructed using the non-local $\Gamma^{p-h,(m/d)}$ computed from Eq. 5.38. For the pairing vertex with DF, we use the full vertex in the particle-hole channel instead of the reducible vertex since $\Gamma^{irr,p-h}$ is assumed to be local and it does not contribute to the non-local SC gap symmetry such as s^{+-} or d-wave. Here, we use the same equation relating the pairing vertex with the reducible vertex function in the particle-hole channel as given in the previous chapter except that the particle-hole vertex function is computed with the DF method.

The pairing bubble $\chi^{0,p-p}$ within the DF method can be computed from the non-local Green's function G related to the DF Green's function G_{dual} by Eq. 5.13. Since the Green's function is dressed by the non-local self energy, $\chi^{0,p-p}$ can treat the non-local correlations beyond DMFT.

$$\chi^{0,p-p}(\mathbf{k}, i\nu) \quad = \quad G_{\uparrow}(\mathbf{k}, i\nu) \cdot G_{\downarrow}(-\mathbf{k}, -i\nu) \tag{5.39}$$

Within the DF method, both the pairing vertex $\Gamma^{irr,p-p}$ and the pairing bubble $\chi^{0,p-p}$ are computed in a consistent way by treating the non-local correlation effect beyond DMFT. From the calculated $\Gamma^{irr,p-p}$ and $\chi^{0,p-p}$, one can compute T_c and the SC gap symmetry by solving the eigenvalue equation of the pairing matrix $\sqrt{\chi^{0,p-p}} \cdot \Gamma^{irr,p-p} \cdot \sqrt{\chi^{0,p-p}}$ using the Lanczos algorithm in a same way as used for DMFT.

Now, we show that the pairing vertex $\Gamma^{irr,p-p}$ computed using the bare DF Green's function $G^{0,dual}$ and the bare DF vertex $\gamma^{(4)}$ can recover $\Gamma^{irr,p-p}$ obtained within DMFT. Hence, one shot DF calculation gives DMFT two-particle response functions as defined in the previous chapter. First, the bare DF polarization bubble in the particle-hole channel $\chi^{0,dual}_{p-h}(i\nu)_{\mathbf{q},i\omega}$ is the same as the purely non-local part of the original fermion $\chi^{0,p-h}$ i.e., $\chi^{0,p-h}(i\nu)_{\mathbf{q},i\omega} - \chi^{0,p-h}_{loc}(i\nu)_{i\omega}$

$$\begin{aligned}
\chi^{0,p-h}_{dual}(i\nu)_{\mathbf{q},i\omega} &= -\frac{T}{N_k}\sum_{\mathbf{k}} G^0_{dual}(\mathbf{k}, i\nu)\cdot G^0_{dual}(\mathbf{k}+\mathbf{q}, i\nu+i\omega) \\
&= -\frac{T}{N_k}\sum_{\mathbf{k}} (g(\mathbf{k}, i\nu) - g_{loc}(i\nu))\cdot (g(\mathbf{k}+\mathbf{q}, i\nu+i\omega) - g_{loc}(i\nu+i\omega)) \\
&= -\frac{T}{N_k}\sum_{\mathbf{k}} g(\mathbf{k}, i\omega)\cdot g(\mathbf{k}+\mathbf{q}, i\omega+i\Omega) + T\cdot g_{loc}(i\nu)\cdot g_{loc}(i\nu+i\omega) \\
&= \chi^{0,p-h}(i\nu)_{\mathbf{q},i\omega} - \chi^{0,p-h}_{loc}(i\nu)_{i\omega} \qquad (5.40)
\end{aligned}$$

Also it can be shown that the non-local vertex Γ^{p-h} within DF is the same as the non-local Γ^{p-h} computed within DMFT. Since $\Sigma_{dual} = 0$ at the first shot calculation, the factor $F_k = \frac{1}{1+g_{imp}\cdot\Sigma_{dual}} = 1$. Therefore, the DF vertex Γ^{p-h}_{dual} is the same as the original fermion vertex Γ^{p-h}. The bare DF vertex $\gamma^{(4)}$ is $\Gamma^{p-h}_{loc}(i\nu, i\nu')_{i\omega}$, and Γ^{p-h}_{dual} is obtained by dressing $\gamma^{(4)}$ by $\chi^{0,dual}_{p-h}$

$$\begin{aligned}
\Gamma^{p-h}(i\nu, i\nu')_{\mathbf{q},i\omega} &= \Gamma^{p-h}_{dual}(i\nu, i\nu')_{\mathbf{q},i\omega} = [(\gamma^{(4)})^{-1}_{i\omega} - (\chi^{0,dual}_{p-h})_{\mathbf{q},i\omega}]^{-1} \\
&= [(\Gamma^{p-h}_{loc})^{-1}_{i\omega} + (\chi^{0,p-h}_{loc})_{i\omega} - (\chi^{0,p-h})_{\mathbf{q},i\omega}]^{-1} \\
&= [(\Gamma^{irr,p-h}_{loc})^{-1}_{i\omega} - (\chi^{0,p-h})_{\mathbf{q},i\omega}]^{-1} \qquad (5.41)
\end{aligned}$$

As a result, the non-local pairing vertex computed within the zeroth order DF method ($\Sigma_{dual} = 0$) is equal to the pairing vertex within DMFT. Since the pairing bubble $\chi^{0,p-p}$ is also same in both methods, T_c and the gap symmetry results within DMFT are recovered.

5.2 The dynamical vertex approximation (DΓA)

5.2.1 Derivation of the approximation

The self energy is the central quantity in the study of correlated many-body systems and it is related to both a two-particle vertex function Γ^{full} and a Green's function G by the Schwinger-Dyson equation [88].

$$\begin{aligned}\Sigma(\mathbf{k}, i\nu) &= U\frac{n_f}{2} - U\frac{T^2}{N_k \cdot N_q}\sum_{\mathbf{k}',\mathbf{q}}\sum_{i\nu',i\omega}\Gamma^{full}(\mathbf{k}, i\nu, \mathbf{k}', i\nu')_{\mathbf{q},i\omega}\cdot G(\mathbf{k}+\mathbf{q}, i\nu+i\omega) \\ &\quad \cdot G(\mathbf{k}', i\nu')\cdot G(\mathbf{k}'+\mathbf{q}, i\nu'+i\omega) \qquad (5.42)\end{aligned}$$

Here, $n_f = T\sum_{\mathbf{k},i\nu} G(\mathbf{k}, i\nu)e^{i\nu\cdot 0^-}$ is the occupation number of fermions, N_k is the number of $\mathbf{k}$ points in the Brillouin zone, and T is temperature. The first term of the self energy is calculated from the lowest order Feynman diagram, so called the Hartree term. This first term accounts for local and static correlations. The non-local and dynamical correlations are captured by the second term.

DMFT treats the dynamical correlation on a given site exactly. As a result, the DMFT self energy is given by the self energy in Eq. 5.42 constructed with the impurity vertex function and the impurity Green's function.

$$\Sigma_{imp}(i\nu) = U\frac{n_f}{2} - UT^2\sum_{i\nu',i\omega}\Gamma^{full}_{imp}(i\nu, i\nu')_{i\omega}\cdot G_{imp}(i\nu+i\omega)\cdot G_{imp}(i\nu')\cdot G_{imp}(i\nu'+i\omega) \quad (5.43)$$

The main idea of the dynamical vertex approximation (DΓA) [76, 85] is to approximate the full two-particle vertex function Γ^{full}_{imp} given in Eq. 5.43 by a non-local quantity in order to incorporate the non-local correlation effect. And also the impurity Green's function is replaced by the non-local DMFT Green's function. Here, we follow the derivation of Ref. [76, 85]. Unlike the DF method, DΓA does not require additional fermionic degrees of freedom but modify the self energy diagram directly in order to include the non-local corrections.

The full vertex function Γ^{full}_{imp} contains the diagrams which are reducible in different channels, i.e., particle-hole channels and particle-particle channels. These vertex functions in different channels are related to each other by a parquet equation. The fully irreducible vertex function

$\Gamma_{imp}^{f.irr}$ can be computed from the full vertex function Γ_{imp}^{full} by subtracting the reducible vertex functions in all channels. By assuming that the fully irreducible vertex function is local, the non-local full vertex function Γ^{full} can be computed by solving the complicated self-consistent equations of different channels related by the parquet formalism [89].

Instead of solving the full parquet equation, one can concentrate only on the non-local correlations in particle-hole channels which are strongly enhanced near the antiferromagnetic region. The full vertex Γ_{imp}^{full} can be represented in terms of the longitudinal $(p-h1)$ channel and the transverse $(p-h2)$ channel by

$$\begin{aligned}
\Gamma_{imp}^{full} &= \Gamma_{imp}^{f,irr} + \widetilde{\Gamma}_{imp}^{p-h1} + \widetilde{\Gamma}_{imp}^{p-h2} + \widetilde{\Gamma}_{imp}^{p-p} \\
&= \Gamma_{imp}^{f,irr} + (\Gamma_{imp}^{full,p-h1} - \Gamma_{imp}^{irr,p-h1}) + (\Gamma_{imp}^{full,p-h2} - \Gamma_{imp}^{irr,p-h2}) + \widetilde{\Gamma}_{imp}^{p-p} \\
&= \Gamma_{imp}^{full,p-h1} + \Gamma_{imp}^{full,p-h2} - (\Gamma_{imp}^{f,irr} + \widetilde{\Gamma}_{imp}^{p-h1} + \widetilde{\Gamma}_{imp}^{p-h2} + \widetilde{\Gamma}_{imp}^{p-p}) \\
&= \Gamma_{imp}^{full,p-h1} + \Gamma_{imp}^{full,p-h2} - \Gamma_{imp}^{full} \qquad (5.44)
\end{aligned}$$

Here, $\widetilde{\Gamma}$ represents the reducible diagram ($\widetilde{\Gamma} = \Gamma - \Gamma^{irr}$. We also omit spin, momentum, and frequency indices. In the above derivation, the relations

$$\Gamma_{imp}^{irr,p-h1} = \Gamma_{imp}^{f,irr} + \widetilde{\Gamma}_{imp}^{p-h2} + \widetilde{\Gamma}_{imp}^{p-p} \qquad (5.45)$$

$$\Gamma_{imp}^{irr,p-h2} = \Gamma_{imp}^{f,irr} + \widetilde{\Gamma}_{imp}^{p-h1} + \widetilde{\Gamma}_{imp}^{p-p} \qquad (5.46)$$

are used.

The momentum dependence of the full vertex function $\Gamma_{imp}^{full,p-h}$ is obtained by approximating the local ladder diagram in the particle-hole channel to the non-local one. Namely, the irreducible vertex $\Gamma_{imp}^{irr,p-h}$ is assumed to be local and it is dressed by the non-local polarization function. This ladder diagram in the particle-hole channel incorporates the non-local spin fluctuation effect First, the local irreducible vertex $\Gamma_{imp}^{irr,p-h}$ is obtained by undressing the local polarization bubble χ_{imp}^{0} from $\Gamma_{imp}^{full,p-h}$

$$\Gamma_{imp}^{irr,p-h,(m/d)}(i\nu, i\nu')_{i\omega} = [(\Gamma_{imp}^{full,p-h,(m/d)})_{i\omega}^{-1} + (\chi_{imp}^{0})_{i\omega}]^{-1} \qquad (5.47)$$

The non-local vertex $\Gamma_{\mathbf{q}}^{full,p-h}$ is obtained by dressing the local $\Gamma_{imp}^{irr,p-h}$ by the non-local $\chi_{\mathbf{q}}^{0}$

$$\Gamma^{full,p-h,(m/d)}(i\nu,i\nu')_{\mathbf{q},i\omega} = [(\Gamma_{imp}^{irr,p-h,(m/d)})_{i\omega}^{-1} - (\chi^{0})_{\mathbf{q},i\omega}]^{-1} \quad (5.48)$$

From the calculated non-local vertex in the particle-hole channel, the local full vertex given in Eq. 5.44 is approximated to a non-local vertex as

$$\begin{aligned}\Gamma_{\substack{\uparrow\downarrow\\\uparrow\downarrow}}^{full}(i\nu,i\nu')_{\mathbf{q},i\omega} &= \frac{1}{2}(\Gamma^{full,p-h1,(m)}(i\nu,i\nu')_{\mathbf{q},i\omega} - \Gamma^{full,p-h1,(d)}(i\nu,i\nu')_{\mathbf{q},i\omega}) \\ &\quad +\Gamma^{full,p-h2,(m)}(i\nu,i\nu+i\omega)_{\mathbf{k}'-\mathbf{k},i\nu'-i\nu} \\ &\quad -\Gamma_{imp}^{full,(m)}(i\nu,i\nu+i\omega)_{i\nu'-i\nu} \quad (5.49)\end{aligned}$$

Here, we restore the spin, momentum, and frequency indices.

Finally, the non-local self energy $\Sigma(\mathbf{k},i\nu)$ is obtained by inserting the non-local vertex function $\Gamma_{\substack{\uparrow\downarrow\\\uparrow\downarrow}\mathbf{q},i\omega}^{full}$ to the local self energy in Eq. 5.43. By changing the indices for the $p-h2$ channel such that $i\nu' \rightarrow i\nu+i\omega$, $i\omega \rightarrow i\nu'-i\nu$, the equation for $\Sigma(\mathbf{k},i\nu)$ is simplified as

$$\begin{aligned}\Sigma(\mathbf{k},i\nu) &= U\frac{n_f}{2} - U\frac{T^2}{N_k\cdot N_q}\sum_{\mathbf{k}',\mathbf{q}}\sum_{i\nu',i\omega}[(\frac{3}{2}\Gamma^{full,(m)}(i\nu,i\nu')_{\mathbf{q},i\omega} - \frac{1}{2}\Gamma^{full,(d)}(i\nu,i\nu')_{\mathbf{q},i\omega}) \\ &\quad -\Gamma_{imp}^{full,(m)}(i\nu,i\nu')_{i\omega}]G(\mathbf{k}+\mathbf{q},i\nu+i\omega)G(\mathbf{k}',i\nu')G(\mathbf{k}'+\mathbf{q},i\nu'+i\omega) \quad (5.50)\end{aligned}$$

However, one should note that the Green's function $G(\mathbf{k},i\nu)$ is still computed within DMFT, i.e., using the local impurity self energy.

5.2.2 The Moriya $\widetilde{\lambda}$ correction

In the previous subsection, we derived the formula to compute the non-local self energy based on two-particle vertex functions. However, as shown in Ref. [85], the calculation of the non-local self energy by Eq. 5.50 overestimates the high frequency result of $Im\Sigma(\mathbf{k},i\nu)$ compared to the exact asymptotic behavior given by.

$$\Sigma(i\nu\rightarrow\infty) = \frac{U^2}{i\nu}\cdot\frac{n_f}{2}\cdot(1-\frac{n_f}{2}) \quad (5.51)$$

In this subsection, we argue that this asymptotic behavior can be satisfied by imposing a sum rule in the two-particle level.

Here, we impose a sum rule in the two particle level in a similar way as in the two-particle self-consistent (TPSC) theory [90, 91]. The sum rule requires that the local susceptibility obtained by summing $\chi_{\mathbf{q}}^{(m/d)}$ over $\mathbf{q}$ and $i\omega$ is the same as the impurity susceptibility $\chi_{imp}^{(m/d)}$.

$$\frac{T}{N_q}\sum_{\mathbf{q},i\omega}\chi_{\mathbf{q},i\omega}^{(m)} = \chi_{imp}^{(m)}(\tau=0^+) = \langle(n_f^\uparrow - n_f^\downarrow)^2\rangle = n_f - 2\langle n_f^\uparrow \cdot n_f^\downarrow\rangle \tag{5.52}$$

$$\frac{T}{N_q}\sum_{\mathbf{q},i\omega}\chi_{\mathbf{q},i\omega}^{(d)} = \chi_{imp}^{(d)}(\tau=0^+) = \langle(n_f^\uparrow + n_f^\downarrow)^2\rangle - \langle(n_f^\uparrow + n_f^\downarrow)\rangle^2 = n_f + 2\langle n_f^\uparrow \cdot n_f^\downarrow\rangle - n_f^2 \tag{5.53}$$

Here, the Pauli principle is used for the rightmost result, i.e., $\langle(n_f^\sigma)^2\rangle = \langle n_f^\sigma\rangle$.

The non-local susceptibility $\chi_{\mathbf{q}}^{(m/d)}$ is computed by dressing the non-local polarization function $\chi_{\mathbf{q}}^0$ the local irreducible vertex Γ_{loc}^{irr}. The local susceptibility obtained by averaging $\chi_{\mathbf{q}}^{(m/d)}$ over $\mathbf{q}$ vectors is not the same as the impurity susceptibility $\chi_{imp}^{(m/d)}$ since

$$\begin{aligned}\frac{1}{N_q}\cdot\sum_{\mathbf{q}}\chi^{(m/d)}(\mathbf{q},i\omega) &= \frac{T^2}{N_q}\cdot\sum_{\mathbf{q}}\sum_{i\nu,i\nu'}\frac{1}{(\chi_0)^{-1}_{\mathbf{q},i\omega} - \Gamma_{imp}^{irr,(m/d)}} \\ &\neq \frac{T^2}{N_q}\cdot\sum_{i\nu,i\nu'}\frac{1}{\sum_{\mathbf{q}}(\chi_0)^{-1}_{\mathbf{q},i\omega} - \Gamma_{imp}^{irr,(m/d)}} = \chi_{imp}^{(m/d)}(i\omega).\end{aligned} \tag{5.54}$$

Therefore, the sum rules in Eq. 5.52 and 5.53 are not satisfied. The averaged susceptibility over $\mathbf{q}$ is the same as the impurity one only in the infinite dimension where the lattice problem is mapped to the impurity problem.

In order to satisfy the sum rules in Eq. 5.52 and 5.53, we introduce the Moriya $\widetilde{\lambda}$ correction in order to incorporate the spin fluctuation effect. This Moriya $\widetilde{\lambda}$ term within DΓA is employed in Ref. [85]. In the self-consistent renormalization theory of spin fluctuation[cite], this $\widetilde{\lambda}$ term takes into account the feedback of the spin fluctuation and in principle it can be computed from the magnetic susceptibility of the system. For simplicity, we determine this $\widetilde{\lambda}$ term to satisfy the sum rules in Eq. 5.52 and 5.53. This Moriya $\widetilde{\lambda}$ correction is given only for the magnetic channel and at the zero $i\omega$ frequency where the spin fluctuation is dominant. Also we assume $\widetilde{\lambda}$ is local i.e., $\widetilde{\lambda}_{\mathbf{q}}^{(m)} \approx \widetilde{\lambda}^{(m)}$.

$$\frac{T^2}{N_q}\sum_{\mathbf{q}}\sum_{i\nu,i\nu'}\frac{1}{(\chi_0)^{-1}_{\mathbf{q},i\omega} - \Gamma_{imp}^{irr,(m)} + \widetilde{\lambda}} = \chi_{imp}^{(m)}(i\omega) \tag{5.55}$$

Now we show that the Moriya $\widetilde{\lambda}$ correction satisfying the sum rule in Eq. 5.55 also produces the exact high frequency asymptotic of the self energy. The non-local self energy in Eq. 5.51 can be calculated using the particle-hole ladder diagram renormalized by Moriya $\widetilde{\lambda}$ term. If only one frequency of the irreducible vertex Γ^{irr}_{p-h} approaches ∞ while other frequencies are finite, Γ^{irr}_{p-h} can be replaced by the bare interaction, i.e,

$$\Gamma^{irr,(m/d)}_{p-h}(i\nu \to \infty, i\nu')_{i\omega} \quad \approx \quad (\mp)U. \tag{5.56}$$

The bare interaction is $-U$ for the magnetic channel and $+U$ for the charge channel. Using Eq. 5.56, the self-energy in Eq. 5.50 in the limit of $i\nu \to \infty$ can be simplified as

$$\Sigma(\mathbf{k}, i\nu \to \infty) = U\frac{n_f}{2} + \frac{U^2}{2}\frac{T}{N_q}\sum_{\mathbf{q},i\omega}\left((\frac{3}{2}\chi^{(m)}_{\mathbf{q},i\omega} + \frac{1}{2}\chi^{(d)}_{\mathbf{q},i\omega}) - \chi^{(m)}_{imp,i\omega}\right)\cdot G(\mathbf{k}+\mathbf{q}, i\nu + i\omega) \tag{5.57}$$

since Γ^{irr}_{p-h} connected with $G(\mathbf{k}+\mathbf{q}, i\nu+i\omega)$ can be replaced by the bare interaction.

Using the sum rules in Eq. 5.52 and 5.53, one can show that the high frequency asymptotic behavior of the DΓA self energy is given by the exact formula in Eq. 5.51.

$$\begin{aligned}
\Sigma(\mathbf{k}, i\nu \to \infty) &= U\frac{n_f}{2} + \frac{U^2}{2\cdot i\nu}\frac{T}{N_q}\sum_{\mathbf{q},i\omega}\left((\frac{3}{2}\chi^{(m)}_{\mathbf{q},i\omega} + \frac{1}{2}\chi^{(d)}_{\mathbf{q},i\omega}) - \chi^{(m)}_{imp,i\omega}\right) \\
&= U\frac{n_f}{2} - \frac{U^2}{4\cdot i\nu}T\sum_{i\omega}(\chi^{(m)}_{imp,i\omega} + \chi^{(d)}_{imp,i\omega}) \\
&= U\frac{n_f}{2} - \frac{U^2}{i\nu}\frac{n_f}{2}(1-\frac{n_f}{2})
\end{aligned} \tag{5.58}$$

5.2.3 The calculation scheme

Unlike the DF method, DΓA is a non-conserving approximation. The DΓA self energy is computed using DMFT $G(\mathbf{k}, i\nu)$ instead of taking the feedback from the DΓA non-local Green's function. Therefore, the DΓA calculation is performed in a non-self-consistent way. The fully self-consistent calculation requires the solution of the complicated full parquet equation. Nevertheless, the sum rule in the two-particle level is enforced by the Moriya $\widetilde{\lambda}$ term. Since this Moriya $\widetilde{\lambda}$ term already includes the non-local fluctuation effect beyond DMFT, the non-self-consistent solution of DΓA will be more reliable. The calculation procedure of DΓA is given as follows.

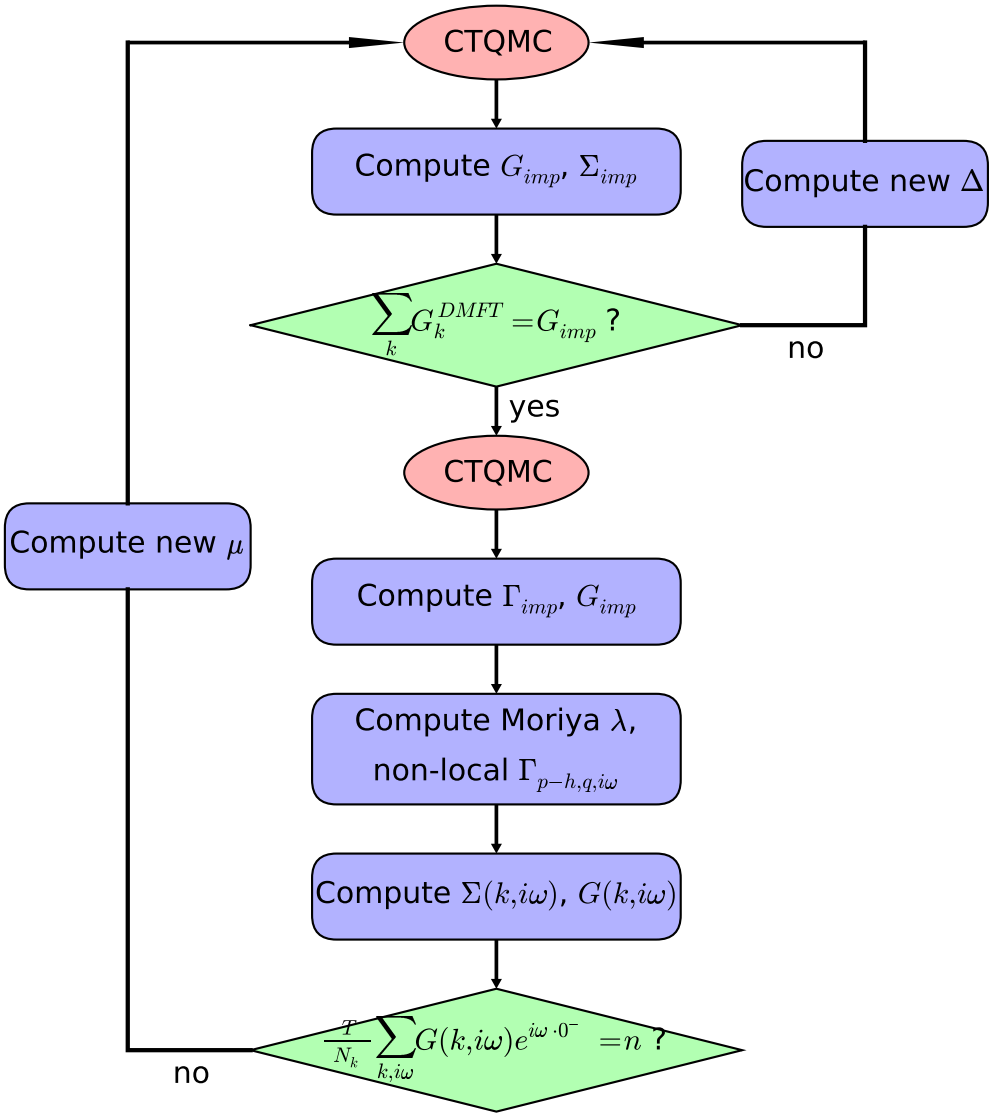

Figure 5.2: The calculation procedure of DΓA.

1. First, the DMFT self-consistent loop is continued until the convergence is reached.

$$\sum_{\mathbf{k}} \frac{1}{i\nu + \mu - \epsilon_{\mathbf{k}} - \Sigma} = \frac{1}{i\nu + \mu - \Delta - \Sigma} \tag{5.59}$$

2. Once the DMFT solution is converged, CTQMC samples the impurity two-particle vertex function Γ_{p-h} from the converged hybridization Δ and the chemical potential μ. The impurity irreducible vertex function Γ^{irr}_{p-h} is computed from the full vertex Γ_{p-h} using Eq. 5.47.

3. The non-local vertex function in the magnetic/charge channel $\Gamma^{full,(m/d)}_{p-h,\mathbf{q},i\omega}$ is computed by dressing Γ^{irr}_{p-h} with the non-local polarization function $(\chi^0)_{\mathbf{q},i\omega}$ (Eq. 5.48).

4. In order to satisfy the sum rule in the two-particle level, the Moriya λ correction is determined from the Eq. 5.55.

5. Finally, the non-local self energy $\Sigma(\mathbf{k}, i\nu)$ within DΓA is computed using Eq. 5.50. And from $\Sigma(\mathbf{k}, i\nu)$, the non-local Green's function $G(\mathbf{k}, i\nu)$ can be computed. In the fixed density n calculation, the chemical potential μ is adjusted to satisfy that the density computed within DΓA is the same as the desired n.

$$\frac{T}{N_k} \sum_{\mathbf{k}, i\nu} G(\mathbf{k}, i\nu) e^{i\nu 0^-} = n \tag{5.60}$$

   Using this new μ, the DMFT loop starts again by going back to the step 1.

5.2.4 The pairing susceptibility within DΓA

Within DΓA, the non-local fluctuation beyond DMFT is taken into account by computing the non-local self energy using Eq.5.50. And the one-particle Green's function is dressed by this DΓA self energy. In the two-particle level, the non-local fluctuation is treated by the Moriya $\widetilde{\lambda}$ term in order to satisfy the sum rule in Eq. 5.55. Unlike the DF method, the non-local fluctuations included in the self-energy and the vertex function are not treated in a self-consistent way.

For computing the pairing susceptibility within DΓA, both the pairing vertex and the pairing bubble includes the non-local correlations beyond DMFT. The pairing vertex $\Gamma^{irr,p-p}(\mathbf{k}, i\nu, \mathbf{k}', i\nu')$

computed within DΓA is computed with the same equation as the DMFT pairing vertex is computed except that the Moriya $\widetilde{\lambda}$ correction is included to satisfy the sum rule in Eq. 5.55. Therefore, the reducible vertex in the particle-hole channel $\widetilde{\Gamma}$ is given by

$$\widetilde{\Gamma}^{p-h,(m/d)}(i\nu, i\nu')_{\mathbf{q},i\omega} = \sum_{i\nu_1, i\nu_2} \Gamma^{irr,p-h,(m/d)}(i\nu, i\nu_1)_{i\omega} \cdot \overline{\chi}^{p-h,(m/d)}(i\nu_1, i\nu_2)_{\mathbf{q},i\omega} \cdot \Gamma^{irr,p-h,(m/d)}(i\nu_2, i\nu')_{i\omega} \tag{5.61}$$

where $\overline{\chi}$ is the renormalized susceptibility due to the Moriya λ term.

$$\overline{\chi}^{p-h,(m)}(i\nu_1, i\nu_2)_{\mathbf{q},i\omega} = [(\chi^{0,p-h})^{-1}_{\mathbf{q},i\omega} - \Gamma^{irr,p-h,(m)} + \lambda]^{-1}(i\nu_1, i\nu_2)_{\mathbf{q},i\omega} \tag{5.62}$$

As a result, the pairing vertex within DΓA is renormalized from the DMFT pairing vertex by the $\widetilde{\lambda}$ correction.

The DΓA pairing bubble $\chi_{0,p-p}(\mathbf{k}, i\nu)$ is computed using the non-local DΓA Green's function which is dressed by the DΓA self energy obtained by Eq. 5.50.

$$\chi^{0,p-p}(\mathbf{k}, i\nu) = G_{\uparrow}(\mathbf{k}, i\nu) \cdot G_{\downarrow}(-\mathbf{k}, -i\nu) \tag{5.63}$$

$$G(\mathbf{k}, i\nu) = \frac{1}{i\nu + \mu - \epsilon_{\mathbf{k}} - \Sigma(\mathbf{k}, i\nu)} \tag{5.64}$$

Finally, the pairing susceptibility is computed by dressing the pairing bubble $\chi^{0,p-p}(\mathbf{k}, i\nu)$ by the pairing vertex $\Gamma^{irr,p-p}(\mathbf{k}, i\nu, \mathbf{k'}, i\nu')$. T_c and the SC gap symmetry can be computed by solving the eigen-problem of the pairing matrix $\sqrt{\chi^{0,p-p}} \cdot \Gamma^{irr,p-p} \cdot \sqrt{\chi^{0,p-p}}$ using the Lanczos algorithm.

Chapter 6

The Application of the Two-particle Vertex Calculation : Model Hamiltonians

In this chapter, we compute the phase diagram of magnetism and superconductivity in the Hubbard model and the periodic Anderson model. For the calculation of the superconducting (SC) critical temperature T_c and the SC gap symmetry, we apply the two-particle vertex function approach derived in Chapter 4 and Chapter 5 to the model Hamiltonian calculation. T_c is computed as a function of the doping for the Hubbard model and as a function of the hybridization for the periodic Anderson model. The pairing vertex and the pairing bubble are computed within the DMFT method, and for comparison, DΓA and DF methods are also employed to incorporate the non-local correlations beyond DMFT. We show that the SC phase is stable near the region where the magnetic fluctuation is strong and that the non-local methods reduce T_c compared to a DMFT result due to the renormalized pairing interaction. To further analyze T_c and the SC gap symmetry results, we also compute the momentum dependent magnetic susceptibility, the Fermi surface, the effective $\overline{U}$, and other relevant quantities.

6.1 The Hubbard Model

6.1.1 The Hamiltonian

The Hubbard model describes the strongly correlated physics in cuprates where doping an electron or a hole induces high T_c superconductivity. This model consists of the kinetic energy term due to the hopping of fermions to adjacent sites and the on-site Coulomb energy term.

We consider the 2D one-band Hubbard model whose Hamiltonian is given as follows.

$$\hat{H} = \sum_{\mathbf{k},\sigma}(\epsilon(\mathbf{k})-\mu)\cdot f^{\dagger}_{\mathbf{k},\sigma}f_{\mathbf{k},\sigma} + U\cdot\sum_{i} f^{\dagger}_{i,\uparrow}f^{\dagger}_{i,\downarrow}f_{i,\downarrow}f_{i,\uparrow} \tag{6.1}$$

$$\epsilon(\mathbf{k}) = -2t(\cos(k_x)+\cos(k_y)) - 4t'\cos(k_x)\cos(k_y) \tag{6.2}$$

The on-site Coulomb interaction U is set to $12t$ where t is the nearest-neighbor hopping interaction. And the next-nearest hopping t' is fixed as -0.3t. These parameters exhibit the Mott insulating state accompanying with the antiferromagnetic state at the half-filling ($n = 1$). As the system is doped away from the half-filling, it is known that the magnetic state is suppressed and the superconducting state emerges. In this section, we compute the critical temperature T_c and the gap symmetry of superconductivity in the hole doping ($\delta = 1 - n$) region of the Hubbard model by applying the vertex function approach based on DMFT and non-local methods beyond DMFT.

6.1.2 The phase diagram of antiferromagnetism and superconductivity

Fig.6.1 displays the phase diagram of antiferromagnetism (AFM) and d-wave superconductivity (SC) in the hole-doped region of the Hubbard model. The Neel temperature (T_N) of the AFM state is determined as the temperature where DMFT magnetic susceptibility at the ordering (π,π) vector diverges. T_c of SC is calculated using different methods. Within the DMFT method, the pairing vertex $\Gamma^{irr,p-p}(\mathbf{k},i\nu,\mathbf{k}',i\nu')$ is computed by dressing the DMFT irreducible particle-hole vertex $\Gamma^{irr,p-h}$ with the non-local polarization bubble $\chi^{0,p-h}_{\mathbf{q}}$. $\chi^{0,p-h}_{\mathbf{q}}$ is computed from DMFT $G(\mathbf{k},i\nu)$ dressed by a local self-energy. The pairing bubble $\chi^{0,p-p}$ in the particle-particle channel is computed from the same $G(\mathbf{k},i\nu)$. The DMFT+$\widetilde{\lambda}$ method renormalizes the pairing vertex by a Moriya $\widetilde{\lambda}$ term to satisfy the sum rule in the two-particle level. However, DMFT $\chi^{0,p-p}$ is still used. The DΓA method uses this renormlized pairing vertex and $\chi^{0,p-p}$ computed from $G(\mathbf{k},i\omega)$ dressed by a non-local DΓA self energy. Within the DF method, the pairing vertex and the pairing bubble diagram are derived from the DF vertex and the DF

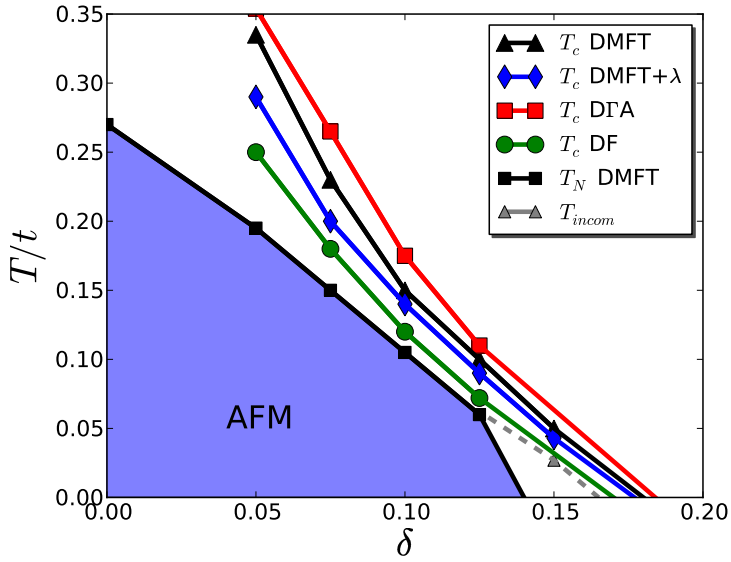

Figure 6.1: The phase diagram of the antiferromagnetic Neel temperature (T_N) and the superconducting critical temperature (T_c) in the one-band Hubbard model. The x-axis is the hole doping (δ) and the y-axis is the temperature T. T_N (black square) is determined within DMFT. As δ increases, T_N is suppressed and the commensurate (π, π) magnetic peak changes to the incommensurate peak (dashed line). T_c is calculated using DMFT (black triangle), DMFT+$\widetilde{\lambda}$ (blue diamond), DΓA (red square), and DF (green circle) methods. d-wave superconductivity emerges near the magnetic phase.

bubble by an exact relation. Both DF quantities are determined in a self-consistent way as a conserving approximation.

Fig. 6.1 shows that T_N computed within DMFT (black square) is decreasing as the doping (δ) increases, and above δ=0.14 T_N is completely suppressed down to T=0. This decrease of the magnetic susceptibility at the large doping is mainly due to the screened $\Gamma^{irr,p-h}$. Namely, $\Gamma^{irr,p-h}$ is screened by the ladder diagram in the particle-particle channel[92] and this screening becomes more enhanced at larger dopings where the quasi-particles are coherent. The magnetic ordering vector is (π, π) due to the nesting of the Fermi surface. This ordering vector changes from the commensurate (π, π) vector to the incommensurate $(\pi - \varepsilon, \pi - \varepsilon)$ and $(\pi, \pi - \varepsilon)$ vector near δ=0.15. This incommensurate magnetism is caused by the frustration due to the doping and, as a result, the change of Fermi surface nesting vector (see Fig. 6.6).

T_c of the SC state is computed using various methods as the temperature at which the eigenvalue of the pairing matrix reaches one. The result shows that the d-wave SC state is stabilized near the magnetic phase where the strong magnetic fluctuation causes the pairing interaction of Cooper pairs. Within the DMFT method, T_c (black triangle in Fig. 6.1) shows a strong enhancement even in the underdoped region (δ=0.05). T_c decreases as δ increases and it becomes completely 0 above δ=0.18. The experimental phase diagram of T_c shows the strong suppression of T_c in the underdoped region and as a result the dome shape with the maximum of T_c at the optimal doping.

Within DMFT, the overestimated T_c in the underdoped region can be caused by mainly two reasons. First, the pairing interaction is overestimated within DMFT. T_N computed within DMFT is exaggerated since the non-local fluctuation effect is neglected. This enhanced T_N causes the strong pairing interaction even in the underdoped region. Second, the pseudo gap physics is not captured within DMFT. In the underdoped region, ARPES experiments found the reduction of spectral weight at the Fermi energy, namely the pseudo-gap. The opening of this pseudo gap will decrease T_c due to the suppression of the pairing bubble, $\chi^{0,p-p}$. Nevertheless, in the overdoped region (δ¿0.125) where this pseudo gap physics becomes less important, the

result of T_c calculated within DMFT shows a good agreement with the experimental phase diagram.

The DMFT+$\widetilde{\lambda}$, DΓA, and DF methods incorporate the non-local fluctuations beyond DMFT. In DMFT+$\widetilde{\lambda}$, the pairing interaction $\Gamma^{irr,p-p}$ is reduced by the Moriya $\widetilde{\lambda}$ correction and accordingly T_c (blue diamond in Fig. 6.1) is decreased compared to DMFT T_c. The decrease is quite pronounced at δ=0.05 and the difference becomes smaller as δ increases to the overdoped region. The DΓA method takes the same pairing interaction as DMFT+$\widetilde{\lambda}$ and the pairing bubble $\chi^{0,p-p}$ is computed from DΓA Green's functions. T_c computed within DΓA (red square in Fig. 6.1) is larger than DMFT+$\widetilde{\lambda}$ T_c and even DMFT T_c. In the overdoped region, T_c computed within DΓA is similar to DMFT T_c. As will be discussed later, this large T_c within DΓA is due to the enhanced $\chi^{0,p-p}$ within DΓA. The DF method computes $\Gamma^{irr,p-p}$ and $\chi^{0,p-p}$ in a self-consistent way, as a result, T_c computed within DF (green circle in Fig. 6.1) is reduced mostly among the methods Nevertheless, the dome-shape of the experimental phase diagram is not captured in any methods.

6.1.3 The eigenvalues and the gap symmetry

The instability of the paramagnetic state towards the SC state can be studied by solving the eigenvalue problem of the matrix equation in the pairing susceptibility as changing T. T_c shown in Fig. 6.1 is determined as the temperature at which this eigenvalue λ reaches one. Fig. 6.2(a) shows the eigenvalues computed as a function of T at different dopings (δ). Here, the DMFT, DMFT+$\widetilde{\lambda}$, DΓA, and DF results are compared.

In all dopings, eigenvalues (shown in Fig.6.2(a)) are enhanced as T is lowered. The eigenvalue computed within DMFT increases strongly compared to other methods as the temperature is approaching to DMFT T_N. Since the pairing interaction is proportional to the magnetic susceptibility, it gets strongly enhanced near the DMFT magnetic phase. Below DMFT T_N, the DMFT method for computing the pairing vertex fails since the ladder diagram in the magnetic channel diverges.

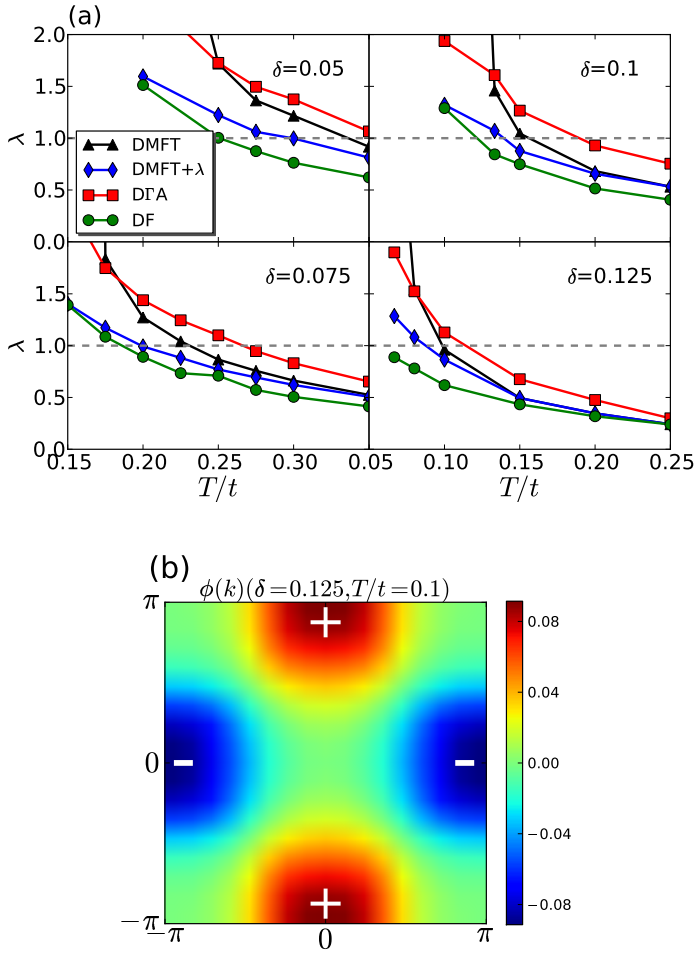

Figure 6.2: (a) The eigenvalue λ of the pairing susceptibility in the particle-particle channel as a function of T at different dopings (δ=0.05, 0.075, 0.1, and 0.125). DMFT, DMFT+λ, DΓA, and DF methods are employed for computing the eigenvalues. (b) The eigenfunction $\phi(\mathbf{k})$ computed at δ=0.125 and T=0.1t. This $\phi(\mathbf{k})$ of the leading eigenvalue corresponds to the SC gap function.

The DMFT+$\widetilde{\lambda}$, DΓA, and DF methods show a rather slow increase of eigenvalues compared to DMFT due to the non-local correlation effect. The eigenvalue computed within DΓA is the largest among at T above T_c in all dopings. As T gets lowered, DMFT eigenvalue is enhanced sharply. The eigenvalue computed within the DMFT+$\widetilde{\lambda}$ method is similar as the DMFT eigenvalues at $T > T_c$ and they are strongly reduced as T is lowered since the Moriya λ correction gets larger. The DF eigenvalues are the smallest in all dopings since the pairing interaction is strongly reduced due to the non-local correlation treated by dual fermions.

As the doping increases, the eigenvalues computed from all methods are reduced showing an agreement with the monotonic decrease of T_c in Fig. 6.1. This monotonic behavior mainly originates from the suppression of the pairing interaction at increased doping. As we will show below, the pairing interaction is quite sensitive to the change of dopings.

The momentum dependence of the eigenfunction $\phi_{\mathbf{k}}$ corresponding to the leading eigenvalue shows the gap symmetry of the SC state. Fig. 6.2(b) shows the eigenfunction $\phi(\mathbf{k}, i\nu = \pi T)$ in the Brillouin zone. Within DMFT, the momentum dependence of ϕ clearly shows that the gap symmetry is d-wave, i.e., $\cos k_x - \cos k_y$. Indeed, the gap symmetry of superconductivity in the one-band Hubbard model has been studied by many theoretical works to be a d-wave. We found that the leading eigenfunction has always d-wave symmetry in all doping parameters shown in Fig. 6.1 and in all methods. Therefore, we confirmed the d-wave symmetry of the SC gap is mostly favored in the one-band Hubbard model compared to other symmetries.

6.1.4 The pairing strength and the pairing bubble

Fig. 6.3 shows the temperature dependence of the projected pairing interaction $\bar{\Gamma}^{p-p,(d)}$ at different dopings. The d wave projection of the pairing interaction is the largest among symmetry channels at all dopings, therefore, only $\bar{\Gamma}^{p-p,(d)}$ results are shown.

In the DMFT method, $\Gamma^{irr,p-p}$ is obtained from the reducible diagram in the particle-hole channels, i.e., $\Gamma^{irr,p-h} \cdot \chi^{p-h} \cdot \Gamma^{irr,p-h}$. As a result, $\bar{\Gamma}^{p-p,(d)}$ gets dominant near DMFT T_N where the magnetic χ^{p-h} is strongly enhanced.

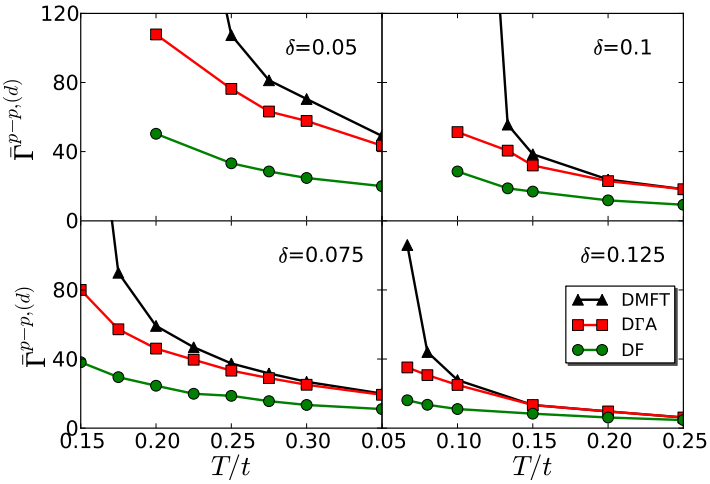

Figure 6.3: The pairing interaction projected to the d wave channel, $\bar{\Gamma}^{p-p,(d)}$ as a function of temperature at different dopings. The results employing the DMFT, DΓA, and DF methods are compared.

In the DΓA method, χ^{p-h} is renomalized from the DMFT value by the Moriya $\widetilde{\lambda}$ correction to satisfy the sum rule in the two-particle level. In principle, this λ correction renormlizes T_N down to zero satisfying the Mermin-Wagner theorem in a 2D system [85]. At δ=0.05, $\bar{\Gamma}^{p-p,(d)}$ is renormlized from quite high T and becomes strongly renormalized at lower T. As the doping increases, this λ correction becomes effective only at lower temperatures where magnetic fluctuation is strong.

The DF method take into account the non-local correction of the vertex function self-consistently in a conserving way. As a result, $\bar{\Gamma}^{p-p,(d)}$ is strongly renormlized in the DF method at all dopings compared to either the DMFT or the DΓA method. In the DΓA calculation, the fully self-consistent calculation without the Moriya $\widetilde{\lambda}$ term should renormalize $\bar{\Gamma}^{p-p,(d)}$ further as the DF method.

As doping increases, $\bar{\Gamma}^{p-p,(d)}$ decreases monotonically in all methods, i.e., the pairing interaction is the strongest at the underdoped region (δ=0.05). This result is related to the overestimated T_c in the underdoped region. This monotonic increase of $\bar{\Gamma}^{p-p,(d)}$ is also shown in the DCA calculation[93]. Nevertheless, the DCA calculation can produce the dome shape

of T_c due to the strong reduction of $\chi^{0,p-p}$ in the underdoped region. It is also possible that $\bar{\Gamma}^{p-p,(d)}$ results computed within the DMFT, DΓA, and DF methods are still overestimated in the underdoped region even at high temperatures compared to the DCA method.

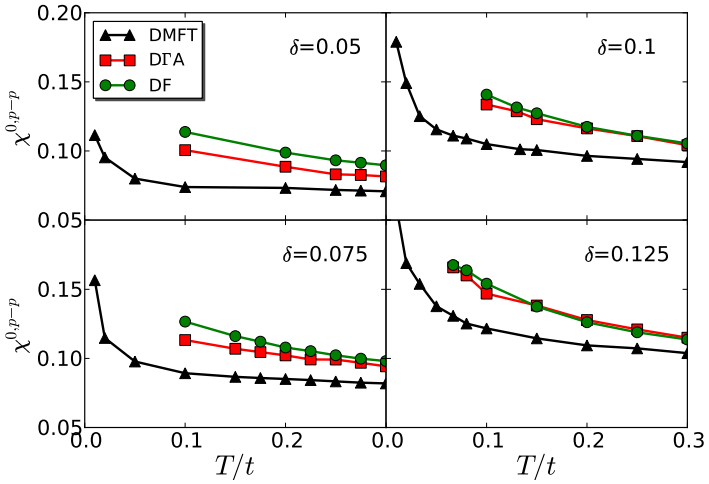

Figure 6.4: The pairing bubble in the particle-particle channel $\chi^{0,p-p}$ projected to the d-wave symmetry channel. The result is obtained as a function of T at different dopings. The DMFT, DΓA, and DF methods are used for the calculation.

Fig. 6.4 displays the temperature dependence of $\chi^{0,p-p}$ at δ=0.05, 0.75, 0.1, and 0.125. The DMFT, DΓA, and DF methods are employed for calculation. At all dopings, $\chi^{0,p-p}$ computed within the non-local methods shows the larger value compared to the DMFT method. This result somehow contradicts with the half-filling Hubbard model results where DΓA and DF methods produce a spin gap at the Fermi energy [85, 94] and as a result the reduction of $\chi^{0,p-p}$.

The eigenvalue in the pairing channel is determined by the combination of $\bar{\Gamma}^{p-p,(d)}$ and $\chi^{0,p-p}$. Even though the DF method gives the largest $\chi^{0,p-p}$ compared to other method, the strong suppression of $\bar{\Gamma}^{p-p,(d)}$ results in the lowest eigenvalue and, as a result, the lowest T_c at all dopings. In the DΓA method, $\chi^{0,p-p}$ is quite enhanced than DMFT, but slightly smaller than DF $\chi^{0,p-p}$. However, $\bar{\Gamma}^{p-p,(d)}$ within DΓA is not strongly suppressed as DF, therefore, T_c within DΓA is even nslightly higher than DMFT T_c. It is suggested that $\chi^{0,p-p}$ within cluster DMFT can be strongly enhanced at the optimal doping within cluster DMFT [93].

In the DMFT result, the temperature dependence of $\chi^{0,p-p}$ near the optimal doping ($\delta \sim$0.125) reveals the logarithmic enhancement at low temperatures showing an agreement with the Fermi liquid behavior of $\chi_{0,p-p} \sim \log(1/T)$. In the BCS argument, this logarithmic enhancement of $\chi^{0,p-p}$ at low temperature gives the pairing instability for a given interaction whose energy scale is limited by the phonon Debye frequency. At the underdoped region (δ=0.05,0.075), this logarithmic enhancement is not clearly present even at low T. This is due to the fact that quasi-paritcles computed within DMFT in the doped Mott insulating region show an incoherent behavior until the very low T is reached. In spite of the incoherent $\chi^{0,p-p}$, the pairing interaction $\bar{\Gamma}^{p-p,(d)}$ within DMFT is strong enough to cause the pairing instability at high T in our calculation.

In the cluster DMFT calculation with large cluster sites, $\chi^{0,p-p}$ in the underdoped region is strongly suppressed compared to the optimal region due to the pseudo-gap in the density of states [93]. In the DΓA and DF methods, the pseudo-gap is not clearly seen even at the underdoped region (δ=0.05) (see Fig. 6.6(b)) until the lowest temperature we could reach. Therefore, stronger fluctuation is expected to be included in DΓA and DF methods. The current DΓA method needs to be implemented as a fully self consistent way without the need of Moriya λ correction. In DF method, the strong non-local fluctuation can be included by computing more relevant diagrams for the DF self energy. For example, the ladder type diagram in the particle-hole channel is possible. The study of superconductivity in the underdoped region by including the strong non-local fluctuation will be the future challenge.

6.1.5 The magnetic susceptibility and the spectral function

Fig. 6.5 shows $\chi^m(\mathbf{q})$ along the special $\mathbf{q}$ path chosen in the Brillouin zone at δ=0.05 and 0.15. At δ=0.05, $\chi^m(\mathbf{q})$ shows a peak at (π, π) in all methods while this peak is splitted to $(\pi-\varepsilon, \pi-\varepsilon)$ and $(\pi, \pi-\varepsilon)$ at δ=0.15. The left figure in Fig. 6.6(a) displays the spectral function at δ=0.05. Although the spectral weight is rather small and broad compared to δ=0.15, this Fermi surface reveals that the particle-hole excitation is dominant at $\mathbf{q}$=(π, π). Within DΓA and DF, $\chi^m(\mathbf{q})$

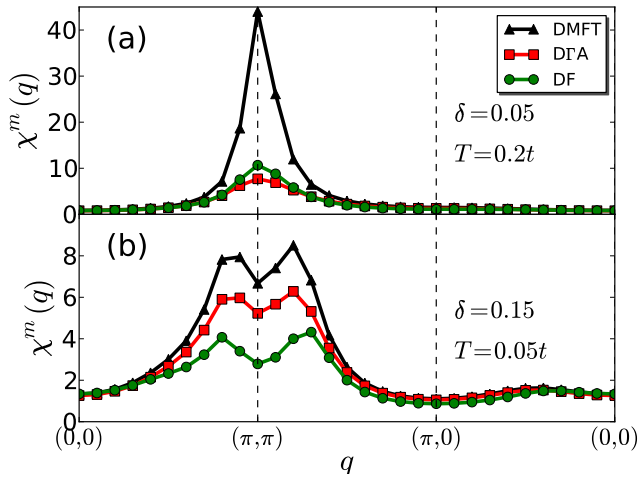

Figure 6.5: The magnetic susceptibility $\chi^m_{\mathbf{q}}$ computed in the Hubbard model as a function of the momentum transfer $\mathbf{q}$ at different dopings. The susceptibilities are computed within DMFT, DΓA, and DF methods for a comparison. (a) The doping δ=0.05 and T=0.2t. (π, π) antiferromagnetism is strongly enhanced. (b) δ=0.15 and T=0.05t. The susceptibility at (π, π) is suppressed and the magnetic ordering vector is splitted to $(\pi - \varepsilon, \pi - \varepsilon)$ and $(\pi, \pi - \varepsilon)$.

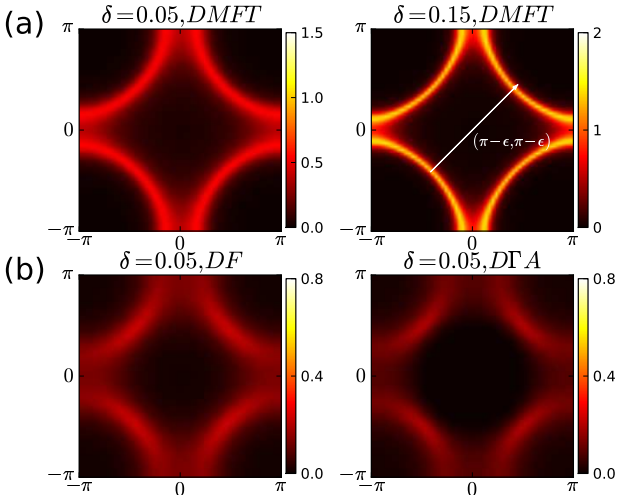

Figure 6.6: The spectral function $A(\mathbf{k}, \omega = 0) = -\frac{1}{\pi} G(\mathbf{k}, \omega = 0)$ in the Hubbard model. (a) $A(\mathbf{k})$ computed within DMFT at δ=0.05 (left) and 0.15 (right). T=0.02t in both dopings. (b) $A(\mathbf{k})$ computed with the non-local methods beyond DMFT at δ=0.05 and T=0.1t. The DF (left) and the DΓA (right) methods are used.

especially at $\mathbf{q}$=(π,π) is strongly decreased due to the non-local effect and as a result, the pairing interaction is also suppressed as shown in Fig. 6.3. Even though $\chi^m(\mathbf{q})$ is slightly more reduced within DΓA, the pairing interaction is more suppressed in the DF method.

This $\mathbf{q}$ dependence of the magnetic susceptibility $\chi^m(\mathbf{q})$ is related to the momentum dependence of the pairing vertex. The (π,π) peak of $\chi^m(\mathbf{q})$ indicates that the pairing interaction is strongly enhanced between Cooper pairs at $\mathbf{k}$ and $\mathbf{k}'$ with $\mathbf{k}-\mathbf{k}' = (\pi,\pi)$. We checked that the contribution to the pairing vertex from the charge channel is much smaller than the magnetic channel. This momentum dependence of the pairing vertex plays a crucial role to determine the SC gap symmetry. Namely, quasi-particles near the Fermi surface at $\mathbf{k} = (\pm\pi, 0)$ and $\mathbf{k}' = (0, \pm\pi)$ (see the Fermi surface in Fig. 6.6(a)) are strongly affected by the pairing interaction induced from (π,π) magnetism. As a result, the gap function is maximum at those anti-nodal $(\pm\pi, 0)$ and $(0, \pm\pi)$ points and the gap changes even a sign going from the $\mathbf{k}$ point to the $\mathbf{k}'$ point for the pairing interaction to be effectively attractive. Therefore, the d-wave symmetry, $\cos(k_x) - \cos(k_y)$, is favored in the Hubbard model.

As δ increases to 0.15, the position of the magnetic peak changes from (π,π) to $(\pi-\varepsilon,\pi-\varepsilon)$ and $(\pi,\pi-\varepsilon)$. This incommensurate magnetism originates from the nesting vector of the Fermi surface at this doping. Fig. 6.6(a) shows that the Fermi surface is slightly shrinked as δ increases and as a result the nesting vector is pronounced at $(\pi-\varepsilon,\pi-\varepsilon)$ shown as the white arrows. Within DΓA and DF, $\chi^m(\mathbf{q})$ is reduced due to the non-local fluctuation and the pairing interaction as well (Fig. 6.3). Nevertheless, this incommensurate magnetism still favors the d-wave SC symmetry as shown in the phase diagram.

Fig. 6.6(b) shows the spectral function at δ=0.05 computed within the non-local methods, DF and DΓA. T is set to $0.1t$ which is higher than T at Fig. 6.6(a). Due to this high T, the spectral weight is heavily reduced and quite broad. Nevertheless, the formation of the Fermi arc due to the non-local effect is still noticeable. Namely, the spectral weight at $(\pm\frac{\pi}{2},\pm\frac{\pi}{2})$ is slightly enhanced than the $(\pm\pi, 0)$ and $(0, \pm\pi)$ points. This Fermi arc formation does not necessarily reduce the paring bubble $\chi^{0,p-p}$ compared to DMFT $\chi^{0,p-p}$ since the overall spectral weight

within DF and DΓA is more coherent than the DMFT spectral weight. This can be understood from the non-local self-energy result as will be shown in the next subsection.

6.1.6 The non-local self-energy

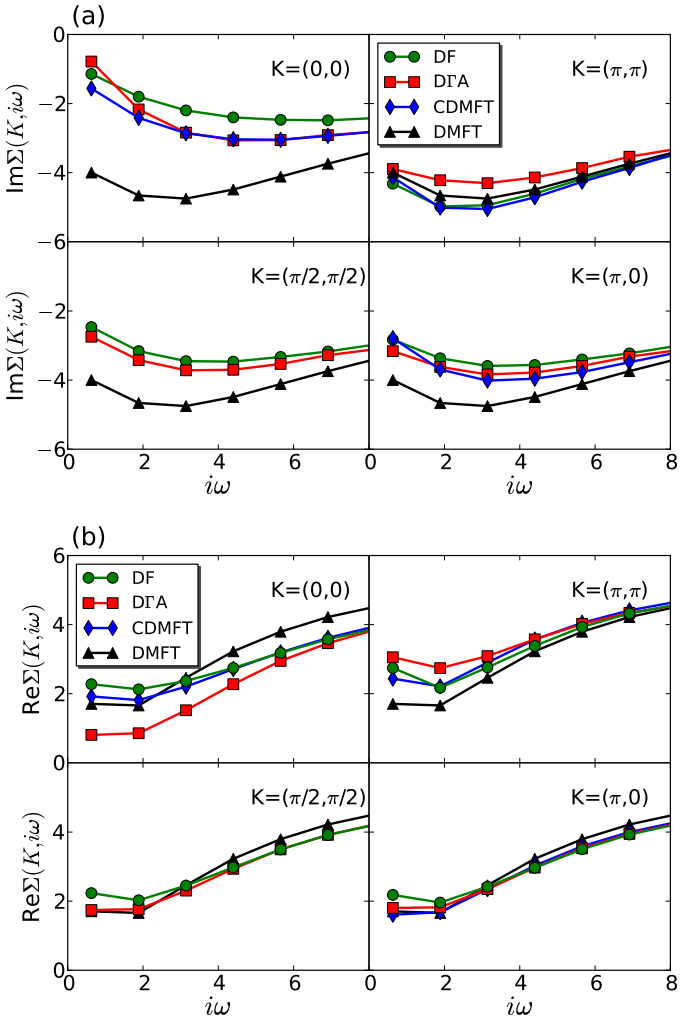

Figure 6.7: The comparison of non-local self energies $\Sigma(\mathbf{k}, i\omega)$ computed using DF (green circle) and DΓA (red square) at $\mathbf{k}$=(0,0), (π,π), (π/2,π/2), and (π,0). The 2×2 cellular DMFT (CDMFT) result (blue diamond) and the single site DMFT result (black triangle) are also shown for comparison. The doping δ is fixed to 0.05 and T=0.2t. (a) The imaginary part of $\Sigma(\mathbf{k}, i\omega)$. (b) The real part of $\Sigma(\mathbf{k}, i\omega)$.

We show the non-local self energy $\Sigma(\mathbf{k}, i\omega)$ at momentum $\mathbf{k}$=(0,0), (π,π), (π/2,π/2), and (π,0) computed within the DF and DΓA methods. The 2×2 CDMFT results at $\mathbf{k}$=(0,0), (π,π),

and (π,0) are also shown for the consistency check. Fig. 6.7 (a) displays the imaginary part of $\Sigma(\mathbf{k}, i\omega)$. In both the DF and D$\Gamma$A methods, the scattering rate $Im\Sigma(\omega = 0)$ at (0,0) gets smaller compared to other momentums namely more coherent while (π,π) self energies are quite incoherent due to the non-local correlations. Both methods give a good agreement with the CDMFT result.

Comparing $\mathbf{k}$=(π/2,π/2) and $\mathbf{k}$=(π,0), $Im\Sigma$ at (π,0) has slightly larger scattering rate than $\mathbf{k}$=(π/2,π/2). This momentum differentiation cause the Fermi arc shape shown in Fig. 6.6(b). At both (π/2,π/2) and (π,0), DΓA results shows a slightly more incoherent $\Sigma(\mathbf{k}, i\omega)$ than DF results. Nevertheless, both $Im\Sigma$ data show the smaller scattering rate than the DMFT $Im\Sigma$. Our result shows that quasi-particles get more coherent at high temperatures in the underdoped region due to the non-local effect. This also coincides with the enhanced $\chi_{0,p-p}$ within DF and DΓA methods compared to DMFT shown in Fig. 6.3.

Fig. 6.7(b) shows the real part of $\Sigma(\mathbf{k}, i\omega)$. At $\mathbf{k}$=(0,0), the DF result shows a better agreement with the CDMFT result while the DΓA $Re\Sigma$ is below the DF $Re\Sigma$. Since $\epsilon_{\mathbf{k}} + Re\Sigma_{\mathbf{k}}$ shows the effective quasi-particle energy, (0,0) orbital computed within DΓA is located more away from the Fermi energy compared to DF and CDMFT. The (π,π) orbital within DF also agrees well with the CDMFT result while the (π,π) orbital within DΓA is slightly increased. At both (π/2,π/2) and (π,0), $Re\Sigma$ within DF and DΓA show a good agreement with DMFT and CDMFT results even though DF result is slightly enhanced at low energy.

6.1.7 The effective $\overline{U}$

In Fig. 6.8, $\overline{U}_{eff}$ in the magnetic channel is shown as a function of T at different dopings (δ). The formula for $\overline{U}_{eff}$ is given in subsection 4.5.3. As the doping δ increase, $\overline{U}_{eff}$ is more renormalized due to the dynamical screening from coherent quasi-particles at large dopings. In the underdoped region (δ=0.05), $\overline{U}_{eff}$ is even greater than the bare interaction $12t$ shown as the dashed line in Fig. 6.8. This strong $\overline{U}_{eff}$ at δ=0.05 causes the strong pairing interaction even at high T (Fig. 6.3) and hence the high T_c in the underdoped region. In real materials,

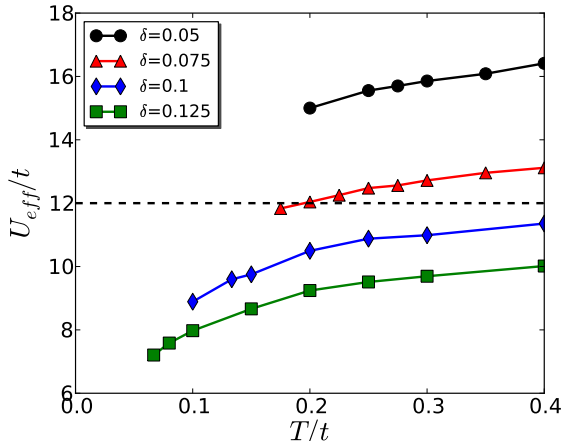

Figure 6.8: The effective interaction ($\overline{U}_{eff}$) for the electron-magnon coupling calculated as a function of T at different dopings (δ=0.05, 0.75, 0.1, and 0.125) in the Hubbard model. The dashed line marks the bare interaction U.

the strong interaction among d or f electrons can be renormlized due to screening channels with other conduction electrons, therefore this strongly enhanced $\overline{U}_{eff}$ might be the artifact of the single orbital model calculation. As T is lowered, the renormalization of $\overline{U}_{eff}$ gets more stronger since the coherence scale is also increased.

Our result of $\overline{U}_{eff}$ shows a similar feature compared to the cluster DMFT and the QMC results[95, 96]. Namely, $\overline{U}_{eff}$ decreases as δ gets larger and T is cooled down. The cluster DMFT result shows even more renormalized $\overline{U}_{eff}$ in the underdoped region This can be caused by the strong non-local correlation treated within cluster DMFT. The cluster DMFT result also shows a slight upturn of $\overline{U}_{eff}$ at very low T which might be due to the pseudo-gap physics which DMFT cannot capture. Nevertheless, $\overline{U}_{eff}$ computed within DMFT reveals a qualitatively similar feature as the $\overline{U}_{eff}$ within cluster DMFT, hence the pairing interaction as well.

6.2 The Periodic Anderson Model

6.2.1 The Hamiltonian

The periodic Anderson model treats strongly correlated fermions (f) with the on-site Coulomb interaction U, which are hybridized with non-interacting fermions (c) by the hybridization function $V(\mathbf{k})$. This model is adequate for describing materials such as the heavy fermion system containing open shells of d or f electrons and the broad s, p or d bands near the Fermi energy. Here, we consider the 2D two-band (one f and one c) periodic Anderson model. The Hamiltonian for the periodic Anderson model is given by

$$\begin{aligned}\hat{H} &= \sum_{\mathbf{k},\sigma}(\epsilon_f(\mathbf{k})-\mu)\cdot f^{\dagger}_{\mathbf{k},\sigma}f_{\mathbf{k},\sigma} + U\cdot\sum_i f^{\dagger}_{i,\uparrow}f^{\dagger}_{i,\downarrow}f_{i,\downarrow}f_{i,\uparrow} \\ &\quad + \sum_{\mathbf{k},\sigma}(\epsilon_c(\mathbf{k})-\mu)\cdot c^{\dagger}_{\mathbf{k},\sigma}c_{\mathbf{k},\sigma} + \sum_{\mathbf{k},\sigma}V(\mathbf{k})\cdot(f^{\dagger}_{\mathbf{k},\sigma}c_{\mathbf{k},\sigma}+c^{\dagger}_{\mathbf{k},\sigma}f_{\mathbf{k},\sigma}) \qquad (6.3)\end{aligned}$$

where

$$\epsilon_f(\mathbf{k}) = \epsilon^0_f + 2\epsilon_f(\cos(k_x)+\cos(k_y)) + 4\epsilon'_f\cos(k_x)\cos(k_y) \qquad (6.4)$$

$$\epsilon_c(\mathbf{k}) = 2\epsilon_c(\cos(k_x)+\cos(k_y)) + 4\epsilon'_c\cos(k_x)\cos(k_y) \qquad (6.5)$$

$$V(\mathbf{k}) = V_{\mathbf{k}}(1-\cos(k_x)\cos(k_y)) \qquad (6.6)$$

The on-site energy ϵ^0_f is -7.8ϵ_c where ϵ_c is the nearest-neighbor hopping energy of c electrons, the hopping energy of f electrons ϵ_f=0.15ϵ_c, the next-nearest neighbor hopping energy ϵ'_f=0.3ϵ_f, the next-nearest hopping energy of c electrons ϵ'_c=0.3ϵ_c, the on-site Coulomb interaction U=8ϵ_c, and the chemical potential μ=-0.4ϵ_c. Note that f electrons also have the hopping energy term unlike the typical periodic Anderson model. The hybridization parameter $V_{\mathbf{k}}$ controls correlations of f electrons from the strong correlation limit at small $V_{\mathbf{k}}$ to the weak correlation limit at large $V_{\mathbf{k}}$. In this section, we compute the superconducting T_c and the gap symmetry in the periodic Anderson model changing the parameter $V_{\mathbf{k}}$. The vertex function calculation is performed on the basis of correlated f electrons. DMFT, DΓA, and DF results are shown for the comparison.

6.2.2 The phase diagram of antiferromagnetism and superconductivity

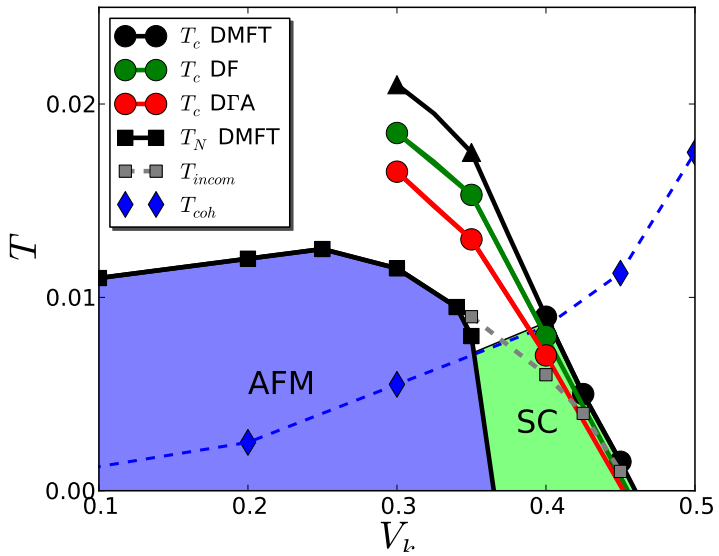

Figure 6.9: The phase diagram of the antiferromagnetic Neel temperature (T_N) and the superconducting critical temperature (T_c) in the periodic Anderson model. The x-axis is the hybridization constant $V_{\mathbf{k}}$ and the y-axis is T. The AFM region is determined as the region where $T < T_N$. T_N (black square dots) is calculated within DMFT. As $V_{\mathbf{k}}$ increases, commensurate (π, π) magnetism changes to incommensurate magnetism (gray square dots). The SC region is determined as the region where both $T < T_{coh}$ and $T < T_c$ are satisfied. T_c is calculated using the DMFT (black triangle and circle), DΓA (red triangle and circle), and DF (green triangle and circle) methods. In the periodic Anderson model, both the extended s-wave (triangular dots) and the d-wave symmetry (circular dots) are possible. The coherence temperature T_{coh} is computed from the scattering rate data. (see Fig. 6.16).

Fig. 6.9 shows the phase diagram of the AFM phase and the SC phase as a function of the hybridization parameter $V_{\mathbf{k}}$ and the temperarature T. In the small $V_{\mathbf{k}}$ region ($V_{\mathbf{k}}$ <0.35), the AFM state is stabilized below the Neel temperature T_N at which the (π, π) magnetic susceptibility within DMFT diverges. As $V_{\mathbf{k}}$ increases, the AFM state stabilized at small $V_{\mathbf{k}}$ is strongly suppressed and the commensurate ordering vector is shifted to the incommensurate $(\pi - \epsilon, \pi - \epsilon)$ vector. This change of the ordering vector is related to the Fermi surface change as a function of $V_{\mathbf{k}}$ (see Fig. 6.14).

The coherence temperature T_{coh} of f electrons (blue dashed line in Fig. 6.9) strongly depends

on $V_{\mathbf{k}}$. T_{coh} is determined from the temperature dependence of the quasi-particle scattering rate (see Fig. 6.16. In the small $V_{\mathbf{k}}$ region, T_{coh} is exponentially suppressed as f electrons become strongly incoherent. At $T > T_{coh}$, f electrons are almost localized since the hybridization with c electrons become negligible. It is known that the magnetic interaction between localized moments in the periodic Anderson model mostly comes via the Friedel oscillation of c electrons as an indirect way. This interaction is so called the RKKY interaction. In our model, the direct hopping between f electrons is also allowed and this hopping can also enhance AFM in this region. As $T < T_{coh}$ in the large $V_{\mathbf{k}}$ region, f electrons are strongly screened by c electrons binding as the Kondo singlet state. In this region, the f electrons behave as coherent quasi-particles below T_{coh}. The incommensurate magnetism through V_k=0.35 0.45 originates from the nesting of the large Fermi surface due to delocalized f electrons.

The SC state is stable near the magnetic phase as computed from various vertex function methods T_c computed within DMFT (black triangle and circle) is strongly enhanced even at the small $V_{\mathbf{k}}$ region ($V_{\mathbf{k}}$ 0.3). As $V_{\mathbf{k}}$ is increased, T_c keeps decreasing and is eventually suppressed to 0 near $V_{\mathbf{k}}$ 0.46 where incommensurate magnetism also disappears. This decrease of T_c occurs because the pairing interaction is weakened as magnetic fluctuations are reduced. This monotonic behavior of T_c is also shown in the previous Hubbard model calculation. For the SC gap symmetry, the extended s-wave (triangular dots in Fig. 6.9) is favored in the incoherent region ($T > T_{coh}$) while the d-wave symmetry (circular dots in Fig. 6.9) is more favored in the coherent region ($T < T_{coh}$) (see Fig. 6.10(b)). The non-local DΓA and DF methods favor the d-wave symmetry near T_c.

The non-local method beyond DMFT reduces T_c in the periodic Anderson model compared to DMFT T_c especially in the small $V_{\mathbf{k}}$ region near 0.3. In the DF method, the non-local fluctuation is included by the non-local DF self energy and the two-particle DF vertex function. As a result, T_c computed within DF is quite reduced compared to the DMFT T_c. In DΓA, the non-local fluctuation in the two-particle level is treated using a Moriya $\widetilde{\lambda}$ constant. Unlike the Hubbard model result, the non-local fluctuation treated within DΓA is even stronger than DF

producing smaller T_c. In both methods, T_c shows the maximum in the small $V_{\mathbf{k}}$ region and it decreases as the pairing interaction is reduced in the large $V_{\mathbf{k}}$ region. As will be shown in Fig. 6.11, the reduction of T_c by the non-local methods is mainly due to the renormalization of the pairing vertex. The pairing bubbles $\chi^{0,p-p}$ at each $V_{\mathbf{k}}$ are similar in both methods.

Similar as the Hubbard model result, the SC state is stable at high T even in the incoherent f electron region. The overestimated T_c at small $V_{\mathbf{k}}$ mainly originates from the enhanced pairing interaction near the magnetic phase. Nevertheless, the reduction of T_c within DΓA and DF shows that the decrease of the pairing interaction due to the non-local fluctuation is important. In our model, the f electrons at $T > T_{coh}$ does not even form a definite Fermi surface as will be shown in Fig. 6.14. This spuriously enhanced T_c in the incoherent region is the artifact of overestimated pairing interaction in the vertex funciton calculaton. Therefore, we claim that the actual SC state can be obtained by the Cooper pairing of coherent quasiparticles, i.e., when both $T < T_{coh}$ and $T < T_c$ conditions are satisfied. In this way, the phase diagram of superconductivity becomes reasonably similar to the experimental phase diagram.

Fig. 6.10(a) shows the leading eigenvalues λ of the Bethe-Salpeter equation in the pairing channel. DMFT, DΓA, and DF methods are employed for computing eigenvalues in the small $V_{\mathbf{k}}$ (=0.3) region and the large $V_{\mathbf{k}}$ (=0.4) region. As T decreases, the eigenvalues are enhanced due to the increase of the pairing interaction and the pairing bubble. λ computed within DMFT shows the largest value compared to other non-local methods at both $V_{\mathbf{k}}$ values. As the non-local effect is included, T_c is reduced in both DΓA and DF methods compared to the DMFT results. Unlike the Hubbard model result where T_c computed within the DF method is the smallest, the DΓA method reduce T_c slightly more than the DF method in the periodic Anderson model.

The SC gap symmetry is computed from the eigenfunction $\phi_{\mathbf{k}}$ of the paramagnetic Bethe-Salpeter equation in the pairing channel within DMFT. In the Hubbard model, a d-wave is always the leading gap symmetry since the large spectral weights at $(\pm\pi, 0)$ and $(0, \pm\pi)$ in the Brillouin zone make the d-wave preferable. In contrast, both a d-wave and an extended s-wave are preferred in the periodic Anderson model and they are close to each other. This is due to

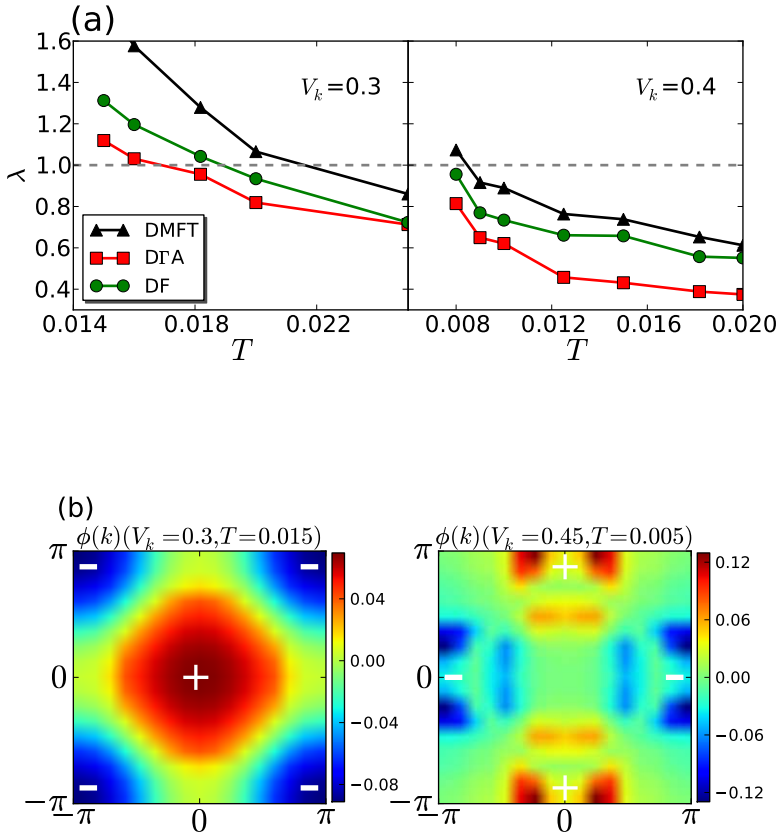

Figure 6.10: (a) The leading eigenvalue λ of the pairing susceptibility in the particle-particle channel as a function of T at $V_{\mathbf{k}}$=0.3 and 0.4. The DMFT, DΓA, and DF methods are employed for computing the eigenvalues. (b) The eigenfunction $\phi(\mathbf{k})$ computed at $V_{\mathbf{k}}$=0.3 and 0.45 near T_c. This $\phi(\mathbf{k})$ is computed within the DMFT method and it corresponds to the SC gap function.

the fact that the Fermi surface of the periodic Anderson model shown in Fig. 6.14(b) have no preference to either a d-wave or an extended s-wave even though the larger Fermi surface is similar as the Fermi surface in the Hubbard model.

The phase diagram in Fig. 6.9 shows that at high $T(\gg T_{coh})$ the extended s-wave is more favorable while the d-wave becomes more stable as T cools down. Fig. 6.10(b) shows $\phi_{\mathbf{k}}$ computed at $V_{\mathbf{k}}$=0.3, T=0.015 and at $V_{\mathbf{k}}$=0.45, T=0.005. At small $V_{\mathbf{k}}$ and large T, the Fermi surface of f electrons is not clearly formed as shown in Fig. 6.14(a) and the d-wave is suppressed due to the absence of the large Fermi surface. As the f electrons regain the coherence at large $V_{\mathbf{k}}$ and small T, the Fermi surface shows the definite shape and the d-wave symmetry becomes more favored (Fig. 6.10(b) right).

6.2.3 The pairing strength and the pairing bubble

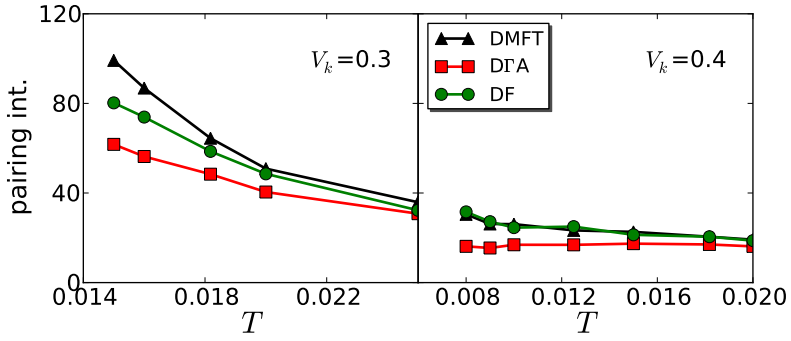

Figure 6.11: The pairing interaction $\bar{\Gamma}^{p-p,(d)}$ computed in the periodic Anderson model. The result is given as a function of T at $V_{\mathbf{k}}$=0.3 and 0.4. The results employing the DMFT, DΓA, and DF methods are compared.

Fig. 6.11 shows the pairing interaction $\bar{\Gamma}^{p-p,(d)}$ computed at $V_{\mathbf{k}}$=0.3 and 0.4 as a function of T. The DMFT, DΓA, and DF methods are used to compute $\bar{\Gamma}^{p-p,(d)}$. At $V_{\mathbf{k}}$=0.3, $\bar{\Gamma}^{p-p,(d)}$ is enhanced as T is lowered due to the enhancement of the magnetic fluctuation. The pairing interaction is slightly decreased in the DF method compared to DMFT and it is more reduced within DΓA. This result is somewhat different from the Hubbard model result where the DF

method renormalize $\bar{\Gamma}^{p-p,(d)}$ the most. The DF method is a perturbative approach around the DMFT result and this perturbation term is smaller in the periodic Anderson model since the hopping term of f electrons is smaller and the local approximation is better applicable in the periodic Anderson model. Within DΓA, the Moriya $\widetilde{\lambda}$ correction results in the strong reduction of $\bar{\Gamma}^{p-p,(d)}$. At $V_{\mathbf{k}}$=0.4, $\bar{\Gamma}^{p-p,(d)}$ values computed within DMFT and DF are similar and they increase only slightly as T decreases. In contrast, $\bar{\Gamma}^{p-p,(d)}$ computed within DΓA is more reduced and almost flat as a function of T. At $V_{\mathbf{k}}$=0.4, the magnetic susceptibility gets smaller and the peak position becomes incommensurate as will be shown in Fig. 6.13, and the pairing interaction is also quite reduced.

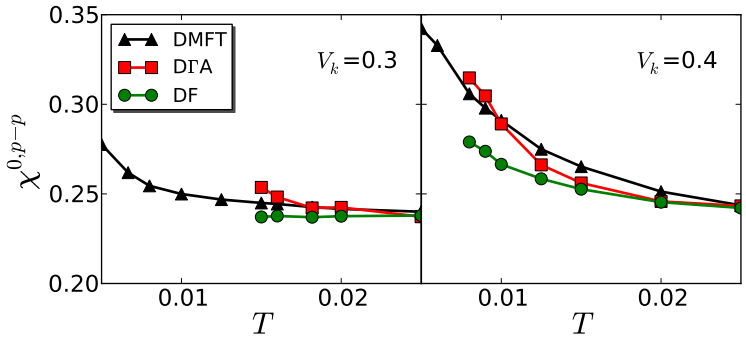

Figure 6.12: The pairing bubble in the particle-particle channel $\chi^{0,p-p}$ projected to the d-wave symmetry channel. $\chi^{0,p-p}$ is calculated as a function of T at $V_{\mathbf{k}}$=0.3 and 0.4. The DMFT, DΓA, and DF methods are used for the comparison.

Fig. 6.12 shows the pairing bubble diagram $\chi^{0,p-p}$ projected to the d-wave symmetry as a function of T. At $V_{\mathbf{k}}$=0.3, $\chi^{0,p-p}$ computed within DMFT is almost flat and only slightly increases at very low T below 0.01 estimated as T_{coh} from Fig. 6.9. Within the DΓA and DF methods, $\chi^{0,p-p}$ shows similar values as DMFT up to the calculated T. At $V_{\mathbf{k}}$=0.4, $\chi^{0,p-p}$ obtained by DMFT is more rapidly increasing at higher T than $V_{\mathbf{k}}$=0.3 since T_{coh} is higher at the large $V_{\mathbf{k}}$. $\chi^{0,p-p}$ computed within DF is a little smaller than the DMFT result while the DΓA $\chi^{0,p-p}$ is quite enhanced at low T. This enhanced $\chi^{0,p-p}$ at $V_{\mathbf{k}}$=0.4 can contribute to superconductivity in this region.

6.2.4 The magnetic susceptibility and the spectral function

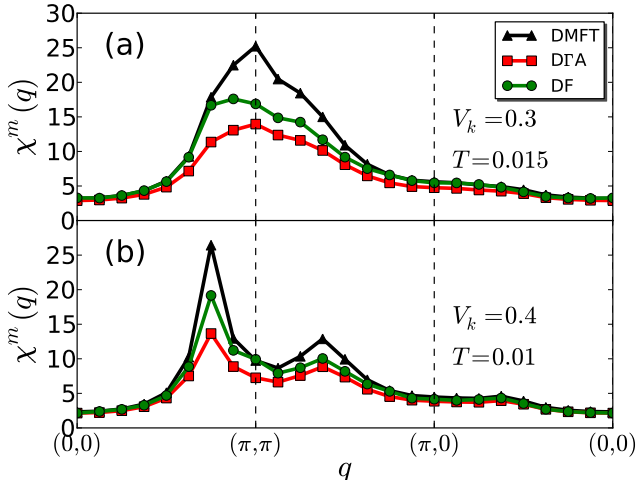

Figure 6.13: The magnetic susceptibility $\chi^m(\mathbf{q})$ of the periodic Anderson model as a function of the momentum transfer $\mathbf{q}$ near T_N. For comparison, $\chi^m(\mathbf{q})$ is computed from the DMFT, DΓA, and DF methods. (a) : $V_\mathbf{k}$=0.3, T=0.015. In this region, the f electrons are rather localized and the ordering vector $\mathbf{q}$ corresponds to $2k_F$ of the c electrons due to the RKKY magnetic interaction. (see Fig. 6.14 (a)). (b) : $V_\mathbf{k}$=0.4, T=0.01. The f electrons bahave as the itinerant quasi-particles and the ordering vector is determined from the nesting of the f electron Fermi surface. (see Fig. 6.14 (b)).

Fig. 6.13 shows $\chi^m(\mathbf{q})$ computed using the DMFT vertex function and non-local vertices (DΓA and DF). At both $V_\mathbf{k}$=0.3 and $V_\mathbf{k}$=0.4, the susceptibilities calculated using non-local methods are reduced than the DMFT susceptibility. This is due to the inclusion of non-local correlations beyond local DMFT correlations. The DΓA susceptibility is more renormalized in the periodic Anderson model at both $V_\mathbf{k}$=0.3 and $V_\mathbf{k}$=0.4. The peak position of $\chi^m(\mathbf{q})$ does not change in both DΓA and DF methods compared to DMFT at $V_\mathbf{k}$=0.4 while the DF $\chi^m(\mathbf{q})$ peak is slightly shifted to $(\pi-\epsilon, \pi-\epsilon)$ at $V_\mathbf{k}$=0.3.

In the small $V_\mathbf{k}$ region ($V_\mathbf{k}$ = 0.3), the magnetic susceptibility $\chi^m(\mathbf{q})$ has a peak at $\mathbf{q} = (\pi, \pi)$ as shown in Fig. 6.13(a). This peak can be understood from the spectral weight data in Fig. 6.14(a). In this small $V_\mathbf{k}$ and $T > T_{coh}$ region, f electrons behave as incoherent localized moments. As a result, Fig. 6.14(a) left shows that f electrons have the strongly reduced and broad spectral weight in the Brillouin zone and they do not form a definite shape of the Fermi

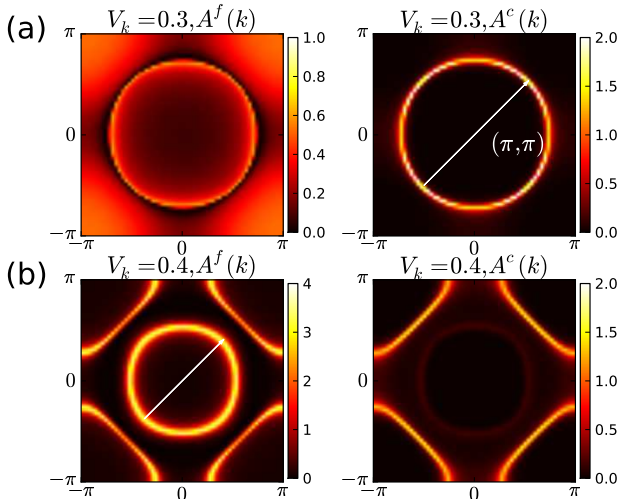

Figure 6.14: The f electron and the c electron spectral function $A^{f,c}(k,\omega=0) = -\frac{1}{\pi}G^{f,c}(k,\omega=0)$. (a) The hybridization $V_{\mathbf{k}}$=0.3ϵ_c and T=0.018ϵ_c. f electrons (left) show the broad and small spectral weight near the Fermi energy due to incoherence ($T > T_{coh}$) while c electrons (right) form a clear Fermi surface. (b) $V_{\mathbf{k}}$=0.4ϵ_c and T=0.005ϵ_c. f electrons are strongly hybridized with c electrons and two definite Fermi surfaces are formed contributed from both f and c electrons. ($T < T_{coh}$)

surface. In contrast, coherent c electrons show a clear circular Fermi surface. The magnetic interaction of localized f electrons is mediated by c electrons, i.e., the RKKY interaction. In this interaction, the magnetic ordering vector is given as $2k_F$ of c electrons as indicated in the white arrow of Fig. 6.14(a). This $2k_F$ vector corresponds to the antiferromagnetic ordering vector (π,π) of f electrons.

As $V_{\mathbf{k}}$ increases to 0.4, the $\chi^m(\mathbf{q})$ peak at $\mathbf{q}=(\pi,\pi)$ is strongly suppressed while the peak position is shifted to $\mathbf{q}=(\pi-\epsilon,\pi-\epsilon)$. This peak position shift is closely related to the change of the f electron Fermi surface. In the large $V_{\mathbf{k}}$ and small T region ($T < T_{coh}$), f electrons are delocalized and they form two clear Fermi surfaces as shown in Fig. 6.14(b) left. The magnetic ordering vector $(\pi-\epsilon,\pi-\epsilon)$ originates from the Fermi surface nesting vector shown as the white arrow in Fig. 6.14(b) left. Fig. 6.14(b) right shows that c electrons are mostly concentrated on the larger Fermi surface.

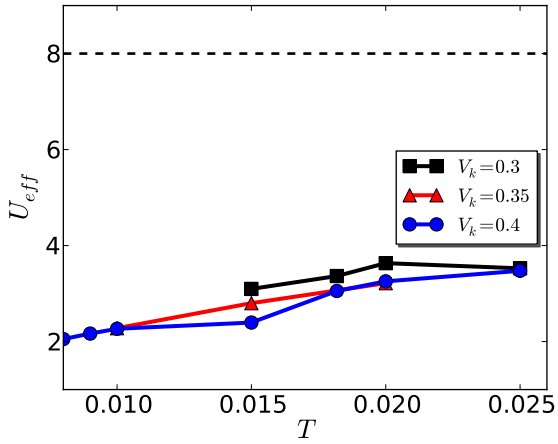

Figure 6.15: The effective $\overline{U}$ calculated as a function of T in the period Anderson model. The data are shown at $V_{\mathbf{k}}$=0.3, 0.35, and 0.4. The bare interaction U is $8\epsilon_c$ shown as the dashed line.

6.2.5 The effective $\overline{U}$

Fig. 6.15 displays the effective interaction $\overline{U}_{eff}$ as a function of T. As $V_{\mathbf{k}}$ gets large and T becomes small, $\overline{U}_{eff}$ is more renormalized since f electrons are screened by the enhanced hybridization with c electrons. Here, $\overline{U}_{eff}$ is quite smaller than the bare U value even at $V_{\mathbf{k}}$=0.3. This implies that the screening of the periodic Anderson model is more effective due to c electrons compared with the one-band Hubbard model with f electron alone. This screening of $\overline{U}_{eff}$ originates from the scattering in the particle-particle channel known as the Kanamori screening [92].

6.2.6 The scattering rate, $Im\Sigma(i\omega = 0^-)$

Fig. 6.16 shows the scattering rate $Im\Sigma(i\omega = 0^-)$ result as a function of T in various $V_{\mathbf{k}}$ values. The $Im\Sigma(i\omega = 0^-)$ value is obtained by extrapolating the lowest Matsubara points of the DMFT $Im\Sigma$ to $i\omega = 0^-$. This $Im\Sigma(i\omega = 0^-)$ data can be used to determine the T_{coh} of the periodic Anderson model (see Fig. 6.9). In a Fermi liquid, the scattering rate scales as T^2 at low T ($T < T_{coh}$). As T increases more than T_{coh}, the scattering rate increases rather slowly and saturates at a maximum value.

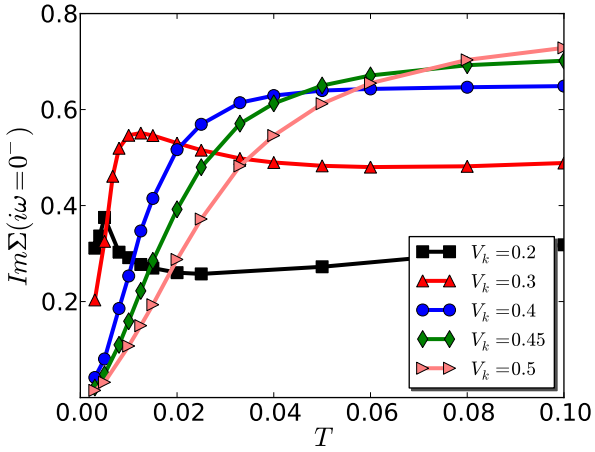

Figure 6.16: The scattering rate $Im\Sigma(i\omega = 0^-)$ as a function of T in the periodic Anderson model. The results are shown varying $V_{\mathbf{k}}$ from 0.2 to 0.5 values. The $Im\Sigma$ data are obtained from the DMFT solution.

At $V_{\mathbf{k}}$ =0.4∼0.5, $Im\Sigma(i\omega = 0^-)$ obeys this Fermi liquid behavior, i.e., it is proportional to T^2 at low T and saturates at much higher T. T_{coh} is the crossover temperature from the low T region to the high T region. Here, we determine T_{coh} as the temperature where $\frac{d(Im\Sigma(i\omega=0^-))}{dT}$ reaches a maximum.

In the small $V_{\mathbf{k}}$ region ($V_{\mathbf{k}}$=0.2∼0.3), $Im\Sigma(i\omega = 0^-)$ shows strongly enhanced values at even low T and the coherence scale below which T scales as T^2 becomes much reduced. As T increases, the scattering rate shows a maximum and it is slowly decreased and saturated. This maximum of $Im\Sigma(i\omega = 0^-)$ in the localized region is indicative of the resistivity maximum at low T in the Kondo impurity model which originates from the impurity scattering with conduction electrons. In this small $V_{\mathbf{k}}$ region, the criterion from the $\frac{d(Im\Sigma(i\omega=0^-))}{dT}$ calculation is ambiguous, therefore, we determine T_{coh} as one half of the temperature where $Im\Sigma(i\omega = 0^-)$ becomes maximum.

6.3 Conclusion

As a conclusion, we computed the phase diagram of the magnetic phase and the superconducting phase in both the Hubbard model and the periodic Anderson model. In both models, the

superconducting phase is stable near the magnetic phase at which the magnetic fluctuation is strong. Different vertex function calculations based on the DMFT, DF, and DΓA methods are employed, and the results are compared. T_c is determined as a combination of the pairing strength and the pairing bubble, i.e., the density of states of the system. The SC gap function is closely related to the momentum dependence of the pairing vertex and the Fermi surface geometry of quasi-particles.

The vertex function calculation based on DMFT, DF, and DΓA is an inexpensive and efficient approach to compute T_c and the SC gap symmetry compared to the cluster extension of DMFT. We showed that these approaches can capture the strong magnetic fluctuation effect causing the pairing instability in both the Hubbard model and the periodic Anderson model. As shown in Chapter 4, this vertex function approach can be applied to the realistic multi-orbital system in a straightforward way. The cluster DMFT is not applicable to the multi-orbital system since it gets numerically too expensive. The RPA calculation of superconductivity is quite inexpensive but it works exclusively in the itinerant limit, and the irreducible vertex in the particle-hole channel is replaced by a constant as an approximation. Therefore, the vertex function calculation approach will be a promising route to study the microscopic origin of the pairing mechanism in many superconducting correlated materials.

Chapter 7

The Magnetic Excitation Spectra in Fe-based Superconductors

In this chapter, we study the magnetic excitation spectra in the paramagnetic state of $BaFe_2As_2$ from the *ab initio* perspective [77]. The one-particle excitation spectrum is determined within the combination of the density functional theory and the dynamical mean-field theory method. The two-particle response function is extracted from the local two-particle vertex function, also computed by the dynamical mean field theory, and the polarization function. This method reproduces all the experimentally observed features in inelastic neutron scattering (INS), and relates them to both the one particle excitations and the collective modes. At low frequency the magnetic excitation spectra, as encoded in $S(q, \omega)$, is strongly peaked at the magnetic ordering wave vector $(1, 0, 1)$. With increasing energy the peak position shifts, and around 230 meV the peak moves to the wave vector $(1, 1, 1)$, in good agreement with inelastic neutron scattering (INS) experiments on $BaFe_2As_2$. This high energy peak is shown to originate mainly from the intra-orbital excitations in the d_{xy} orbital from the momentum space regions near the two electron pockets. The magnetic excitation dispersion is well accounted for by our theoretical calculation in the paramagnetic state without any broken symmetry, hence nematic order is not needed to explain the INS experimental data.

7.1 Introduction to Fe-based superconductors

7.1.1 History

In 2008, Hideo Hosono and the co-workers discovered that fluorine-doped LaOFeAs shows superconductivity with as high T_c as 26K [97]. Right after this discovery, it was reported that fluorine-doped LaOFeAs can show T_c around 43K by the application of pressure [98] and the T_c value can be further increased by replacing La by other rare earth elements [99]. Following this discovery of the Fe-based superconductor, tremendous research efforts have been stimulated to synthesize new Fe-based compounds with higher T_c and to understand the origin of superconductivity in these new materials. After the experimental discovery, theoretical electronic structure calculation [70] showed that these materials have both localized and itinerant aspects of correlated electrons, and the pairing mechanism of superconductiviy can be non-phonon mediated similar as the cuprate superconductors. However, it is not unraveled until now what is really the mediator of pairing in these systems and it requires new theoretical advances and experimental efforts. Therefore, the discovery of the Fe-based superconductors has opened a new avenue of research to understand the origin of superconductivity in strongly correlated condensed matter systems.

7.1.2 Crystal structure

The crystal structure of Fe-based superconductors has a common feature, i.e., it has a layered structure based on Fe atoms joined by tetrahedrally coordinated pnictogens (P, As) or chalcogens (S, Se, Te). And these layers are arranged in a stacked sequence separated by alkali, alkaline-earth or rare-earth and oxygen/fluorine layers. The Fe-based superconductors with Fe atoms surrounded by pnictogens are usually called as Fe pnictides and the materials with Fe atoms surrounded by chalcogens are called as Fe chalcogenides. Similar to the CuO_2 plane in cuprate superconductors, the two-dimensional Fe plane plays an important role for magnetism and superconductivity in these materials.

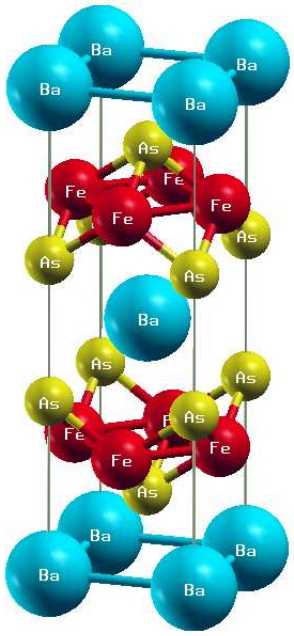

Figure 7.1: The crystal structure of $BaFe_2As_2$. This figure depicts the conventional unit cell of the body-centered tetragonal structure.

The five distinct tetragonal structures are known to exist in Fe-based superconductors [4]. Fig. 7.1 shows the body-centered tetragonal structure of $BaFe_2As_2$, so called the 122 structure. This structure is the most studied one among the five structures. The known experimental lattice constants for $BaFe_2As_2$ are shown in Table. 7.1. The large c/a ratio indicates that two-dimensional physics may be crucial for the study in 122 systems. Moreover, z_{As} plays an crucial role in determining T_c of Fe-based superconductors and T_c is highest when the As-Fe-As tetrahedral bond angle is closest to the ideal value of 109.47°

a	3.9625Å
c	13.0168Å
z_{As}	1.3603Å

Table 7.1: The lattice constants of $BaFe_2As_2$. a is the length in the x- (y-) direction of the conventional unit cell, c is the height of the unit cell, and z_{As} is the height of the As atom from the Fe plane.

7.1.3 Phase diagram

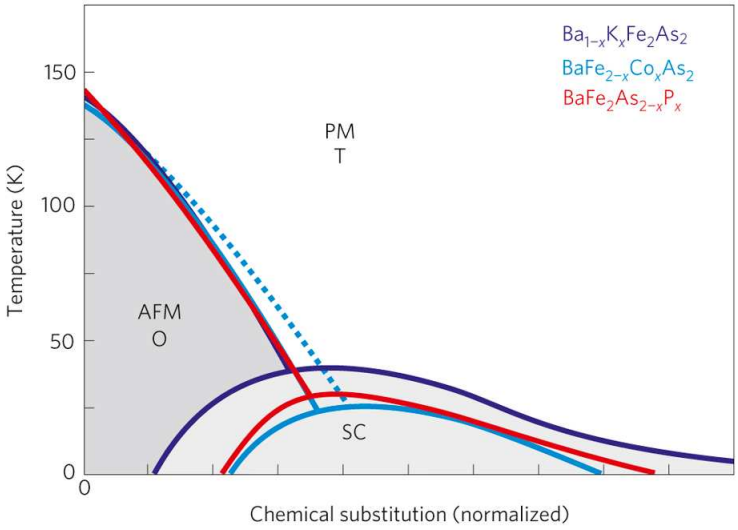

Figure 7.2: The phase diagram of $BaFe_2As_2$ obtained by the chemical substitution of either Ba with K [1] (dark blue), Fe with Co [2] (blue), or As with P [3] (red). The dashed line shows the structural transition. This figure is taken from Ref. [4].

Fig. 7.2 displays the phase diagram of $BaFe_2As_2$ obtained by manipulating the chemical doping/substitution of the material. By substituting either the alkaline-earth (Ba), transition-metal (Fe), or pnictogen (As) atom with a different element, one can produce the similar phase diagrams once the chemical substitution is normalized to overlap the descent of the AFM transition. The chemical substitution or alternatively applied external pressure drives an antiferromagnetic (AFM) state to a superconducting (SC) state. Between the AFM and the SC states, two states also coexist within a certain range. A structural phase transition from the tetragonal (T) structure to the orthorhombic (O) phase is observed for Co substitution, which is coincident with the paramagnetic to AFM phase transition in $BaFe_2As_2$. This phase diagram of iron pnictide is quite similar with the phase diagram of cuprates. However, a significant difference is the AFM state of the parent compound in $BaFe_2As_2$ is metallic while the parent compound of cuprates shows the Mott insulating behavior. Due to the metallic nature of magnetism in iron pnictides, it is crucial to understand whether magnetism in these materials

can be described with either the localized picture or the itinerant picture, or both pictures are required.

7.1.4 Inelstic neutron scattering in Fe-based superconductors

Neutron scattering [100] is a powerful experimental technique since it sheds light on studying the magnetic structure and dynamics of condensed matter system. A neutron has zero chage and hence it does not interact with other charged particles such as an electron or a proton by the Coulomb interaction. Therefore, a neutron can penetrate deeply into a material and it can measure the bulk property. However, a neutron has one half spin, therefore it readily interacts with the magnetic moment of an electron by the dipole-dipole interaction.

Since neutron scattering acts as a weak perturbation to the system, the differential cross section can be calculated from the Fermi Golden rule. In inelastic neutron scattering (INS), the differential cross section is given by

$$\frac{d^2\sigma}{d\Omega dE} = \frac{k_f}{k_i}(\frac{m_N}{2\pi\hbar^2})^2 |\langle k_f\lambda_f|V|k_i\lambda_i\rangle|^2\delta(\hbar\omega + E_i - E_f) \tag{7.1}$$

where V is the interaction operator for the neutron, $\lambda_{i(f)}$ is the quantum numbers for initial(final) state of the sample, $k_{i(f)}$ is initial(final) momentum, $E_{i(f)}$ is the initial(final) energy, and m_N is the neutron mass. The magnetic field generated inside matter can be produced by either the electron spin or the electron orbital motion. Here, we consider only the contribution from the electron spin. A neutron interacts with this electron spin by the dipole-dipole interaction. Therefore, the magnetic interaction V is given by

$$V = -\mu_N \cdot B = -\frac{\mu_0\mu_N}{4\pi}[\nabla \times (\frac{\mu_e \times \hat{R}}{R^2})] \tag{7.2}$$

Here, μ_0 is the magnetic constant, μ_e is the electron magnetic moment, and μ_N is the neutron magnetic moment.

By inserting Eq. 7.2 to Eq. 7.1, the magnetic cross section is given by

$$\frac{d^2\sigma}{d\Omega dE} = (\gamma r_0)^2 N\frac{k_f}{k_i}\cdot f(\mathbf{q})^2\cdot e^{-2W}\sum_{\alpha\beta}(\delta_{\alpha\beta} - \hat{q}_\alpha\cdot\hat{q}_\beta)\cdot S^{\alpha\beta}(\mathbf{q},\omega) \tag{7.3}$$

where α, β means the coordinates (x, y, z) and $\delta_{\alpha\beta} - \hat{q}_\alpha \cdot \hat{q}_\beta$ term means only the magnetic moment perpendicular to $\hat{q}$ contributes to the cross section. And $f(\mathbf{q})$ is the magnetic form factor obtained by the Fourier transform of the unpaired electron density. Here, $S(\mathbf{q}, \omega)$ is the dynamical structure factor which is the Fourier transform of the spin-spin correlation function and given by

$$S^{\alpha\beta}(\mathbf{q}, \omega) = \frac{1}{2\pi\hbar} \int dt e^{-i\omega t} \sum_l e^{i\mathbf{q}\cdot\mathbf{r}_l} \left\langle S_0^\alpha(0) \cdot S_l^\beta(t) \right\rangle. \tag{7.4}$$

Due to the fluctuation-dissipation theorem, the imaginary part of the magnetical susceptibility is related to the correlation funciton by the following equation

$$S(\mathbf{q}, \omega) = \frac{\chi''(\mathbf{q}, \omega)}{1 - e^{-\frac{\hbar\omega}{kT}}}. \tag{7.5}$$

Neutron scattering experiments provide strong constraints on the theory of iron pnictides. Both the localized picture and the itinerant picture of the magnetic response have had some successes in accounting or even predicting aspects of the experiments. Calculations based on a spin model with frustrated exchange constants [101, 102] or with biquadratic interactions [103] described well the neutron scattering experiments [104, 105]. The itinerant magnetic model, based on an random phase approximation (RPA) form of the magnetic response, uses polarization functions extracted from density functional theory (DFT) [106] or tight binding fits [107, 81, 108] and produces equally good descriptions of the experimental data.

Furthermore, DFT calculations predicted the stripe nature of the ordering pattern [109] and the anisotropic values of the exchange constants which fit well the spin wave dispersion in the magnetic phase [110]. The tight binding calculations based on DFT bands also predicted the existence of a resonance mode in the superconducting state [111].

In spite of these successes, both itinerant and localized models require significant extensions to fully describe the experimental results. DFT fails to predict the observed ordered moment [110]. Furthermore, adjusting parameters such as the arsenic height to reproduce the ordered moment, leads to a peak in the density of states at the Fermi level [106], instead of the pseudogap, which is observed experimentally. The localized picture cannot describe the

magnetic order in the FeTe material without introducing additional longer range exchange constants. Given that this material is more localized than the 122, the exchange constants would be expected to be shorter range. Furthermore, fits of the INS data require the use of anisotropic exchange constants well above the magnetic ordering temperature [5]. However no clear phase transition to a nematic phase in this range has been detected.

In this chapter, we argue that the combination of density functional theory and dynamical mean field theory (DFT+DMFT) provides a natural way to improve both the localized and the itinerant picture, and connects the neutron response to structural material specific information and to the results of other spectroscopies.

7.2 Calculation methods

7.2.1 The dynamical magnetic susceptibility $\chi(\mathbf{q}, \omega)$

In this subsection, we explain the method for computing the dynamical magnetic susceptibility $\chi(\mathbf{q}, \omega)$ using a combination of density functional theory (DFT) and dynamical mean field theory (DMFT). The equations for computing $\chi(\mathbf{q}, i\omega)$ are already derived in Section 4.4 in details. Therefore, we explain here how to compute $\chi(\mathbf{q}, i\omega)$ briefly and discuss how to analytically continue the obtained $\chi(\mathbf{q}, i\omega)$ to $\chi(\mathbf{q}, \omega)$ on the real axis.

Within DFT+DMFT, the dynamical magnetic susceptibility $\chi(\mathbf{q}, i\omega)$ is computed from the *ab initio* perspective using the polarization bubble χ^0 and the two-particle irreducible vertex function Γ^{irr}_{loc} of DFT+DMFT solution [112], which is assumed to be local in the same basis in which the DMFT self-energy is local, implemented here by the projector to the muffin-tin sphere [14]. χ^0 is computed from the fully interacting one particle Greens function. We compute the one-particle Green's function using the charge self-consistent full potential DFT+DMFT method, as implemented in Ref. [14], based on Wien2k code [113]. We used the continuous-time quantum Monte Carlo (CTQMC) [17, 16] as the quantum impurity solver, and the Coulomb interaction matrix as determined in Ref. [114]. (U=5eV and J=0.7eV respectively) In order to

extract Γ^{irr}_{loc}, we employ the Bethe-Salpeter equation which relates the local two-particle Green's function (χ_{loc}), sampled by CTQMC, with both the local polarization function (χ^0_{loc}) and Γ^{irr}_{loc}:

$$\Gamma^{irr}_{loc\,\substack{\alpha_1\sigma_1,\alpha_2\sigma_2\\ \alpha_3\sigma_3,\alpha_4\sigma_4}}(i\nu, i\nu')_{i\omega} = [(\chi^0_{loc})^{-1}_{i\omega} - \chi^{-1}_{loc}]. \tag{7.6}$$

Γ^{irr}_{loc} depends on three Matsubara frequencies ($i\nu$, $i\nu'$; $i\omega$), and both the spin (σ_{1-4}) and the orbital (α_{1-4}) indices, which run over $3d$ states on the iron atom.

The momentum dependent two-particle Green's function χ is constructed using the Bethe-Salpeter equation by replacing the local polarization function χ^0_{loc} by the non-local one $\chi^0_{\mathbf{q},i\omega}$:

$$\chi_{\substack{\alpha_1\sigma_1,\alpha_2\sigma_2\\ \alpha_3\sigma_3,\alpha_4\sigma_4}}(i\nu, i\nu')_{\mathbf{q},i\omega} = [(\chi^0)^{-1}_{\mathbf{q},i\omega} - \Gamma^{irr}_{loc}]^{-1}. \tag{7.7}$$

Finally, the dynamic magnetic susceptibility $\chi(\mathbf{q}, i\omega)$ is obtained by closing the two particle green's function with the magnetic moment $\mu = \mu_B(\mathbf{L}+2\mathbf{S})$ vertex, and summing over frequencies ($i\nu$,$i\nu'$), orbitals (α_{1-4}), and spins (σ_{1-4}) on the four external legs

$$\chi(\mathbf{q}, i\omega) = \sum_{i\nu, i\nu'} \sum_{\substack{\alpha_1\alpha_2\\ \alpha_3\alpha_4}} \sum_{\substack{\sigma_1\sigma_2\\ \sigma_3\sigma_4}} \mu^z_{\alpha_1\sigma_1}{}_{\alpha_3\sigma_3}\, \mu^z_{\alpha_2\sigma_2}{}_{\alpha_4\sigma_4}\; \chi_{\substack{\alpha_1\sigma_1,\alpha_2\sigma_2\\ \alpha_3\sigma_3,\alpha_4\sigma_4}}(i\nu, i\nu')_{\mathbf{q},i\omega} \tag{7.8}$$

The resulting dynamical magnetic susceptibility is obtained in Matsubara frequency ($i\omega$) space and it needs to be analytically continued to real frequencies ($\chi(\mathbf{q}, \omega)$) in order to compare with the INS data. For the low frequency region, on which we concentrate here, the vertex Γ^{irr}_{loc} is analytically continued by a quasiparticle-like approximation. We replace the frequency dependent vertex with a constant, i.e.,

$$\Gamma^{irr}_{loc\,\substack{\alpha_1\sigma_1,\alpha_2\sigma_2\\ \alpha_3\sigma_3,\alpha_4\sigma_4}}(i\nu, i\nu')_{i\omega} \approx \bar{U}_{\substack{\alpha_1\sigma_1,\alpha_2\sigma_2\\ \alpha_3\sigma_3,\alpha_4\sigma_4}}(\mathbf{q}) \tag{7.9}$$

and require $\chi(\mathbf{q}, i\omega = 0) = \chi(\mathbf{q}, \omega = 0)$. This vertex $\bar{U}$ however retains important spin and orbital dependence. And $\bar{U}$ acquires even the weak momentum $\mathbf{q}$ dependence to satisfy the above condition.

The analytic continuation of the one-particle Green's function to the real axis is achieved by analytically continuing the self energy using the method implemented in Ref. [14]. Since the

two-particle vertex is approximated to a frequency independent constant on the real axis, the internal Matsubara frequency $i\nu$ of the polarization bubble χ^0 can be summed over:

$$\begin{aligned}
\chi^0_{\substack{\alpha\beta\\ \delta\gamma}}(\mathbf{q}, i\omega) &= -\frac{1}{N_k}\sum_{\mathbf{k}, i\nu} G_{\alpha\beta}(\mathbf{k}, i\nu)\cdot G_{\gamma\delta}(\mathbf{k}+\mathbf{q}, i\nu+i\omega) \\
&= -\frac{1}{N_k}\sum_{\mathbf{k}} \frac{1}{2\pi i}\oint dz G_{\alpha\beta}(\mathbf{k}, z)\cdot G_{\gamma\delta}(\mathbf{k}+\mathbf{q}, z+i\omega) \\
&= -\frac{1}{N_k}\sum_{\mathbf{k}} \int d\nu \left[A_{\alpha\beta}(\mathbf{k},\nu)\cdot G_{\gamma\delta}(\mathbf{k}+\mathbf{q},\nu+i\omega) - G_{\alpha\beta}(\mathbf{k},\nu-i\omega)\cdot A_{\gamma\delta}(\mathbf{k}+\mathbf{q},\nu)\right] \\
&\quad \cdot f(\nu) \qquad (7.10)
\end{aligned}$$

where $f(\nu)$ is the Fermi function. Here, we replace the Matsubara sum to the integral over the complex plane. And χ^0 can be obtained on the real axis:

$$\begin{aligned}
(\chi^0)''_{\substack{\alpha\beta\\ \delta\gamma}}(\mathbf{q}, \omega) &= -\frac{\pi}{N_k}\sum_{k} \int d\nu [A_{\alpha\beta}(\mathbf{k},\nu)\cdot A_{\gamma\delta}(\mathbf{k}+\mathbf{q},\nu+\omega) - A_{\alpha\beta}(\mathbf{k},\nu-\omega)\cdot A_{\gamma\delta}(\mathbf{k}+\mathbf{q},\nu)] f(\nu) \\
&= -\frac{\pi}{N_k}\sum_{k} \int d\nu A_{\alpha\beta}(\mathbf{k},\nu)\cdot A_{\gamma\delta}(\mathbf{k}+\mathbf{q},\nu+\omega)\cdot [f(\nu) - f(\nu+\omega)] \qquad (7.11)
\end{aligned}$$

Here, $(\chi^0)''(\mathbf{q},\omega) \equiv \frac{1}{2i}[\chi^0(\mathbf{q},\omega+i\delta) - \chi^0(\mathbf{q},\omega+i\delta)]$ and $A(\mathbf{k},\nu) \equiv \frac{1}{2\pi i}[G(\mathbf{k},\nu+i\delta) - G(\mathbf{k},\nu-i\delta)]$. The real part of χ^0 can be computed using the Kramers-Kronig relation from $(\chi^0)''$.

The two-particle Green's function $\chi_{\substack{\alpha\beta\\ \gamma\delta}}(\mathbf{q},\omega)$ is computed using $\chi^0(\mathbf{q},\omega)$ and $\bar{U}$ by the following Bethe-Salpeter equation

$$\chi_{\substack{\alpha\sigma_\alpha\beta\sigma_\beta\\ \gamma\sigma_\gamma\delta\sigma_\delta}}(\mathbf{q},\omega) = \chi^0_{\substack{\alpha\sigma_\alpha\beta\sigma_\beta\\ \gamma\sigma_\gamma\delta\sigma_\delta}}(\mathbf{q},\omega) + \sum_{\substack{\eta\mu\\ \lambda\nu}}\sum_{\substack{\sigma_\eta\sigma_\mu\\ \sigma_\lambda\sigma_\nu}} \chi^0_{\substack{\alpha\sigma_\alpha\eta\sigma_\eta\\ \gamma\sigma_\gamma\lambda\sigma_\lambda}}(\mathbf{q},\omega)\cdot \bar{U}_{\substack{\eta\sigma_\eta\mu\sigma_\mu\\ \lambda\sigma_\lambda\nu\sigma_\nu}}(\mathbf{q})\cdot \chi_{\substack{\mu\sigma_\mu\beta\sigma_\beta\\ \nu\sigma_\nu\delta\sigma_\delta}}(\mathbf{q},\omega) \qquad (7.12)$$

Finally, the magnetic susceptibility $\chi(\mathbf{q},\omega)$ is obtained by closing the four external legs with the magnetic moment $\mu = \mu_B(\mathbf{L}+2\mathbf{S})$ vertex by summing orbitals (α_{1-4}) and spins (σ_{1-4}) in a similar way as Eq. 7.8, i.e.,

$$\chi(\mathbf{q},\omega) = \sum_{\substack{\alpha_1\alpha_2\\ \alpha_3\alpha_4}}\sum_{\substack{\sigma_1\sigma_2\\ \sigma_3\sigma_4}} \mu^z_{\substack{\alpha_1\sigma_1\\ \alpha_3\sigma_3}}\mu^z_{\substack{\alpha_2\sigma_2\\ \alpha_4\sigma_4}}\ \chi_{\substack{\alpha_1\sigma_1,\alpha_2\sigma_2\\ \alpha_3\sigma_3,\alpha_4\sigma_4}}(\mathbf{q},\omega) \qquad (7.13)$$

For the analytic continuation of $\chi(\mathbf{q}, i\omega)$ to the real axis, we approximated Γ^{irr} to $\bar{U}$ as shown in Eq. 7.9. This approximation ensures that $\chi(\mathbf{q}, \omega=0)$ value is always exact to $\chi(\mathbf{q}, i\omega=0)$ within vertex calculation since $\bar{U}$ is determined to satisfy this condition. In order to check how this approximation is reliable at finite frequencies, we compare $\chi(\mathbf{q}, i\omega)$ computed from Γ^{irr} using Eq. 7.7 with $\chi^{\bar{U}}(\mathbf{q}, i\omega)$ obtained from the approximated $\bar{U}$.

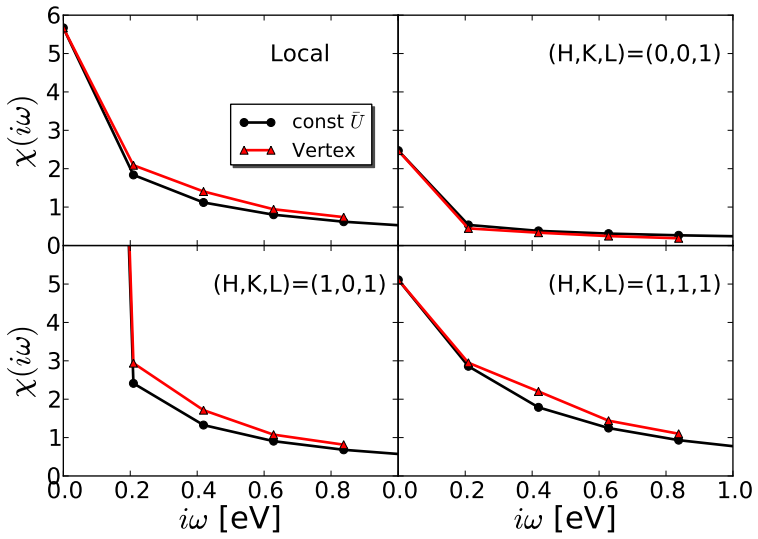

Figure 7.3: The comparison between $\chi(\mathbf{q}, i\omega)$ (red triangle) computed using vertex function Γ^{irr} and $\chi^{\bar{U}}(\mathbf{q}, i\omega)$ (black circle) obtained by $\bar{U}$. Both quantities are given on the five lowest Matsubara frequencies and at distinct wave vectors $\mathbf{q}$=(0,0,1), (1,0,1), and (1,1,1) and for the local value.

Fig 7.3 shows both $\chi(\mathbf{q}, i\omega)$ (red triangle) and $\chi^{\bar{U}}(\mathbf{q}, i\omega)$ (black circle) at $\mathbf{q}$=(0,0,1), (1,0,1), and (1,1,1) and for the local value. $\chi^{\bar{U}}(\mathbf{q}, i\omega)$ values are slightly smaller than $\chi(\mathbf{q}, i\omega)$ values except for $\mathbf{q}$=(0,0,1) where both values are almost the same. This is because the approximated $\bar{U}$ is estimated for ω=0 and the value is more renormlized compared to the vertex at high frequency ω. The discrepancy between $\chi(\mathbf{q}, i\omega)$ and $\chi^{\bar{U}}(\mathbf{q}, i\omega)$ is pronounced at $\mathbf{q}$=(1,0,1) especially at the second and the third $i\omega$ points, however, $\chi^{\bar{U}}(\mathbf{q}, i\omega)$ values show an overall good agreement with $\chi(\mathbf{q}, i\omega)$ values.

7.2.2 The phase factor for one Fe atom per unit cell

The primitive unit cell of $BaFe_2As_2$ contains two Fe atoms due to two nonequivalent positions of As atoms. Since almost entire magnetic moment is concentrated on Fe atoms, which form a square lattice, the inelastic neutron scattering (INS) data should be compared to calculation of magnetic susceptibility in the large Brillouin zone coming from this square lattice. This is because the folding of the bands is noticeable only in those quantities which have finite

contribution from the As atoms. Therefore, we computed the dynamical magnetic susceptibility within DFT+DMFT in this large Brillouin zone.

Due to inequivalent As atoms within a unit cell, the naive projection to orbital basis does not results in correct translational symmetry between Fe atoms within the unit cell. Let us consider a tight-binding Hamiltonian, written in some orbital basis, i.e.,

$$H_{\alpha\tau,\alpha'\tau'}(R,R') = \langle\varphi_{\alpha\tau}(r+R)|H|\varphi_{\alpha'\tau'}(r+R')\rangle. \tag{7.14}$$

Here, τ goes over the two Fe sites in the unit cell, which we label by a sublattice A and a sublattice B. α is the orbital index. This Hamiltonian does not have the required translational symmetry $H_{\alpha\tau,\alpha'\tau'}(R,R') \neq H_{\alpha,\alpha',\tau-\tau'}(R,R')$. However, we can restore the translational symmetry by choosing a different wave function on each sublattice, such that the new basis function on sublatice A is $\phi^A_\alpha(r) \equiv \varphi_\alpha(x,y,z)$ and on sublattice B is $\phi^B_\alpha(r) \equiv \varphi_\alpha(x,y,-z)$. This is because the As atom is positioned above the Fe plane in A sublattice and below the iron plane in B sublattice, hence the local environment on Fe atom looks translational invariant only in this new ϕ_α orbital basis. Consequently, the tight-binding Hamiltonian expressed in ϕ_α basis in translationally invariant.

Our DFT+DMFT implementation does not require construction of tight-binding Hamiltonians, but it rather employs the projection technique. The projection matrix $P_K(i,j;\tau,\alpha,\tau'\alpha')$ project physical quantities, such as the Green's function, written in Kohn-Sham basis in terms of bands $|i,j\rangle$ and the momentum K, to a local orbital subspace $|\tau\alpha,\tau'\alpha'\rangle$(see Eq.12 in Ref. [14]). By adopting the different local orbital basis for τ^A and τ^B as mentioned in the previous paragraph, this projection matrix defined for two Fe atoms per unit cell can restore the translational symmetry for one Fe atom per unit cell.

The projection matrix $P_k(i,j;\alpha,\alpha')$ in one Fe atom per unit cell acquries the phase factor that modulates with the internal vectors (τ) within the unit cell in addition to $P_K(i,j;\tau,\alpha,\tau'\alpha')$. In one Fe atom per unit cell, the momentum k is defined in the unfolded Brillouine zone (BZ) due to the smaller unit cell. The detailed derivation is given as the following equations using several unitary transformations with the real space basis ($|R\rangle$). A similar derivation is used in

the previous literature [115].

$$\begin{aligned}\langle k,\alpha|K,i\rangle &\cong \sum_{R\tau\alpha'}\langle k,\alpha|R,\tau,\alpha'\rangle\langle R,\tau,\alpha'|K,i\rangle = \frac{1}{N_R\sqrt{N_\tau}}\sum_{R\tau\alpha'}e^{-ik\cdot(R+\tau)}\delta_{\alpha\alpha'}e^{iK\cdot R}\langle\tau,\alpha'|K,i\rangle \\ &= \frac{1}{\sqrt{N_\tau}}\sum_{\tau}\delta_{k,[K]}e^{-ik\cdot\tau}\langle\tau,\alpha|K,i\rangle \end{aligned} \tag{7.15}$$

$$\begin{aligned}P_k(i,j;\alpha,\alpha') &= \langle k,\alpha|K,i\rangle\langle K,j|k,\alpha'\rangle = \frac{1}{N_\tau}\sum_{\tau\tau'}\delta_{k,[K]}e^{-ik\cdot(\tau-\tau')}\langle\tau,\alpha|K,i\rangle\langle K,j|\tau',\alpha'\rangle \\ &= \frac{1}{N_\tau}\sum_{\tau\tau'}\delta_{k,[K]}e^{-ik\cdot(\tau-\tau')}P_K(i,j;\tau\alpha,\tau'\alpha') \end{aligned} \tag{7.16}$$

Here, $K(k)$ is the momentum in the (un)folded Brillouin zone, $[K]$ means the set of momentum vectors which are equivalent to K by the modulo of the reciprocal vector G. i,j are the band indices, R is the lattice vector for a primitive unit cell (two Fe per cell), τ is the internal vector within the unit cell, α is the local orbital basis defined inside the Fe atom, and N_τ is the number of Fe atoms inside the unit cell.

The spectral quantities which are mostly concetrated on the Fe atoms can be computed in the symmetry of one Fe atom per unit cell using this projection matrix (Eq.7.16). For example, the Green's function projected to one Fe atom per unit cell can be given by

$$G_{\alpha\beta}(k,\nu) = \sum_{K,i,j} g_{ij}(K,\nu)\cdot P_k(i,j;\alpha,\beta) \tag{7.17}$$

where $g_{ij} = \left(\frac{1}{\nu+\mu-\epsilon_K-P^{-1}\Sigma}\right)_{ij}$ is the Green's function on the band indices.

7.3 Magnetic excitation spectra in $BaFe_2As_2$: DFT+DMFT results

7.3.1 The dynamical structure factor $S(\mathbf{q},\omega)$ results

Fig. 7.4(a) shows the calculated constant energy plot of the dynamical structure factor, $S(\mathbf{q},\omega)$ in the paramagnetic state of $BaFe_2As_2$. Our theoretical results are calculated in the unfolded Brillouin zone of one Fe atom per unit cell, because magnetic excitations are concentrated primarily on Fe atoms, therefore folding, which occurs due to the two inequivalent arsenic atoms in the unit cell, is not noticeable in magnetic response [107]. For comparison we also reproduce in Fig. 7.4(b) the INS experimental data from Ref. [5]. At low energy (around ω=50meV),

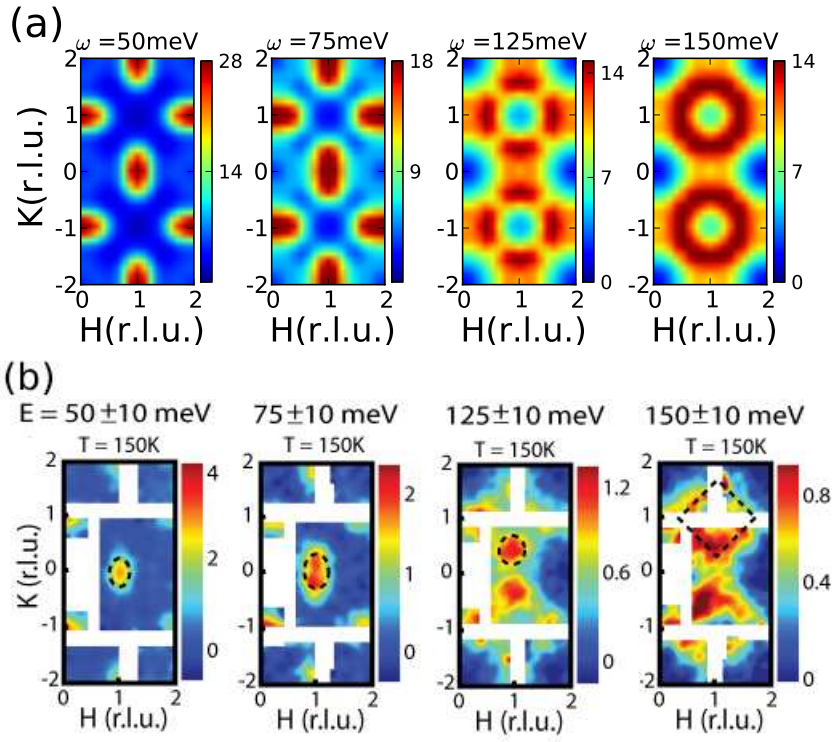

Figure 7.4: (a) The constant energy plot of the theoretical dynamical structure factor, $S(\mathbf{q},\omega)$ $(=\frac{\chi''(\mathbf{q},\omega)}{1-e^{-\hbar\omega/k_BT}})$ at different energies (50meV, 75meV, 125meV, and 150meV) in the paramagnetic state (T=386 K) of $BaFe_2As_2$ as a function of momentum $\mathbf{q}$ =(H,K,L). L is here fixed at 1. (b) The corresponding inelastic neutron scattering data from Ref. [5].

the theoretical $S(\mathbf{q},\omega)$ is strongly peaked at the ordering wave vector (H,K,L)=$(1,0,1)$ and it forms a clear elliptical shapes elongated in K direction. The elongation of the ellipse increases with energy (ω=75meV) and around ω =125meV the ellipse splits into two peaks, one peak centered at $(1,0.4,1)$ and the other at $(1,-0.4,1)$. At even higher energy (ω ≈150meV) the magnetic spectra broadens and peaks from four equivalent wave vectors merge into a circular shape centered at wave vector $(1,1,1)$. At even higher energy (230meV, not shown in the figure) the spectra broadens further, and the peak becomes centered at the point $(1,1,1)$. These trends are all in good quantitative agreement with INS data from Fig. 7.4(b).

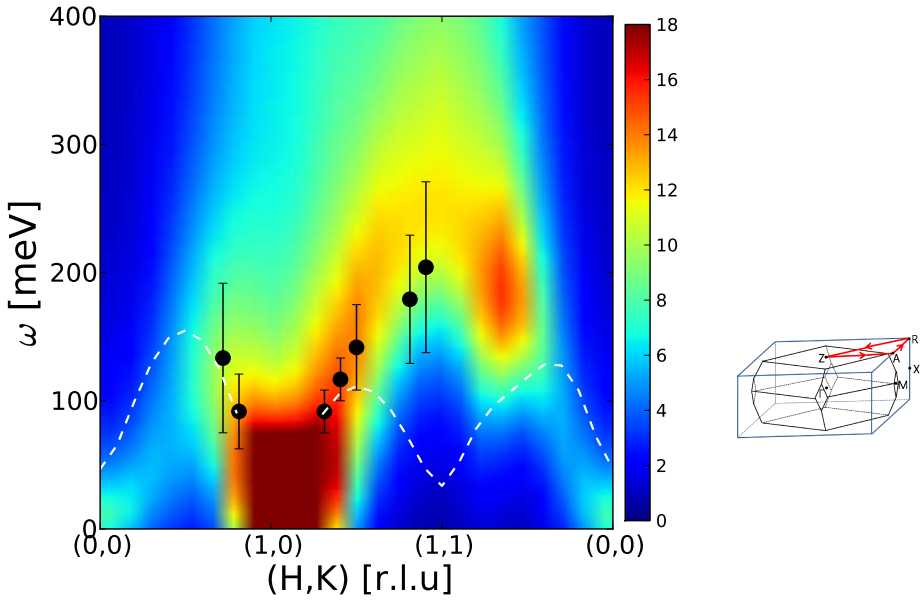

Figure 7.5: $S(\mathbf{q},\omega)$ along the special path in Brillouin zone marked by red arrow in the inset on the right. The inset shows the body-centered tetragonal (black line) and the unfolded (blue line) Brillouin zone. Black dots with error bars correspond to INS data from Ref. [5]. The white dashed line shows the isotropic Heisenberg spin wave dispersion.

In Fig. 7.5, we display a contour plot of the theoretical $S(\mathbf{q},\omega)$ as a function of frequency ω and momentum $\mathbf{q}$ along the special path in the unfolded Brillouin zone, sketched by a red line in the right figure. At low energies (ω <80meV), $S(\mathbf{q},\omega)$ is mostly concentrated in the region near the ordering vector $(1,0,1)$. Consistent with the elongation of the ellipse along the K direction in Fig.7.4, the low energy (ω <80meV) bright spot in Fig.7.5 is extended further towards $(1,1,1)$

direction but quite abruptly decreases in the $(0,0,1)$ direction. The magnetic spectra in the two directions $(1,0,1) \rightarrow (0,0,1)$ and $(1,0,1) \rightarrow (1,1,1)$ are clearly different even at higher energy $\omega > 100$meV. The peak position is moving to higher energy along both paths, but it fades away very quickly along the first path, such that the signal practically disappears at $(0.5,0,1)$. Along the second path $(1,0,1) \rightarrow (1,1,1)$, there remains a well defined excitation peak for which the energy is increasing, and at $(1,1,1)$ reaches the maximum value of ≈ 230meV. Continuing the path from $(1,1,1)$ towards $(0,0,1)$ the peak energy decreases again and it fades away around $(0.5,0.5,1)$. The black dots display INS data with errors bars from Ref. [5]. Notice a very good agreement between theory and experiment.

The white dashed line in Fig.7.5 represents the spin wave dispersion obtained for the isotropic Heisenberg model using nearest neighbor J_1 and next nearest neighbor J_2 exchange constants and performing the best fit to INS data. This fit was performed in Ref. [5]. The magnetic excitation spectra of an isotropic Heisenberg model show a local minimum at the wave vector $\mathbf{q} = (1,1,1)$, which is inconsistent with our theory and with the experiment. To better fit the experimental data with a Heisenberg-like model, very anisotropic exchange constants need to be assumed [5], which raised speculations about possible existence of nematic phase well above the structural transition of $BaFe_2As_2$. Since the DFT+DMFT results can account for all the features of the measured magnetic spectra without invoking any rotationally symmetry breaking the presence of nematicity in the paramagnetic tetragonal state at high temperature is unlikely.

In Fig. 7.6(a) we show constant frequency cuts in the K direction (from $(1,-1,1)$ through $(1,0,0)$ to $(1,1,1)$) of $S(\mathbf{q},\omega)$ displayed in Fig. 7.5. For comparison we also show the corresponding INS measurements from Ref. [5] as red circles in Fig. 7.6(b) and (c). At ω=20meV, the spectrum has a sharp peak centered at the ordering vector $(1,0,1)$. At ω=50meV, the spectrum still displays a peak at $(1,0,1)$ but the intensity is significantly reduced. With increasing frequency ω, the peak position in $S(\mathbf{q},\omega)$ moves in the direction of $(1,1,1)$, and at 128meV peaks around $(1,0.4,1)$. The shift of the peak is accompanied with substantial reduction of intensity at ordering wave vector $(1,0,1)$. At even higher energy of 250meV only a very weak

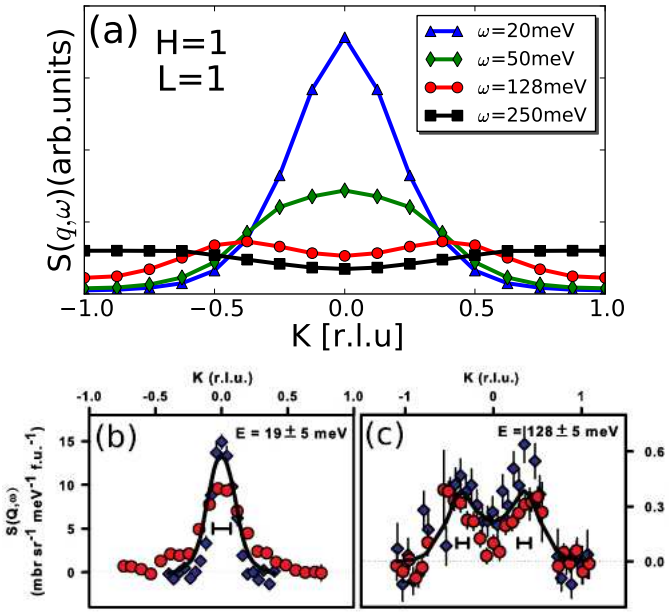

Figure 7.6: (a) The wave vector K dependence (H=1,L=1) of S($\mathbf{q}, \omega$) at several frequencies. (b) The corresponding INS data at ω=19meV and (c) 128meV reproduced from Ref. [5]. The red circles correspond to the paramagnetic state at T=150K and the blue diamonds to the magnetic state at T=7K.

peak remains, and it is centered at the wave vector $(1, 1, 1)$. The position of peaks as well as their frequency dependence is in very good agreement with INS experiments of Ref. [5] displayed in Fig. 7.6(b) and (c).

7.3.2 The d orbital resolved $\chi(\mathbf{q}, \omega)$

Fig. 7.7(a) resolves the dynamical magnetic susceptibility χ of Eq. 7.8 in the orbital space $\chi_\alpha = T\sum_{i\nu,i\nu'}\sum_\beta \sum_{\substack{\sigma_1\sigma_2\\ \sigma_3\sigma_4}} \mu^z_{\sigma_1\sigma_3}\mu^z_{\sigma_2\sigma_4}\, \chi^{\alpha\sigma_1,\beta\sigma_2}_{\alpha\sigma_3,\beta\sigma_4}(i\nu, i\nu')$ such that $\chi = \sum_\alpha \chi_\alpha$. At the magnetic ordering vector $\mathbf{q}$=$(1, 0, 1)$, χ''_α increases sharply with frequency near $\omega = 0$ for all orbitals and is strongly suppressed above 100meV reaching the maximum around 20meV. At this wave vector, the dominant contributions at low energy come from the d_{xy} and the d_{yz} orbitals. The magnetic susceptibility at $\mathbf{q}$=$(0, 1, 1)$ in Fig. 7.7(a) shows the same trend as orbitally resolved spectra at $\mathbf{q}$=$(1, 0, 1)$, except that d_{xz} and d_{yz} switch their roles due to the C_4 symmetry of the Fe square lattice. Magnetic excitation spectra at q=(0,0,1) and q=(1,1,1) show the noticeable difference.

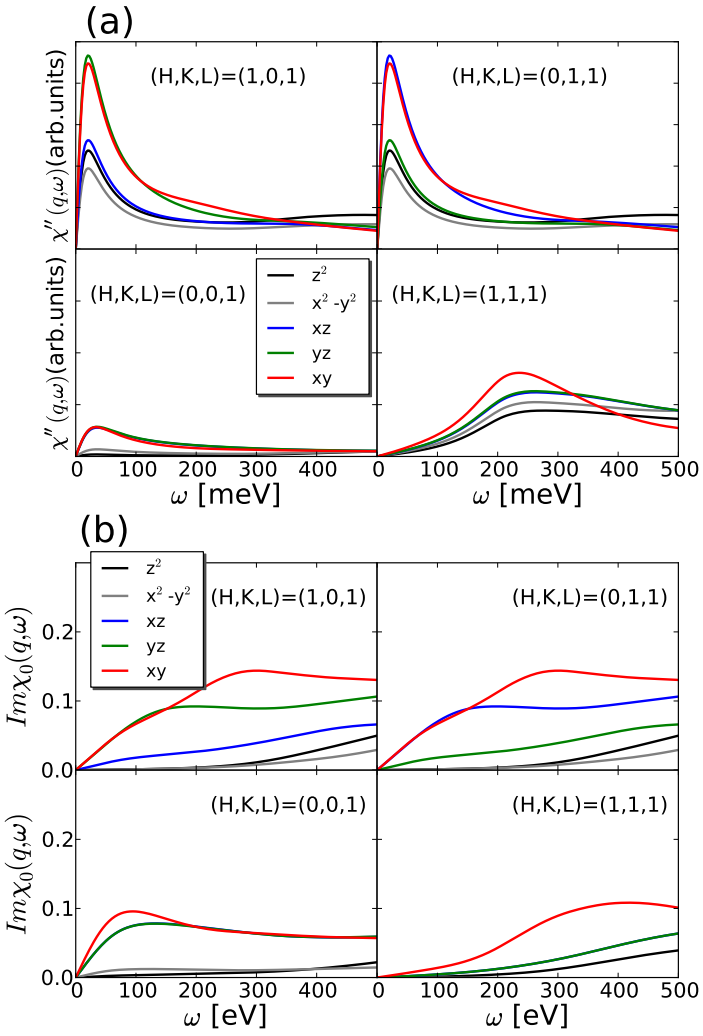

Figure 7.7: (a) The Fe d orbital resolved dynamical magnetic susceptibility $\chi(\mathbf{q},\omega)$ at T=386K for distinct wave vectors $\mathbf{q}$=$(1,0,1)$, $(0,1,1)$, $(0,0,1)$, and $(1,1,1)$. Different colors correspond to different orbital contributions. (b) The Fe d orbital resolved polarization bubble $\chi^0(\mathbf{q},\omega)$ at the same T and the same wave vectors $\mathbf{q}$ as (a)

These wave vectors are at the center of the lattice C_4 symmetry, therefore, the spectra from the d_{xz} orbital and the d_{yz} orbital are always degenerate. At q=(0,0,1), d_{xz}, d_{yz}, and d_{xy} orbitals are mostly contributed to low energy while high energy excitations are strongly suppressed at all d orbitals. In contrast, q=(1,1,1) the excitation spectra at q=(1,1,1) show only slight increase at low energy while the high energy spectra are peaked near 230meV for all orbitals but with the large d_{xy} contribution.

Fig. 7.7(b) displays the orbital resolved χ^0 calculated at the same $\mathbf{q}$ vectors as (a). The dominant orbital contributions to χ shown in (a) are also reasonably captured in the polarization bubble χ^0. At $\mathbf{q}$=$(1,0,1)$, the d_{xy} and the d_{yz} orbitals show the large spectra compared to other orbitals increasing almost linearly at low energy. At $\mathbf{q}$=$(0,1,1)$, the d_{xy} and the d_{xz} orbitals show the enhanced spectra. Other orbitals are strongly suppressed at low energy and they are increasing with a slow rate. At $\mathbf{q}$=$(0,0,1)$, the d_{xy}, the d_{xz}, and the d_{yz} orbitals have large spectral weights showing the peak near 100meV. The d_{z^2} and the $d_{x^2-y^2}$ orbitals show the negligible contribution. At $\mathbf{q}$=$(1,1,1)$, all d orbitals exhibit strongly suppressed spectra at low energy and increases slowly even at higher energies. Only d_{xy} orbital shows a quite enhanced spectra around 350-400meV and this peak can be attributed to the intra-orbital excitation between d_{xy} bands as will be shown in Fig. 7.8(b). One can note that the full χ at $\mathbf{q}$=$(1,1,1)$ has the peak at the smaller energy around 230meV due to strong correlations treated by the irreducible vertex function Γ^{irr}. These different orbital contributions to χ^0 can be understood from the orbital resolved Fermi surface and the spectral function as will be shown below.

7.3.3 The d orbital resolved Fermi surface

The orbital resolved Fermi surface is displayed in Fig. 7.8(a) at both the Γ-plane and the Z-plane. Most of the weight in χ^0 shown in Fig. 7.7(b) comes from the diagonal terms, i.e., $\chi^0_{\alpha,\alpha}$, hence the Fermi surfaces with the same color in Fig. 7.8(a) but separated by the wave vector $(1,0,1)$ give dominant contribution. The intra-orbital d_{yz} low energy spectra comes mostly from the transitions between the green parts of the hole pocket at Γ and the green parts of the

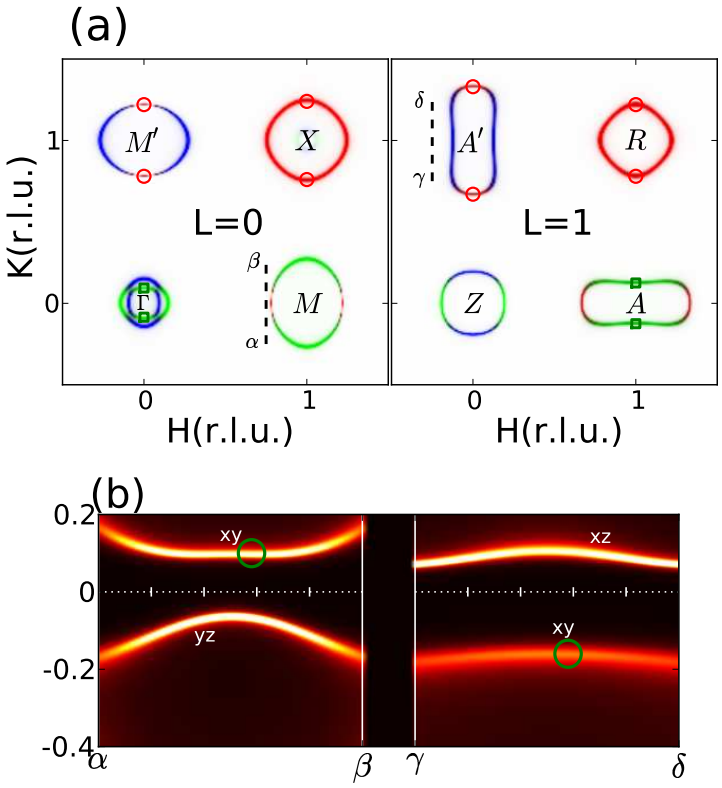

Figure 7.8: (a) The Fermi surface in the Γ and Z plane at T=73K colored by the orbital characters: d_{xz}(blue), d_{yz}(green), and d_{xy}(red). The small symbols mark the regions in the Fermi surface, where nesting for the wave vector $\mathbf{q}=(1,0,1)$ is good. (b) The zoom-in of $A(\mathbf{k},\omega)$ along the path marked by black dashed line in Fig. 7.8(a). The green open circles indicate the two relevant bands of d_{xy} character which give rise to the peak in magnetic excitation spectra near 230meV at $\mathbf{q}=(1,1,1)$.

electron pocket at A, marked with green squares ($\square$) in Fig. 7.8(a). Since the electron pocket at A is elongated in H direction, the nesting condition occurs mostly in the perpendicular K direction, hence the elliptical excitations at low energy in Fig. 7.4 are elongated in K but not in H direction. The intra-orbital d_{xy} transitions are pronounced between the electron pocket at M' and the hole pocket at R, as well as between the electron pocket at A' and the hole pocket at X (marked with red $\bigcirc$). This large spin response at $(1, 0, 1)$ gives rise to the low energy peak in Fig. 7.5.

We note that the particle-hole response, encoded in polarization bubble χ^0, is especially large when nesting occurs between an electron pockets and a hole pocket, because the nesting condition extends to the finite frequency, and is not cut-off by the Fermi functions.

The low energy magnetic excitations at wave vectors $\mathbf{q} = (0, 0, 1)$ and $\mathbf{q} = (1, 1, 1)$ can come only from electron-electron or hole-hole transitions, hence both responses are quite small, as seen in Fig. 7.7(a). While the magnetic response at $\mathbf{q} = (0, 0, 1)$ is small but finite, the spin response at $\mathbf{q} = (1, 1, 1)$ is almost gapped. This is because the hole-hole transitions from Γ to R or electron-electron transitions from M to A' do not involve any intra-orbital transitions, and hence are even smaller than transitions at the wave vector $(0, 0, 1)$.

At finite energy transfer, the spin excitations come from electronic states away from the Fermi energy, and can not be easily identified in the Fermi surface plot. Hence it is more intriguing to find the dominant contribution to the peak at $\omega \approx 230$meV and $\mathbf{q} = (1, 1, 1)$. This peak gives rise to the 230meV excitations at $(1, 1, 1)$ in Fig. 7.5. A large contribution to this finite frequency excitation comes from a region near the two electron pockets at M and A' marked with black dashed line in Fig. 7.8(a). We display in Fig. 7.8(b) the one electron spectral function across these dashed lines in the Brillouin zone to show an important particle hole transition from the electrons above Fermi level at the M point and the flat band at -200meV around the A' point, both of d_{xy} character. We note that due to large off diagonal terms in the two particle vertex Γ, all orbital contributions to χ develop a peak at the same energy, although only d_{xy} orbital displays a pronounced peak in χ^0.

7.3.4 Spectral function

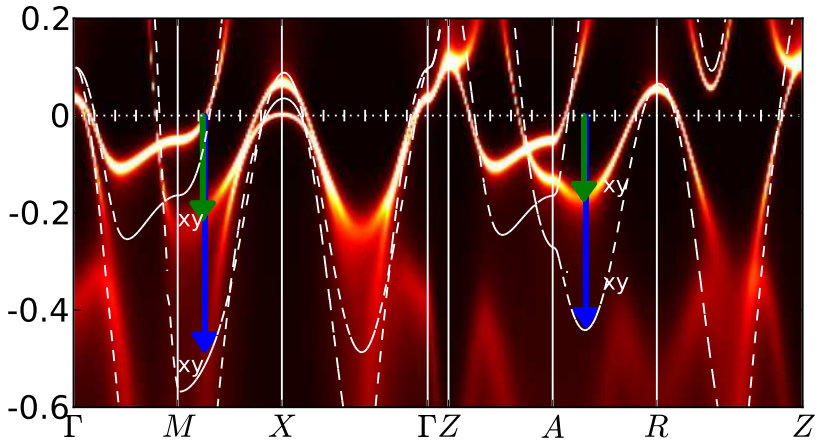

Figure 7.9: $A(\mathbf{k},\omega)$ computed in one Fe atom per unit cell at T=73K. The green arrows mark the same bands which give rise to 230meV peak. The DFT bands are overlayed by white dashed lines. The blue arrows mark corresponding DFT bands of d_{xy} character.

Fig. 7.9 displays the one electron spectral function in a path through the Brillouin zone, corresponding to one Fe atom per unit cell. Within DFT+DMFT the quasi-particle bands are renormalized by a factor of 2-3 compared to the corresponding DFT bands (white dashed lines). The green arrow marks the d_{xy} band which contributes to the peak in $S(\mathbf{q},\omega)$ near 230meV and $\mathbf{q}=(1,1,1)$. In DFT calculation, this d_{xy} intra-orbital transition is also present, but occurs at much higher energy of the order of 400-600meV, marked by blue arrows. The over-estimation of the peak energy at $\mathbf{q}$=$(1,1,1)$ was reported in LSDA calculation of Ref. [106].

7.3.5 Eigenvalue as a function of T

The Neel temperautre T_N for $BaFe_2As_2$ within DFT+DMFT can be computed as the temperature at which the paramagnetic magnetic susceptibility at the ordering vector (π,0) diverges. This is equivalent to computing the eigenvalues of the matrix $\Gamma^{irr}\cdot\chi^0$ and determining T_N as the temperature at which the leading eigenvalue reach one. The computation of T_N can be performed on the Matsubara frequencies, therefore, it is free from the problem of the analytic

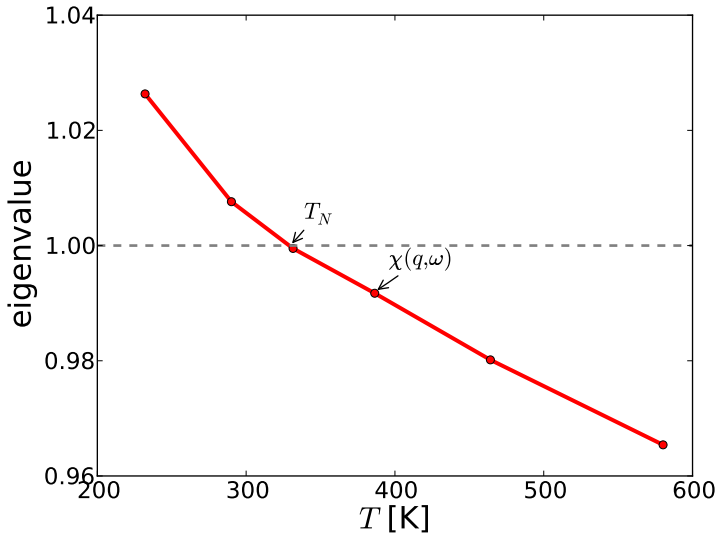

Figure 7.10: The leading eigenvalue of the $\Gamma^{irr} \cdot \chi^0$ matrix in the magnetic channel as a function of T.

continuation. Fig. 7.10 shows the leading eigenvalue for $BaFe_2As_2$ as a function of temperature. The eigenvalue increases almost linearly as T decreases and T_N is estimated as 330K which is 2.5 times larger than the experimental one (138K). This overestimation is due to the local approximation of Γ^{irr}. $\chi(\mathbf{q}, \omega)$ results shown in this chapter are computed at T=386K which is slightly above T_N.

7.4 The magnetic excitation spectra in the localized limit

The magnetic excitation of the localized spins originates from a weak distortion of a ground state spin configuration. This low-lying energy excitation is called as "spin waves" and the spin wave dispersion is a crucial quantity to understand the nature of magnetism in correlated materials. In this section, we compute the spin wave dispersion of $BaFe_2As_2$ assuming the d electrons in Fe atoms are localized. The magnetic exchange interaction J is considered for localized Fe spins. The Hamiltonian of the Heisenberg model is given by

$$\hat{H} = J_{1a} \sum_{i,j} \hat{S}_{i,j} \cdot \hat{S}_{i+1,j} + J_{1b} \sum_{i,j} \hat{S}_{i,j} \cdot \hat{S}_{i,j+1} + J_2 \sum_{i,j} (\hat{S}_{i,j} \cdot \hat{S}_{i+1,j+1} + \hat{S}_{i,j} \cdot \hat{S}_{i+1,j-1}) \quad (7.18)$$

where $\hat{S}_{i,j}$ is the spin operator at the (i,j) site, J_{1a} and J_{1b} are the nearest neighbor exchange energies, and J_2 is the next-nearest neighbor exchange energy. Here, we consider the two-dimensional square lattice with localized Fe spins at each site.

The magnetic ordering vector of $BaFe_2As_2$ is $(\pi,0)$. Since the spin direction is alternating in the x-direction while it is same in the y-direction, it is convenient to apply a canonical transformation such that the axis on the other sublattice is rotated through 180° about the x-axis, i.e., $\hat{S}^x_{i+1,j} \rightarrow \hat{S}^x_{i+1,j}$ and $\hat{S}^{y/z}_{i+1,j} \rightarrow -\hat{S}^{y/z}_{i+1,j}$. Moreover, the Hamiltonian can be written in terms of $\hat{S}^z$, $\hat{S}^+(=\hat{S}^x+i\hat{S}^y)$, and $\hat{S}^-(=\hat{S}^x\text{-}i\hat{S}^y)$.

$$\begin{aligned}
\hat{H} &= J_{1a}\sum_{i,j}[-\hat{S}^z_{i,j}\cdot\hat{S}^z_{i+1,j}+\frac{1}{2}(\hat{S}^+_{i,j}\cdot\hat{S}^+_{i+1,j}+\hat{S}^-_{i,j}\cdot\hat{S}^-_{i+1,j})] \\
&+J_{1b}\sum_{i,j}[\hat{S}^z_{i,j}\cdot\hat{S}^z_{i,j+1}+\frac{1}{2}(\hat{S}^+_{i,j}\cdot\hat{S}^-_{i,j+1}+\hat{S}^-_{i,j}\cdot\hat{S}^+_{i,j+1})] \\
&+J_2\sum_{i,j}[-\hat{S}^z_{i,j}\cdot\hat{S}^z_{i+1,j+1}-\hat{S}^z_{i,j}\cdot\hat{S}^z_{i+1,j-1} \\
&+\frac{1}{2}(\hat{S}^+_{i,j}\cdot\hat{S}^+_{i+1,j+1}+\hat{S}^-_{i,j}\cdot\hat{S}^-_{i+1,j+1})+\frac{1}{2}(\hat{S}^+_{i,j}\cdot\hat{S}^+_{i+1,j-1}+\hat{S}^-_{i,j}\cdot\hat{S}^-_{i+1,j-1})] \quad (7.19)
\end{aligned}$$

The low-lying bosonic excitation of the system can be studied by expressing the spin operators in terms of bosonic operators a and $a^\dagger$. The Holstein-Primakoff transformation [116] is one of such representations and it is given by $\hat{S}^z = S - a^\dagger a$, $\hat{S}^+ = \sqrt{2S-a^\dagger a}\cdot a \simeq \sqrt{2S}\cdot a$, and $\hat{S}^- = a^\dagger\sqrt{2S-a^\dagger a} \simeq \sqrt{2S}\cdot a^\dagger$ if $S \gg 1$. The Hamiltonian in Eq. 7.19 can be expressed in terms of these bosonic operators by keeping the leading order in S as the form

$$\begin{aligned}
\hat{H} &\cong J_{1a}\sum_{i,j}[-S^2+S(a^\dagger_{i,j}a_{i,j}+a^\dagger_{i+1,j}a_{i+1,j}+a_{i,j}a_{i+1,j}+a^\dagger_{i,j}a^\dagger_{i+1,j})] \\
&+J_{1b}\sum_{i,j}[S^2+S(-a^\dagger_{i,j}a_{i,j}-a^\dagger_{i,j+1}a_{i,j+1}+a_{i,j}a^\dagger_{i,j+1}+a^\dagger_{i,j}a_{i,j+1})] \\
&+J_2\sum_{i,j}[-2S^2+S(2a^\dagger_{i,j}a_{i,j}+a^\dagger_{i+1,j+1}a_{i+1,j+1}+a^\dagger_{i+1,j-1}a_{i+1,j-1} \\
&+a_{i,j}a_{i+1,j+1}+a^\dagger_{i,j}a^\dagger_{i+1,j+1}+a_{i,j}a_{i+1,j-1}+a^\dagger_{i,j}a^\dagger_{i+1,j-1})] \quad (7.20)
\end{aligned}$$

Using the Fourier transform of the bosonic operators, the above Hamiltonian is transformed as

$$\begin{aligned}\hat{H} &= -NS^2(J_{1a}-J_{1b}+2J_2) \\ &\quad +SJ_{1a}\sum_k[2a_k^\dagger a_k+\cos(k_x)\cdot(a_k a_{-k}+a_k^\dagger a_{-k}^\dagger)] \\ &\quad +SJ_{1b}\sum_k[-2a_k^\dagger a_k+\cos(k_y)\cdot(a_k a_k^\dagger+a_k^\dagger a_k)] \\ &\quad +SJ_2\sum_k[4a_k^\dagger a_k+2\cos(k_x)\cos(k_y)\cdot(a_k a_{-k}+a_k^\dagger a_{-k}^\dagger)] \end{aligned} \tag{7.21}$$

and as a more accessible matrix form

$$\hat{H} = -NS^2(J_{1a}-J_{1b}+2J_2)+S\sum_k\begin{pmatrix} a_k^\dagger & a_{-k}\end{pmatrix}\begin{pmatrix} A_k & B_k \\ B_k & A_k\end{pmatrix}\begin{pmatrix} a_k \\ a_{-k}^\dagger\end{pmatrix} \tag{7.22}$$

where $A_k = J_{1a}+J_{1b}(\cos(k_y)-1)+2J_2$ and $B_k = J_{1a}\cos(k_x)+2J_2\cos(k_x)\cos(k_y)$.

The above Hamiltonian has the non-particle-number-conserving terms such as $a^\dagger a^\dagger$ and aa, therefore, it can be diagonalized using Bogoliubov transformation. Under the transformation, eigenvalues are obtained by diagonalizing the matrix $\sigma_3\cdot\begin{pmatrix} A_k & B_k \\ B_k & A_k\end{pmatrix}$ and as a result the spin-wave dispersion is given by

$$E(k) = 2S\sqrt{A_k^2-B_k^2} \tag{7.23}$$

The spin-wave calculation result using SJ_{1a}=SJ_{1b}=18.3meV and SJ_2=28.7meV is depicted in Fig. 7.5 as a white dashed line. As shown in Fig. 7.5, the spin-wave dispersion of the Heisenberg model using the isotropic parameters shows qualitative discrepancy with the experimental dispersion at $\mathbf{q}=(1,1)$.

7.5 The magnetic excitation spectra in the itinerant limit

In the itinerant picture, the magnetic susceptibility $\chi(\mathbf{q},\omega)$ is computed using an random phase approximation (RPA). Within RPA, the polarization bubble $\chi^0(\mathbf{q},\omega)$ is computed from the DFT Kohn-Sham Green's functions

$$\begin{aligned}\chi^0_{\substack{\alpha\beta\\ \delta\gamma}}(\mathbf{q},\omega) &= -\frac{1}{N_k}\sum_{\mathbf{k}}\int d\nu\,[A_{\alpha\beta}(\mathbf{k},\nu)\cdot G_{\gamma\delta}(\mathbf{k}+\mathbf{q},\nu+\omega)-G_{\alpha\beta}(\mathbf{k},\nu-\omega)\cdot A_{\gamma\delta}(\mathbf{k}+\mathbf{q},\nu)]\,f(\nu) \\ &= -\frac{1}{N_k}\sum_{\mathbf{k}ij}\frac{P_{\mathbf{k}}(i;\alpha,\beta)\cdot P_{\mathbf{k}+\mathbf{q}}(j;\gamma,\delta)}{\omega+\varepsilon^i(\mathbf{k})-\varepsilon^j(\mathbf{k}+\mathbf{q})+i\delta}[f(\varepsilon^i(\mathbf{k}))-f(\varepsilon^j(\mathbf{k}+\mathbf{q}))] \end{aligned} \tag{7.24}$$

Here,$A_{\alpha\beta}(\mathbf{k},\nu)$ is defined as $\frac{1}{2\pi i}[G_{\alpha\beta}(\mathbf{k},\nu+i\delta)-G_{\alpha\beta}(\mathbf{k},\nu-i\delta)] = \frac{1}{\pi}\sum_i P_{\mathbf{k}}(i;\alpha,\beta)\cdot\delta(\nu-\varepsilon^i(\mathbf{k}))$ where the DFT Kohn-Sham Green's function $G_{\alpha\beta}(\mathbf{k},\nu+i\delta) = \sum_i \frac{P_{\mathbf{k}}(i;\alpha,\beta)}{\nu-\varepsilon^i(\mathbf{k})+i\delta}$ and $P_{\mathbf{k}}(i;\alpha,\beta)$ is the projection operator. One can note that this DFT Green's function is not dressed by the DMFT self energy since local dynamical correlations are ignored within RPA. The two-particle irreducible vertex Γ^{irr} is approximated by the screened Coulomb interaction $\overline{U}_{\substack{\alpha\beta\\\gamma\delta}}$. Finally, $\chi_{\substack{\alpha\beta\\\gamma\delta}}(\mathbf{q},\omega)$ is obtained by solving the following Bethe-Salpeter equation.

$$\chi_{\substack{\alpha\beta\\\gamma\delta}}(\mathbf{q},\omega) = \chi^0_{\substack{\alpha\beta\\\gamma\delta}}(\mathbf{q},\omega) + \sum_{\substack{\eta\mu\\\lambda\nu}} \chi^0_{\substack{\alpha\eta\\\gamma\lambda}}(\mathbf{q},\omega)\cdot\overline{U}_{\substack{\eta\mu\\\lambda\nu}}(\mathbf{q})\cdot\chi_{\substack{\mu\beta\\\nu\delta}}(\mathbf{q},\omega) \tag{7.25}$$

And the magnetic susceptibility $\chi(\mathbf{q},\omega)$ is obtained by closing the external legs, i.e., $\chi(\mathbf{q},\omega) = \sum_{\alpha,\beta}\chi_{\substack{\alpha\beta\\\alpha\beta}}(\mathbf{q},\omega)$.

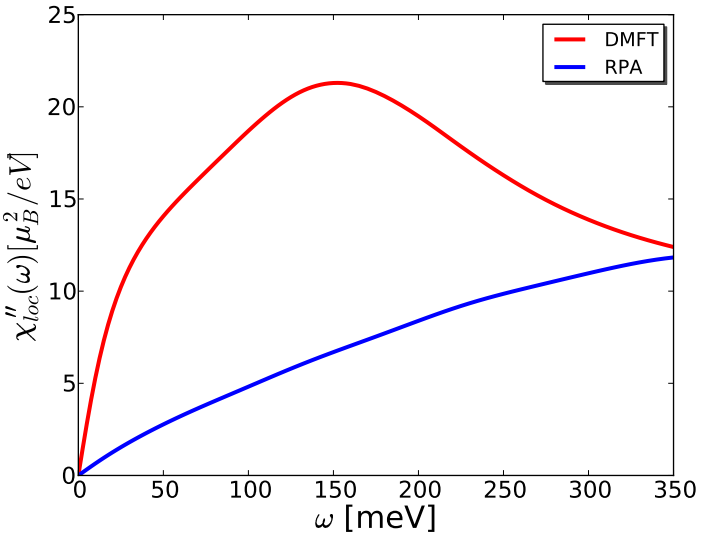

Figure 7.11: The local magnetic susceptibility $\chi''_{loc}(\omega)$ computed for $BaFe_2As_2$ in absolute units. The LDA+DMFT calculation (red) and the RPA calculation (blue) are compared. For the RPA calculation, we use the intra-orbital interaction $\widetilde{U}$=1.3eV and the Hund's coupling $\widetilde{J}$=0.4eV.

In Fig. 7.11, the local magnetic susceptibilities $\chi''(\omega)$ are computed using the LDA+DMFT (red) method and the RPA (blue) method. The local susceptibility is obtained by averaging $\chi''(\mathbf{q},\omega)$ over $\mathbf{q}$ vectors in the Brillouin zone, i.e., $\chi''(\omega) = \int d\mathbf{q}\chi''(\mathbf{q},\omega)/\int d\mathbf{q}$. The LDA+DMFT method can capture both the localized and the itinerant aspects of the magnetic excitation. $\chi''(\omega)$ computed within LDA+DMFT shows a peak around 150meV and has

the large spin spectral weight compared to the RPA spectral weight. $\chi''(\omega)$ computed within RPA misses this peak around 150meV and it keeps increasing almost linearly with energy. This is because the RPA calculation can not describe both the localized and the itinerant aspects of magnetic excitation in $BaFe_2As_2$.

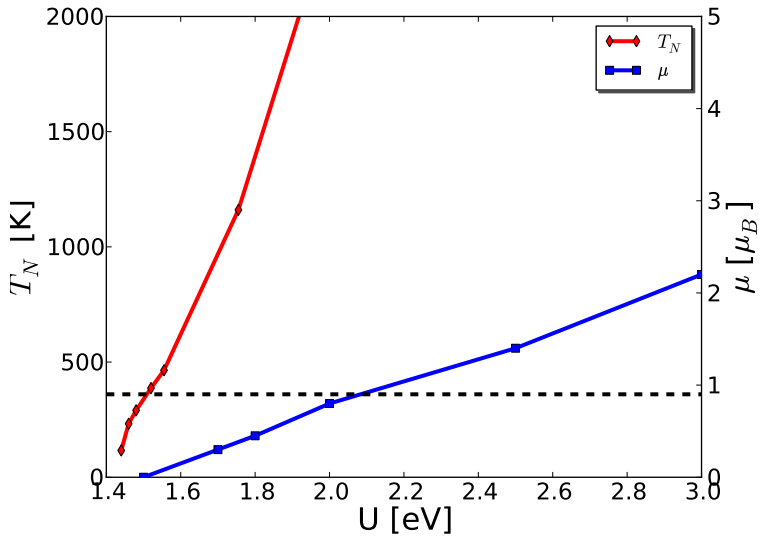

Figure 7.12: The Neel temperature T_N (left y-axis) and the ordered magnetic moment μ (right y-axis) computed within RPA as a function of the intra-orbital interaction $\widetilde{U}$. The Hund's coupling $\widetilde{J}$ is fixed to 0.4eV. The dashed line indicates both DMFT T_N around 380K and the experimental moment around $0.9\mu_B$ [6].

Fig. 7.12 displays the Neel temperature T_N computed using the RPA method and the corresponding ordered magnetic moment μ at the same interaction $\widetilde{U}$. T_N is determined as the temperature at which RPA $\chi(\mathbf{q}=(\pi,0),\omega=0)$ diverges. And $\mu=(n_\uparrow-n_\downarrow)$ is computed from the magnetic ordered state determined within a self-consistent Hartree-Fock approximation. Both T_N and μ start to increase almost linearly above 1.45eV indicating the instability towards a magnetically ordered state although T_N is increasing very sharply compared to μ. At around 2eV where the ordered magnetic moment is $0.9\mu_B$, T_N exceeds even more than 2000K which is unphysical. Within the DFT+DMFT calculation, the interaction parameters, U=5eV and J=0.7eV, give both reasonable T_N ($\sim$330K) and the magnetic moment ($\sim 0.9\mu_B$). The RPA calculation in Fig. 7.11 is performed using $\widetilde{U}$=1.3eV and $\widetilde{J}$=0.4eV which are reasonably close

to the magnetic phase and above T_N. Although the RPA calculation depends on Coulomb parameters used, we note that the 5-orbital Hubbard model calculation using $\widetilde{U}$=0.8eV and $\widetilde{J}$=0.2eV produces the similar local magnetic spectra [81] as in Fig. 7.11.

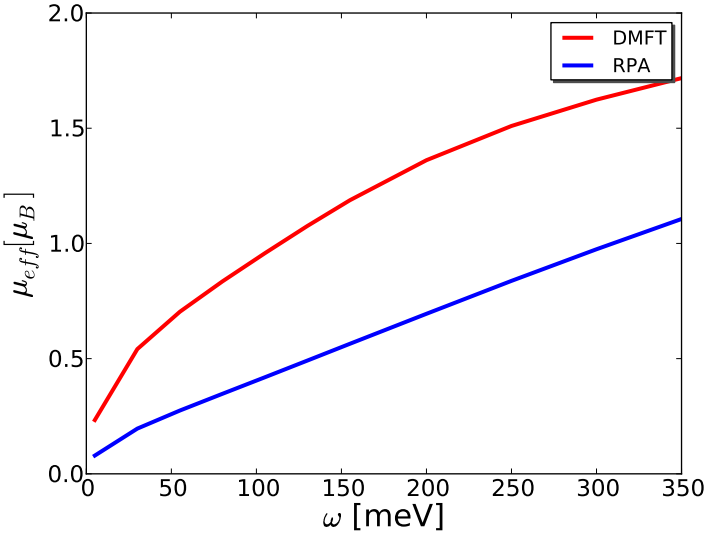

Figure 7.13: The fluctuating magnetic moment μ_{eff} as a function of energy. The μ_{eff} is computed within both DFT+DMFT (red) and within RPA (red), and the results are compared.

Fig.7.13 shows the fluctuating magnetic moment μ_{eff} in $BaFe_2As_2$ computed within DFT+DMFT (red) and the corresponding result computed within RPA (blue). μ_{eff} can be obtained by integrating the local magnetic susceptibility as the following formula:

$$\mu^2_{eff}(\omega_0) = \frac{3\hbar}{\pi}\int_{-\omega_0}^{\omega_0} d\omega \frac{\chi''(\omega)}{1-e^{-\hbar\omega/kT}} \tag{7.26}$$

The fluctuating moment within DFT+DMFT increases sharply below 50meV and keeps increasing at high energy while the RPA moment increases rather slowly. This large fluctuating moment within DFT+DMFT is a result of heavy quasi-particles and the large Hund's coupling which RPA can not capture. However, the ordered moment computed within DFT+DMFT [117] is much smaller that the fluctuating moment.

7.6 Conclusion

In this chapter, we have extended the DFT+DMFT methodology to compute the two particle responses in a realistic multi-orbital DFT+DMFT setting. With the same parameters which were used to successfully describe the optical spectra and the magnetic moments of this material [117], we obtained a coherent description of the experimental neutron scattering results. Our theory ties the magnetic response to the fermiology of the model, and quantifies the departure from both purely itinerant and localized pictures.

Conclusions

In this thesis, we studied two-particle response functions, i.e., the magnetic susceptibility and superconducting (SC) pairing susceptibility in strongly correlated electron systems. These two-particle quantities are calculated based on the realistic electronic structure calculation using the combination of the density functional theory (DFT) and the dynamical mean field theory (DMFT) and by extracting a two-particle irreducible vertex function from an auxiliary impurity problem treated within DMFT. The study of two-particle response functions enables us to investigate various phases with a long-range order such as antiferromagnetism and d-wave superconductivity. This calculation scheme is applied to the study of a phase diagram in the one-band Hubbard model and in the periodic Anderson model. The dynamical magnetic susceptibility, a two-particle quantity for the magnetic response, is also calculated for the Fe-based superconductor, $BaFe_2As_2$. In addition to the two-particle response function calculation, we also addressed the Nagaoka problem in the $U = \infty$ Hubbard model and the Mott transition problem in the two-dimensional Hubbard model using a DMFT approach and a cluster extension of the DMFT method, respectively.

The stability of ferromagnetic (FM) state in the $U = \infty$ Hubbard model with nearest neighbor hopping t and next-nearest neighbor hopping t' is investigated using a DMFT approach with continuous time quantum Monte Carlo (CTQMC) as an impurity solver. The FM state computed within DMFT is more stable for $t' = -0.1t$ than $t' = 0$ and $t' = 0.1t$ values and this is supported by other methods, i.e., a slave boson approximation and the diagonalization of the four site plaquette. The FM transition treated within DMFT is the first order at $t' = -0.1t$, while the second order transition occurs at $t' = 0$. The original Nagaoka problem refers to the stability of a fully polarized FM phase at finite doping, and this state is stable only at

$t' = -0.1t$.

The nature of the Mott transition in the half-filled Hubbard model is studied using cluster DMFT which includes the short-range correlations on top of the on-site correlations of DMFT. The cluster DMFT result shows that the transition between the paramagnetic metal to the paramagnetic Mott insulator is first order, which is also captured within single-site DMFT. However, the short-range correlations reduce substantially the critical U and modify the shape of transition lines. The transition line of cluster DMFT shows the reentrant behavior of the Mott transition, namely, the system is insulating at very low temperature, but becomes metallic at intermediate temperature and insulating again at higher temperature. We showed that this behavior originates from small entropy of the insulating state at very low temperature due to short-range singlet formation.

We then studied the phase diagram of model Hamiltonians by computing two-particle response functions using a vertex function approach within DMFT. The SC pairing susceptibility is calculated in the Hubbard model and the periodic Anderson model. The critical temperature T_c, SC gap symmetry, and other relevant quantities for superconductivity are obtained by solving the eigenvalue problem of the gap equation in the pairing channel. The pairing vertex is constructed within DMFT assuming that the irreducible particle-hole vertex is local. In the Hubbard model, the SC phase is stable near the magnetic phase where the pairing interaction mediated by the spin fluctuation is strongly enhanced. As a result, the SC phase overwhelms the magnetic phase even in the underdoped region and T_c is reduced as the doping increases. The calculated SC gap symmetry in the Hubbard model is d-wave. In the periodic Anderson model, T_c is strongly enhanced in the small hybridization $V_{\mathbf{k}}$ region where correlated electrons are almost localized owing to the strong pairing interaction. T_c is decreased as the pairing interaction gets smaller in the large $V_{\mathbf{k}}$ region where electrons become itinerant. The SC phase for only coherent quasi-particles is determined as the region below both T_c and the coherence temperature T_{coh}, and our calculation results in a dome shape which is similar with the experimental one.

Moreover, the non-local correlation effect is incorporated into the SC pairing susceptibility calculation. We employ the dual fermion (DF) approach and the dynamical vertex approximation (DΓA) in order to treat non-local correlations beyond DMFT. Both the pairing vertex and the pairing bubble are computed within the DF and DΓA methods, and they are compared with the corresponding DMFT quantities. In the Hubbard model, the pairing interaction calculated within the DF method is strongly reduced compared to the DMFT pairing interaction, as non-local fluctuations ignored within DMFT are included. In contrast, the pairing bubble calculated within DF and DΓA is slightly enhanced compared to the corresponding DMFT one. As a result, T_c calculated within the DF method is reduced compared to DMFT T_c while T_c within DΓA is slightly enhanced. In the periodic Anderson model, the pairing interaction is strongly renormalized within DΓA while the pairing bubble computed within DF and DΓA is similar to the DMFT one. Therefore, T_c in the periodic Anderson model is the smallest within DΓA, and the DF method also reduces T_c compared to DMFT T_c.

Finally, we apply the vertex function approach within the DFT+DMFT framework to a Fe-based superconductor, $BaFe_2As_2$, and calculate the dynamic magnetic susceptibility to investigate the magnetic excitation spectra in this material. The calculation of the susceptibility captures both one-particle excitations and the collective modes. Our results can reproduce all features observed in neutron scattering experiments. At low frequency, the magnetic excitation spectrum is strongly peaked at the magnetic ordering vectors (1,0,1) and (0,1,1). As the excitation energy increases, the peak position shifts, and around 230meV the peak position moves to the wave vector (1,1,1) in a good agreement with the experimental result. We found that this peak position shift at high energy originates from the intra-orbital excitations in the Fe d_{xy} orbital from momentum space regions near two electron pockets. The theoretical magnetic excitation spectrum is obtained in the paramagnetic state of $BaFe_2As_2$; therefore, no symmetry breaking is needed to explain the neutron scattering experimental data.

The calculation scheme of two-particle quantities derived in this thesis can be generally applied to various materials with strong correlations such as Fe based superconductors, cuprate

superconductors, and heavy fermion materials. The dynamical magnetic susceptibility calculation can treat a localized and an itinerant aspect in these materials on an equal footing; therefore it can unravel the nature of the magnetic excitation, which is essential to understand the pairing mechanism of unconventional superconductivity. For the study of superconductivity, the pairing susceptibility is the response function in which physicists are particularly interested. By applying the vertex function approaches derived in this thesis to various unconventional superconductors, one can study T_c and the SC gap symmetry in these materials. The theoretical study of trends in T_c and the SC gap symmetry in various unconventional superconductors can provide an essential clue to understand the origin of superconductivity. For future research, the recently discovered Fe-based superconductors are adequate to be studied using the multi-orbital vertex function approach based on DFT+DMFT because the study of distinct orbital contributions to the pairing interaction is essential to understand the pairing mechanism of superconductivity in these materials.

Bibliography

[1] Marianne Rotter, Michael Pangerl, Marcus Tegel, and Dirk Johrendt. Superconductivity and crystal structures of $(Ba_{1-x}K_x)Fe_2As_2$ (x=0-1). *Angewandte Chemie International Edition*, 47(41):7949–7952, 2008.

[2] N. Ni, M. E. Tillman, J.-Q. Yan, A. Kracher, S. T. Hannahs, S. L. Bud'ko, and P. C. Canfield. Effects of co substitution on thermodynamic and transport properties and anisotropic Hc_2 in $Ba(Fe_{1-x}Co_x)_2As_2$ single crystals. *Phys. Rev. B*, 78(21):214515, Dec 2008.

[3] Shuai Jiang, Hui Xing, Guofang Xuan, Cao Wang, Zhi Ren, Chunmu Feng, Jianhui Dai, Zhuan Xu, and Guanghan Cao. Superconductivity up to 30 k in the vicinity of the quantum critical point in $BaFe_2(As_{1-x}P_x)_2$. *Journal of Physics: Condensed Matter*, 21(38):382203, 2009.

[4] Johnpierre Paglione and Richard L. Greene. High-temperature superconductivity in iron-based materials. *Nature Physics*, advance online publication, 2010.

[5] Leland W. Harriger, Huiqian Luo, Mengshu Liu, T. G. Perring, C. Frost, Jiangping Hu, M. R. Norman, and Pengcheng Dai. Nematic spin fluid in the tetragonal phase of $BaFe_2As_2$. *arXiv:1011.3771*, 2010.

[6] Q. Huang, Y. Qiu, Wei Bao, M. A. Green, J. W. Lynn, Y. C. Gasparovic, T. Wu, G. Wu, and X. H. Chen. Neutron-diffraction measurements of magnetic order and a structural transition in the parent $BaFe_2As_2$ compound of FeAs-based high-temperature superconductors. *Phys. Rev. Lett.*, 101(25):257003, Dec 2008.

[7] A. Georges, G. Kotliar, W. Krauth, and M.J. Rozenberg. Dynamical mean-field theory of strongly correlated fermion systems and the limit of infinite dimensions. *Rev. Mod. Phys.*, 68(1):13 – 25, 1996.

[8] Walter Metzner and Dieter Vollhardt. Correlated lattice fermions in $d = \infty$ dimensions. *Phys. Rev. Lett.*, 62(3):324–327, Jan 1989.

[9] P. Hohenberg and W. Kohn. Inhomogeneous electron gas. *Phys. Rev.*, 136(3B):B864–B871, Nov 1964.

[10] W. Kohn and L. J. Sham. Self-consistent equations including exchange and correlation effects. *Phys. Rev.*, 140(4A):A1133–A1138, Nov 1965.

[11] D. M. Ceperley and B. J. Alder. Ground state of the electron gas by a stochastic method. *Phys. Rev. Lett.*, 45(7):566–569, Aug 1980.

[12] Richard M. Martin. *Electronic Structure: Basic Theory and Practical Methods*. Cambridge University Press, 2004.

[13] G. Kotliar, S. Y. Savrasov, K. Haule, V. S. Oudovenko, O. Parcollet, and C. A. Marianetti. Electronic structure calculations with dynamical mean-field theory. *Rev. Mod. Phys.*, 78(20):865, 2006.

[14] Kristjan Haule, Chuck-Hou Yee, and Kyoo Kim. Dynamical mean-field theory within the full-potential methods: Electronic structure of $CeIrIn_5$, $CeCoIn_5$, and $CeRhIn_5$. *Phys. Rev. B*, 81(19):195107, May 2010.

[15] D. J. Singh and L. Nordstrom. *Planewaves, Pseudopotentials, and the LAPW Method*. Springer, New York, 2006.

[16] P. Werner, A. Comanac, Ld. Medici, M. Troyer, and A.J. Millis. Continuous-time solver for quantum impurity models. *Phys. Rev. Lett.*, 97(7):076405 – 1, 2006.

[17] Kristjan Haule. Quantum Monte Carlo impurity solver for cluster dynamical mean-field theory and electronic structure calculations with adjustable cluster base. *Phys. Rev. B*, 75(15):155113, 2007.

[18] Emanuel Gull, Andrew J. Millis, Alexander I. Lichtenstein, Alexey N. Rubtsov, Matthias Troyer, and Philipp Werner. Continuous-time monte carlo methods for quantum impurity models. *Rev. Mod. Phys.*, 83(2):349–404, May 2011.

[19] Hyowon Park, K. Haule, C. A. Marianetti, and G. Kotliar. Dynamical mean-field theory study of Nagaoka ferromagnetism. *Phys. Rev. B*, 77(3):035107, 2008.

[20] Yosuke Nagaoka. Ferromagnetism in a Narrow, Almost Half-Filled s Band. *Phys. Rev.*, 147(1):392–405, Jul 1966.

[21] Patrick Fazekas. *LECTURE NOTES ON ELECTRON CORRELATION AND MAGNETISM Series in Modern Condensed Matter Physics - Vol. 5*. World Scientific Pub Co Inc, 1999.

[22] B.S. Shastry, H.R. Krishnamurthy, and P.W. Anderson. Instability of the Nagaoka ferromagnetic state of the $U = \infty$ Hubbard model. *Phys. Rev. B*, 41(4):2375 – 9, 1990.

[23] A.G. Basile and V. Elser. Stability of the ferromagnetic state with respect to a single spin flip: variational calculations for the $U = \infty$ Hubbard model on the square lattice. *Phys. Rev. B*, 41(7):4842 – 5, 1990.

[24] W. von der Linden and D.M. Edwards. Ferromagnetism in the Hubbard model. *J. Phys. Condens. Matter.*, 3(26):4917 – 40, 1991.

[25] Th. Hanisch and E. Muller-Hartmann. Ferromagnetism in the Hubbard model: instability of the Nagaoka state on the square lattice. *Ann. Phys*, 2(4):381 – 97, 1993.

[26] P. Wurth, G. Uhrig, and E. Mueller-Hartmann. Ferromagnetism in the Hubbard model on the square lattice: improved instability criterion for the Nagaoka state. *Ann. Phys.*, 5(2):148 – 55, 1996.

[27] B. Moller, K. Doll, and R. Fresard. A slave-boson approach to ferromagnetism in the large-U Hubbard model. *J. Phys., Condens. Matter.*, 5(27):4847 – 54, 1993.

[28] D. Boies, F.A. Jackson, and A.-M.S. Tremblay. Nagaoka ferromagnetism as a test of slave-fermion and slave-boson approaches. *Int. J. Mod. Phys. B*, 9(9):1001 – 24, 1995.

[29] X.Y. Zhang, Elihu Abrahams, and G. Kotliar. Quantum Monte Carlo algorithm for constrained fermions: application to the infinite-U hubbard model. *Phys. Rev. Lett.*, 66(9):1236 – 9, 1991.

[30] F. Becca and S. Sorella. Nagaoka ferromagnetism in the two-dimensional infinite-U hubbard model. *Phys. Rev. Lett.*, 86(15):3396 – 9, 2001.

[31] A.M. Oles and P. Prelovsek. Instability of the Nagaoka ferromagnetic state in the Hubbard model with next-nearest-neighbor hopping. *Phys. Rev. B*, 43(16):13348 – 51, 1991.

[32] Hal Tasaki. Ferromagnetism in the Hubbard models with degenerate single-electron ground states. *Phys. Rev. Lett.*, 69(10):1608–1611, Sep 1992.

[33] Eduardo Gagliano, Silvia Bacci, and Elbio Dagotto. Hole motion in the t-J and Hubbard models: Effect of a next-nearest-neighbor hopping. *Phys. Rev. B*, 42(10):6222–6227, 1990.

[34] T. Hanisch, G.S. Uhrig, and E. Muller-Hartmann. Lattice dependence of saturated ferromagnetism in the Hubbard model. *Phys. Rev. B*, 56(21):13960 – 82, 1997.

[35] J. Wahle, N. Blumer, J. Schlipf, K. Held, and D. Vollhardt. Microscopic conditions favoring itinerant ferromagnetism. *Phys. Rev. B*, 58(19):12749 – 57, 1998.

[36] L. Arrachea. Itinerant ferromagnetism in the two-dimensional t-t' Hubbard model. *Phys. Rev. B*, 62(15):10033 – 7, 2000.

[37] M. Ulmke. Ferromagnetism in the Hubbard model on FCC-type lattices. *Eur. Phys. J. B*, 1(3):301 – 4, 1998.

[38] T. Wegner, M. Potthoff, and W. Nolting. Temperature-dependent electronic structure and ferromagnetism in the $d = \infty$ Hubbard model studied by a modified perturbation theory. *Phys. Rev. B*, 57(11):6211 – 14, 1998.

[39] R. Hlubina, S. Sorella, and F. Guinea. Ferromagnetism in the two dimensional t-t' Hubbard model at the Van Hove density. *Phys. Rev. Lett.*, 78(7):1343 – 1346, 1997.

[40] T. Obermeier, T. Pruschke, and J. Keller. Ferromagnetism in the large-U Hubbard model. *Phys. Rev. B, Condens. Matter*, 56(14):8479 – 82, 1997.

[41] R. Zitzler, T. Pruschke, and R. Bulla. Magnetism and phase separation in the ground state of the Hubbard model. *Eur. Phys. J. B*, 27(4):473 – 81, 2002.

[42] M. Jarrell and J.E. Gubernatis. Bayesian inference and the analytic continuation of imaginary-time quantum Monte Carlo data. *Phys. Rep.*, 269(3):133 – 95, 1996.

[43] H. Kajoeter, G. Kotliar, and G. Moeller. Doped Mott insulator: results from mean-field theory. *Phys. Rev. B*, 53(24):16214 – 26, 1996.

[44] A. M. Polyakov. Interaction of goldstone particles in two dimensions. Applications to ferromagnets and massive yang-mills fields. *Physics Letters B*, 59(1):79 – 81, 1975.

[45] D. Jaksch and P. Zoller. The cold atom Hubbard toolbox. *Ann. Phys.*, 315(1):52 – 79, 2005.

[46] A. Georges. Condensed matter physics with light and atoms: Strongly correlated cold fermions in optical lattices. *cond-mat/0702122v1*, 2007.

[47] H. Park, K. Haule, and G. Kotliar. Cluster dynamical mean field theory of the Mott transition. *Phys. Rev. Lett.*, 101(18):186403, Oct 2008.

[48] Masatoshi Imada, Atsushi Fujimori, and Yoshinori Tokura. Metal-insulator transitions. *Rev. Mod. Phys.*, 70(4):1039–1263, 1998.

[49] P.Limelette, A.Georges, D.Jerome, P.Wzietek, P.Metcalf, and J.M.Honig. Universality and Critical Behavior at the Mott transition. *Science*, 302(4):89, 2003.

[50] Takuma Ohashi, Tsutomu Momoi, Hirokazu Tsunetsugu, and Norio Kawakami. Finite temperature Mott transition in Hubbard model on anisotropic triangular lattice. *Phys. Rev. Lett.*, 100(7):076402, 2008.

[51] O. Parcollet, G. Biroli, and G. Kotliar. Cluster dynamical mean field analysis of the Mott transition. *Phys. Rev. Lett.*, 92(22):226402, 2004.

[52] Shigeki Onoda and Masatoshi Imada. Mott transitions in the two-dimensional half-filled hubbard model: Correlator projection method with projective dynamical mean-field approximation. *Phys. Rev. B*, 67(16):161102(R), 2003.

[53] S. Moukouri and M. Jarrell. Absence of a slater transition in the two-dimensional Hubbard model. *Phys. Rev. Lett.*, 87(16):167010, 2001.

[54] Y. Z. Zhang and Masatoshi Imada. Pseudogap and Mott transition studied by cellular dynamical mean-field theory. *Phys. Rev. B*, 76(4):045108, 2007.

[55] Gabriel Kotliar, Sergej Y. Savrasov, Gunnar Pálsson, and Giulio Biroli. Cellular Dynamical Mean Field Approach to Strongly Correlated Systems. *Phys. Rev. Lett.*, 87(18):186401, 2001.

[56] Thomas Maier, Mark Jarrell, Thomas Pruschke, and Matthias H. Hettler. Quantum cluster theories. *Rev. Mod. Phys.*, 77(3):1027, 2005.

[57] B. Kyung and A.-M. S. Tremblay. Mott transition, antiferromagnetism, and d-wave superconductivity in two-dimensional organic conductors. *Phys. Rev. Lett.*, 97(20):046402, 2006.

[58] K. Haule and G. Kotliar. Strongly correlated superconductivity: a plaquette dynamical mean field theory study. *Phys. Rev. B*, 76(20):104509, 2007.

[59] M. Vekic and S. R. White. Pseudogap formation in the half-filled Hubbard model. *Phys. Rev. B*, 47(20):1160, 1993.

[60] Andriy H. Nevidomskyy, Christian Scheiber, David Sénéchal, and A.-M. S. Tremblay. Magnetism and d -wave superconductivity on the half-filled square lattice with frustration. *Phys. Rev. B*, 77(6):064427, Feb 2008.

[61] F. Kagawa, T. Itou, K. Miyagawa, and K. Kanoda. Transport criticality of the first-order Mott transition in the quasi-two-dimensional organic conductor $\kappa - (BEDT - TTF)_2Cu[N(CN)_2]Cl$. *Phys. Rev. B*, 69(6):64511 – 1, 2004.

[62] R. Preuss, W. Hanke, and W. von der Linden. Quasiparticle dispersion of the 2D Hubbard model: From an insulator to a metal. *Phys. Rev. Lett.*, 75(7):1344–1347, 1995.

[63] B. Kyung, S. S. Kancharla, D. Senechal, A.-M. S. Tremblay, M. Civelli, and G. Kotliar. Pseudogap induced by short-range spin correlations in a doped Mott insulator. *Phys. Rev. B*, 73(16):165114, 2006.

[64] K. Haule, A. Rosch, J. Kroha, and P. Wölfle. Pseudogaps in an incoherent metal. *Phys. Rev. Lett.*, 89(20):236402, 2002.

[65] M. M. Qazilbash, K. S. Burch, D. Whisler, D. Shrekenhamer, B. G. Chae, H. T. Kim, and D. N. Basov. Correlated metallic state of vanadium dioxide. *Phys. Rev. B*, 74(20):205118, 2006.

[66] J.-S. Zhou, J. B. Goodenough, and B. Dabrowski. Pressure-induced non-Fermi-liquid behavior of $prnio_3$. *Phys. Rev. Lett.*, 94(22):226602 – 1, 2005.

[67] G. Kotliar, S. Y. Savrasov, K. Haule, V. S. Oudovenko, O. Parcollet, and C. A. Marianetti. Electronic structure calculations with dynamical mean-field theory. *Rev. Mod. Phys.*, 78(3):865–951, Aug 2006.

[68] J. H. Shim, K. Haule, and G. Kotliar. Fluctuating valence in a correlated solid and the anomalous properties of δ-plutonium. *Nature*, 446:513–516, March 2007.

[69] J. H. Shim, K. Haule, and G. Kotliar. Modeling the localized-to-itinerant electronic transition in the heavy fermion system ceirin$_5$. *Science*, 318(5856):1615–1617, 2007.

[70] K. Haule, J. H. Shim, and G. Kotliar. Correlated electronic structure of $LaO_{1-x}F_xFeAs$. *Phys. Rev. Lett.*, 100(22):226402, Jun 2008.

[71] T. A. Maier, M. S. Jarrell, and D. J. Scalapino. Structure of the pairing interaction in the two-dimensional Hubbard model. *Phys. Rev. Lett.*, 96(4):047005, Feb 2006.

[72] G. Sordi, K. Haule, and A.-M. S. Tremblay. Finite doping signatures of the Mott transition in the two-dimensional Hubbard model. *Phys. Rev. Lett.*, 104(22):226402, Jun 2010.

[73] Kristjan Haule and Gabriel Kotliar. Avoided criticality in near-optimally doped high-temperature superconductors. *Phys. Rev. B*, 76(9):092503, Sep 2007.

[74] N. S. Vidhyadhiraja, A. Macridin, C. Şen, M. Jarrell, and Michael Ma. Quantum critical point at finite doping in the 2D Hubbard model: A dynamical cluster quantum Monte Carlo study. *Phys. Rev. Lett.*, 102(20):206407, May 2009.

[75] Avraham Schiller and Kevin Ingersent. Systematic $1/d$ corrections to the infinite-dimensional limit of correlated lattice electron models. *Phys. Rev. Lett.*, 75(1):113–116, Jul 1995.

[76] A. Toschi, A. A. Katanin, and K. Held. Dynamical vertex approximation: A step beyond dynamical mean-field theory. *Phys. Rev. B*, 75(4):045118, Jan 2007.

[77] H. Park, K. Haule, and G. Kotliar. The magnetic excitation spectra in bafe$_2$as$_2$: a two-particle approach within DFT+DMFT. *arXiv:1104.2942*, 2011.

[78] Jan Kuneš. Efficient treatment of two-particle vertices in dynamical mean-field theory. *Phys. Rev. B*, 83(8):085102, Feb 2011.

[79] T. A. Maier, M. Jarrell, and D. J. Scalapino. Spin susceptibility representation of the pairing interaction for the two-dimensional Hubbard model. *Phys. Rev. B*, 75(13):134519, Apr 2007.

[80] Tetsuya Takimoto, Takashi Hotta, and Kazuo Ueda. Strong-coupling theory of superconductivity in a degenerate Hubbard model. *Phys. Rev. B*, 69(10):104504, Mar 2004.

[81] S. Graser, A. F. Kemper, T. A. Maier, H.-P. Cheng, P. J. Hirschfeld, and D. J. Scalapino. Spin fluctuations and superconductivity in a three-dimensional tight-binding model for bafe$_2$as$_2$. *Phys. Rev. B*, 81(21):214503, Jun 2010.

[82] A. N. Rubtsov, M. I. Katsnelson, and A. I. Lichtenstein. Dual fermion approach to nonlocal correlations in the Hubbard model. *Phys. Rev. B*, 77(3):033101, Jan 2008.

[83] A. N. Rubtsov, M. I. Katsnelson, A. I. Lichtenstein, and A. Georges. Dual fermion approach to the two-dimensional hubbard model: Antiferromagnetic fluctuations and Fermi arcs. *Phys. Rev. B*, 79(4):045133, Jan 2009.

[84] Tudor D. Stanescu and Gabriel Kotliar. Strong coupling theory for interacting lattice models. *Phys. Rev. B*, 70(20):205112, Nov 2004.

[85] A. A. Katanin, A. Toschi, and K. Held. Comparing pertinent effects of antiferromagnetic fluctuations in the two- and three-dimensional Hubbard model. *Phys. Rev. B*, 80(7):075104, Aug 2009.

[86] S. Brener, H. Hafermann, A. N. Rubtsov, M. I. Katsnelson, and A. I. Lichtenstein. Dual fermion approach to susceptibility of correlated lattice fermions. *Phys. Rev. B*, 77(19):195105, May 2008.

[87] Gang Li, Hunpyo Lee, and Hartmut Monien. Determination of the lattice susceptibility within the dual fermion method. *Phys. Rev. B*, 78(19):195105, Nov 2008.

[88] Michael Peskin and Daniel Schroeder. *An Introduction to Quantum Field Theory*. Westview Press, 1995.

[89] S. X. Yang, H. Fotso, J. Liu, T. A. Maier, K. Tomko, E. F. D'Azevedo, R. T. Scalettar, T. Pruschke, and M. Jarrell. Parquet approximation for the 4×4 hubbard cluster. *Phys. Rev. E*, 80(4):046706, Oct 2009.

[90] Y. M. Vilk, Liang Chen, and A.-M. S. Tremblay. Theory of spin and charge fluctuations in the Hubbard model. *Phys. Rev. B*, 49(18):13267–13270, May 1994.

[91] Y. M. Vilk and A.-M. S. Tremblay. Destruction of Fermi-liquid quasiparticles in two dimensions by critical fluctuations. *EPL (Europhysics Letters)*, 33(2):159, 1996.

[92] Junjiro Kanamori. Electron correlation and ferromagnetism of transition metals. *Progress of Theoretical Physics*, 30(3):275–289, 1963.

[93] S.-X. Yang, H. Fotso, S.-Q. Su, D. Galanakis, E. Khatami, J.-H. She, J. Moreno, J. Zaanen, and M. Jarrell. Proximity of the superconducting dome and the quantum critical point in the two-dimensional Hubbard model. *Phys. Rev. Lett.*, 106(4):047004, Jan 2011.

[94] H. Hafermann, G. Li, A. N. Rubtsov, M. I. Katsnelson, A. I. Lichtenstein, and H. Monien. Efficient perturbation theory for quantum lattice models. *Phys. Rev. Lett.*, 102(20):206401, May 2009.

[95] T. A. Maier, A. Macridin, M. Jarrell, and D. J. Scalapino. Systematic analysis of a spin-susceptibility representation of the pairing interaction in the two-dimensional Hubbard model. *Phys. Rev. B*, 76(14):144516, Oct 2007.

[96] Z. B. Huang, W. Hanke, E. Arrigoni, and A. V. Chubukov. Renormalization of the electron-spin-fluctuation interaction in the $t - t' - U$ Hubbard model. *Phys. Rev. B*, 74(18):184508, Nov 2006.

[97] Yoichi Kamihara, Takumi Watanabe, Masahiro Hirano, and Hideo Hosono. Iron-based layered superconductor La[$O_{1-x}F_x$]FeAs (x = 0.05-0.12) with T_c = 26 k. *Journal of the American Chemical Society*, 130(11):3296–3297, 2008.

[98] Hiroki Takahashi, Kazumi Igawa, Kazunobu Arii, Yoichi Kamihara, Masahiro Hirano, and Hideo Hosono. Superconductivity at 43k in an iron-based layered compound $LaO_{1-x}F_xFeAs$. *Nature*, 453(7193):376–378, 2008.

[99] Kenji Ishida, Yusuke Nakai, and Hideo Hosono. To what extent iron-pnictide new superconductors have been clarified: A progress report. *Journal of the Physical Society of Japan*, 78(6):062001, 2009.

[100] G. Shirane, S. M. Shapiro, and J. M. tranquada. *Neutron Scattering with a Triple-Axis Spectrometer: Basic Techniques*. Cambridge University Press, 2002.

[101] Pallab Goswami, Rong Yu, Qimiao Si, and Elihu Abrahams. Spin dynamics of a $J_1 - J_2$ antiferromagnet and its implications for iron pnictides. *arXiv:1009.1111*, 2010.

[102] R. Applegate, J. Oitmaa, and R. R. P. Singh. Spin waves in J_{1a}-J_{1b}-J_2 orthorhombic square-lattice heisenberg models: Application to iron pnictide materials. *Phys. Rev. B*, 81(2):024505, Jan 2010.

[103] Aleksander L. Wysocki, Kirill D. Belashchenko, and Vladimir P. Antropov. Consistent model of magnetism in ferropnictides. *doi:10.1038/nphys1933*, 2011.

[104] S. O. Diallo, V. P. Antropov, T. G. Perring, C. Broholm, J. J. Pulikkotil, N. Ni, S. L. Bud'ko, P. C. Canfield, A. Kreyssig, A. I. Goldman, and R. J. McQueeney. Itinerant magnetic excitations in antiferromagnetic $CaFe_2As_2$. *Phys. Rev. Lett.*, 102(18):187206, May 2009.

[105] Jun Zhao, D. T. Adroja, Dao-Xin Yao, R. Bewley, Shiliang Li, X. F. Wang, G. Wu, X. H. Chen, Jiangping Hu, and Pengcheng Dai. Spin waves and magnetic exchange interactions in $CaFe_2As_2$. *Nature Physics*, 5(8):555–560, 2009.

[106] Liqin Ke, Mark van Schilfgaarde, Jiji Pulikkotil, Takao Kotani, and Vladimir Antropov. Low-energy coherent stoner-like excitations in $CaFe_2As_2$. *Phys. Rev. B*, 83(6):060404, Feb 2011.

[107] J. T. Park, D. S. Inosov, A. Yaresko, S. Graser, D. L. Sun, Ph. Bourges, Y. Sidis, Yuan Li, J.-H. Kim, D. Haug, A. Ivanov, K. Hradil, A. Schneidewind, P. Link, E. Faulhaber, I. Glavatskyy, C. T. Lin, B. Keimer, and V. Hinkov. Symmetry of spin excitation spectra in the tetragonal paramagnetic and superconducting phases of 122-ferropnictides. *Phys. Rev. B*, 82(13):134503, Oct 2010.

[108] E. Kaneshita and T. Tohyama. Spin and charge dynamics ruled by antiferromagnetic order in iron pnictide superconductors. *Phys. Rev. B*, 82(9):094441, Sep 2010.

[109] J. Dong, H. J. Zhang, G. Xu, Z. Li, G. Li, W. Z. Hu, D. Wu, G. F. Chen, X. Dai, J. L. Luo, Z. Fang, and N. L. Wang. Competing orders and spin-density-wave instability in $La(O_{1-x}F_x)FeAs$. *Europhys. Lett.*, 83(2):27006, 2008.

[110] Myung Joon Han, Quan Yin, Warren E. Pickett, and Sergey Y. Savrasov. Anisotropy, itineracy, and magnetic frustration in high-T_C iron pnictides. *Phys. Rev. Lett.*, 102(10):107003, Mar 2009.

[111] T. A. Maier, S. Graser, D. J. Scalapino, and P. Hirschfeld. Neutron scattering resonance and the iron-pnictide superconducting gap. *Phys. Rev. B*, 79(13):134520, Apr 2009.

[112] M. Jarrell. Hubbard model in infinite dimensions: A quantum Monte Carlo study. *Phys. Rev. Lett.*, 69(1):168–171, Jul 1992.

[113] P. Blaha, K. Schwarz, G. K. H. Madsen, K. Kvasnicka, et al. *Wien2K*. Karlheinz Schwarz, Technische Universitat Wien, Austria, 2001.

[114] A. Kutepov, K. Haule, S. Y. Savrasov, and G. Kotliar. Self-consistent *GW* determination of the interaction strength: Application to the iron arsenide superconductors. *Phys. Rev. B*, 82(4):045105, Jul 2010.

[115] Wei Ku, Tom Berlijn, and Chi-Cheng Lee. Unfolding first-principles band structures. *Phys. Rev. Lett.*, 104(21):216401, May 2010.

[116] T. Holstein and H. Primakoff. Field dependence of the intrinsic domain magnetization of a ferromagnet. *Phys. Rev.*, 58(12):1098–1113, Dec 1940.

[117] Z. P. Yin, K. Haule, and G. Kotliar. Magnetism and charge dynamics in iron pnictides. *Nature Physics*, 7(4):294–297, 2011.

Vita

Hyowon Park

Education

2005-current Ph. D. candidate in Department of Physics, Rutgers, the State University of New Jersey, NJ, USA
Thesis advisor: Kristjan Haule

2000-2004 B. Sc. Department of Physics, Pohang University of Science and Technology (POSTECH), Republic of Korea

Positions

2006-2011 Graduate assistant, Department of Physics, Rutgers University.

2007 summer Teaching assistant, Department of Physics, Rutgers University.

Publication List

2011 Mengshu Liu, Leland W. Harriger, Huiqian Luo, Meng Wang, R. A. Ewings, T. Guidi, **Hyowon Park**, Kristjan Haule, Gabriel Kotliar, S. M. Hayden, and Pengcheng Dai, *Nature of Magnetic Excitations in Superconducting* $BaFe_{1.9}Ni_{0.1}As_2$, submitted to Nature Physics.

2011 **Hyowon Park**, Kristjan Haule, Gabriel Kotliar, *The Magnetic Excitation Spectra in* $BaFe_2As_2$*: a two-particle approach within DFT+DMFT*, submitted to Phys. Rev. Lett. (arXiv:1104.2942).

2008 **Hyowon Park**, Kristjan Haule, Gabriel Kotliar, *Cluster Dynamical Mean Field Theory of the Mott Transition*, Phys. Rev. Lett. 101, 186403.

2008 **Hyowon Park**, Kristjan Haule, C. A. Marianetti, and Gabriel Kotliar, *Dynamical Mean-Field Theory Study of Nagaoka Ferromagnetism*, Phys. Rev. B 77, 035107.